OPTIMISATION STRATEGIES FOR PROTON ACCELERATION FROM THIN FOILS WITH PETAWATT ULTRASHORT PULSE LASERS

Tim Ziegler

WISSENSCHAFTLICH-
TECHNISCHE BERICHTE

HZDR

HELMHOLTZ ZENTRUM
DRESDEN ROSSENDORF

Tim Ziegler

OPTIMISATION STRATEGIES
FOR PROTON ACCELERATION FROM THIN FOILS
WITH PETAWATT ULTRASHORT PULSE LASERS

HZDR

HELMHOLTZ ZENTRUM
DRESDEN ROSSENDORF

Optimisation strategies for proton acceleration from thin foils with petawatt ultrashort pulse lasers

Tim Ziegler

Born on: 27th November 1991 in Plauen

Dissertation

to achieve the academic degree

Doctor rerum naturalium (Dr. rer. nat)

Referee
Prof. Dr. Ulrich Schramm
Prof. Dr. Thomas E. Cowan
Prof. Dr. Jörg Schreiber
Supervisor
Dr. Karl Zeil

Submitted on: 15th January 2024

" We are trying to prove ourselves wrong as quickly as possible,
because only in that way can we find progress.'"

— Richard Feynman

Abstract

Laser-driven plasma accelerators can produce high-energy, high peak current ion beams by irradiating solid materials with ultra-intense laser pulses. This innovative concept attracts a lot of attention for various multidisciplinary applications as a compact and energy-efficient alternative to conventional accelerators. The maturation of plasma accelerators from complex physics experiments to turnkey particle sources for practical applications necessitates breakthroughs in the generated beam parameters, their robustness and scalability to higher repetition rates and efficiencies.

This thesis investigates viable optimisation strategies for enhancing ion acceleration from thin foil targets in ultra-intense laser-plasma interactions. The influence of the detailed laser pulse parameters on plasma-based ion acceleration has been systematically investigated in a series of experiments carried out on two state-of-the-art high-power laser systems. A central aspect of this work is the establishment and integration of laser diagnostics and operational techniques to advance control of the interaction conditions for maximum acceleration performance. Meticulous efforts in continuously monitoring and enhancing the temporal intensity contrast of the laser system, enabled to optimise ion acceleration in two different regimes, each offering unique perspectives for applications.

Using the widely established target-normal sheath acceleration (TNSA) scheme and adjusting the temporal shape of the laser pulse accordingly, proton energies up to 70 MeV were reliably obtained over many months of operation. Asymmetric laser pulses, deviating significantly from the standard conditions of an ideally compressed pulse, resulted in the highest particle numbers and an average energy gain $\geq 37\%$. This beam quality enhancement is demonstrated across a broad range of parameters, including thickness and material of the target, laser energy and temporal intensity contrast.

To overcome the energy scaling limitations of TNSA, the second part of the thesis focuses on an advanced acceleration scheme occurring in the relativistically induced transparency (RIT) regime. The combination of thin foil targets with precisely matched temporal contrast conditions of the laser enabled a transition of the initially opaque targets to transparency upon main pulse arrival. Laser-driven proton acceleration to a record energy of 150 MeV is experimentally demonstrated using only 22 J of laser energy on target. The low-divergent high-energy component of the accelerated beam is spatially and spectrally well separated from a lower energetic TNSA component. Start-to-end simulations validate these results and elucidate the role of preceding laser light in pre-expanding the target along with the detailed acceleration dynamics during the main pulse interaction. The ultrashort pulse duration of the laser facilitates a rapid succession of multiple known acceleration regimes to cascade efficiently at the onset of RIT, leading to the observed beam parameters and enabling ion acceleration to unprecedented energies. The discussed acceleration scheme was successfully replicated at two different laser facilities and for different temporal contrast levels. The results demonstrate the robustness of this scenario and that the optimum target thickness decreases with improved laser contrast due to reduced pre-expansion. Target transparency was found to identify the best-performance shots within the acquired data sets, making it a suitable feedback parameter for automated laser and target optimisation to enhance stability of plasma accelerators in the future.

Overall, the obtained results and described optimisation strategies of this thesis may become the guiding step for the further development of laser-driven ion accelerators.

Publications by the author

This thesis contains content which has in parts also been published in scientific journals and presented at international conferences. These parts directly led to the following publications which might contain textual and graphical overlap.

TZ1 **T. Ziegler**, I. Goethel, S. Assenbaum, C. Bernert, F.-E. Brack, T. E. Cowan, N. Dover, L. Gaus, T. Kluge, S. Kraft, F. Kroll, J. Metzkes-Ng, M. Nishiuchi, I. Prencipe, T. Pueschel, M. Rehwald, M. Reimold, H.-P. Schlenvoigt, M. E. P. Umlandt, M. Vescovi, U. Schramm, K. Zeil. "Laser-driven high-energy proton beams from cascaded acceleration regimes" In: *Nature Physics* (2024). DOI: 10.1038/s41567-024-02505-0

TZ2 N. P. Dover, **T. Ziegler**, S. Assenbaum, C. Bernert, S. Bock, F.-E. Brack, T. E. Cowan, E. J. Ditter, M. Garten, L. Gaus, I. Goethel, G. S. Hicks, H. Kiriyama, T. Kluge, J. Koga, A. Kon, K. Kondo, S. Kraft, F. Kroll, H. F. Loewe, J. Metzkes-Ng, T. Miyatake, Z. Nadjumdin, T. Pueschel, M. Rehwald, M. Reimold, H.-P. Schlenvoigt, K. Shiokawa, M. E. P. Umlandt, U. Schramm, K. Zeil, M. Nishiuchi. "Enhanced ion acceleration from transparency-driven foils demonstrated at two ultraintense laser facilities" In: *Light: Science & Applications* 12 (2023). DOI: 10.1038/s41377-023-01083-9

TZ3 **T. Ziegler**, D. Albach, C. Bernert, S. Bock, F.-E. Brack, T. E. Cowan, N. P. Dover, M. Garten, L. Gaus, R. Gebhardt, U. Helbig, A. Irman, H. Kiriyama, T. Kluge, A. Kon, S. Kraft, F. Kroll, M. Loeser, J. Metzkes-Ng, M. Nishiuchi, L. Obst-Huebl, T. Pueschel, M. Rehwald, H.-P. Schlenvoigt, U. Schramm, K. Zeil. "Proton beam quality enhancement by spectral phase control of a PW-class laser system" In: *Scientific Reports* 11 (2021). DOI: 10.1038/s41598-021-86547-x

TZ4 **T. Ziegler**, M. Rehwald, L. Obst, C. Bernert, F.-E. Brack, C. B. Curry, M. Gauthier, S. H. Glenzer, S. Goede, L. Kazak, S. D. Kraft, M. Kuntzsch, M. Loeser, J. Metzkes-Ng, C. Roedel, H.-P. Schlenvoigt, U. Schramm, M. Siebold, J. Tiggesbaeumker, S. Wolter, K. Zeil. "Optical probing of high intensity laser interaction with micron-sized cryogenic hydrogen jets" In: *Plasma Physics and Controlled Fusion* 60 (2018). DOI: 10.1088/1361-6587/aabf4f

Additionally, this PhD project contributed to the following publications:

TZ5 M. Rehwald, S. Assenbaum, C. Bernert, F.-E. Brack, M. Bussmann, T. E. Cowan, C. B. Curry, F. Fiuza, M. Garten, L. Gaus, M. Gauthier, S. Göde, I. Göthel, S. H. Glenzer, L. Huang, A. Huebl, J. B. Kim, T. Kluge, S. Kraft, F. Kroll, J. Metzkes-Ng, T. Miethlinger, M. Loeser, L. Obst-Huebl, M. Reimold, H.-P. Schlenvoigt, C. Schoenwaelder, U. Schramm, M. Siebold, F. Treffert, L. Yang, **T. Ziegler**, K. Zeil. **"Ultra-short pulse laser acceleration of protons to 80 MeV from cryogenic hydrogen jets tailored to near-critical density"** In: *Nature Communications* 14(1) (2023). DOI: 10.1038/s41467-023-39739-0

TZ6 L. Yang, L.Huang, S. Assenbaum, T. E. Cowan, I. Goethel, S. Göde, T. Kluge, M. Rehwald, X. Pan, U. Schramm, J. Vorberger, K. Zeil, **T. Ziegler**, C. Bernert. **"Time-resolved optical shadowgraphy of solid hydrogen jets as a testbed to benchmark particle-in-cell simulations"** In: *Communications Physics* 6 (2023). DOI: 10.1038/s42005-023-01473-w

TZ7 J. Metzkes-Ng, F.-E. Brack, F. Kroll, C. Bernert, S. Bock, E. Bodenstein, M. Brand, T. E. Cowan, R. Gebhardt, S. Hans, U. Helbig, F. Horst, J. Jansen, S. Kraft, M. Krause,E. Lessmann, S. Löck, J. Pawelke, T. Pueschel, M. Reimold, M. Rehwald, C. Richter, H.-P. Schlenvoigt, U. Schramm, M. Schürer, J. Seco, E. R. Szabó, M. E. P. Umlandt, K. Zeil, **T. Ziegler**, E. Beyreuther. **"The DRESDEN PLATFORM is a research hub for ultra-high dose rate radiobiology"** In: *Scientific Reports* 13(1) (2023). DOI: 10.1038/s41598-023-46873-8

TZ8 H. Kiriyama, Y. Miyasaka, A. Kon, M. Nishiuchi, A. Sagisaka, H. Sasao, A. S. Pirozhkov, Y. Fukuda, K. Ogura, K. Kondo, N. Nakanii, Y. Mashiba, N. P. Dover, L. Chang, M. Kando, S. Bock, **T. Ziegler**, T. Püschel, H.-P. Schlenvoigt, K. Zeil, U. Schramm. **"Laser Output Performance and Temporal Quality Enhancement at the J-KAREN-P Petawatt Laser Facility"** In: *Photonics* 10(9) (2023). DOI: 10.3390/photonics10090997

TZ9 C. Bernert, S. Assenbaum, S. Bock, F.-E. Brack, T. E. Cowan, C. B. Curry, M. Garten, L. Gaus, M. Gauthier, R. Gebhardt, S. Göde, S. H. Glenzer, U. Helbig, T. Kluge, S. Kraft, F. Kroll, L. Obst-Huebl, T. Püschel, M. Rehwald, H.-P. Schlenvoigt, C. Schoenwaelder, U. Schramm, F. Treffert, M. Vescovi, **T. Ziegler**, K. Zeil. **"Transient Laser-Induced Breakdown of Dielectrics in Ultrarelativistic Laser-Solid Interactions"** In: *Physical Review Applied* 19(1) (2023). DOI: 10.1103/PhysRevApplied.19.014070

TZ10 M. Reimold, S. Assenbaum, C. Bernert, E. Beyreuther, F.-E. Brack, L. Karsch, S. D. Kraft, F. Kroll, A. Nossula, J. Pawelke, M. Rehwald, H.-P. Schlenvoigt, U. Schramm, M. E. P. Umlandt, K. Zeil, **T. Ziegler**, J. Metzkes-Ng. **"Dosimetry for radiobiological in vivo experiments at laser plasma-based proton accelerators"** In: *Physics in Medicine & Biology* 68(18) (2023). DOI: 10.1088/1361-6560/acf025

TZ11 M. Reimold, S. Assenbaum, E. Beyreuther, E. Bodenstein, F.-E. Brack, C. Eisenmann, F. Engelbrecht, F. Kroll, F. Lindner, U. Masood, J. Pawelke, U. Schramm, M. Schneider, M. Sobiella, M. E. P. Umlandt, M. Vescovi, K. Zeil, **T. Ziegler**, J. Metzkes-Ng. **"OCTOPOD: single bunch tomography for angular-spectral characterization of laser-driven protons"** In: *High Power Laser Science and Engineering* (2023). DOI: 10.1017/hpl.2023.55

TZ12 S. Bock, T. Oksenhendler, T. Püschel, R. Gebhardt, U. Helbig, R. Pausch, **T. Ziegler**, C. Bernert, K. Zeil, A. Irman, T. Toncian, H. Kiriyama, M. Nishiuchi, A. Kon, U. Schramm. **"Spectral-temporal measurement capabilities of third-order correlators"** In: *Opt. Express* 31(6) (2023). DOI: 10.1364/OE.475575

TZ13 F. Kroll, F.-E. Brack, C. Bernert, S. Bock, E. Bodenstein, K. Brüchner, T. E. Cowan, L. Gaus, R. Gebhardt, U. Helbig, L. Karsch, T. Kluge, S. Kraft, M. Krause, E. Lessmann, U. Masood, S. Meister, J. Metzkes-Ng, A. Nossula, J. Pawelke, J. Pietzsch, T. Pueschel, M. Reimold, M. Rehwald, C. Richter, H.-P. Schlenvoigt, U. Schramm, M. E. P. Umlandt, **T. Ziegler**, K. Zeil, E. Beyreuther. "Tumor irradiation in mice with a laser-accelerated proton beam" In: *Nature Physics* 18(3) (2022). DOI: 10.1038/s41567-022-01520-3

TZ14 C. Bernert, S. Assenbaum, F.-E. Brack, T. E. Cowan, C. B. Curry, M. Garten, L. Gaus, M. Gauthier, S. Göde, S. H. Glenzer, T. Kluge, S. Kraft, F. Kroll, M. Kuntzsch, J. Metzkes-Ng, M. Loeser, L. Obst-Huebl, M. Rehwald, H.-P. Schlenvoigt, C. Schoenwaelder, U. Schramm, M. Siebold, F. Treffert, **T. Ziegler**, K. Zeil. "Off-harmonic optical probing of high intensity laser plasma expansion dynamics in solid density hydrogen jets" In: *Scientific Reports* 12(1) (2022). DOI: 10.1038/s41598-022-10797-6

TZ15 I. Göthel, C. Bernert, M. Bussmann, M. Garten, T. Miethlinger, M. Rehwald, K. Zeil, **T. Ziegler**, T. E. Cowan, U. Schramm, T. Kluge. "Optimized laser ion acceleration at the relativistic critical density surface" In: *Plasma Physics and Controlled Fusion* 64(4) (2022) DOI: 10.1088/1361-6587/ac4e9f

TZ16 M. Reimold, S. Assenbaum, C. Bernert, E. Beyreuther, F.-E. Brack, L. Karsch, S. Kraft, F. Kroll, M. Loeser, A. Nossula, J. Pawelke, T. Püschel, H.-P. Schlenvoigt, U. Schramm, M. E. P. Umlandt, K. Zeil, **T. Ziegler**, J. Metzkes-Ng. "Time-of-flight spectroscopy for laser-driven proton beam monitoring" In: *Scientific Reports* 12(1) (2022). DOI: 10.1038/s41598-022-25120-6

TZ17 A. Kon, M. Nishiuchi, Y. Fukuda, Y., K. Kondo, K. Ogura, A. Sagisaka, Y. Miyasaka, N. P. Dover, M. Kando, A. S. Pirozhkov, I. Daito, L. Chang, I. W. Choi, C. H. Nam, **T. Ziegler**, H.-P. Schlenvoigt, K. Zeil, U. Schramm, H. Kiriyama. "Characterization of the plasma mirror system at the J-KAREN-P facility" In: *High Power Laser Science and Engineering* 10 (2022). DOI: 10.1017/HPL.2022.15

TZ18 A. Laso Garcia, A. Hannasch, M. Molodtsova, A. Ferrari, J. P. Couperus Cadabağ, M. C. Downer, A. Irman, S. D. Kraft, J. Metzkes-Ng, L. Naumann, I. Prencipe, U. Schramm, K. Zeil, R. Zgadzaj, **T. Ziegler**, T. E. Cowan. "Calorimeter with Bayesian unfolding of spectra of high-flux broadband x rays" In: *Review of Scientific Instruments* 93(4) (2022). DOI: 10.1063/5.0078443

TZ19 M. Nishiuchi, N. P. Dover, M. Hata, H. Sakaki, Ko. Kondo, H. F. Lowe, T. Miyahara, H. Kiriyama, J. K. Koga, N. Iwata, M. A. Alkhimova, A. S. Pirozhkov, A. Y. Faenov, T. A. Pikuz, A. Sagisaka, Y. Watanabe, M. Kando, K. Kondo, E. J. Ditter, O. C. Ettlinger, G. S. Hicks, Z. Nadjmudin, **T. Ziegler**, K. Zeil, U. Schramm, Y. Sentoku. "Dynamics of laser-driven heavy-ion acceleration clarified by ion charge states" In: *Physical Review Research* 2(3) (2020). DOI: 10.1103/PhysRevResearch.2.033081

TZ20 N. P. Dover, M. Nishiuchi, H. Sakaki, Ko. Kondo, H. F. Lowe, M. A. Alkhimova, E. J. Ditter, O. C. Ettlinger, A. Y. Faenov, M. Hata, G. S. Hicks, N. Iwata, H. Kiriyama, J. K. Koga, T. Miyahara, Z. Najmudin, T. A. Pikuz, A. S. Pirozhkov, A. Sagisaka, U. Schramm, Y. Sentoku, Y. Watanabe, **T. Ziegler**, K. Zeil, M. Kando, K. Kondo. "Demonstration of repetitive energetic proton generation by ultra-intense laser interaction with a tape target" In: *High Energy Density Physics* 37 (2020). DOI: 10.1016/j.hedp.2020.100847

TZ21 A. Huebl, M. Rehwald, L. Obst-Huebl, **T. Ziegler**, M. Garten, R. Widera, K. Zeil, T. E. Cowan, M. Bussmann, U. Schramm, T. Kluge. "Spectral control via multi-species effects in

PW-class laser-ion acceleration" In: *Plasma Physics and Controlled Fusion* 62(12) (2020). DOI: 10.1088/1361-6587/abbe33

TZ22 F.-E. Brack, F. Kroll, L. Gaus, C. Bernert, E. Beyreuther, T. E. Cowan, L. Karsch, S. Kraft, L. A. Kunz-Schughart, E. Lessmann, J. Metzkes-Ng, L. Obst-Huebl, J. Pawelke, M. Rehwald, H.-P. Schlenvoigt, U. Schramm, M. Sobiella, E. R. Szabó, **T. Ziegler**, K. Zeil. "Spectral and spatial shaping of laser-driven proton beams using a pulsed high-field magnet beamline" In: *Scientific Reports* 10(1) (2020). DOI: 10.1038/s41598-020-65775-7

TZ23 H. Kiriyama, A. S. Pirozhkov, M. Nishiuchi, Y. Fukuda, A. Sagisaka, A. Kon, Y. Miyasaka, K. Ogura, N. P. Dover, Ko. Kondo, H. Sakaki, J. K. Koga, T. .Z. Esirekepov, K. Huang, N. Nakanii, M. Kando, K. Kondo, S. Bock, **T. Ziegler**, T. Püschel, K. Zeil, U. Schramm. "Petawatt Femtosecond Laser Pulses from Titanium-Doped Sapphire Crystal" In: *Crystals* 10(9) (2020). DOI: 10.3390/cryst10090783

TZ24 Ko. Kondo, M. Nishiuchi, H. Sakaki, N. P. Dover, H. F. Lowe, T. Miyahara, Y. Watanabe, **T. Ziegler**, K. Zeil, U. Schramm, E. J. Ditter, G. S. Hicks, O. C. Ettlinger, Z. Najmudin, H. Kiriyama, M. Kando, K. Kondo. "High-Intensity Laser-Driven Oxygen Source from CW Laser-Heated Titanium Tape Targets" In: *Crystals* 10(9) (2020). DOI: 10.3390/cryst10090837

TZ25 S. Bock, F. M. Herrmann, T. Püschel, U. Helbig, R. Gebhardt, J. J. Lötfering, R. Pausch, K. Zeil, **T. Ziegler**, , A. Irman, T. Oksenhendler, A. Kon, M. Nishiuchi, H. Kiriyama, K. Kondo, T. Toncian, U. Schramm. "Characterization of Accumulated B-Integral of Regenerative Amplifier Based CPA Systems" In: *Crystals* 10(9) (2020). DOI: 10.3390/cryst10090847

TZ26 A. Kon, M. Nishiuchi, H. Kiriyama, M. Kando, S. Bock, **T. Ziegler**, T. Püschel, K. Zeil, U. Schramm, K. Kondo. "Single-Shot Measurement of Post-Pulse-Generated Pre-Pulse in High-Power Laser Systems" In: *Crystals* 10(8) (2020). DOI: 10.3390/cryst10080657

TZ27 L. Obst-Huebl, **T. Ziegler**, F.-E. Brack, J. Branco, M. Bussmann, T. E. Cowan, C. B. Curry, F. Fiuza, M. Garten, M. Gauthier, S. Göde, S. H. Glenzer, A. Huebl, A. Irman, J. B. Kim, T. Kluge, S. Kraft, F. Kroll, J. Metzkes-Ng, R. Pausch, I. Prencipe, M. Rehwald, C. Roedel, H.-P. Schlenvoigt, U. Schramm, K. Zeil. "All-optical structuring of laser-driven proton beam profiles" In: *Nature Communications* 9(1) (2018). DOI: 10.1038/s41467-018-07756-z

TZ28 L. Obst, J. Metzkes-Ng, S. Bock, G. E. Cochran, T. E. Cowan, T. Oksenhendler, P. L. Poole, I. Prencipe, M. Rehwald, C. Roedel, H.-P. Schlenvoigt, U. Schramm, D. W. Schumacher, **T. Ziegler**, K. Zeil. "On-shot characterization of single plasma mirror temporal contrast improvement" In: *Plasma Physics and Controlled Fusion* 60(5) (2018). DOI: 10.1088/1361-6587/aab3bb

TZ29 L. Obst, S. Göde, M. Rehwald, F.-E. Brack, J. Branco, S. Bock, M. Bussmann, T. E. Cowan, C. B. Curry, F. Fiuza, M. Gauthier, R. Gebhardt, U. Helbig, A. Huebl, U. Hübner, A. Irman, L. Kazak, J. B. Kim, T. Kluge, S. Kraft, M. Loeser, J. Metzkes, R. Mishra, C. Roedel, H.-P. Schlenvoigt, M. Siebold, J. Tiggesbäumker, S. Wolter, **T. Ziegler**, U. Schramm, S. H. Glenzer, K. Zeil. "Efficient laser-driven proton acceleration from cylindrical and planar cryogenic hydrogen jets" In: *Scientific Reports* 7(1) (2017). DOI: 10.1038/s41598-017-10589-3

Contents

1 Introduction

1.1 Motivation

The remarkable development of laser technology and the associated ability to generate extremely high energy densities has given rise to a fundamentally new and disruptive technology in the field of particle beam physics – laser-driven plasma acceleration.

This innovative approach harnesses the strong electromagnetic fields supported by a plasma to accelerate particles in an exceptionally compact way, representing a paradigm shift from conventional high-frequency-based accelerator technology, where the maximum achievable field gradients are limited by the breakdown of the vacuum inside the accelerating structure [1]. Plasma, as an already broken down state of matter, is an ideal accelerating medium capable of sustaining field gradients with almost no physical limitations. In today's scientific landscape, particle accelerators serve as vital drivers for fundamental research and play a pivotal role in advancing methods across various applications in industry and medicine. Plasma accelerators hold the potential to expand the portfolio of achievable beam parameters and to significantly shrink the size of particle accelerators, thereby reducing the need for large infrastructures at considerable financial cost. Particular attention has been paid to the generation of pulsed, highly laminar, multi-MeV ion beams produced by irradiating solid materials with ultra-intense laser pulses [2, 3]. In 2000, several groups reported the first generation of intense, high-energy (> 10 MeV) proton beams using the high-power lasers Nova Petawatt in Livermore [4] and Vulcan in Oxford [5]. This achievement sparked the vision of realising applications of societal relevance, including the fast ignition approach to inertial confinement fusion [6, 7] and laser-driven medical proton therapy [8, 9]. To date, laser-driven ion accelerators are already applied as diagnostic tools and ultrafast drivers in high energy density science [10] and material science studies [11, 12], as well as efficient sources for neutron generation [13, 14] and high dose rate radiobiology [15, 16]. Despite these achievements, progress has been slower than anticipated and several outstanding issues still need to be addressed before laser-driven ion accelerators can evolve from physics experiments to turnkey particle sources for practical and impactful applications. This maturation necessitates breakthroughs in the generated beam parameters, such as the maximum energy, the spectral distribution and conversion efficiency. Additionally, reproducibility, robustness and scalability of the laser-plasma interaction to high repetition rates also require increased attention.

In the historical context, new record energies were attained using large-scale high-energy lasers with limited shot rate and the **Target Normal Sheath Acceleration (TNSA)** scheme [17]. This extensively studied and well-established acceleration method involves irradiating

micrometer-thick solid-state targets with a high-intensity laser, resulting in the creation of a plasma at the target front side. Free electrons within the plasma are accelerated by the laser and traverse through the target, establishing a quasi-static electric field at the target's rear. Subsequently, protons and ions from the target rear surface are accelerated over a very short distance, reaching relativistic energies and typically forming a broad exponential energy spectra. TNSA, however, inherently lacks specific energy selection options and increasing the maximum energy of the accelerated particles primarily relies on increasing the amount of laser energy coupled into the plasma [18]. Throughout the last twenty years, there was a huge effort to optimise the laser and target parameters to enhance this coupling and hence the acceleration performance for a given laser energy. This involves special structuring of the target surface and composition as well as extensive laser pulse parameter scans. Although these approaches have achieved energy enhancement effects [19–21] and produced quasi-monoenergetic particle spectra [22, 23], it has proved difficult to reproduce these results and to compare data from different laser systems.

The recent advent of high-power ultrashort pulse lasers [24], which are now commercially available and capable of high repetition rates (> 1 Hz), opens up new avenues to accelerate the exploration of this multi-parameter space. Gaining a comprehensive understanding of how to efficiently harness the capabilities of these increasingly available laser systems is fundamental on the path to meeting application-specific requirements with plasma accelerators and a central aspect of this thesis. These laser systems can approach new intensity frontiers (> 10^{22} W cm^{-2}) and provide additional options for control, diagnostics, analysis and real-time feedback. This unique combination makes these systems particularly suited to study advanced acceleration mechanisms that are conceptually different to TNSA. In recent years, various advanced ion acceleration schemes have been identified and investigated through both theoretical and numerical studies. Central to all these schemes is the presence of electromagnetic field structures to achieve a more coherent acceleration, aiming for improved particle beam parameters such as higher maximum ion energies, reduced divergence, minimised energy spread and a more favourable energy scaling. These advanced concepts already enabled compact high intensity lasers with significantly reduced laser energy (< 10 J) and repetition rates relevant for practical applications to achieve performance levels similar to large-scale high-energy lasers (> 100 J) [25–29]. However, the experimental differentiation of these advanced acceleration schemes has proven challenging. This difficulty arises due to the coexistence of multiple acceleration mechanisms throughout the entire laser-plasma interaction, compounded by insufficiently characterised laser and target parameters that serve as input for numerical simulations. Particularly, non-ideal temporal laser contrast, i.e. laser energy arriving at the target before the intense main pulse, results in substantial heating and pre-expansion of the target, consequently effecting the entire plasma interaction dynamics. Given that state-of-the-art laser systems can easily reach relativistic peak intensities, consideration of electric field contributions with high dynamic range and high temporal resolution becomes crucial. This necessitates the development and implementation of appropriate laser pulse diagnostics and measurement strategies, revealing the intensity distribution in the focal plane during or parallel to the plasma interaction.

Another important challenge faced by the community of laser-driven plasma accelerators is the reliable comparison of data and results from numerous experiments, as well as laser parameters. Despite the use of similar technologies at various high-power laser facilities, many system-specific features persist that have a significant impact on accelerator performance.
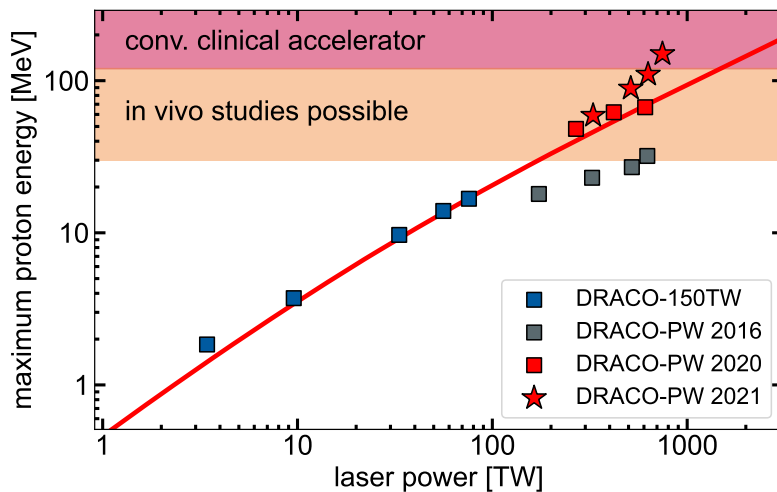
Figure 1.1: **Proton acceleration performance at DRACO-PW:** The blue and black squares show the maximal achievable proton energies at the beginning of this thesis. The red line shows an extrapolated energy scaling. The red squares and stars show the results, obtained from experiments with optimised interaction conditions, that were developed in the context of this thesis.

1.2 Thesis outline

The work presented in this thesis focuses on significantly advancing the performance of plasma-based proton acceleration from thin foil targets that were irradiated with ultrashort laser pulses with ultra-high intensity ($\geq 10^{21}$ W cm^{-2}). A series of experimental campaigns, conducted at the DRACO-PW laser in Dresden and at the J-KAREN-P laser in Kyoto, addressed key aspects for the realisation of laser-driven ion sources for applications. A unique advantage of this research was the continuous access to these laser systems and the ongoing development of the experimental setup over the course of this thesis. This allowed to establish standardised techniques for temporal pulse contrast characterisation and optimisation. These advances were key to enabling a detailed investigation of the laser pulse parameters and their effect on plasma acceleration, ultimately allowing for the identification of optimal interaction conditions for maximum performance. This development is illustrated in Figure 1.1, showing the ion acceleration performance achieved in different years using the DRACO laser system. Based on the results that were achieved with the 150 TW DRACO laser [30] (blue squares) an energy scaling could be extrapolated (red line), suggesting that proton energies close to 100 MeV can be achieved, once the petawatt level is reached. However, the experimental results fell short (black squares), failing to follow the established scaling. This performance level marked the starting point of the thesis, making it imperative to unravel the underlying reasons and develop optimisation strategies to enhance maximum proton energies – the primary objective of this Ph.D. project.

The thesis is divided into six chapters, starting with this introduction, followed by chapter 2 which lays the theoretical foundations for understanding the underlying physical concepts related to laser-driven plasma acceleration. The experimental methodologies of this thesis are detailed in chapter 3, describing the different laser systems and the diagnostic techniques used to conduct the experiments.
Results on optimising laser-driven ion acceleration from plastic foil targets in the TNSA regime at DRACO-PW are presented in chapter 4. Initially, this involved implementing a single-shot plasma mirror system, along with on-shot pulse diagnostic and metrology

ports to characterise the temporal laser parameters in the target environment. Precise measurement and control of the temporal pulse properties of the laser enabled the identification of the ideal laser pulse shape for optimal acceleration performance. The highest proton cut-off energies and particle numbers were observed for temporal pulse parameters significantly different from the standard conditions of a nearly ideally compressed pulse. This robust optimisation procedure became a daily preparation routine for proton acceleration experiments at the DRACO-PW laser, facilitating an energy scaling (red squares in Figure 1.1) that aligns with the previously established extrapolation. The resulting performance optimisation was the basis for conducting worlds first "*in vivo*" small animal pilot study using laser-driven protons. However, the modest energy scaling of TNSA makes it difficult to further increase the achievable particle energies without upgrading the DRACO-PW laser to significantly higher pulse energies.

The combination of thin foil targets with matched temporal contrast conditions of the laser allowed access to an advanced acceleration regime where the initially opaque target undergoes a transition to transparency during the interaction with the laser pulse. This phenomenon is known as **Relativistically Induced Transparency (RIT)**, resulting from the combined effects of electron heating, expansion, and the relativistic mass increase of the electrons. The impact of RIT on ion acceleration with ultrashort laser pulses and solid-density foil targets is studied both experimentally and theoretically in chapter 5. The results demonstrate that the preceding laser light can be utilised to prime the target for transparency upon main pulse arrival, simplifying the complexity of the ion source and enhancing its robustness. Protons with energies exceeding 60 MeV and fully ionised carbon ions with energies surpassing $30\,\mathrm{MeV\,u^{-1}}$ were experimentally demonstrated. Start-to-end simulations verify these results and elucidate the role of the preceding laser light in pre-expanding the target as well as the detailed acceleration dynamics during the main pulse interaction. The most energetic particles are accelerated by the extreme space charge-induced electric field that is generated due to electron expulsion from the target core when the foil becomes transparent, followed by further acceleration in a diffuse sheath. This acceleration scheme was replicated at two different laser facilities and different temporal contrast levels, emphasising the level of control and understanding of this scheme and that the optimum target thickness decreases as laser contrast improves due to reduced pre-expansion.

Building on these findings, chapter 6 marks the culmination of all previous efforts to optimise ion acceleration in the RIT regime, which has ultimately led to breakthrough achievements for plasma-accelerated proton beams. Using the rep-rated laser system DRACO-PW and only 22 J laser energy on target, laser-driven proton beams clearly exceeding 100 MeV kinetic energy and bandwidth-limited energy spectra have been generated with application-relevant particle yields. These results were achieved by strategically choosing an initial target thickness, that ensures the interaction of the main laser pulse with a near-critical target due to the pre-expansion earlier in the interaction. Furthermore, the experimental setup was optimised to enable an angularly resolved proton beam measurement with multiple detectors based on different detection methods. The experimental findings are supported by full-scale 3D particle-in-cell simulations, revealing that multiple known acceleration regimes cascade efficiently at the onset of RIT. The ultrashort pulse duration of the laser facilitates a rapid succession of these regimes at highest intensity, leading to the observed beam parameters and enabling proton acceleration to unprecedented energy levels. In particular, the scaling of the maximum proton energy in this regime is very promising (red stars in Figure 1.1), allowing to access an energy range of considerable interest for applications.

Finally, chapter 7 summarises the main results of this thesis and discusses future prospects for laser-driven ion acceleration, concluding this research.

2 Fundamentals of laser-matter interactions

This chapter is intended to provide the fundamental concepts of relativistic laser-matter interaction and the basic concept of laser-driven particle acceleration physics.
When intense laser light is irradiated onto a solid-state material, the high electromagnetic fields start to ionise the front surface of this material. For modern short-pulse lasers with ultra-high intensities, ionisation can occur well before the arrival of the main laser pulse through preceding laser light components such as pre-pulses, coherently compressed light, or finally during the rising edge of the main pulse. As a result, the highest field components of the laser interact with a plasma instead of an initially solid-state material. The energy of the laser can now be transferred directly to free electrons, which can thus be accelerated to relativistic velocities. In the further course of the interaction, the energy absorbed by the plasma electrons can be partially converted into kinetic energy of ions.

2.1 Plasma

Almost all of the matter in the observable universe is in the plasma state (which is sometimes also referred to as the "fourth state of matter" since it clearly differs from the other states of aggregation). In contrast, plasma is rarely found in our natural environment, so it was not before 1879 when William Crookes conducted the first documented experiment to create plasma under laboratory conditions [31]. Today, various artificial technologies exist that generate plasma for a range of applications in medicine, material processing, energy, display and propulsion technology. The word "plasma" was first introduced by Irving Langmuir as a description for an ionised gas with an equal number of electrons and ions [32]. A more formal definition was given by Francis F. Chen [33]:

> "*A plasma is a quasi-neutral gas of charged and neutral particles which exhibits collective behaviour*"

The two concepts quasi-neutral and collective behaviour are central for this definition of plasma. Collective behaviour means in this context, that even though the plasma is made of a mix of free electrons and ions, these particles continuously interact with each other as their motion creates currents and local regions of positive and negative charge. This leads to electric and magnetic fields that can also influence charged particles at large distances, thereby causing a collective macroscopic behaviour of the plasma. It is partly this effect that explicitly distinguishes a plasma from a normal ionised gas.

Quasi-neutrality describes the fact that the overall charge of a plasma is close to zero when averaged in time and over large volumes. In contrast, at smaller scales, the plasma may have local positive and negative charge distributions that give raise to electric field structures (as described above). This characteristic distance beyond which the plasma is neutralising any discrete charge is called **Debye-length λ_D** and defined as follows:

$$\lambda_D = \sqrt{\frac{\varepsilon_0 \, k_B \, T_e}{n_e \, e^2}} \tag{2.1}$$

where ε_0 is the vacuum permittivity[1], k_B the Boltzmann constant[2], e the electron charge[3], T_e the electron temperature and n_e the electron density. Quasi-neutrality is given when the dimension L of a system is much larger than $\lambda_D : L \gg \lambda_D$

Note that Equation 2.1 has only two variable parameters, T_e and n_e that can influence the Debye-length. These are two fundamental parameters to characterise a plasma, from which a lot of subsidiary parameters and properties can be derived.

2.1.1 Plasma properties

A comprehensive description of the properties of plasma at a microscopic level would require the self-consistent calculation of all electric and induced magnetic fields between all particles. However, in many cases, it is not necessary to consider individual particles in the plasma and simplified models can be used to reduce complexity. Models from fluid mechanics, which describe the plasma in terms of collective effects and properties, allow for the consideration of macroscopic parameters rather than microscopic ones. In this model, electrons and ions are treated as separate fluids that are in thermal equilibrium. The velocity distribution of those particles is characterised by their temperature (T_e for electrons, T_i for ions). The number of electrons N_e and ions N_i per volume V defines the **electron density n_e** and the **ion density n_i** of a plasma, respectively. The electron density for any kind of material with ionisation state Z and atomic mass A can be obtained as:

$$n_e = \frac{N_e}{V} \simeq Z \, n_i = \frac{Z \, N_i}{V} = \frac{Z \, N_A \, \rho}{A} \tag{2.2}$$

where N_A is the Avogadro constant[4] and ρ the mass density of the material.

The mass of electrons (m_e) is much smaller than that of protons (m_p) or ions (m_i), which allows for the assumption that ions can be treated as a stationary positive background for the free-moving electrons. This simplification, known as the Drude model [34, 35], assumes that the electrons move freely through an ionic background and collide with it in a similar way to gas molecules. Solving the Poisson equation allows to derive the scalar electric potential $\varphi(r)$ of the plasma:

$$\nabla^2 \varphi = \frac{-e \, (n_i - n_e)}{\varepsilon_0} \tag{2.3}$$

The electron density n_e is assumed to follow a Boltzmann distribution:

$$n_e = n_0 \exp\left(\frac{e \, \varphi}{k_B \, T_e}\right) \tag{2.4}$$

---

[1] $\varepsilon_0 = 8.854 \times 10^{-12} \, \mathrm{F \, m^{-1}}$, ε_0 is a fundamental physical constant
[2] $k_B = 1.381 \times 10^{-23} \, \mathrm{J \, K^{-1}}$
[3] $e = 1.602 \times 10^{-19} \, \mathrm{C}$, e is a fundamental physical constant
[4] $N_A = 6.022 \times 10^{23} \, \mathrm{mol^{-1}}$

After substituting Equation 2.4 in Equation 2.3, expanding the exponential in a Taylor series and solving the remaining differential equation, the resulting potential for a test charge q reads:

$$\varphi(r) = \frac{q}{4\pi\varepsilon_0 r} \exp\left(\frac{-r}{\lambda_D}\right) \tag{2.5}$$

Hence, the potential of the test charge q at distance λ_D will be dropped by 1/e. This result mathematically justifies the introduction of λ_D as an effective shielding distance. Furthermore, this characteristic screening is only satisfied, when there are enough particles available in the plasma to shield the influence of the test charge. Using Equation 2.5 enables to calculate the number of particles in a Debye sphere:

$$N_D = \frac{4}{3}\pi n_e \lambda_D^3 \tag{2.6}$$

The collective behaviour of a plasma also requires $N_D \gg 1$.

When plasma electrons are deflected from the stationary ionic background, an electric field is generated to restore the quasi-neutrality of the plasma. However, the inertia of the electrons causes them to be accelerated beyond their original position and to oscillate at a characteristic frequency known as **plasma frequency ω_P** or **Langmuir frequency**, named after Irving Langmuir who first derived the equation to describe this oscillation [32]:

$$\omega_P = \sqrt{\frac{n_e e^2}{\varepsilon_0 \gamma m_e}} \tag{2.7}$$

with Lorentz factor γ which is defined as:

$$\gamma = \frac{1}{\sqrt{1 - \frac{v^2}{c^2}}} \tag{2.8}$$

where v is the relative velocity between inertial reference frames (i.e. the velocity of the oscillating electrons) and c the speed of light in vacuum[5]. It is important to note, that ω_P only depends on the plasma density (demonstrating again why n_e is a fundamental plasma parameter) and not on the wave vector k, which is perpendicular to the wave front, indicating the propagation direction of the wave.

2.1.2 Dispersion relation of a plasma

The **permittivity ε** of the plasma describes its ability to support electric fields and is generally represented by a tensor that accounts for any anisotropy of the medium. However, if plasma is treated as a linear, non-dispersive homogeneous and isotropic medium, ε simplifies to a scalar. The propagation of transverse electromagnetic waves in such a medium can be described using the wave equation (which can be derived from the Maxwell equation):

$$\nabla^2 \vec{E} - \varepsilon_0 \mu_0 \frac{\partial^2}{\partial t^2}\vec{E} = \mu_0 \frac{\partial}{\partial t}\vec{j} \tag{2.9}$$

with electric field vector $\vec{E}$ and vacuum permeability μ_0[6] and electric current density $\vec{j}$. The current density $\vec{j}$ originates on short time scales only from moving electrons and can be described as:

$$\vec{j} = -e\, n_e\, \vec{v_e} \tag{2.10}$$

---

[5]$c = 299792458\,\mathrm{m\,s^{-1}} \simeq 3 \times 10^8\,\mathrm{m\,s^{-1}}$, c is a fundamental physical constant
[6]$\mu_0 = 1.256 \times 10^{-6}\,\mathrm{N\,A^{-2}}$

The velocity of the electrons $\vec{v_e}$ can be calculated using Newton's second law of motion and the Lorentz force:

$$m_e \frac{d\vec{v_e}}{dt} = q(\vec{E} + \vec{v_e} \times \vec{B}) \tag{2.11}$$

For plasmas where $|\vec{v_e} \times \vec{B}| \ll |E|$, Equation 2.10 becomes:

$$\vec{j} = \frac{e^2 n_e \vec{v_e}}{i \omega m_e} \vec{E} \tag{2.12}$$

Furthermore, the relation between $\vec{j}$ and $\vec{E}$ is simplified by assuming a linear relation:

$$\vec{j} = \sigma \vec{E} \tag{2.13}$$

with σ representing the plasma conductivity.
Substituting now Equation 2.12 into Equation 2.9 and assuming a plane monochromatic wave as solution one gets:

$$-k^2 + \varepsilon_0 \mu_0 \omega^2 = \mu_0 \frac{e^2 n_e}{m_e} \tag{2.14}$$

where $\vec{E}$ is defined as:

$$\vec{E} = E_0 \exp\left(i(\vec{k}\vec{r} - \omega t)\right) \tag{2.15}$$

with amplitude E_0, wave vector k and angular frequency ω.
Rearranging Equation 2.14 and using $\varepsilon_0 \mu_0 = c^{-2}$ finally results in the dispersion relation for an electromagnetic field in a plasma:

$$\omega^2 = \omega_P^2 + k^2 c^2 \tag{2.16}$$

with plasma frequency ω_P as introduced in Equation 2.7 and wavenumber k:

$$k = \frac{\omega}{c} \sqrt{1 - \frac{\omega_P^2}{\omega^2}} \tag{2.17}$$

2.1.3 Laser propagation in a plasma

When an electromagnetic field (e.g. a laser) with frequency ω is applied to a plasma, one can distinguish two different cases:

If $\boldsymbol{\omega > \omega_P}$, the term inside the root of Equation 2.17 will be positive, meaning that the incoming wave is able to propagate through the plasma. In such a scenario the plasma is called **underdense** or **undercritical**. In the limit of very high frequencies the propagation tends to c.

Contrary if $\boldsymbol{\omega < \omega_P}$, the root of Equation 2.17 will be negative, resulting in an imaginary wavenumber. Such a plasma is called **overdense** or **overcritical** as the electrons inside the plasma respond sufficiently fast on any perturbation. Hence, no energy is transmitted through the plasma and the incident wave simply reflected. The electromagnetic field decays exponentially in space as can be seen by putting the imaginary k into Equation 2.15. The distance at which the amplitude of this "evanescent" electric field has dropped to 1/e is called **plasma skin depth l_s** and defined as:

$$l_s = \frac{c}{\sqrt{\omega_P^2 - \omega^2}} = \frac{c}{\sqrt{\frac{n_e e^2}{\varepsilon_0 \gamma m_e} - \omega^2}} \tag{2.18}$$

The case where $\omega = \omega_P$ defines the threshold density or **classical critical density of the plasma** n_c being a fundamental concept in plasma physics. If $n_e > n_c$, the plasma is able to effectively reflect or refract the electromagnetic wave, and if $n_e < n_c$ the wave is able to propagate through the plasma.

If the amplitude of the incident electric field is so high, that the electron velocity becomes relativistic, the γ factor reduces the plasma frequency (as the electron mass increases) and hence lower frequencies can still propagate through the plasma. The **relativistic critical density** n_c^{rel} accounts for this effect:

$$n_c^{rel} = \gamma\, n_c = \frac{\gamma\, m_e\, \varepsilon_0\, \omega^2}{e^2} \tag{2.19}$$

Figure 2.1 illustrates the consequence of this effect on the dispersion relation (c.f. Equation 2.17) for an electromagnetic wave propagating in a plasma. For sufficiently high
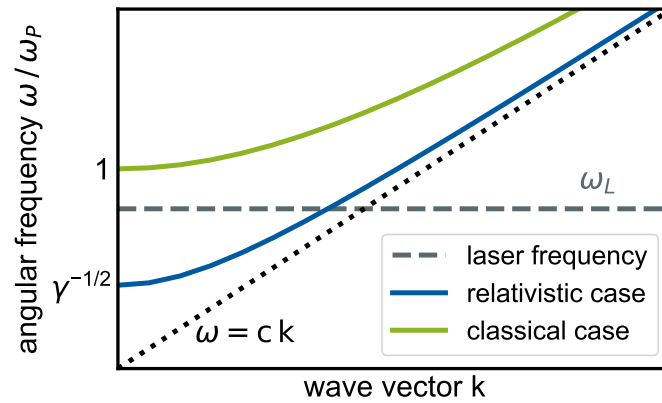
Figure 2.1: Dispersion relation for an electromagnetic wave in a plasma. The dispersion relation of an electromagnetic wave in vacuum (black dotted line) is shown for comparison. In the classical case (green solid line), the lower cutoff is given by the plasma frequency ω_P. In the relativistic case (blue solid line), the lower cutoff is reduced due to the relativistic mass increase. Depending on the angular frequency of the laser, the plasma electrons can either follow the oscillation of the electromagnetic wave and the laser can propagate into the underdense plasma ($\omega_L > \omega_P$) or the plasma electrons react faster than the perturbation of the electromagnetic wave ($\omega_L < \omega_P$), effectively shielding the plasma from the laser, which is reflected instead.

values of γ, the relativistically corrected plasma frequency ω_P / γ can decrease below the laser frequency ω_L, making the plasma transparent to the laser. This effect is one important factor contributing to the onset of relativistically induced transparency in a plasma, a phenomenon that is explained in subsubsection 2.3.3.

It is important to note here, that n_c is frequency dependent, a fact of particular relevance when considering ultrashort laser pulses, which naturally possess a finite spectral bandwidth (e.g. 1000's of THz for fs pulses). If $n_e \gg n_c$, Equation 2.18 simplifies to $l_s \simeq c / \omega_P$

The dispersion relation Equation 2.17 also allows to derive the phase velocity v_p and the group velocity v_g of the plasma wave:

$$v_p = \frac{\omega}{k} = \frac{c}{\sqrt{1 - \omega_P^2 / \omega^2}} \tag{2.20}$$

and

$$v_g = \frac{d\omega}{dk} = v_p + k\frac{dv_P}{dk} = c\sqrt{1 - \frac{\omega_P^2}{\omega^2}} \qquad (2.21)$$

It is noteworthy, that in a plasma the phase velocity v_p of an electromagnetic wave is clearly different from the group velocity v_g, especially since $v_p > c$ is possible. However, any information transfer of an electromagnetic wave is mediated with group velocity v_g, which always satisfies $v_g < c$.

Finally, we can define the **refractive index η** of a plasma as:

$$\eta = \frac{c}{v_p} = \frac{ck}{\omega} = \sqrt{1 - \frac{\omega_P^2}{\omega^2}} = \sqrt{1 - \frac{n_e}{\gamma n_c}} = \sqrt{1 - \frac{n_e}{n_c^{rel}}} \qquad (2.22)$$

allowing to easily distinguish between regions where η is real, allowing the laser (with angular frequency ω_L) to propagate into the underdense plasma, and regions where η is an imaginary number, causing the laser to be reflected at the critical density of the overdense plasma.

From Equation 2.22 it becomes also apparent that a spatial variation of γ and the plasma density n_e (e.g. caused by any realistic spatial intensity distribution of a laser) results in a spatially varying refractive index, which can lead to self-focusing of the laser as it propagates through the plasma. As a consequence the plasma acts as a focusing lens on the laser, leading to further focusing and increased intensity along the laser propagation axis. Relativistic self-focussing requires the incident laser to excess a certain threshold (critical) power P_{cr} which is defined as [36]:

$$P_{cr} = \frac{m_e c^5 \omega^2}{e^2 \omega_P^2} \simeq 17 \left(\frac{\omega}{\omega_P}\right)^2 [GW] \qquad (2.23)$$

Laser pulses exceeding P_{cr} and propagating through an underdense plasma can experience relativistic self-guiding, where the laser pulse is confined in a very small spatial area over distances much larger than the Rayleigh length.

2.2 Laser-matter interactions

The previous section introduced plasma as a special state of matter with unique properties. Building upon this basis, this section studies how matter and solid-state materials interact with intense laser light. This includes an examination of the plasma generation processes, the interactions between laser light and charged particles within the plasma, and how these interactions result in the acceleration of particles to very high energies.

2.2.1 Ionisation processes

According to the definition provided in section 2.1, plasma is a gaseous state of matter consisting of charged and neutral particles. The transition from a solid-state material to the plasma state is achieved through ionisation of bound electrons. This ionisation can result from different mechanisms, such as impact-ionisation, which occurs through collisions with energetic particles like electrons, or photo-ionisation, which occurs through interactions with photons. These mechanisms are visualised in Figure 2.2 and will be detailed in the following section. Mathematically these ionisation processes can be rep-
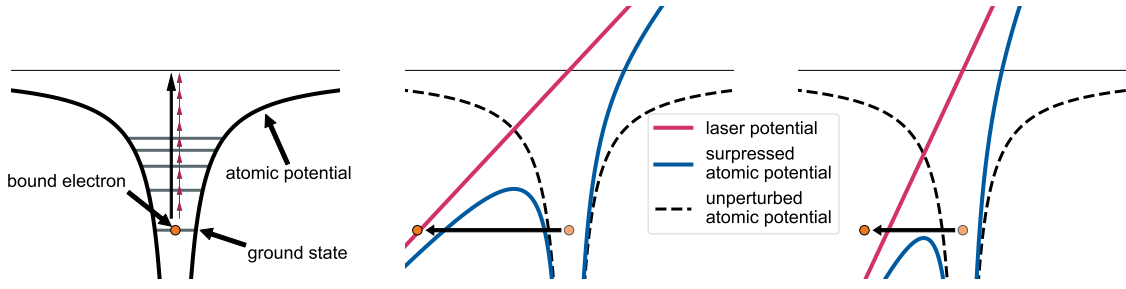
Figure 2.2: Illustration of different ionisation processes relevant for laser-plasma interaction. A bound ground-sate electron can overcome the binding potential by Multi-Photon (left), Tunnelling (middle) or Barrier-suppression ionisation (right).

resented using reaction equations:

$$e^- + A \rightarrow A^+ + 2e^- \qquad \text{impact-ionisation} \qquad (2.24)$$
$$h\nu + A \rightarrow A^+ + e^- \qquad \text{photo-ionisation} \qquad (2.25)$$

with Planck constant[7] $h = 2\pi\hbar$. At the beginning of the laser-matter interaction there are no free electrons which can be accelerated by the laser and cause impact-ionisation. As a result, the only remaining possibility for ionisation is photo-ionisation by laser photons. The energy of such a photon must be high enough to overcome the Coulomb binding energy of the atom. The energy of a single photon with frequency ω_{ph} and wavelength λ_{ph} (e.g. 800 nm, which is a typical value for Ti:Sa lasers) can be calculated using Planck's equation:

$$E_{ph} = \hbar\omega_{ph} = 2\pi\frac{c}{\lambda_{ph}} = 1.54\,\text{eV} \qquad \text{for } \lambda_{ph} = 800\,\text{nm} \qquad (2.26)$$

This photon energy can be compared to the binding energy of a hydrogen atom with Bohr radius a_B[8]:

$$E_{at} = \frac{e^2}{8\pi\varepsilon_0}\frac{1}{a_B} = 13.61\,\text{eV} \qquad (2.27)$$

indicating that the energy of a single photon at $\lambda_{ph} = 800\,\text{nm}$ is insufficient to ionise a hydrogen atom. However, achieving ionisation is possible by using the energy of multiple photons whose total energy exceeds the energy threshold for ionisation.

Multiphoton ionisation

MultiPhoton Ionisation (MPI) is a physical process in which multiple photons interact within a certain time interval with an atom to overcome the binding energy of an electron. The number of photons (n) required for MPI of a hydrogen atom can be estimated as $n = E_{at}/E_{ph} \geq 9$. If the total number of photons is higher than this value (n), the electron will absorb the energy of the additional photons (s) resulting in a final energy E_f of:

$$E_f = (n+s)\hbar\omega_{ph} - E_{at} = s\hbar\omega_{ph} \qquad (2.28)$$

This process is known as **Above Threshold Ionisation (ATI)**. Experimentally, it has been shown, that MPI and ATI dominate for laser intensities below $10^{13}\,\text{W}\,\text{cm}^{-2}$.

---

[7]$h = 6.6 \times 10^{-34}\,\text{J}\,\text{s}$
[8]$a_B = 4\pi\varepsilon_0\hbar^2/(m_e e^2) \approx 0.529 \times 10^{-10}\,\text{m}$

Field ionisation

If the laser intensity is further increased, the electric field of the laser becomes strong enough to significantly alter the Coulomb potential, leading to a change in the potential barrier experienced by the electrons. Depending on the strength of the electric field, two distinct mechanisms can be distinguished. **Tunnelling Ionisation (TI)** occurs, if electrons can escape the atom by tunnelling through the lowered potential barrier. This process dominates for laser intensities $I_L \simeq 10^{14}\,\text{W}\,\text{cm}^{-2}$. Once the electric field of the lasers surpasses this intensity regime, the potential barrier may become even lower than the electron's bound state energy and the electron can simply escape the atom. This process is known as **Barrier Suppression Ionisation (BSI)**.

Using Equation 2.27 enables to calculate the binding field of a hydrogen atom:

$$\mathcal{E}_{at} = \frac{e}{4\,\pi\,\varepsilon_0\,a_B^2} \simeq 5.1 \times 10^9\,\text{V}\,\text{m}^{-1} \tag{2.29}$$

To free electrons from this atomic binding field, the intensity of a laser must be at least:

$$I_{at} = \frac{\varepsilon_0\,c}{2}\,\mathcal{E}_{at}^2 \approx 4 \times 10^{16}\,\text{W}\,\text{cm}^{-2} \tag{2.30}$$

As soon as the laser intensity is higher than I_{at}, the potential becomes lower than the binding energy of the electrons. As a consequence the electrons can freely escape.

Modern laser systems can easily achieve peak intensities that well exceed I_{at}, meaning that ionisation can already occur much earlier due to laser light components which precedes the laser main pulse. Most solid-state materials are thus already fully ionised upon main pulse arrival.

A good method to determine which of the aforementioned ionisation processes dominates under different interaction conditions is provided by the **Keldysh parameter** γ_K which was introduced by Leonid Keldysh [37]:

$$\gamma_K = \omega_L \sqrt{\frac{2\,E_{at}}{I_L}} \tag{2.31}$$

where E_{at} is the atomic binding energy, ω_L the angular frequency and I_L the intensity of the laser, respectively. MPI is the prevailing process for $\gamma_K \gg 1$, while for $\gamma_K \ll 1$ the electric field of the laser is so high that BSI dominates. In addition to these clearly separable cases, the Keldysh theory [38] also allows the ionisation rates to be described by analytical formulae for intermediate parameter values.

Impact ionisation

Once free electrons are available, impact or collisional ionisation, as described in Equation 2.24, becomes another relevant ionisation process during the laser-matter interaction. Electrons which were initially field ionised can now absorb energy from the laser through inverse Bremsstrahlung (detailed in subsubsection 2.2.4) and get accelerated to high kinetic energies. When these fast-moving electrons collide with other atoms, they can transfer some of their energy to bonded electrons in the valence band, exciting them to the conduction band and causing further ionisation. This can lead to an avalanche effect and a rapid increase in the number of free electrons in the material. The electron-ion collision frequency ν_{ei} can be calculated by [39]:

$$\nu_{ei} = \frac{4\sqrt{2\pi}}{3}\frac{n_e\,Z\,e^4}{m_e^2\,v_{te}}\,\ln\Lambda \simeq 2.91 \times 10^{-6}\,\frac{Z\,n_e}{T_e^{3/2}}\,\ln\Lambda\;[\text{s}^{-1}] \tag{2.32}$$

where v_{te} the electron's thermal velocity and "ln Λ" the Coulomb logarithm, which is a dimensionless plasma parameter and defined as:

$$\Lambda = \frac{b_{max}}{b_{min}} = \lambda_D \frac{k_B T_e}{Z e^2} \tag{2.33}$$

where b_{max} and b_{min} describe the maximum and minimum impact parameters (perpendicular distance between the colliding particle's trajectories) of the electron-ion scattering cross-section. In general, collisions in a plasma involve particle interactions that result in a significant change in energy and momentum, e.g. due to Coulomb interactions between charged particles. Consequently, Coulomb collisions with impact parameters larger than λ_D (c.f. Equation 2.1) will rarely occur as the plasma neutralises any discrete charge. The Coulomb logarithm thus describes the dominance of small-angle deflections for Coulomb collisions in a plasma. A plasma is dominated by collisions if $v_{ei}/\omega_P \geq 1$ and considered collision-free if $v_{ei}/\omega_P \ll 1$.

2.2.2 Electron dynamics in the laser field

In order to understand the mechanisms by which the laser can transfer its energy to the plasma (detailed in subsection 2.2.4), it is necessary to understand first the interaction of a single charged particle with an external electromagnetic field. The motion of a charged particle in the presence of an electromagnetic field (with electric and magnetic field components $\vec{E}$ and $\vec{B}$) can be described by using the Lorentz force $\vec{F}_L$:

$$\vec{F}_L = q\,(\vec{E} + \vec{v} \times \vec{B}) = \frac{\mathrm{d}\vec{p}}{\mathrm{d}t} \tag{2.34}$$

where q is the charge, $\vec{v}$ the velocity and $\vec{p}$ the relativistic momentum of the particle. At currently achievable laser intensities and for laser intensities relevant to the experiments of this thesis ($I_L < 10^{22}\,\mathrm{W\,cm^{-2}}$), ions experience a negligible displacement under the influence of the laser field due to their high mass. Electrons, on the other hand, are significantly affected by electromagnetic fields of this intensity once they are released from their binding potential. This again justifies the assumption made in subsection 2.1.1 and the discussion in this section will be therefore restricted to electrons.

As long as the momentum of the electron is nonrelativistic (e.g. for low laser intensities), the $\vec{v} \times \vec{B}$ term of Equation 2.34 can be ignored and the electrons will oscillate with the frequency of the driving electric field, along the laser polarisation direction and with the following maximum oscillation velocity:

$$v_{osc} = \frac{e\,|\vec{E}|}{m_e\,\omega_L} \tag{2.35}$$

For strong laser fields and thus high oscillation velocities (approaching c), the electron mass increases (as γ becomes relevant) and the $\vec{v} \times \vec{B}$ component can get to the same order as $\vec{E}$. Consequently, the influence of the magnetic field can no longer be ignored, resulting in a longitudinal force at twice the laser frequency that pushes the electrons along the laser propagation axis. The maximum longitudinal oscillation velocity can be calculated via:

$$v_{long} = \frac{e^2\,|\vec{E}|^2}{4\,m_e^2\,\omega_L^2\,c} \tag{2.36}$$

A comparison between Equation 2.35 and Equation 2.36 shows, that the longitudinal velocity of he electrons scales much faster with the electric field strength than their oscillation velocity.

To easily distinguish between the relativistic and nonrelativistic regimes of electron motion, the **normalised vector potential** a_0 can be introduced. This dimensionless parameter is derived from the electron quiver velocity and characterises the relative strength of the laser field:

$$a_0 = \frac{v_{max}}{c} = \frac{e\,|\vec{E}|}{m_e\,\omega_L\,c} = \sqrt{\frac{e^2\,\xi\,I_L\,\lambda_L^2}{4\,\pi^2\,\varepsilon_0\,m_e^2\,c^5}} \simeq \sqrt{\frac{\xi\,I_L\,\lambda_L^2}{2.74\times 10^{18}\,\text{W cm}^{-2}\,\mu\text{m}}} \tag{2.37}$$

where λ_L is the laser wavelength, I_L the laser intensity and $\xi = 2$ for linear polarisation and $\xi = 1$ for circular polarisation. As soon as $a_0 \simeq 1$ the electrons oscillation velocity becomes so high that relativistic effects must be considered, while $a_0 \ll 1$ represents the nonrelativistic case. After defining a_0, Equation 2.35 and Equation 2.36 can now be easily rewritten to:

$$v_{osc} = a_0\,c \tag{2.38}$$

$$v_{long} = \frac{a_0^2\,c}{4} \tag{2.39}$$

This result clearly shows how the two velocity components scale with a_0, which is particularly interesting when the laser intensity is increased. Apart from the oscillating component in the longitudinal direction, there is also a static drift velocity:

$$v_{drift} = \frac{a_0^2\,c}{a_0^2 + 4} \tag{2.40}$$

For a linearly polarised laser, the combination of all velocity components results in a figure-of-eight motion of electrons in their rest frame and a zig-zag motion in the laboratory frame. For a circularly polarised laser, the oscillating $\vec{v} \times \vec{B}$ component vanishes and the electrons move radially in their rest frame, while following a helix trajectory in the laboratory frame. Figure 2.3 visualises this behaviour of the electrons for different polarisations, which is of central importance for the plasma heating mechanisms introduced in subsection 2.2.4.
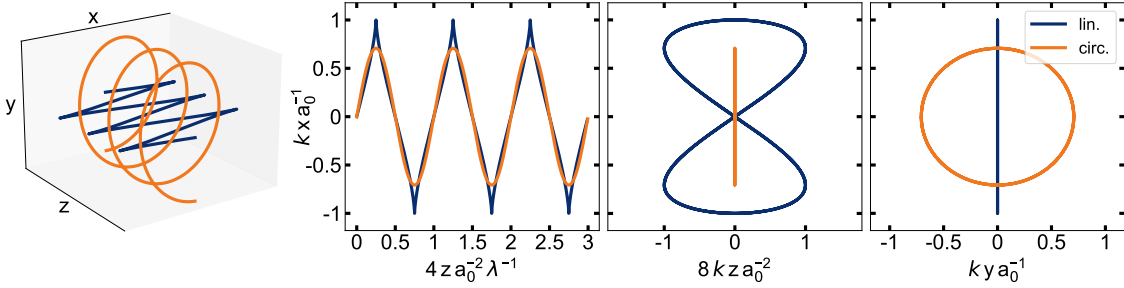
Figure 2.3: Visualisation of relativistic electron motion in an electromagnetic field with an intensity of $a_0 = 1$ for both linear (blue) and circular (orange) polarisations:
The left plot shows the 3D electron trajectories in the laboratory frame, while the other three plots depict the electron motion in the x-direction (electric field oscillation direction) against the z-direction (electromagnetic field propagation direction) in the laboratory frame (left) as well as in the rest frame of the electron (center) and against the y-direction (magnetic field oscillation direction) in the rest frame of the electron (right).

2.2.3 Ponderomotive force

The previous section considered the electromagnetic field as a plane wave, where the intensity is constant in space and only slowly varying in time. According to the Woodward-Lawson theorem [40, 41], isolated, relativistic electrons will not gain a net energy transfer

from the laser in this scenario, as they return to their initial position after a full laser cycle. However, this principle is altered in the presence of additional static fields or if the oscillating electromagnetic field features a spatial or temporal intensity gradient. To achieve relativistic intensities in realistic experimental conditions, ultrashort laser pulses are usually tightly focused to a small spatial area and strongly compressed in time. This creates inhomogeneous electromagnetic fields that affect the electron trajectories. During their oscillation, electrons are accelerated in the first half-cycle into regions of lower laser intensity, causing them to experience a lower restoring force during the second half-cycle. This results in electrons being pushed away by the so-called **ponderomotive force** $\vec{F_P}$ from regions of highest laser intensity. A quantitative expression for the ponderomotive force was first derived by Bauer *et al.* [42] as well as Quesnel and Mora [43]. In the nonrelativistic regime, the ponderomotive force averaged over a laser cycle becomes:

$$\vec{F_P} = \frac{-e^2}{2\, m_e\, \omega_L^2} \nabla \langle \vec{E}^2 \rangle = \frac{-e^2}{8\, \pi^2\, \varepsilon_0\, m_e\, c^3} \nabla (I_L \lambda^2) \propto \nabla a_0^2 \tag{2.41}$$

where $\langle \vec{E}^2 \rangle = |\vec{E}|^2/2$ is the time averaged squared electric field. This also allows to define a **ponderomotive potential** Φ_P by considering $\vec{F_P} = -\nabla \Phi_P$:

$$\Phi_P = \frac{e^2 \langle \vec{E}^2 \rangle}{2\, m_e\, \omega_L^2} \tag{2.42}$$

As discussed in subsection 2.2.2, relativistic electrons experience an additional longitudinal drift due to the non-negligible influence of the magnetic field and an relativistic mass increase, yielding:

$$\vec{F_P} = -m_e\, c^2\, \nabla \langle \gamma \rangle \tag{2.43}$$

where $\langle \gamma \rangle$ is the time averaged Lorentz factor of an electron, being $\langle \gamma \rangle = \sqrt{1 + a_0^2/2}$ for linear polarisation and $\langle \gamma \rangle = \sqrt{1 + a_0^2}$ for circular polarisation. The relativistic ponderomotive potential can then be derived as:

$$\Phi_P = m_e\, c^2\, (\langle \gamma \rangle - 1) \tag{2.44}$$

2.2.4 Plasma heating processes

After electrons have been freed from their binding potential, they are able to interact with the electromagnetic field of the laser. During this interaction the electrons can absorb energy from the laser by multiple mechanisms which depend on laser parameters like wavelength, intensity, polarisation and angle of incidence but also on the plasma density distribution. The transfer of laser energy into kinetic energy of electrons is referred to as plasma heating, since the final Maxwellian velocity distribution of the electrons can be described by an average temperature T_e. This temperature of the heated and thus hot electrons is different from the background or unheated, cold electrons, which are not affected by the laser. As previously discussed in subsection 2.1.3, the laser can only interact efficiently with an overdense plasma up to a certain distance, introduced as skin depth l_s. Beyond this distance, the electromagnetic field of the laser is rapidly attenuated and the heating of the plasma becomes less efficient. Therefore, most of the interaction and absorption processes occur at the interface between the underdense and overdense plasma. The most important absorption mechanisms during laser-matter interaction are discussed in the following section, while detailed information can be found in the literature [33, 39, 44, 45].

Plasma expansion

As realistic laser pulses always feature preceding laser light components which can interact with the plasma, a significant amount of thermal pressure is applied before the main pulse arrival. This causes the plasma to expand into surrounding vacuum with a velocity which can be approximated by the ion sound speed c_s:

$$c_s = \sqrt{\left(\frac{Z\,k_B\,(T_e + T_i)}{m_e} \right)} \tag{2.45}$$

with T_e and T_i beeing the average electron and ion temperature, respectively.
Depending on the detailed temporal intensity profile of the laser pulse, expansion of the plasma can happen long before the main laser pulse arrives. This results in a reduction of the plasma core-density and a deviation from the initially step-like spatial plasma density profile resulting in an altered exponential plasma density profile:

$$n_e(z) = n_0 \exp\left(\frac{-z}{L_P} \right) \tag{2.46}$$

where z is the distance from the target surface, n_0 the initial electron density and $\boldsymbol{L_P}$ the characteristic **plasma scale length**, which can be calculated with the plasma expansion time t_s as $L_P = c_s\,t_s$. Such calculations deliver a simple estimation for L_P, while more realistic values can be obtained by performing hydrodynamic simulations and fitting L_P to the resultant plasma density profile.

Inverse Bremsstrahlung

When an electron collides with another charged particle, it decelerates and emits electromagnetic radiation, a process known as Bremsstrahlung radiation. Inverse Bremsstrahlung is the reverse process and one of the most common absorption mechanisms. Thereby, the electron is accelerated by the electric field of the laser, resulting in a transfer of energy from the laser photon to the electron. Typically, the electron will not gain energy due to experiencing an equal and opposite acceleration in the oscillating field of the laser pulse. However, if the electron collides with an ion during the oscillation, energy will be transferred from the electron to the ion, resulting in a net loss of energy by the laser through collisions of charged particles. The frequency for those electron-ion collisions (c.f. Equation 2.32) was introduced in subsection 2.2.1 and can be simplified for the following discussion to:

$$\nu_{ei} \simeq 2.91 \times 10^{-6}\, \frac{n_e\,Z}{T_e^{3/2}}\, \ln\left(\frac{\lambda_D\,k_B\,T_e}{Z\,e^2} \right) \;\propto\; \frac{n_e\,Z}{T_e^{3/2}} \tag{2.47}$$

High plasma densities n_e, high-Z materials and low electron temperatures T_e are leading to an increase of ν_{ei} and thus to higher absorption. As the laser intensity increases, the electron temperature rises accordingly, leading to a reduction of the collision frequency ν_{ei} and thus reduced absorption via inverse Bremsstrahlung. As a result, inverse Bremsstrahlung is most efficient for lower laser intensities where the plasma remains collisional. The relevant intensity regime for collisional absorption is limited to intensities below $10^{17}\,\mathrm{W\,cm^{-2}}$.

Resonance absorption

Resonance absorption is a mechanism where energy is transferred from the laser to the plasma electrons through the excitation of resonant plasma waves at the critical density

surface. To facilitate this process, the incident laser pulse must be p-polarised and directed at an oblique angle θ relative to the target. Laser light will only propagate up to $n_e = n_c \cos^2(\theta)$ before being reflected. However a fraction of the laser field can tunnel up to the critical density n_c where it will excite a resonant plasma wave at $\omega_P = \omega_L$ [45]. As the laser pulse propagates under an oblique angle through the plasma, it also continually experiences refraction due to the inhomogeneity of the plasma density (c.f. Equation 2.22). This results in a modification of the laser intensity and phase, which in turn affects the excitation of resonant plasma waves. To effectively drive a plasma wave, the plasma scale length L_p must be greater than the laser wavelength λ_L, and there must be an electric field component parallel to the density gradient. The excited plasma wave will further transfer energy to the cold plasma via collisional damping effects of the wave or wave breaking. Resonance absorption is dominant for laser intensities below $10^{17}\,\mathrm{W\,cm^{-2}}$ but the efficiency is reduced for steep plasma density gradients and when the incident laser is directed perpendicular to the target surface.

Vacuum heating

Vacuum heating, which is also referred to as Brunel heating or "not-so-resonant, resonant absorption" [46] occurs under very similar conditions as described for resonance absorption, but in the presence of steep plasma gradients where $L_p < \lambda_L$. In this regime, the sharp transition from vacuum to an overdense plasma prevents the excitation of plasma waves at the critical density n_c. Instead, during one half cycle of the laser's electromagnetic field electrons are pulled out from the plasma into vacuum. In the subsequent half cycle of the oscillation, the electrons get accelerated back into the overdense target and may even surpass the critical density surface. There, the electromagnetic field of the laser quickly decays within the skin depth l_s, resulting in a weaker or even vanishing restoring force acting on the electrons. Consequently, the electrons get a net positive energy gain and continue to propagate into the target with the laser frequency ω_L. Numerical simulations of this phenomenon have provided a more detailed understanding, revealing that electrons can undergo multiple oscillations before they are finally pushed beyond the critical density.

j x B heating

As soon as the laser intensity is within the relativistic regime $a_0 \geq 1$, electrons get rapidly accelerated close to c within a single laser cycle. As introduced in subsection 2.2.2, the $\vec{v} \times \vec{B}$ term of the Lorentz force becomes relevant, leading to $2\,\omega_L$ oscillations of electrons along the laser propagation direction for linearly polarised light. As a consequence, electrons located at the plasma front are accelerated at twice the laser frequency into the overdense plasma region, where they experience reduced electromagnetic fields. This process resembles vacuum heating and the ponderomotive force, as electrons are ejected from regions of high laser intensity into the laser propagation direction. The electrons will thereby acquire a mean energy which can be approximated by the ponderomotive potential Φ_P:

$$k_B T_e \simeq \Phi_P = m_e c^2 (\langle \gamma \rangle - 1) \propto \sqrt{I_L \lambda_L^2} \qquad (2.48)$$

For circular polarisation, the oscillating term of the electron motion disappears, resulting in a steady push forward with the previously introduced drift velocity v_{drift}. When combined with normal incidence, this leads to a significant suppression of electron heating,

which is advantageous for processes that primarily rely on laser pressure as the dominating mechanism (e.g. radiation pressure acceleration, which will be discussed in subsection 2.3.2).

Scaling laws

The previous paragraphs discussed different heating mechanisms through which laser energy can be transferred to electrons. These mechanisms lead to the generation of relativistic "hot" electrons, which propagate away from the target, as well as a population of "colder", less energetic electrons that remain within the bulk of the target. The interaction between the target and a high-intensity laser pulse typically involves a complex interplay of these heating mechanisms, as their dominance varies for different laser (intensity I_L, **Angle Of Incidence (AOI)**, polarisation) and target parameters (plasma scale length L_P, material). For various applications of laser-plasma interactions, especially laser-driven ion acceleration, understanding and optimising the efficiency of this laser to electron energy transfer for different interaction parameters is of great importance. To comprehend and anticipate experiments, there have been numerous analytical and empirical endeavours, to establish a scaling of the hot electron temperature T_{hot}. During laser-solid interaction with high-intensity laser pulses, $\vec{J} \times \vec{B}$ heating is usually the dominating heating mechanism. The scaling of the hot electron temperature for this mechanism, known as ponderomotive or Wilks scaling [47], suggests $T_{hot} \propto (I_L \lambda_L^2)^{1/2}$ (c.f. Equation 2.48). However, experiments with ultra-high laser intensities struggled to follow the ponderomotive scaling. Beg *et al.* reported an empirical scaling of experimental data (10^{17} W cm^{-2} < I_L < 10^{19} W cm^{-2}, linear polarisation, AOI = 30°), where $T_{hot} \propto (I_L \lambda_L)^{1/3}$ [48]. These results could be reproduced and extended up to $I_L \simeq 5 \times 10^{21}$ W cm^{-2} for different pulse durations (0.5 – 5 ps), AOI (0° – 40°) and target materials [49, 50]. Haines *et al.* developed an analytic models based on momentum conservation, which is in agreement with Beg's empirical scaling of experimental data [51]. Another analytical approach was derived by Kluge *et al.*, which utilises a weighted average of the kinetic energy of the electrons and is applicable to both relativistic and non-relativistic laser intensities [52]. This model showed high agreement to both experimental and simulation data and is given by:

$$T_{hot} \simeq \begin{cases} I_L \lambda_L^2, & a_0 \ll 1. \\ \sqrt{I_L \lambda_L^2} \left(\ln \left(\sqrt{I_L \lambda_L^2} \right) \right)^{-1}, & a_0 \gg 1. \end{cases} \tag{2.49}$$

Dover *et al.* proposed a heuristic model that also considers the focal spot size of the laser and thereby restricts the effective electron acceleration length [53]. Their model reflects that electrons escape the focal spot of the laser and undergo transverse scattering before reaching the maximum ponderomotive potential, explaining a slower scaling of T_{hot}. Other experimental and simulation results infer, that the deviation from the ponderomotive scaling is related to non-ideal pre-plasma conditions and reduced energy coupling efficiency at the target front side [54, 55].

2.3 Laser-driven ion acceleration mechanisms

The previous sections of this chapter studied in detail how plasma electrons are affected and accelerated by the electromagnetic field of a laser pulse. So far, ion motion has been ignored during this interaction due to their significantly higher mass compared to electrons ($m_i \geq 1836\, m_e$). This approximation is justified on the sub-ps time scale and as long as the laser intensity is below $I_L \lambda_L^2 \approx 5 \times 10^{24}$ W cm^{-2} μm^2 (corresponds to

$a_0 < 1836$). Such intensities are currently unattainable even with the most advanced high-power laser systems.

However, ions can still be accelerated indirectly through a secondary process mediated by plasma electrons. As described in subsection 2.2.4, electrons get accelerated and expand from the target, leading to a charge separation of electrons and ions. This process generates quasi-static electric fields within the plasma, which can reach magnitudes of several $TV\,m^{-1}$, far exceeding the field strengths achievable by conventional radio-frequency technology (tens of $MV\,m^{-1}$) [56]. Irradiating micrometer-thick targets with high-intensity laser light generates these sheath fields and has established as the most reliable method for laser-driven ion acceleration. The achievable maximum ion energies for this process primarily depend on the amount of laser energy which can be converted into hot electrons.

In recent years, a number of advanced and conceptually different ion acceleration schemes have been identified and investigated in both theoretical and numerical studies. These schemes aim to utilise electromagnetic field structures to achieve a more coherent acceleration of ions, with the prospect of improved particle beam parameters such as higher maximum ion energies, reduced divergence, reduced energy spread and others. However, the experimental realisation and differentiation of these advanced acceleration schemes has proven to be difficult, especially since several acceleration mechanisms can coexist during the entire laser-plasma interaction.

This section provides an introduction to the physics of the different ion acceleration schemes, building on the previously discussed principles of laser-plasma interaction and laying the foundation for the experimental studies in chapter 4, chapter 5 and chapter 6. A comprehensive overview and more details about the different mechanisms can be found in the review papers by Daido *et al.* [2] and Macchi *et al.* [3].

2.3.1 Target normal sheath acceleration

To date, the most extensively studied and robust method to accelerate ions is the **Target-Normal Sheath Acceleration (TNSA)** mechanism. This process is illustrated in Figure 2.4 and involves the acceleration of ions from a contamination layer located on the surface of a typically micrometre-thick solid-state target when irradiated by a high-intensity laser. The pioneering experiments conducted by Snavely *et al.* [4] and Clark *et al.* [5] demonstrated the acceleration of ions to multi-MeV energies per nucleon. Maksimchuk *et al.* reported at the same time also the generation of a $\approx 1\,MeV$ proton beam using ultrashort laser pulses with significantly lower laser energy [57]. These experimental breakthroughs were later explained theoretically by Wilks *et al.*, providing a comprehensive understanding of the underlying physics and mechanisms involved in TNSA [17].

The interaction of the preceding light of the laser pulse with the target front side initiates the formation of a plasma and subsequent heating through laser energy absorption, as discussed in subsection 2.2.1 and subsection 2.2.4. Front side accelerated electrons propagate into the bulk of the target, thereby causing further ionisation and the generation of return currents within the target. Electrons which acquired sufficiently high energies can even propagate through the entire target and expand from the target rear into the surrounding vacuum. As more and more electrons leave the target, the target gets a net positive charge balance, resulting in Coulomb forces that are pulling back the escaping electrons. However, very energetic ("fast") electrons can overcome this restoring force and freely propagate into the vacuum. Lower energetic electrons, re-enter the target and begin to recirculate between the front and rear side of the target [58, 59]. As a consequence, electrons start to effectively accumulate at the target rear, forming
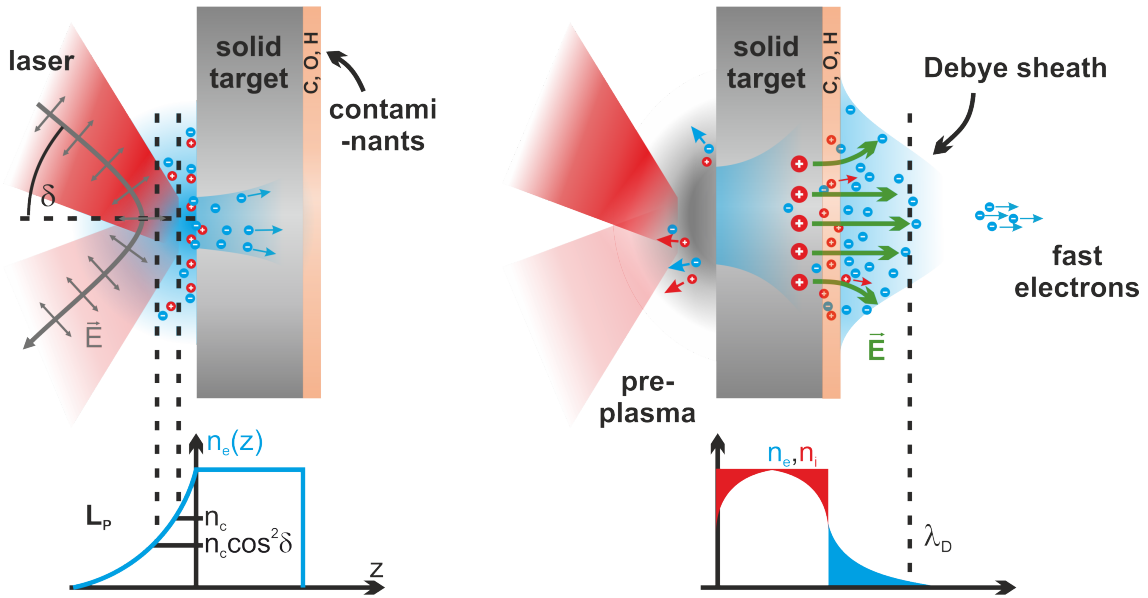
Figure 2.4: Schematic of the target normal sheath acceleration process: The preceding laser light starts to generate a plasma with pre-plasma scale length L_P at the target front side where electrons are heated and accelerated into the target by absorbing energy from the laser. As electrons exit the target rear, they form the Debye sheath, leading to a quasi-static electric field and subsequent accelerations of ions from the contamination layer on the target rear.

a Debye sheath with a longitudinal spatial extension which is determined by the Debye length λ_D (see Equation 2.1). The lateral extension of the sheath is related to the dynamic of the electrons as they propagate through the target in a diverging cone geometry [60, 61]. An estimation for the lateral sheath radius B was proposed by Schreiber *et al.* [62] using the following equation:

$$B = r_L + d \tan \theta \tag{2.50}$$

where r_L denotes the laser spot size, d the initial target thickness and θ the half opening-angle for electrons propagating through the target. Experimental and numerical studies have shown that θ ranges between $20° – 50°$ [63, 64].

The Debye sheath and the positively charged target generate a very intense ($\geq 10^{12}\,\mathrm{V\,m^{-1}}$) quasi-static electric field which is oriented perpendicular to the target normal surface. The electric field quickly ionises atoms from the contaminant layer as well as in the bulk of the target and accelerates them to relativistic energies. The contaminant layer primarily includes hydrocarbons and water vapour that adhere on the target surface under the vacuum environment conditions of a typical experiment. Multiple ion species are usually accelerated from the target, resulting in a layered expansion of the ion population, where ions with the highest charge-to-mass ratio (q/m) are accelerated first and with highest efficiency. This leads to an overall sequential acceleration process, where additional screening effects between different ion species need to be considered [65, 66]. There have been experimental attempts to modify the rear surface of the target, e.g. by ablation of the contaminant through a heating lasers [67]. Finally, electrons and ions expand as a quasi-neutral plasma into the vacuum.

Analytic modelling

Several analytical models have been developed by different authors to understand the TNSA process and the scaling of maximum ion energy with laser power. Although these

models often oversimplify the complex interaction, they remain a valuable tool for estimating the overall efficiency of the acceleration process and predicting the ion energy under optimal conditions. Perego *et al.* conducted a comprehensive review that compared these models with experimental data to evaluate their predictive capabilities [68].

The widely recognised **Mora model** [69], describes an isothermal, collisionless expansion of a quasi-neutral plasma as a fluid in one dimension to estimate the position and velocity of the ion front. The model assumes initially cold ions with a step-like density distribution and electrons at a single temperature following a Boltzmann distribution (c.f. Equation 2.4). The charge separation generates an electric potential which satisfies the Poisson equation (c.f. Equation 2.3) and leads upon integration (half space from target rear to infinity) to the following simple expression for the initial ($t = 0$) electric field at the ion front:

$$E_{front,0} = \sqrt{\frac{2\,E_0^2}{\exp(1)}} \tag{2.51}$$

where $E_0 = \sqrt{n_0\,k_B\,T_e\,/\,\varepsilon_0}$ is the characteristic electric field strength of the self-similar solution.

For $t > 0$ the expansion of the ions into the vacuum needs to be considered which can be described e.g. as an isothermal fluid. Assuming quasi-neutrality $n_e(z,t) = Z\,n_i(z,t)$ for $z > \lambda_D$ and using the continuity and force equations for an ion fluid, finally results in the self-similar solution for the ion density $n_{i,ss}$, ion velocity $v_{i,ss}$ and the electric field E_{ss} [33, 44]:

$$n_{i,ss} = n_{i,0}\,\exp\left(\frac{-z}{c_s\,t} - 1\right) \tag{2.52}$$

$$v_{i,ss} = c_s + \frac{z}{t} \tag{2.53}$$

$$E_{ss} = \frac{\partial\varphi_{ss}}{\partial z} = \frac{E_0}{\omega_P\,t} \tag{2.54}$$

with initial ion density $n_{i,0}$ and ion sound speed c_s (c.f. Equation 2.45). However, the self-similar solution lacks a physical meaning when the plasma scale length $L_P = c_s\,t$ is smaller than the local Debye length (i.e. $\omega_P\,t < 1$) as well as when t goes towards infinity (as $v_{i,ss}$ would also go to infinity). The self-similar solution for $v_{i,ss}$ predicts in the asymptotic limit ($\omega_P\,t \gg 1$) an electric field at the ion front of:

$$E_{front} \simeq 2\,E_{ss} = \frac{2\,E_0}{\omega_P\,t} \tag{2.55}$$

Mora studied this problem with numerical methods and introduced an expression for E_{front}, which empirically describes the electric field at the ion front for all values of t, i.e. reproducing Equation 2.51 and Equation 2.55 within their valid limits:

$$E_{front} \simeq \frac{2\,E_0}{\sqrt{2\,\exp(1) + \omega_P^2\,t^2}} \tag{2.56}$$

By integrating $\mathrm{d}v_{i,front}\,/\,\mathrm{d}t = Z\,e\,E_{front}\,/\,m_i$, the ion front velocity $v_{i,front}$ and thus the maximum ion energy $E_{max,Mora}$ can be estimated as:

$$E_{max,Mora} \simeq 2\,Z\,k_B\,T_e\left(\ln\left(\tau + \sqrt{\tau^2 + 1}\right)\right)^2 \tag{2.57}$$

where $\tau = \omega_P\,t\,/\,\sqrt{2\,\exp(1)}$ is the normalised acceleration time. Equation 2.57 then simplifies in the asymptotic limit ($\omega_P\,t \gg 1$) to:

$$E_{max,Mora} \simeq 2\,Z\,k_B\,T_e\,[\ln(2\,\tau)]^2 \tag{2.58}$$

The Mora model also predicts the experimentally observed exponentially decaying particle spectrum:

$$\frac{\mathrm{d}N}{\mathrm{d}E} = \frac{n_{i,0}\, c_s\, t}{\sqrt{2\, E\, Z\, k_B\, T_e}}\, \exp\left(-\sqrt{\frac{2\, E}{Z\, k_B\, T_e}}\right) \tag{2.59}$$

The clear limitations of this model are the assumption of only one single and temporally constant electron temperature, neglecting energy transfer between electrons and ions and an arbitrary relationship between the density of front side accelerated hot electrons and the ion density at the target rear. Another important point is that the effective acceleration time t has to be limited due to the finite nature of the laser pulse duration τ_L. Without this limitation $E_{max,\,Mora}$ would otherwise get a logarithmically diverging character which is clearly unphysical. Fuchs $et\ al.$ empirically found that $t = 1.3\,\tau_L$ applied to the Mora model fitted their collection of experimental data [18]. They refined this result later in a dedicated study to $t = \alpha\,(\tau_L + 60\,\mathrm{fs})$, where $\alpha = 1.3$ for laser intensities $I_L > 3 \times 10^{19}\,\mathrm{W\,cm^{-2}}$ [70].

Mora later proposed an extended model considering the collisionless expansion of a thin foil into vacuum [71]. In this improved model, the assumption of an isothermal expansion is replaced with an adiabatic expansion (i.e. accounting for cooling of the electron fluid) and a time-dependent electron temperature $T_e\,(t)$ is introduced.

Schreiber $et\ al.$ introduced an alternative approach to describe the TNSA process from thick foil targets. He linked this process to a backside illuminated photo-anode and introduced a non-relativistic **quasi-static model** to analyse the phenomenon analytically in 1D [62]. According to the model, front side generated hot electrons induce a radially confined surface charge on the target rear, resulting in the acceleration of ions. Schreiber assumed that the laser pulse, characterised by energy E_L and pulse duration τ_L, accelerates a specific number of electrons given by $N_e = \eta\,E_L\,/\,E_e$ to an average energy of E_e. η is the only freely selectable parameter of this model and represents the conversion efficiency from laser energy into dominantly kinetic energy of electrons $E_e \simeq k_B\,T_e$. The electrons follow an exponential energy distribution and are confined within a bunch of length $L = c\,\tau_L$. It should be noted that only the most energetic electrons exit the target completely. The majority of the electrons propagate to λ_D, where they reverse their direction and re-enter the foil. On average, a certain number of electrons remain permanently outside the target, thereby inducing a surface charge at the target rear denoted as $Q = 2\,N_e\,\lambda_D\,/\,L$. The specific radius B (c.f. Equation 2.50) of the induced surface charge also represents the effective source size from which ions can be accelerated. With the above assumptions, the Poisson equation (c.f. Equation 2.3) can be solved in a cylindrically symmetric geometry (electron propagation direction z), yielding the following expression for the on-axis electric potential:

$$-e\,\Phi(z) = E_\infty \left(1 + \frac{z}{B} - \sqrt{1 + \left(\frac{z}{B}\right)^2}\right) \tag{2.60}$$

where E_∞ is the potential barrier that electrons must overcome to escape the potential of the foil target:

$$E_\infty = \frac{Q\,e^2}{2\,\pi\,\varepsilon_0\,B} = 2\,m_e\,c^2\sqrt{\frac{\eta\,P_L}{8.71\,[\mathrm{GW}]}} \tag{2.61}$$

Using Equation 2.60 the following expression for the electric field can be obtained:

$$E(z) = \frac{k_B\,T_e}{e\,\lambda_D}\left(1 - \frac{z}{\sqrt{B^2 + z^2}}\right) \tag{2.62}$$

In the case of an infinitely long laser pulse (i.e. the electric field $E(z)$ is stationary), an ion with charge $Z_i e$ can get the following maximum kinetic energy $E_{i,max}$:

$$E_{i,max} = Z_i E_\infty = 2 Z_i m_e c^2 \sqrt{\frac{\eta P_L}{8.71\,[\text{GW}]}} \propto \sqrt{P_L} \tag{2.63}$$

This is clearly different to the Mora model, where the ion energy would tend to infinity for an infinitely long laser pulse. To account for a time depending acceleration process, the electron bunch is only present for a limited time. Integrating the equation of motion and introducing $X = \sqrt{E_{i,norm}/E_{i,max}}$ and the normalised maximum ion energy $E_{i,norm} = E_{max,Schreiber}/(m_i c^2)$ finally yields:

$$\frac{\tau_L}{\tau_0} = X + \frac{X}{2(1-X^2)} + \frac{1}{4} \ln\left(\frac{1+X}{1-X}\right) \tag{2.64}$$

where $\tau_0 = B/v_\infty = \sqrt{B^2 m_i/(2 E_\infty)}$. After a Taylor expansion of Equation 2.64 around $X = 0$ the following expressions for X and $E_{max,Schreiber}$ are obtained:

$$X = \tanh\left(\frac{\tau_L}{2\tau_0}\right) \tag{2.65}$$

$$E_{max,Schreiber} = X^2 E_{i,max} \tag{2.66}$$

The developed model was later extended to solve also the relativistic equation of motion which requires to add a relativistic correction term to Equation 2.64 [72].

Passoni and Lontano developed another quasi-static model focusing only on the contribution of hot electrons that are trapped by the electrostatic potential at the rear surface [73]. Electrons which are accelerated above a certain threshold energy will be ignored as they escape the system and do not contribute to the ion acceleration. This also ensures that after solving the Poisson equation, all physical quantities (electron density distribution, electrostatic potential and electrostatic field) tend to 0 for large distances $z \gg \lambda_D$. Their analysis predicts a finite spatial extend of the acceleration field and a relation between the characteristics of the hot electrons and the accelerated ions.

Furthermore, several models have been proposed specifically for layered targets, incorporating a thin hydrocarbon layer on the rear surface of the target. These models take into account the presence of the hydrocarbon layer and its effects on the acceleration process [74–76].

2.3.2 Radiation pressure acceleration

Radiation Pressure Acceleration (RPA) is an advanced laser-driven acceleration mechanism that exploits the momentum transfer from intense electromagnetic radiation, i.e. photons, to electrons upon reflection on the target surface. This concept dates back to a theoretical description by Veksler [77] in 1957 and the visionary idea by Marx in 1966, proposing the utilisation of laser-generated radiation pressure to enable the interstellar transportation of a spacecraft [78].
The pressure P_{rad} exerted by the laser light upon reflection from a plane surface of a medium at rest can be calculated for a monochromatic, plane electromagnetic wave of intensity I_L under normal incidence using the following equation [3]:

$$P_{rad} = (1 + R - T)\frac{I_L}{c} = (2R + A)\frac{I_L}{c} \tag{2.67}$$

where R, T and A represent the coefficients for reflection, transmission and absorption, respectively. The energy conservation principle further requires that $R + T + A = 1$.

In the context of laser-plasma interaction, RPA occurs when a high-intensity laser pulse interacts with an overdense plasma. The immense photon pressure exerted by the laser pulse drives the acceleration of plasma electrons, leading to charge separation and the establishment of strong electrostatic fields, subsequently accelerating target ions to high kinetic energies. This process happens when the radiation pressure P_{rad} of the laser gets greater than the thermal pressure of the plasma $P_{th} = n_e k_b T_e$. Numerical simulations conducted by Esirkepov *et al.* showed that RPA is dominating over TNSA for laser intensities $I_L > 10^{23}\,\mathrm{W\,cm^{-2}}$ and that a quasi-monoenergetic ion spectrum with small divergence is generated [79, 80]. Furthermore, numerous theoretical studies have extensively investigated RPA for different configurations of laser and target parameters to provide insights into the optimal acceleration conditions for RPA (e.g. [81–90] and references therein). Results from those analytical and simulation studies have shown that RPA can be split into two distinct phases, namely **hole boring** and **light sail**, which are illustrated in Figure 2.5.
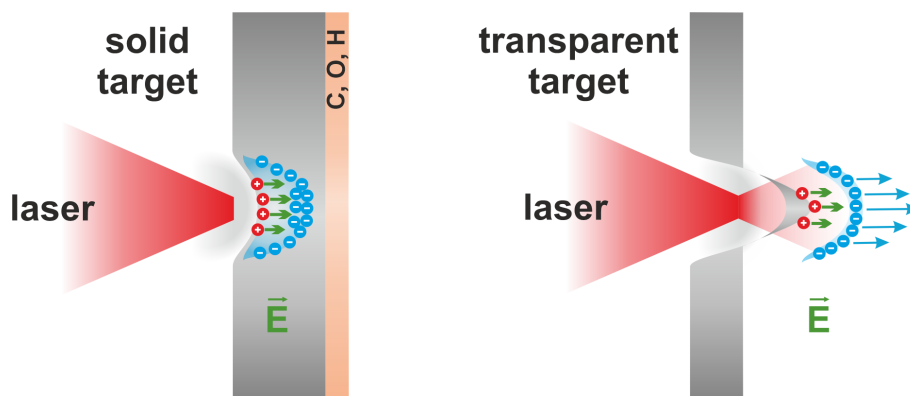
Figure 2.5: Schematic of the Radiation Pressure Acceleration (RPA) process: In hole boring RPA (left) the laser pressure pushes electrons from the target front side collectively into the target, effectively boring a hole into the plasma distribution. This leads to a charge separation between those electrons and immobile ions which results in the generation of a strong electrostatic field, subsequently accelerating the ions to high velocities. If the target is sufficiently thin, the moving hole boring front can reach the target rear before the laser ends, resulting in an acceleration of the entire plasma slab. As long as the plasma slab remains overcritical, the laser pulse exerts pressure to it, thereby continuously accelerating the electrons with ions following closely. This is referred to as the light sail RPA scenario (right).

Hole Boring

Initially, for thick overdense targets, the high-intensity laser pulse interacts with the front side of a solid-density target. In this context, a "thick" target implies that the laser pulse cannot interact with the target rear, i.e. the plasma skin depth (introduced in subsection 2.1.3) is smaller than the target thickness: $l_s < d$.
The laser pulse exerts a ponderomotive pressure on the electrons at the critical density surface, pushing them forward into the overdense plasma. Effectively, the laser bores a hole in the plasma, resulting in the formation of a peaked plasma layer of high electron density. As the heavier ions are left behind, a positively charged region is formed at the front surface and partially in the bulk of the target. This charge separation creates

an electrostatic field, which in turn accelerates ions from the positively charged region, producing a highly collimated, high-energy ion beam.

Wilks *et al.* derived an expression for the velocity of the hole boring front $v_{hb,nr}$ in the non-relativistic case by balancing the momentum flux of the mass flow with the light pressure, resulting in the following expression [47]:

$$v_{hb,nr} = \left(\frac{c^2}{2} \frac{n_c}{n_e} \frac{Z}{A} \frac{m_e}{m_p} \frac{\xi I_L \lambda_L^2}{2.74 \times 10^{18}} \right)^{1/2} \tag{2.68}$$

where Z is the ionisation state, A the mass number and $\xi = 2$ for linear polarisation and $\xi = 1$ for circular polarisation, respectively. Similar expressions for v_{hb} were derived by Macchi *et al.* [91], Zhang *et al.* [81] and Robinson *et al.* [85]. Furthermore, Robinson introduced the dimensionless piston parameter Ξ:

$$\Xi = \frac{\xi I_L}{m_i n_i c^3} = a_0^2 \frac{n_c}{n_e} \frac{Z}{A} \frac{m_e}{m_p} \tag{2.69}$$

with ion mass $m_i = A m_p$, ion density $n_i = Z n_e$ and the dimensionless vector potential $a_0 = \sqrt{\xi I_L / m_e c^3 n_c}$ as introduced in Equation 2.37. Using Equation 2.69 simplifies Equation 2.68 to:

$$v_{hb,nr} = c \sqrt{\Xi} \tag{2.70}$$

The balance of mass and momentum flow at the moving hole boring front necessitates the presence of an ion flow that is reflected from the recession front with ion velocity $v_i = 2 v_{hb}$. The energy of the accelerated ions can then be calculated by:

$$E_{hb,nr} = \frac{m_i (2 v_{hb,nr})^2}{2} = \frac{2 \xi I_L}{n_i c} = 2 m_i c^2 \Xi \propto a_0^2 \tag{2.71}$$

However, it is important to note that the expressions in Equation 2.68 and Equation 2.71 are only valid in the non-relativistic regime. At relativistic intensities, $v_{hb,nr}$ is predicted to exceed the speed of light, which is a physically meaningless result. Robinson therefore derived a relativistic correction and obtained a fully relativistic description for the hole boring velocity:

$$v_{hb} = \frac{c \sqrt{\Xi}}{1 + \sqrt{\Xi}} \tag{2.72}$$

Using this expression for v_{hb} and the corresponding Lorentz transformation, the maximum ion energy $E_{max,hb}$ in the laboratory frame can then be calculated by:

$$E_{max,hb} = m_i c^2 \left(\frac{2 \Xi}{1 + 2 \sqrt{\Xi}} \right) \propto \frac{2 a_0^2}{1 + 2 a_0} \tag{2.73}$$

To achieve highest ion energies within this scheme, it is advantageous to reduce the electron density of the target to values slightly above n_c, whereas only modest ion energies might be obtained for highly overdense targets, e.g. solid density foils with $n_e \geq 200 n_c$. First experimental signatures for hole boring were obtained in the mid-nineties by measuring spectral changes from laser light which was reflected from the plasma [92–94]. The observed red-shift of the laser spectrum allowed for an estimation of the velocity of the moving plasma front and for a comparison to the theoretical treatment by Wilks. This approach has been extended by incorporating a model that also considers the pre-plasma formation and the steepening of the plasma density profile throughout the entire interaction with the laser pulse [95, 96]. This extended model enables the characterisation of pre-plasma properties on time-scales preceding the arrival of the laser pulse

peak. Palmer and Haberberger reported the first experiments where the accelerated particle beam featured the typical RPA signature of a quasi-monoenergetic energy spectrum. The first experiments to report a characteristic signature of hole boring RPA for the accelerated particle beam, namely a quasi-monoenergetic particle spectrum, were conducted by Palmer *et al.* [97] and Haberberger *et al.* [98] using near-critical gas-jet targets and CO_2 lasers. Another theoretically studied variant of the hole boring process occurs, when the laser propagates into a relativistically transparent plasma, propelling the **Relativistic Transparency Front (RTF)** [99, 100]. At the RTF the plasma density equals the relativistic critical density $n_e = \gamma n_c$ and the laser is reflected. Upon reflection, the laser pressure at the RTF generates a charge separation front, resulting in accelerations of ions similar to the classic hole boring scenario. When γ is still icreasing during the interaction and electrons are simultaneously pushed forward by the laser pressure, the actual position of the RTF also moves forward. When this movement of the RTF is synchronised to the movement of the initially accelerated ions, a highly efficient energy transfer from the laser to the ions can be realised.

Collisionless Shock Acceleration

The experimental results by Haberberger *et al.* [98] were attributed to **Collisionless Shock Acceleration (CSA)** which is theoretically very similar to hole boring RPA. The ponderomotive force of the laser at the front surface of the target creates a steepening electrostatic wave that evolves into a shock wave. This shock wave propagates through the target material, relatively undisturbed, and accelerates ions that are reflected from the shock front. The ions gain energy as they interact with the shock, reaching velocities up to twice the shock speed. As hole boring RPA involves the reflection of ions from the charge separation front created by the laser interaction with a solid target, this process can only be sustained as long as the laser pushes against the critical surface. CSA, however, relies on the formation and propagation of a collisionless electrostatic shock to accelerate ions, a process that can continue long after the laser pulse has ended. Denavit first observed the formation of electrostatic shocks in numerical simulations, when an intense laser pulse is interacting with an overdense plasma [101]. Silva *et al.* [102] and d'Humières *et al.* [103] studied in detail, under which interaction parameters CSA dominates over TNSA. Numerical studies by Chen *et al.*, Zhang *et al.* and Macchi *et al.* explored how different target properties (e.g. thickness, density, temperature, ion species) affect the shock characteristics [104–106]. Experimental work by various research groups demonstrated CSA features using gas jets [98, 107, 108] and pre-expanded solid foil targets [109–113] or microspheres [114]. Especially this scenario, where the preceding laser light or an artificial pre-pulse leads to ionisation and expansion of a solid target before the main pulse arrival, is particularly relevant for the experimental results in chapter 5 and chapter 6. Theoretical work by Fiuza *et al.* [115] and numerical simulations by Kim *et al.* [116], Stockem Novo *et al.* [117] and Zhang *et al.* [113] demonstrated that this pre-expansion and subsequent electron heating in a near-critical plasma, plays a crucial role in shock formation and subsequent ion acceleration.

Light Sail

Hole boring RPA is sustained until either the laser pulse ends or the target thickness d is such that the moving hole boring front reaches the target rear surface $d < v_{hb} \tau_L$ before the laser pulse ends. In the latter scenario, the entire target volume is accelerated

by the laser and as long as this plasma slab stays overcritical ($n_e > n_c$), the laser pulse will continuously push against it. Laser light which is reflected from this moving surface undergoes a redshift and transfers momentum to the plasma. This leads to a continuous acceleration process, where ions, which are no longer screened by surrounding plasma, rapidly reach relativistic velocities and closely follow the motion of the electrons. Since the whole plasma slab co-propagates with the laser pulse, this acceleration scheme is referred to as the **light sail** or **moving mirror** scenario of RPA.

In the non-relativistic case, the velocity of the moving plasma slab $v_{ls,nr}$ can be estimated by considering the momentum change of the plasma slab due to the radiation pressure (assuming no transmission $T = 0$):

$$P_{rad} S = \frac{(1 + R) I_L}{c} S = \frac{dp}{dt} = m_i n_i S d \frac{dv}{dt} \tag{2.74}$$

where S is the surface area and d the thickness of the plasma slab. Rearranging for the velocity and integrating over the pulse duration τ_L yields:

$$v_{ls,nr} = \frac{(1 + R) I_L}{c} \frac{\tau_L}{n_i m_i d} \tag{2.75}$$

To derive the light sail acceleration velocity in the relativistic limit, a similar calculation can be done after applying a Lorentz transformation into the rest frame of the moving plasma slab, as detailed in [118]. Assuming that the plasma slab is perfectly reflecting ($R = 1$) and that the fluence of the laser F can be approximated by a flat-top intensity profile multiplied by the pulse duration ($F = I_L \tau_L$), the following expression for the relativistic light sail velocity v_{ls} can be achieved:

$$v_{ls} = \frac{[1 + \mathcal{E}]^2 - 1}{[1 + \mathcal{E}]^2 + 1} \tag{2.76}$$

where the dimensionless parameter $\mathcal{E}$ is defined as:

$$\mathcal{E} = \frac{2F}{m_i n_i d c^2} = \frac{2 n_c Z m_e \tau_L c}{n_e A m_p \xi d} a_0^2 = \frac{2 \tau_L c \Xi}{\xi d} \tag{2.77}$$

Using this expression also Equation 2.75 can be simplified to:

$$v_{ls,nr} = \frac{\mathcal{E}}{c} \tag{2.78}$$

The maximum energy per nucleon of an ion of the plasma slab can then be calculated with Equation 2.76:

$$E_{max,ls} = m_p c^2 \frac{\mathcal{E}^2}{2(1 + \mathcal{E})} \propto \frac{a_0^4 \tau_L^2}{d^2 + a_0^2 \tau_L d} \tag{2.79}$$

In the non-relativisitc limit ($a_0 \ll 1$) and in the ultra-relativistic limit ($a_0 \gg 1$), Equation 2.79 can be simplified to:

$$E_{max,ls} \propto \left(\frac{a_0^2 \tau_L}{d} \right)^b \qquad \begin{cases} b = 2, & a_0 \ll 1. \\ b = 1, & a_0 \gg 1. \end{cases} \tag{2.80}$$

In summary, the light sail regime predicts highest ion energies for the thinnest targets with the lowest possible plasma density and the highest laser intensity. Kar *et al.* [119] and Gonzales-Izquierdo *et al.* [120] performed experimental studies to investigate the transition from the hole boring regime to the light sail regime of RPA. They systematically

reduced the thickness of the target material and observed characteristic changes in the particle spectra as well as the properties of reflected and transmitted light, respectively. By maintaining an overcritical plasma density for sufficiently thin targets and efficiently suppressing electron heating as well as the growth of plasma instabilities, light sail RPA offers a superior scaling of maximum ion energies compared to TNSA and hole boring RPA. This makes light sail RPA to one of the most promising regimes for laser-driven ion acceleration. However, simulations under more realistic conditions [83, 90, 121, 122] and experimental studies [25, 123–129] have shown, that light sail acceleration can be achieved but still faces several demanding challenges that need to be addressed before it can become a reliable source of high-energy ions for practical applications. In general, the hot electron generation and the onset of instabilities reduces the maximum achievable velocity of the ion beam and increases the energy spread in the ion bunch due to the strong oscillation of the acceleration field from the action of the ponderomotive force in the transverse direction. This might explain why the experimentally observed ion spectra were still relatively broad compared to what simulations suggested. Circular polarisation, ultra-high laser contrast and ultrathin targets are therefore usually a prerequisite for conducting studies in the light sail regime.

2.3.3 Acceleration in the relativistically induced transparency regime

The phenomenon of **Relativistically Induced Transparency (RIT)** is of major importance for the physics and the plasma interaction processes that are discussed in chapter 5 and chapter 6. Therefore, the following section provides a detailed introduction to the RIT regime and discusses the relevant ion acceleration scenarios that were explored.

Recent advances in target fabrication techniques and improved temporal laser contrast cleaning have enabled a significant number of experiments in the RIT regime. These experiments have shown promising results, including increased ion energies, reduced beam divergence and spectrally peaked particle spectra [13, 127, 130–141]. Extensive simulation work has been carried out to investigate the underlying physical mechanisms responsible for the observed characteristics of the particle beams [74, 142–157]. While several schemes have been identified in numerical simulations, there is only limited experimental evidence for one specific scheme or the other, especially since they may all occur at different stages of the entire interaction. A detailed discussion of the different schemes and their differences is given below. Furthermore, some experiments have focused on studying nonlinear optical phenomena (e.g. plasma shuttering) that can arise in the RIT regime [158–164].
Overall, despite all the work done so far, the optimal RIT interaction parameters that can actually be realised experimentally and lead to the desired improved particle beams have not yet been determined.

Onset of RIT

In the RIT regime, the initially opaque target undergoes a transition to transparency during the interaction with the laser pulse. This transition occurs due to the combined effects of electron heating, expansion, and the relativistic mass increase. The expansion leads to a reduced electron density and the increased electron mass slows down the motion of the electrons by the Lorentz factor γ (c.f. Equation 2.8). Both effects decrease the relativistic critical density (c.f. Equation 2.19). However, the ponderomotive force exerted by the laser pushes electrons forward, causing a compression of the electron density profile. The onset of RIT occurs when all effects combined lead to a scenario,

where electrons are no longer able to shield the plasma from the incident laser. As a result, the laser induced RPA is curtailed, as the laser can no longer push against the critical density. Instead, the laser pulse propagates now into the underdense plasma and volumetrically heats electrons from the bulk of the target. This leads to the generation of strong electric fields, which enable efficient acceleration of ions from the target bulk. If the target undergoes RIT too early, the peak of the laser can also directly accelerate electrons to relativistic energies [165–168].

Vshivkov *et al.* [169] introduced a simplified one-dimensional model to analytically describe the interaction between laser light and an initially overdense plasma. This model allows to determine a threshold value for the onset of transparency when assuming a laser pulse with perfect contrast, i.e. a Dirac delta function:

$$a_0 > \pi \, \frac{n_e}{n_c} \frac{d}{\lambda} = \frac{\omega_P^2}{\omega_L} \frac{d}{2\,c} \tag{2.81}$$

Further theoretical work by various groups was dedicated to understand the onset of RIT when a high-intensity pulse interacts with a cold plasma slab. This included analytical solutions and numerical modelling of interaction at the plasma-vacuum interface [170–172] and the influence of the plasma density [173, 174] as well as electron heating [172, 175] on the onset of RIT.

In 2006, research groups at the Lund Laser Centre and at the Laboratoire pour l'utilisation des lasers intenses greatly improved their temporal laser contrast by implementing a plasma mirror to their experimental setup. This improvement allowed them to investigate, for the first time, ion acceleration from targets with sub-micrometer thickness, which showed a significant increase in the maximum energies of the accelerated protons [176–178]. The results motivated Yin *et al.* to study theoretically the interaction of a short laser pulses with carbon foil targets of a few nanometre thickness [144]. The results of their numerical simulations showed indeed an increase in maximum ion energies, surpassing by more than an order of magnitude what would by expected from TNSA. According to their simulations, this energy enhancement was caused by a new acceleration scheme which they referred to as Laser Break-out Afterburner.

Laser Break-out Afterburner

The **Laser Break-out Afterburner (BOA)** acceleration scheme was proposed by Yin *et al.* as a result of their one-dimensional simulation study [144]. Further investigations extended the numerical simulations to 2D [146] and 3D [150], thereby demonstrating the scalability of this scheme to higher dimensions. Yan *et al.* developed an analytical model describing the ion acceleration from thin targets in the BOA regime [148].

BOA is a three-stage process that starts with a regime similar to TNSA and later transitions into a phase where the target becomes transparent, allowing the laser to effectively break through the plasma. In the early phase of the interaction, energy is converted from the laser into hot electrons giving rise to a charge separation field at the rear of the target (TNSA phase). For sufficiently thin targets, the plasma skin depth (c.f. Equation 2.18) is comparable to the target thickness. In such a case, the laser can effectively heat a large fraction of electrons from the entire target, resulting in an increased conversion efficiency (enhanced TNSA phase). As the interaction progresses, the combined effects of plasma expansion and laser intensity increase lead to the formation of a relativistically transparent plasma. Consequently, the laser can propagate through this transparent plasma, allowing for volumetric interaction with the hot electrons (BOA phase).

Through the ponderomotive force, the laser further accelerates these electrons to relativistic velocities. The resulting difference in drift velocity between electrons (close to c) and ions (non-relativistic) leads to the formation of streaming instabilities, such as the Buneman instability [179]. These instabilities have a low phase velocity and resonate with the ions, resulting in ion acceleration through the generation of a large longitudinal electrostatic field that co-moves with the ions. A detailed one-dimensional simulation study conducted by Albright et al. [145] specifically investigated the relativistic version of the Buneman instability. As long as the laser continues to accelerate the electrons and maintain their substantial longitudinal bulk velocity, the laser energy will be efficiently converted into ion kinetic energy through the action of these electrostatic fields. Tracking individual particles in detailed 2D and 3D simulations allowed Stark et al. to analyse the contribution of different acceleration mechanisms throughout the full interaction with the laser [154].

Experimental studies attributing their results to the BOA scheme have been primarily conducted at the TRIDENT laser facility at the Los Alamos National Laboratory. In a pioneering study by Henig et al., they utilised a double plasma-mirror setup to achieve ultra-high laser contrast and diamond-like carbon foil targets of a few tens of nanometres thickness. Their experimental results demonstrated the acceleration of ion beams with significantly enhanced energies compared to TNSA [130]. Hegelich et al. extended these studies by employing circular polarisation and spatial pulse shaping [131], as well as special nano targets [133] and observed spectral modulation of the accelerated ion beams. Jung et al. conducted a series of experiments investigating ion acceleration in the BOA regime using circular polarised laser light. They observed the generation of carbon beams with quasi-monoenergetic spectra [132, 134, 180] and the formation of ring-like structures in the beam profiles [181]. By analysing both experimental and simulation data, they were able to infer the scaling of ion energies in the BOA regime [182]. Further experiments, using the TRIDENT laser and similar interaction conditions, also observed these quasi-monoenergetic spectra for heavier ions (aluminium and titanium) [136, 140]. However, these studies came to different conclusions about the cause of these features. Their numerical simulations showed the emergence of self-organising field structures at the rear side of the target playing a crucial role in generating the observed features of the accelerated ion beam over picosecond-long acceleration time scales. An important factor influencing the spectral shape of the ion beam is the formation of a forward-propagating electron jet, which occurs after the onset of RIT. This phenomenon shares similarities with the hybrid RPA-TNSA acceleration scheme, which has also been reported by other research groups for similar experimental conditions [135, 139].

Hybrid schemes

In the RIT regime, the plasma changes its density significantly during the interaction and can therefore be subject to several acceleration mechanisms if the interaction duration (i.e. the laser pulse duration) is long enough. Using numerical simulations, it is now possible to try to identify the ideal combination of known mechanisms and thus develop a dynamic scenario where ions are subjected to multiple acceleration regimes. Zhuo et al. performed 2D simulations, where they observed that a dual-peaked electrostatic-field can efficiently accelerate quasi-monoenergetic ion beams from a thin foil target using a linearly polarised laser pulses [149]. This occurs due to a perfect interplay of RPA at the target front and TNSA at the target rear. In a series of 2D simulations, Qiao et al. studied how different mechanisms compete during the laser-plasma interaction and under which laser and target parameters one of them dominates the ion acceleration [155,

183]. Mishra *et al.* performed simulations in 1D, 2D, and 3D and found that optimal ion acceleration is achieved when RIT sets in during the arrival of the peak of the laser pulse. This allows the remaining part of the laser to propagate through the target and efficiently re-heat electrons, thereby enhancing the sheath field at the target rear [153].

A lot of experiments studying nanometre foil targets undergoing RIT has been carried out at the VULCAN laser at the Rutherford Appleton Laboratory in Oxford and at the PHELIX laser at the GSI Helmholtzzentrum für Schwerionenforschung in Darmstadt. Both systems provide linearly polarised laser pulses with pulse durations of several hundred's of femtoseconds and 150 J – 250 J of pulse energy. Wagner *et al.* experimentally observed proton beams with two spatially separated components. They attributed the high- energy component in the forward direction to the BOA mechanism, and the low-energy component in target normal direction to the TNSA regime [184]. A similar observation was made by Powell *et al.*, reporting proton beams with a ring-like spatial intensity profile in the target normal direction and a narrow divergence high-energy component directed at an angle between the laser forward and target normal axes [135].
Through 2D and 3D simulations, they inferred that after the onset of RIT, a jet of super-thermal electrons is formed at the rear side of the target. This plasma jet of hot electrons is confined and guided by a self-generated azimuthal magnetic field. The transmitted laser pulse co-propagates with the jet and transfers additional energy to the electrons, which attain significantly higher velocities compared to the surrounding plasma. Subsequently, the streaming of these high-energy electrons into the pre-expanded ion layers increases the energy of the ions in the vicinity of the jet. According to their analysis, this electron jet leads to the energy enhancement and the deflection of the high energy component of the proton beam.

Further experiments tried to optimise the onset of RIT for different target parameters and therefore studied the influence of the target angle [137] and target thickness on this scheme [152]. Another follow-up experiment by Higginson *et al.* revealed record proton energies close to 100 MeV which they attributed to the **transparency enhanced TNSA-RPA hybrid acceleration scheme** [139].

At the initial stage of this specific interaction process, when the laser intensity is still relatively low, ion acceleration is primarily driven by TNSA, where a sheath field is formed at the target rear surface. As the process continues and the laser intensity increases, the radiation pressure becomes more dominant. This results in the deformation of the critical density surface of the plasma and the induction of an electric field component. Consequently a dual-peaked, longitudinal, electrostatic field structure is formed, comprising the sheath field at the rear and the radiation pressure generated field at the front of the target. The onset of RIT and the subsequent heating of the plasma electrons by the portion of the laser pulse that propagates through the transparent foil leads to an increase in the magnitude of both electrostatic field components.

The dual-peaked field structure, along with the presence of the super-thermal electron jet, enables effective acceleration of protons and heavier ions from the target front, resulting in unprecedented ion energies. While simulations can provide optimal interaction parameters and detailed insights into the energy enhancement process [157], directly addressing and controlling this mechanism remains challenging. Another experiment aimed to reproduce these results but yielded a slightly different outcome with lower maximum proton energies [141], highlighting the complexity of the detailed dynamics of the different acceleration stages.

Coulomb Explosion

Coulomb Explosion (CE) can be achieved by having very high laser intensities and sufficiently thin targets. Under such conditions, a significant amount of electrons can be expelled from the target. The ion core remains unaffected by the laser, resulting in a positively charged ion cloud, that experiences a strong repulsion from the Coulomb force among the ions. This repulsion leads to an explosive expansion of the ion cloud. Several groups performed numerical simulations [185, 186] and developed analytical models [187, 188] to study and describe the CE regime. Experiments have been carried out, using cluster targets [189, 190], ultrathin solid foils [191] and levitating microspheres [192].

For thicker, multi-layer targets composed of a high-Z and low-Z layer, the RPA effect as discussed in subsection 2.3.2 must be considered. In this case, the high-intensity laser pulse not only expels electrons from the irradiated area but also accelerates the remaining high-Z ion core. The excess of positive charge results in a Coulomb repulsion, causing the ion cloud to expand predominantly in the direction of the laser pulse propagation. This expanding ion cloud is accompanied by a strong longitudinal electric field that moves ahead and accelerates protons from the second layer of the target. This modification of the CE regime, referenced as **Directed Coulomb Explosion (DCE)**, was described by Fourkal *et al.* [193] and Bulanov *et al.* [194, 195]. A one-dimensional analytical model of this scenario for a thin multi-species foil was developed by Govras *et al.* [196–198].

Magnetic Vortex Acceleration

When an ultra-intense laser pulse is tightly focused onto a target with undercritical or near-critical density, the **Magnetic Vortex Acceleration (MVA)** regime can be reached. As the laser propagates through the plasma, the ponderomotive force of the laser expels electrons and thereby creates a channel with reduced electron and ion densities. Some electrons within the channel get accelerated by the non-linear wake behind the laser pulse in the direction of the laser pulse propagation. As these electrons start to move, they form an electron filament along the laser axis, that generates a magnetic field confined within the self-generated channel, acting as a waveguide and containing the magnetic field. Simultaneously, an ion filament is generated within the channel due to the exisiting field structure. As the laser pulse and the magnetic field exit the target, the magnetic field expands into the vacuum, forming a toroidal vortex shape in three dimensions. The magnetic field pressure causes displacement between the electron and ion components of the plasma. This displacement leads to the generation of a strong quasistatic electric field, where ions can get accelerated from the filament into a collimated particle beam. MVA was first studied by multi-dimensional particle-in-cell simulations [142, 143, 147], providing valuable insights into the behavior described above and serving as a foundation for analytic modeling [199]. Recent advancement in computer technology allowed for very detailed three-dimensional simulations, studying the detailed interaction characteristics of MVA and the obtained particle beam parameters [200, 201]. Experimental investigations of MVA have been conducted with different target systems. These include, pre-expanded µm-thick solid foil targets [202, 203], special low density foam targets [204, 205] and underdens gas targets [206–208]. The properties of the particle beam observed in these experiments were attributed to MVA on the basis of simulations. However, the experimental data is ambiguous and leaves room for different interpretations of the dominant mechanism at play [209, 210].

3 Methodology for high-power laser experiments

The main content of this thesis is to analyse the results obtained from several experimental campaigns studying plasma-based ion acceleration using ultra-intense laser light. In order to gain a deeper understanding of the laser-plasma interaction processes and the acceleration dynamics, measuring and understanding experimentally accessible parameters is crucial.

This chapter aims to provide an understanding of how such experiments are set-up, conducted and what results and parameters can be measured. This will be enabled by giving a brief description of the laser systems used, the general experimental setup and the most important diagnostic methods and instruments.

3.1 High-power lasers

High-power lasers have revolutionised the field of science and technology, offering today unprecedented capabilities for research as well as industrial and medical applications. These lasers can generate intense beams of coherent light with power levels reaching into the petawatt ($1\,\text{PW} = 10^{15}\,\text{W}$) range, enabling them to access new research frontiers in laser-induced plasma physics such as laser fusion or particle acceleration. The section begins with an overview of the relevant techniques that have enabled substantial progress in achievable laser peak powers. The ion accelerations experiments in this thesis were conducted at two different laser facilities: the DRACO-PW laser system at the Helmholtz-Zentrum Dresden-Rossendorf in Germany and the J-KAREN-P laser system at the Kansai Photon Science Institute in Japan. Table 3.1 provides an overview of the laser parameters of these systems. Detailed descriptions of both facilities and their specific laser parameters will be presented later in this section.

3.1.1 High-power laser techniques

Since the first demonstration of a laser by Theodore Maimann [211] in 1960, the maximum achievable power and focussed intensity have increased steadily as a result of continuous developments in laser technology, lasing materials and optics.

Laser system comparison		
Parameter	DRACO-PW	J-KAREN-P
Gain medium	Ti:Sa	OPCPA Ti:Sa
Number of CPA stages	2	2
Max. energy (amplified)	35 J	63 J
Max. energy (experiment)	22.5 J	10 J
Min. pulse duration	30 fs (FWHM)	25 fs (FWHM)
Pulse duration (experiment)	33 fs (FWHM)	45 fs (FWHM)
Central wavelength	810 nm	800 nm
Polarisation	horizontal	horizontal
Beam diameter (experiment)	200 mm	250 mm
OAP (oa-angle | f-number)	90°	f / 2.3	45°	f / 1.4
Focal spot size (experiment)	2.3 μm	1.5 μm
Peak intensity (experiment)	6.5×10^{21} W cm^{-2}	3.5×10^{21} W cm^{-2}

Table 3.1: Comparison of laser parameters from the DRACO-PW and the J-KAREN-P system. Both were used for the experiments presented in this thesis.

Q-switching and mode-locking

Soon after Maimanns pioneering work, free-running lasers were able to achieve pulse powers of $\approx 10^3$ W and just two years later, the newly developed **Q-switching** technology [212] enabled a leap into a new power range, reaching up to one million watts (1 MW $= 10^6$ W). By manipulating the loss of an optical system (defined as Q-factor) through passive or active means (e.g. by allowing light to escape the resonating cavity), the amount of stimulated emission is minimised during the pumping of the gain medium. Subsequently, the system is switched to a high loss (i.e. a high Q-factor), triggering the rapid release of the stored energy in a short pulse.

Another two years later, the discovery of **mode locking** [213, 214] further propelled laser pulse power capabilities forward, enabling the generation of gigawatt pulses (1 GW $= 10^9$ W). The mode locking technique synchronises the phase of multiple longitudinal modes within the laser cavity, resulting in constructive interference and the generation of short (usually between 10^{-12} s to 10^{-15} s) pulse trains. Mode locking can be achieved either passively (e.g. by saturable absorbers or by nonlinear optical effects, such as the Kerr effect) or actively (e.g. by implementing electro-/acousto-optic modulators or synchronous pumping). Passing laser pulses from a mode-locked oscillator through additional power amplifiers to boost the total output power is today an established and widely used laser system architecture. Furthermore, mode locking enabled to reach near-gain-bandwidth-limited pulses at high-repetition rates and tens of megawatt peak power [215].

Following the discovery of mode locking, laser technology experienced a slowdown as the maximum power of the laser systems approached the upper limits of optical damage thresholds. To overcome this limit, the spatial beam diameter of the laser beam was increased. However, this strategy faced challenges related to the beam quality and cost-effectiveness due to larger optics required. Consequently, the amount of laser facilities was limited and the laser systems operated at an intensity of approximately 10^{16} W cm^{-2}, delivering nanosecond pulses with kilojoule energy.

Titanium doped sapphire crystals

Another important step for laser technology was the invention of titanium-doped sapphire crystals (Ti:Sa or $Ti^{3+}Al_2O_3$) in 1982 by Peter Moulton [216]. This material is characterised by its large gain bandwidth ranging from 650 nm to 1100 nm with a maximum intensity gain at $\simeq$ 800 nm. The absorption band (peak at 490 nm) is also quite large, enabling a wide range of possible pump wavelengths. Ti:Sa is a 4-level-system, where electrons can relax not only by emitting photons but also via phonons and displacement of titanium ions, leading to a continuum of photon energies and a broad emission spectra. Furthermore, the high thermal conductivity of Ti:Sa facilitates intense pumping at high repetition rates. Mode-locked Ti:Sa lasers are today the most popular and established type of laser used to generate ultrashort laser pulses.

Chirped pulse amplification

A major breakthrough in maximum attainable laser pulse powers was the development of the **Chirped Pulse Amplification (CPA)** technique. First introduced by Donna Strickland and Gérard Mourou in 1985 [217] and Nobel Prize awarded in 2018, CPA revolutionised laser technology and enabled the generation of ultrashort, yet extremely high-energy laser pulses. This technique helped overcoming the main limitations of laser amplification at that time, namely the damage to optics caused by nonlinear effects, such as self-focussing, in the amplifier medium. By inserting a dispersive element, e.g. a grating pair, prisms or a fibre (as realised in [217]) before the actual amplification, the laser pulse was stretched in time and thus the intensity reduced. The instantaneous frequency of the laser pulse becomes linearly time-variable due to the dispersive element, hence the pulse is chirped. After amplification to high energies at long pulse durations, the introduced chirp is compensated by a second set of dispersive optics, effectively reversing the frequency shift in time. The CPA technique enables the use of small beam diameters throughout the entire laser system, except for the final compressor. Strickland and Mourou's work showcased the development of a compact, tabletop laser system capable of producing picosecond pulses with nearly 100 GW peak power. This power output was previously only attainable by large-aperture, national-laboratory-scale laser systems, characterised by their large sizes and high costs.

In 1992, a new type of CPA has been proposed, known as **Optical Parametric Chirped Pulse Amplification (OPCPA)** [218–220]. OPCPA offers a novel approach to amplify broadband short-pulse lasers by using the nonlinear interaction between a signal pulse and a pump pulse in a nonlinear crystal. This process generates a new broadband signal that can then be amplified through standard CPA techniques. OPCPA offers the advantage of achieving high amplification efficiencies and significantly broader bandwidths than with a standard CPA systems, allowing for the amplification of even shorter and more intense pulses.

High-power lasers worldwide

In the following decades, the CPA technology was implemented in numerous laser systems across the globe, paving the way for applications in industry, medicine, and national security but also leading to an increased number of high-power laser facilities for academic research. The currently most up-to-date and complete overview of planned and operating high-power laser facilities worldwide was published in 2019 by Danson *et al.* [24].

For investigating fundamental high-energy density physics, such as relativistic laser-matter interactions and particle acceleration, several high-power laser facilities have been constructed primarily in North America, Asia and Europe (c.f. list below). The early

progress in developing multi-TW lasers with ultrashort pulses predominantly relied on Nd:glass amplifiers. However, the exceptional capabilities of Ti:Sa to amplify light across a wide spectrum and at high-repetition rates, quickly made it the preferred choice for high-power CPA lasers. This shift towards Ti:Sa-based lasers can be seen in Figure 3.1, which shows the laser parameters reported from laser-ion acceleration experiments conducted between 2003, three years after the first high-energy proton beam was generated at NOVA-PW [4], and 2023, the year of this thesis. The growth in the total number and attainable peak power of Ti:Sa lasers underlines their importance in the field of laser-driven ion acceleration.
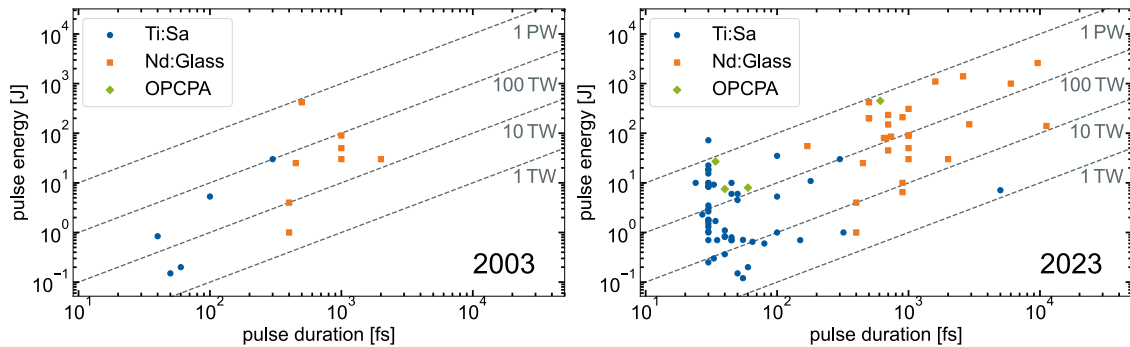
Figure 3.1: Reported on-target laser parameters from ion acceleration experiments in 2003 (left) and 2023 (right). The dashed lines represent different laser peak powers, different markers indicate different gain materials.

List of high-power laser systems, performing experiments on laser-driven ion acceleration:

- North America:
    - USA: BELLA-PW [221], HERCULES [222], Texas-PW [223], OMEGA-EP [224], ARC laser [225]
    - Canada: ALLS [226]

- Asia:
    - China: SG-II [227], SULF-1PW [228], SULF-10PW [229], XL-III [230], CLAPA [231], CAEP-PW [220], SILEX-II [232]
    - Japan: J-KAREN-P [233]
    - Korea: CoReLs [234]
    - Russia: PEARL [235]
    - Israel: HIGGINS [236]

- Europe:
    - Germany: PHELIX [237], ARCTURUS [238], DRACO [239], PEnELOPE [240], PO-LARIS [241], JETi-200 [22], ATLAS3000 [242]
    - UK: Vulcan [243], Astra-Gemini [244], SCAPA [245]
    - France: LMJ [246], PETAL [247], UHI10 [248], LOA [249], LULI [250], APPOLON [251]
    - Spain: VEGA-3 [252]
    - Czech Republic: ELI-BEAMLINES [253]
    - Hungary: ELI-ALPS [254]
    - Romania: ELI-NP [255]

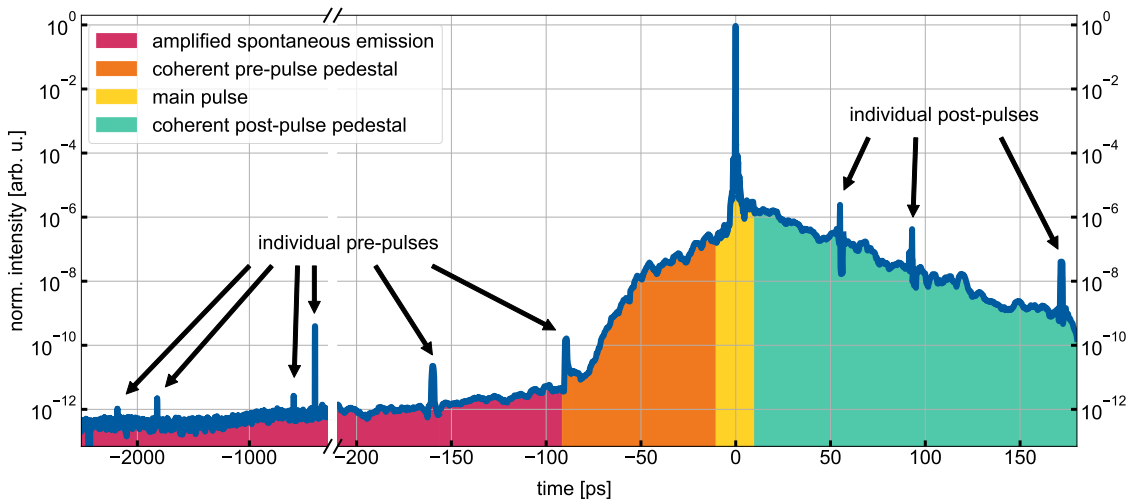## 3.1.2 Temporal contrast of high-power laser systems

High-power laser systems typically concentrate the majority of pulse energy within the short duration of the main pulse. However, there is also a small but significant portion of pulse energy distributed over a wider time range around the peak. The ratio between these different components is defined as **temporal laser contrast**. If these additional components are too intense (i.e. the temporal laser contrast is too low), there will be substantial heating and pre-expansion of the target as discussed in section 2.2. This pre-expansion has the potential to significantly influence the laser-plasma interaction upon arrival of the main pulse. In particular, ion acceleration from initially solid targets is strongly compromised by this effect. The characterisation and optimisation of the temporal contrast of a laser system is therefore crucial for performing high-quality experiments on laser-driven ion acceleration.

There are two types of temporal contrast: energy contrast and intensity contrast. Energy contrast represents the ratio of energy in the main pulse to the accumulated energy up to a certain time. The precise temporal sequence of energy deposition is irrelevant for the energy contrast.

Contrary to this, the intensity contrast K_{int} is a time-dependent parameter and defined as the ratio of the intensity maximum I_{max} to the intensity at a given time $I(t)$:

$$K_{int}(t) = \frac{I_{max}}{I(t)} \tag{3.1}$$

A schematic illustration of a typical temporal intensity distribution of a high-power laser is shown in Figure 3.2. The displayed temporal intensity profile highlights distinct re-

Figure 3.2: Illustration of a typical temporal intensity distribution of a high-power laser system with ultrashort (tens of fs) pulse duration. Colour-shaded areas highlight characteristic regions that contribute to the temporal intensity contrast of the laser.

gions on different timescales, characteristic for Ti:Sa-based CPA laser systems. A detailed description of these regions, elucidating their origin and discussing possible mitigation strategies, will be given in the following.

Amplified spontaneous emission

During the amplification process, the inverted gain medium produces **Amplified Spontaneous Emission (ASE)**, resulting in a low-intensity plateau underneath the main pulse.

Spontaneous emission is a parasitic process inversely proportional to the upper-state lifetime of the gain medium (e.g. Ti:Sa: $\approx 3.2\,\mu s$ at $300\,K$ [216]).

The ASE process results in the emission of radiation in all directions. If this spontaneous emission propagates in the same direction as the main pulse, it undergoes further amplification, resulting in the emission of radiation in all directions. This ASE plateau, typically spanning over several nanoseconds before and after the main pulse, is incoherent to the main pulse and remains largely unaffected after passing through the final grating compressor.

Combining **Pockels Cells (PC's)** and polarisation filters (e.g. thin film polarisers) within the CPA stage, enables to subtract a substantial part of the ASE by rapidly switching the laser pulse polarisation between the ASE component and the stretched main laser pulse. Another effective ASE mitigation strategy involves the implementation of two successive CPA stages linked by a nonlinear temporal filter [256], e.g. saturable absorbers [257, 258], nonlinear rotation of the polarization ellipse [259] or filtering by **cross-polarised wave (XPW)** generation [260]. Additionally, the OPCPA technique also helps to achieve very low ASE levels due to the absence of population inversion and energy storage within the gain medium.

Individual pre- and post-pulses

Replicas of the main pulse can appear as individual coherent **pre- and post-pulses** occurring on both nanosecond and picosecond time scales.

Pre- and post-pulses on the nanosecond time scale typically arise due to leakages in laser cavities and are often associated with regenerative amplifiers. Effective control of these pre- and post-pulses can be achieved by using fast optical switches, such as PC's, with precise timing.

On the picosecond time scale, pre- and post-pulses are usually generated by optical components with parallel surfaces (e.g. lenses, gain medium, Faraday isolators, windows). These components can cause multiple internal reflections of the main pulse, leading to the appearance of powerful post-pulses. In CPA systems, the stretched main pulse can temporally overlap with these post-pulses, resulting in spectral interference. This modulated intensity distribution can introduce temporal phase changes due to the intensity dependence of the refractive index. After temporal compression, this causes the generation of pulse replicas before and after the main pulse. This effect, also known as B-integral coupling, has been described theoretically by Didenko *et al.* [261] and measured experimentally by Schimpf *et al.* [262] and Kiriyama *et al.* [263].

Eliminating these pre-pulses can be achieved by preventing the generation of post-pulses. This can be accomplished by reducing the number of transmissive optics in the laser system. In cases where using transmissive optics is unavoidable, their surfaces can be carefully designed (i.e. wedged), allowing reflected pulses to be spatially separated from the main pulse [263].

Coherent pre- and post-pulse pedestal

In addition to the continuous ASE and discrete pre- and post-pulses, another characteristic feature of the temporal contrast of high-power laser systems is a pedestal starting tens to hundreds of picoseconds before the main peak and extending to hundreds of picoseconds after. This **pre- and post-pulse pedestal** comprises coherent components of the stretched pulse that were not perfectly recompressed. The pedestal's origin is multifaceted and an area of active research. Previous studies identified that the pedestal arises from scattering at the grating surfaces in the stretcher and compressor

stages [264], as well as from spectral clipping or phase distortions in the stretcher [265]. Particularly, the surface quality (i.e. surface roughness) of the optics in the stretcher is important, as imperfect surfaces lead to spectral phase shifts. Ranc *et al.* and Kiriyama *et al.* demonstrated that the convex mirror in an Oeffner stretcher can have an immense impact on the coherent pedestal [266, 267]. Lu *et al.* showed that changing the stretcher design from an Oeffner type to two concave mirrors reduces the intensity level of the pedestal significantly. This stretcher modification proved advantageous for ion acceleration, enhancing performance from 7 MeV to 16 MeV [268]. Achieving a low coherent pedestal is essential not only on the pre-pulse but also on the post-pulse side, as demonstrated by Khodakovskiy *et al.*, who studied how the pre-pulse pedestal is affected by the post-pulse pedestal under the influence of self-phase modulation [269].

3.1.3 DRACO laser system

The **DRACO (DResden lAser aCceleration sOurce)** laser system is located at the **Helmholtz-Zentrum Dresden-Rossendorf (HZDR)** in the north-eastern part of Dresden. In 2008, the first version of DRACO - based on Amplitude's PULSAR system - was installed and commissioned with a peak power of 150 TW. Over the years, the system has seen numerous modifications, all aimed to improve the beam quality and thus the experimental results. The most significant change took place between 2012 and 2015, when DRACO was upgraded to a dual-beam system and the peak power increased to 1 PW, with 750 TW consistently achieved in routine operation.

DRACO's system architecture is based on a double CPA design. Cleaning of the temporal contrast is achieved by using XPW-filtering between the two CPA stages. Throughout all amplification stages Ti:Sa crystals (doping concentration between 0.15 – 0.25 %) are utilised. These crystals are pumped by multiple neodymium doped yttrium aluminium garnet ($Nd^{3+}:Y_3Al_5O_{12}$ = Nd:YAG) pump lasers, which are themselves inverted via flash lamps. To pump the Ti:Sa crystals efficiently, the wavelength of the pump laser is frequency-doubled from 1032 nm to 516 nm.
DRACO can deliver laser pulses into two different experimental areas, one dedicated to electron acceleration and the other to ion acceleration.

Setup

A schematic of the DRACO laser architecture is shown in Figure 3.3. The DRACO pulse source is the mode-locked Ti:Sa oscillator *SynergyPro* from Femtolasers (now belonging to Spectra-Physics), emitting nJ-class laser pulses with > 100 nm bandwidth at a central wavelength of 800 nm and at a repetition rate of 78 MHz. Before entering the first CPA stage (CPA1), the pulse energy is increased to the µJ-level by a high gain multipass bulk amplifier - labelled as Booster amplifier - and a fast PC selects a 10 Hz pulse train as seed for further amplification.

The laser pulses enter the all-reflective Oeffner stretcher [270] of the CPA1 stage, where they are stretched to $\approx$ 500 ps. An **Acousto-Optic Programmable Dispersive Filter (AOPDF)**, *Dazzler* from Fastlite (now belonging to Amplitude), is implemented behind the stretcher to control the spectral phase distribution for ideal pulse compression or modification [271, 272]. A piezoelectric transducer generates a polychromatic acoustic wave that is sent collinear to the laser propagation direction into a birefringent crystal (e.g. TeO_2). Inside the crystal the acoustic wave overlaps with the optical wave of the laser, resulting in a local variation of the refractive index. Consequently, each spectral component of the
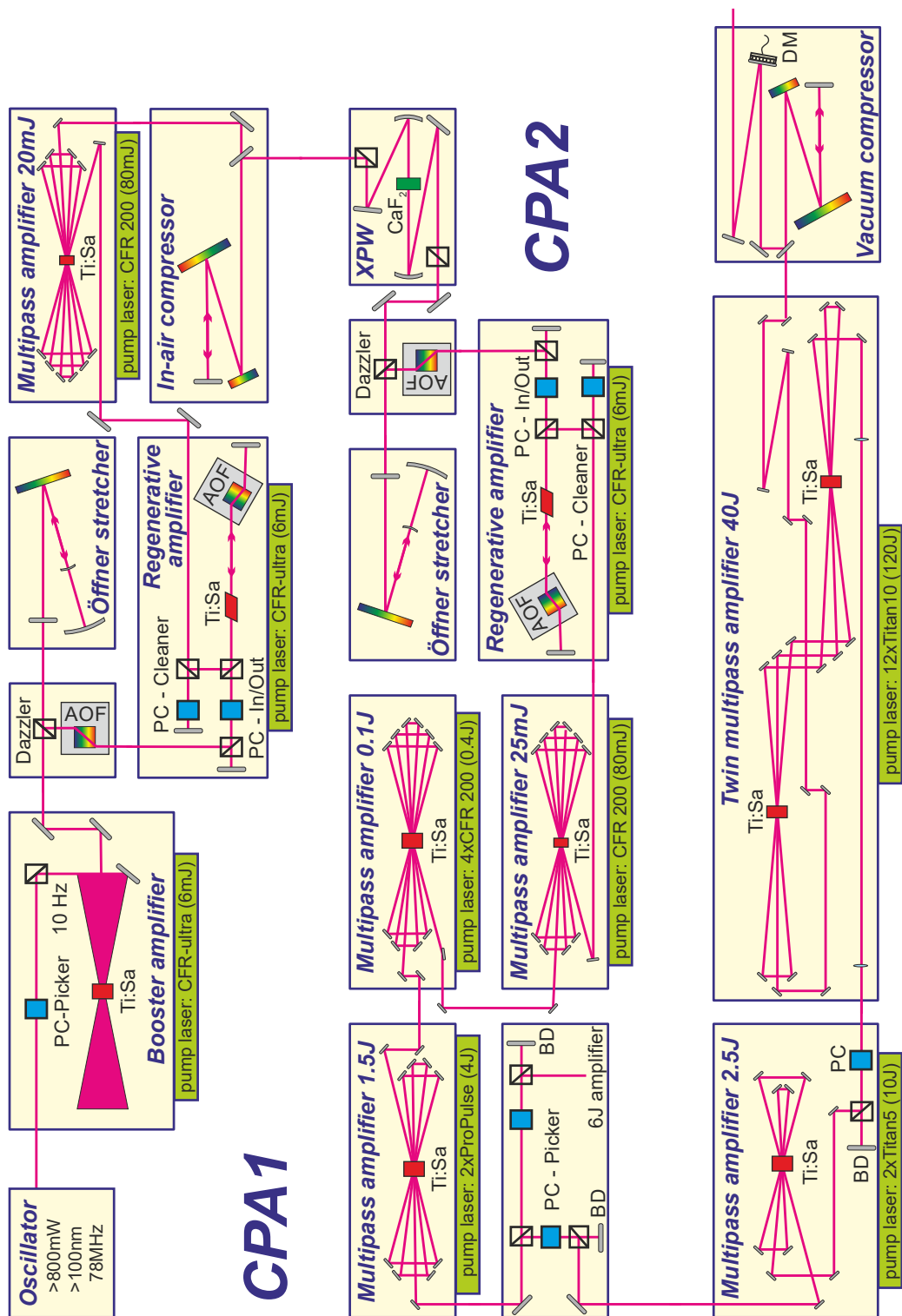
Figure 3.3: Schematic layout of the DRACO laser system including CPA1, CPA2 and the final amplification and pulse compression stages of the 1 PW beamline.
PC - Pockels cell, BD - beam dump, AOF - acousto-optical filter, DM - deformable mirror

incident laser pulse experiences an individually phase matched acoustic grating, leading to an individual diffraction. The exiting laser pulse consists of the diffracted spectral components, now having an arbitrarily adjustable phase and amplitude profile.

The first amplification stage of CPA1 is a 12-pass **Regenerative Amplifier (RA)** where the pulse energy is increased by a factor of 10^3 to the mJ-level. The resonator design defines a clean TEM_{00} transversal laser mode, ensuring an excellent spatial beam profile for further propagation through the system. The spectral laser amplitude is controlled by an **Acousto-Optic Programmable Gain Filter (AOPGF)** - *Mazzler* from Fastlite - which is inside the resonator cavity of the RA [273]. Similar in functionality to the *Dazzler*, the AOPGF selectively diffracts undesired spectral components. Specifically, parts of the laser spectrum that experience a high gain during the amplification process are selectively reduced to pre-compensate for both the gain narrowing and the red-shift of the spectrum. Instead, the outer wings of the spectrum are increased to maintain the $\approx 55\,nm$ bandwidth.

The laser pulses are then amplified to 25 mJ in a 6-pass multipass amplifier before being recompressed in air. A standard two-grating compressor with $\approx 65\,\%$ transmission efficiency is used to recompress the laser pulses to an **Full Width at Half Maximum (FWHM)** pulse duration of $\approx 30\,fs$, representing the end of CPA1. The intensity level of the intermediately recompressed laser pulses is sufficient for XPW generation ($> 10^{12}\,W\,cm^{-2}$). XPW generation and subsequent filtering has become a widely used technique in high-power laser systems, due to its superior performance for contrast improvement and spectral broadening [274]. However, the practical performance is mostly restricted by the extinction ratio of the polarisers. The compressed pulses at DRACO are focussed into a CaF_2 crystal, located in vacuum to prevent ionisation of air. Inside the crystal, only the most intense part of the laser pulse undergoes the nonlinear χ^3 process, leading to a polarisation modification. The lower intensity parts of the laser remain relatively unaffected by the CaF_2 crystal. Subsequently, the laser pulses propagate through polarisers positioned to effectively block the low-intensity portions.

The temporally cleaned pulses enter the second CPA stage (CPA2), which has a similar design to CPA1. An all-reflective Oeffner stretcher increases the pulse duration to $\geq 1\,ns$, before a RA increases the pulse energy by a factor of 10^3 to $\approx 1\,mJ$. The spectral amplitude and phase are controlled analogous to CPA1 by an AOPGF (*Mazzler* - inside the resonator cavity of the RA) and an AOPDF (*Dazzler* - in front of the RA). Three consecutive multipass amplifier (referred to as 25 mJ, 0.1 J and 1.5 J amplifier) increase the pulse energy to $E_L \approx 1.3\,J$. At this point, the laser pulses are split (50:50) into two individual seed beams for final amplification to different energy levels. One beam is sent towards the 6 J cryostat amplifier, serving as final amplification stage for the 150 TW section of the DRACO laser system. The other part seeds the PW section of the system, incorporating a 2.5 J and 40 J amplifier. Both amplification sections can be operated individually as well as simultaneously with inherent synchronisation up to the splitting point. Pulse picking PC's behind the splitter enable different operation modes of the main amplifiers, ranging from single-shot up to the maximum repetition rate of 10 Hz at 150 TW or 1 Hz at the PW section. To handle the heat load inside the gain material and to reduce thermal lensing as well as transverse lasing effects, liquid (1.5 J, 2.5 J and 40 J amplifier) or cryogenic cooling (6 J amplifier) is applied to the Ti:Sa crystals.

Finally, the laser pulse is recompressed in vacuum using a two grating compressor to an FWHM pulse duration of $\approx 30\,fs$. A deformable mirror behind the compressor gratings can compensate wavefront distortions of the laser beam and thus ensures excellent focus quality at the experimental area (further details below).

Spatial intensity distribution

The laser wavefront can suffer aberrations caused by air inhomogeneities and imperfections in optical components during propagation through the system, the pulse compressor and the transport beamline towards the experimental area. These aberrations degrade the quality and spatial properties of the laser beam. To achieve highest peak intensities in the focussed beam, a wavefront sensor and a **Deformable Mirror (DM)** can be used to compensate for such effects [275].

At DRACO-PW a high resolution wavefront sensor SID4 from Phasics measures the spatial aberrations of the laser behind the focussing **Off-Axis Parabola (OAP)** at the experimental chamber. The *quadriwave lateral shearing interferometry* technique [276] is used to sample the phase of the laser beam. Two different measurement options are available: A measurement directly behind the focussing OAP inside the vacuum chamber or imaging of the laser beam towards a diagnostic port outside the vacuum chamber. Analysis of the measurement allows the wavefront of the beam to be described by Zernike polynomials [277]. The coefficients of these polynomials correspond to different types of aberrations in geometrical optics and help to identify the origin of the measured distortion. The analysis software compares the measurement result to a flat spatial phase, resulting in an error signal. This error signal is then forwarded to the DM (ILAO from ISP systems), positioned between the vacuum compressor and the experimental chamber. Equipped with 53 piezo actuators, the surface of the DM can be precisely adjusted to correct and reshape the wavefront of the laser beam. Therefore, the error signal is converted into specific voltages for the individual actuators. This closed-loop system ensures efficient and real-time wavefront correction, leading to a substantial improvement in beam quality for experiments.

Figure 3.4 shows the focus of the attenuated DRACO-PW laser behind the f/2.3 OAP (off-axis angle: 90°) with applied wavefront optimisation. The focus in the target chamber was imaged onto a camera outside the chamber. The peak intensity of 6.58×10^{21} W cm^{-2}
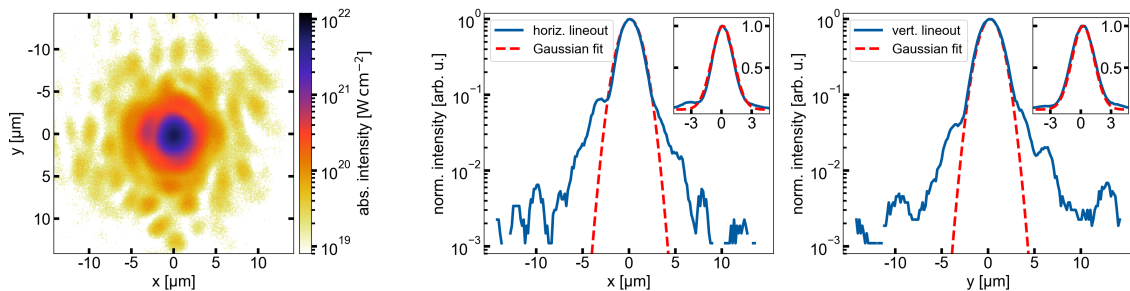
Figure 3.4: Focal spot measurement of attenuated DRACO-PW laser behind the f/2.3 off-axis parabola with logarithmic colour scale representing calculated abolute intensities (left). The normalised horizontal (middle) and vertical (right) lineouts through the focal spot centre show excellent agreement to a Gaussian fit with an FWHM width of 2.57 µm.

was calculated from the measured FWHM pulse duration of ≈ 30 fs and maximum on-target laser energy of $E_L \approx 22.5$ J. The $1/e^2$ width and $1/e^4$ width was calculated from an effective area, yielding an average intensity inside this effective area. The results of this focal spot analysis are summarised in Table 3.2.

Temporal intensity distribution

Figure 3.5 shows a representative temporal intensity distribution of the DRACO laser. The

DRACO-PW focal spot analysis			
parameter	value in µm	energy ratio in parameter area	average intensity in parameter area
FWHM width	2.57	33.8 %	4.80×10^{21} W cm^{-2}
$1/e^2$ width	4.36	57.9 %	2.86×10^{21} W cm^{-2}
$1/e^4$ width	9.52	81.8 %	0.84×10^{21} W cm^{-2}

Table 3.2: Focal spot analysis for DRACO-PW. The energy ratio and the average intensity were calculated for a circular area, defined by the respective parameter.
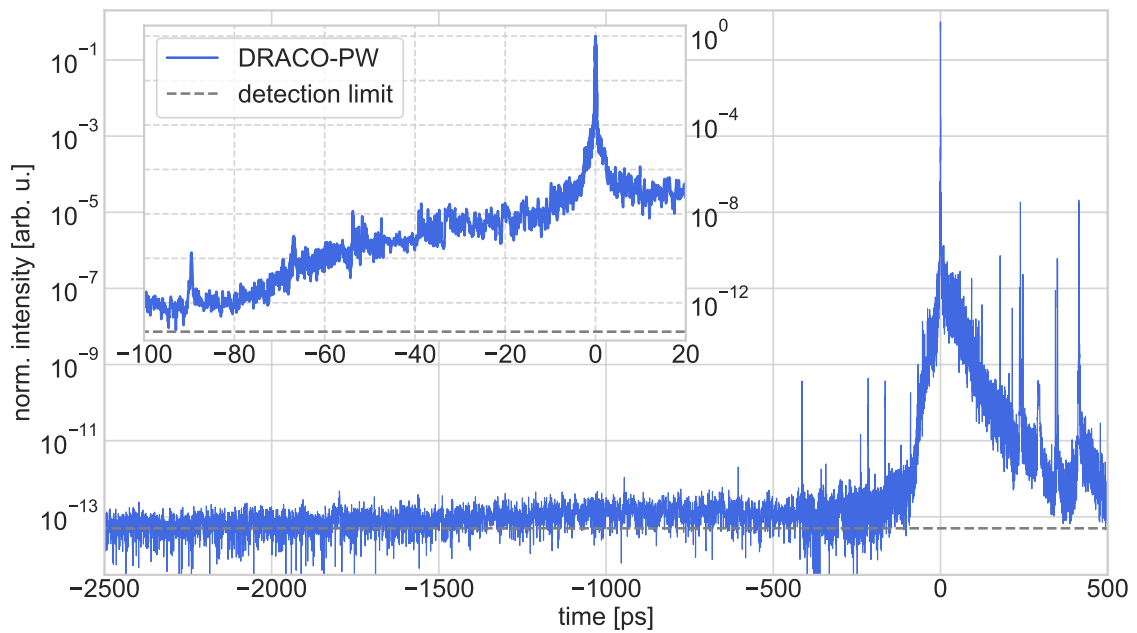
Figure 3.5: Temporal intensity contrast of the DRACO-PW laser, measured with a scanning third-order auto-correlator (SeqouiaHD) at the experimental area. The scan ranges from –2500 ps to 500 ps. Pre-pulses between –500 ps and –100 ps remain below an intensity level of 10^{-9}. The inset provides a detailed look at the rise of the coherent pedestal at $\approx$ –100 ps.

measurement was conducted using a scanning **Third-Order AutoCorrelator (TOAC)** at the experimental area and a half inch beam, which was picked off from the collimated, amplified ($E_L = 1.5\,J$, i.e. unpumped main amplifiers) and recompressed (using the vacuum compressor) laser beam. The typical characteristics of a CPA laser system as discussed in subsection 3.1.2 are visible. The ASE influence on the nanosecond range was minimised by employing a series of fast PC's with optimised timing structure and minimal timing jitter. This results in an intensity contrast ratio better than 10^{-12} up to $-100\,ps$ prior to the main pulse. The few visible pre-pulses between $-500\,ps$ and $-100\,ps$ remain below a level of 10^{-9}. They were identified to origin from post-pulses generated by internal reflections in remaining planar transmission optics (e.g. amplifier crystals, PC's, windows) in the laser chain. During the amplification process of the laser pulse, these post-pulses are converted into real pre-pulses by self-phase modulation associated with the accumulated B-integral [261–263]. For further optimisation, all remaining post-pulses should be ideally eliminated (e.g. by changing to wedged optics). The inset in Figure 3.5 shows the rise of the coherent pedestal at $-75\,ps$ which persists at 10^{-8} until $-10\,ps$. Optimising the intensity level of this part is difficult and requires either stretcher and compressor optics of higher surface quality [278], a changed stretcher design [268] or contrast cleaning techniques (e.g. plasma mirrors c.f. section 4.3).
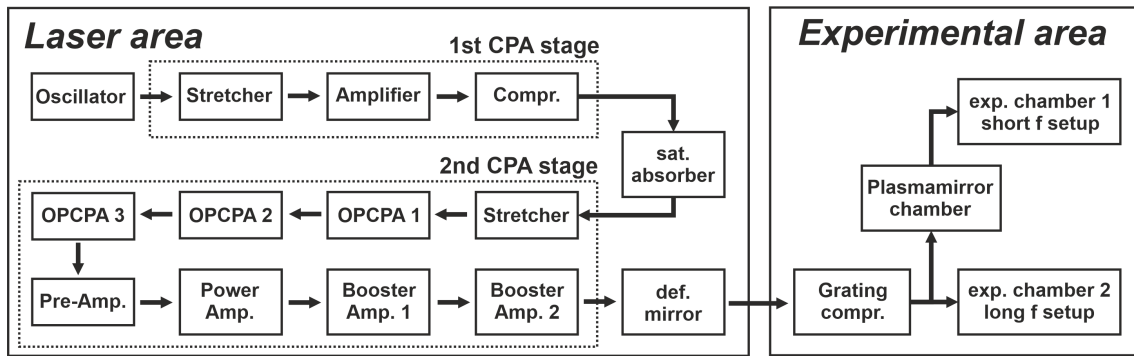
3.1.4 J-KAREN-P laser system

The **Kansai Photon Science Institute (KPSI)**, a part of Japan's **National Institute for Quantum and Radiological Science and Technology (QST)**, houses and operates the **Japan-Kansai Advanced Relativistic ENgineering-Petawatt (J-KAREN-P)** laser system and several experimental areas. The institute is located in the southern part of the Kyoto prefecture in Japan.

In 2003, the predecessor version (J-KAREN), was commissioned and the first Ti:Sa based laser system to reach nearly one petawatt (0.85 PW) peak power with a pulse duration of $\approx 33\,fs$ [279]. Over the years, the system has been continuously improved, particularly focussing on enhancing the temporal contrast [233, 258, 263, 280, 281]. These developments resulted in different operational modes at high or moderate contrast, each offering a certain level of maximum laser energy. The capabilities of the J-KAREN-P system have been demonstrated by individually generating laser pulses with energies of up to 63 J before compression and pulse durations of 28 fs [282]. During routine operation at high-contrast settings, J-KAREN-P delivers laser pulses with $\approx 10\,J$ within $\approx 45\,fs$ at a repetition rate of 0.1 Hz on target.

Setup

A schematic overview of the J-KAREN-P laser system is illustrated in Figure 3.6. The system comprises two CPA stages, each equipped with an AOPDF to actively control the spectral phase and fast PC's for contrast enhancement as well as a saturable absorber between the two CPA stages.
The first CPA stage (FEMTOPOWER compact PRO from Spectra-Physics) is a compact combination of an ultrafast mode-locked Ti:Sa oscillator, stretcher, multipass amplifier and AOPDF, as well as a grating compressor for dispersion correction. The output of this first stage are high-contrast laser pulses at the sub-mJ level with a pulse duration of 25 fs and excellent pulse-to-pulse stability. The pulses pass through a saturable absorber (colour glass filter) [257, 258], acting as a nonlinear temporal filter and improving the temporal contrast. This makes them making them an almost ideal seed for the sec-

Figure 3.6: Schematic layout of the J-KAREN-P laser system and the experimental area. Laser pulses from an fs-oscillator enter the first CPA stage, where the pulse energy is increased to the sub-mJ level. The laser pulses are then transmitted through a saturable absorber, acting as a nonlinear filter to increase the temporal pulse contrast, before the laser pulses enter the second CPA stage. Several OPCPA stages and multipass amplifiers increase the pulse energy to tens of joules. A deformable mirror compensates spatial phase distortions of the laser beam, ensuring that a flat wavefront is sent to the final compressor. The recompressed laser beam can be directed towards two different experimental chambers.

ond CPA stage.

In the second CPA stage an aberration-free, all-reflective Oeffner stretcher [270] increases the pulse duration to > 1 ns before the laser pulses propagate through another AOPDF. Afterwards, the laser pulses enter three consecutive OPCPA [218–220] stages, each consisting of a Type 1 **β-Barium Borate (BBO)** crystal as amplification medium. The spectral gain profile of each OPCPA stage can be tailored by adjusting the temporal intensity profile of the pump laser, thereby allowing to pre-compensate gain narrowing at downstream amplification stages. However, fluctuations in the pump laser also influence the stability of the spectral intensity profile of the amplified laser pulse, presenting a significant challenge of the OPCPA technique. On the other hand, OPCPA provides substantial advantages, including higher peak power and enhanced temporal contrast. The laser pulses from the OPCPA stage are directed to several multipass amplifiers, increasing the laser energy from several millijoules to several tens of joules after the last amplifier. Cryogenic cooling of the "Power Amplifier" facilitates laser operation up to a repetition rate of 10 Hz. The last two amplification stages, labelled "Booster-Amplifiers - 1" and "Booster-Amplifier - 2", employ commercially available frequency-doubled Nd:glass lasers to pump the Ti:Sa crystals (diameter 80 mm and 120 mm, respectively).

A deformable mirror (ILAO STAR B95-52 from Imagine Optics) compensates the spatial phase distortions measured by a Shack-Hartmann wavefront sensor (HASO3-32 from Imagine Optics) after "Booster-Amplifier - 2" to ensure that laser pulses enter the vacuum compressor with a flat wavefront. From the laser area, the beam is guided towards the radiation controlled experimental area, enclosed by 1 m thick concrete walls to shield ionising radiation. The experimental area comprises the vacuum compressor, a plasma mirror chamber for temporal contrast improvement and two experimental chambers. The amplified laser pulses are recompressed to an FWHM pulse duration $\leq$ 30 fs, using four gold-coated holographic gratings (1480 grooves mm^{-1}, size: 565×360 mm^2). Finally, the laser beam is distributed towards the different experimental chambers.

Spatial and temporal intensity distribution

For achieving best spatial contrast, a deformable mirror corrects the wavefront of the collimated beam before the compressor (as detailed above). Subsequently, the beam

is directed through a low-distortion beamline towards the experimental area. After focussing by an f / 1.4 OAP (off-axis angle: 45°), a nearly diffraction limited FWHM spot size of 1.5 μm can be achieved [283], yielding a peak intensity of $(3.5 \pm 0.5) \times 10^{21}\,\mathrm{W\,cm^{-2}}$. A representative temporal intensity distribution of the J-KAREN-P laser is shown in Figure 3.7. Contrast measurements at the experimental area were performed by picking off
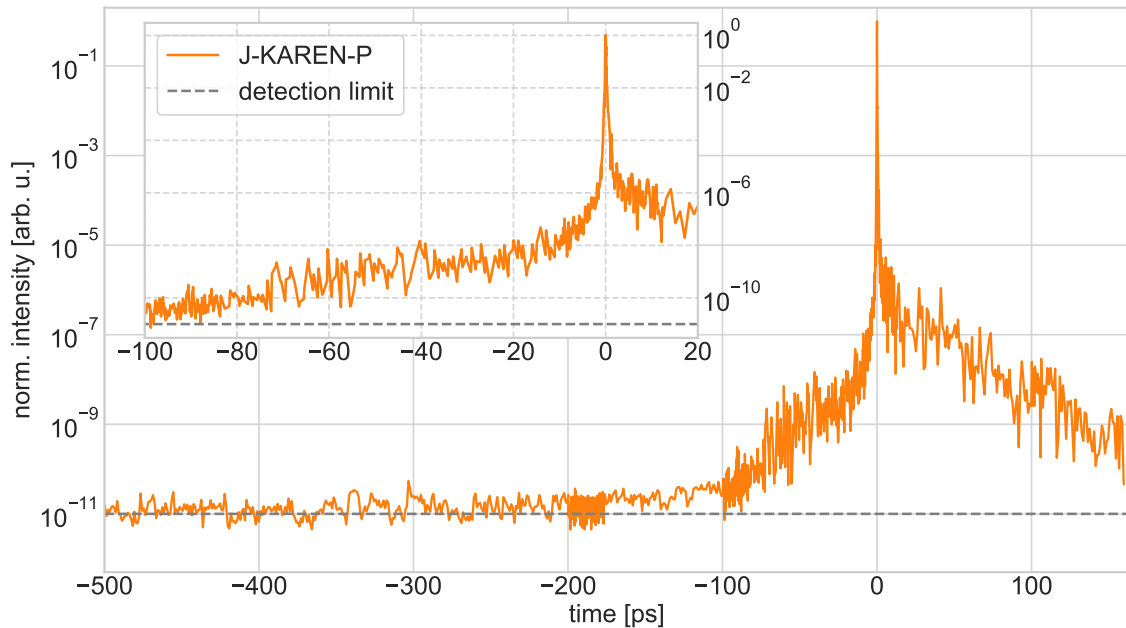
Figure 3.7: Temporal intensity contrast of the J-KAREN-P laser, measured with a scanning third-order autocorrelator (Seqouia) at the experimental area. No significant pre- or post-pulses can be detected over the entire scan range from –500 ps to 160 ps. The inset provides a detailed view on the coherent pedestal.

a half inch beam from the collimated, recompressed and attenuated laser beam. Up to –100 ps before the main pulse, the ASE level is $\approx 10^{-11}$ (detection limit of TOAC) or better. Throughout the entire scan range (–500 ps to 160 ps), no notable pre- or post-pulses are detected (achieved by introducing a small wedge to the post-pulse generating Ti:sapphire crystals and windows). The intensity level of the coherent pre-pulse pedestal increases from $\approx 10^{-10}$ at –100 ps to $\approx 10^{-7}$ at –10 ps. Improving the quality of the convex mirror in the stretcher enhanced the contrast level of this pedestal, showing a reduction of one to two orders of magnitude within the –33 ps to –7 ps time window [267].

3.2 Experimental Area

This section provides an overview of the experimental infrastructure and the target chamber configuration at HZDR and KPSI, where the experiments of this thesis were conducted. Figure 3.8 shows the experimental area at HZDR to give an impression of the range of technical equipment required to perform and diagnose experiments on plasma acceleration with high-power lasers.
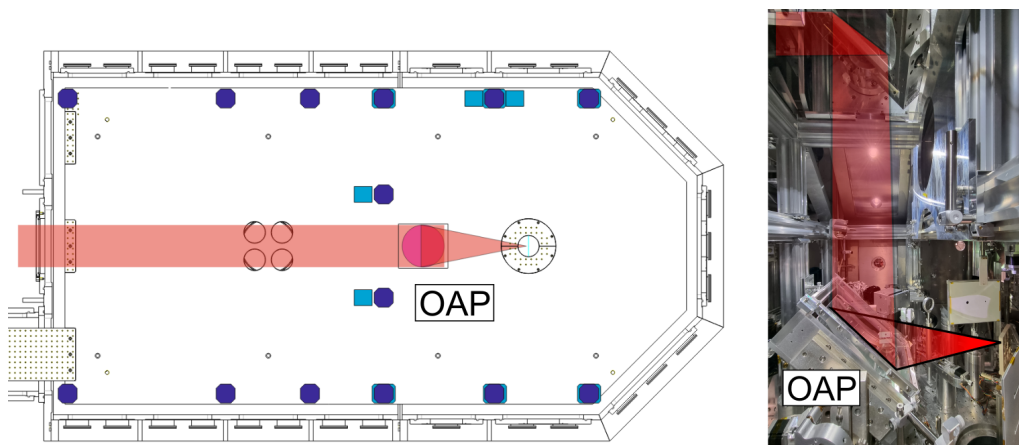
3.2.1 Short-f chamber at HZDR

The experimental area at HDZR is equipped with two different target chambers, designed for experimental studies on laser-driven ion acceleration. While in the smaller target
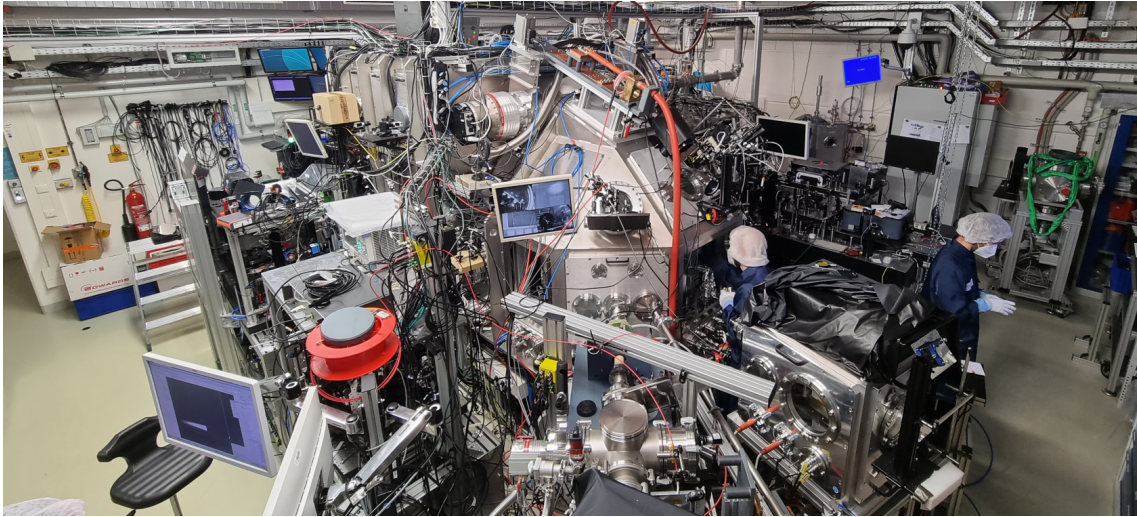
Figure 3.8: Photograph of the experimental area at HZDR and the big target chamber, dedicated for high-intensity interaction studies.

chamber the 150 TW laser beam can be used only, the bigger chamber provides the option to use both laser beams, DRACO-150 TW and DRACO-PW, for experiments. In this thesis, only the big chamber was used during all experiments at HZDR.

The shape of the big target chamber is a combination of a large rectangle and an additional semi-hexagonal structure. A schematic can be seen in Figure 3.9. The compressed DRACO-PW laser beam enters the rectangular part of the target chamber on an upper level. On demand plasma-mirror cleaning can be applied at this level by moving turning mirrors into the beam path of the incoming laser. Subsequently, a 90° turning mirror directs the laser beam towards the OAP. The OAP features a dielectric coating, a 90° off-axis angle and a focal length of $\approx$ 400 mm, yielding a nominal f-number of f / 2.3 for a clear aperture of $\approx$ 175 mm. The focal point of the OAP represents the centre of the semi-hexagonal structure of the target chamber, providing versatile options for positioning various diagnostics.
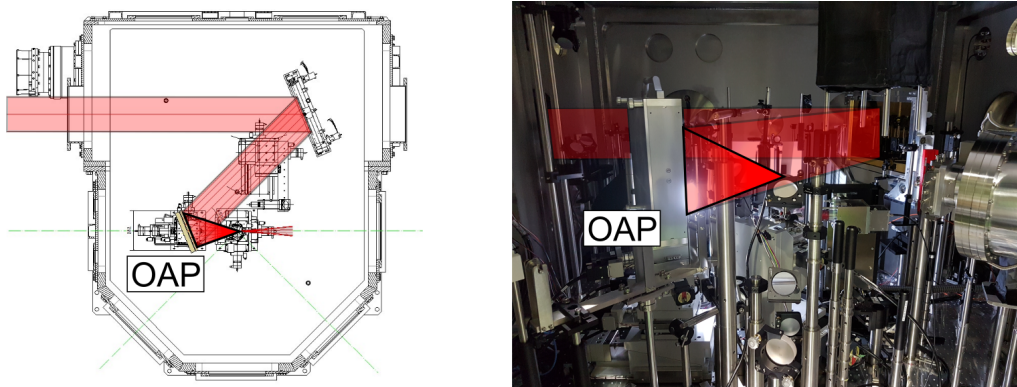

Figure 3.9: Short-f target chamber at HZDR: Left: Sketch of the target chamber at HZDR and the corresponding laser beam path. Right: Photograph of the target chamber at HZDR. The laser beam path is illustrated in red.

3.2.2 Short-f chamber at KPSI

A schematic of the short-f target chamber at KPSI can be seen in Figure 3.10. The target

Figure 3.10: Short-f target chamber at KPSI: Left: Sketch of the target chamber at KPSI and the corresponding laser beam path. Right: Photograph of the target chamber at KPSI. The laser beam path is illustrated in red.

chamber has a semi-hexagonal shape, allowing for several ports directed to the centre of the chamber. The p-polarised laser beam, 250 mm in diameter, enters the chamber from the side and is directed towards the OAP by a gold-coated 45° turning mirror. The gold coated OAP has an off-axis angle of 45° and a focal length of f = 350 mm, resulting in a nominal f-number of f / 1.4.
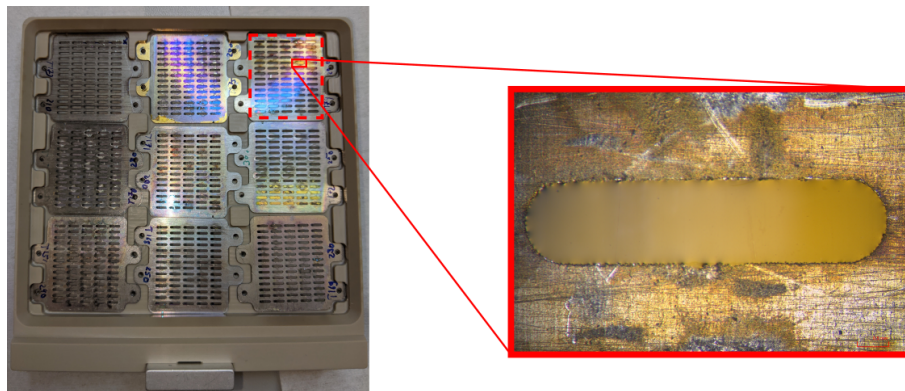
3.3 Targets

Ion acceleration experiments require not only stable and well-characterised laser pulses, but also high-quality targets that effectively interact with the laser. The morphology of a target plays a vital role in the absorption of laser energy, thus influencing the performance of laser-driven ion acceleration. A wide range of targets with different geometrical shapes (e.g. thin foils, cones, spheres, rods), structures (e.g. foam-like, micro-structured, multi-layer, pillars, nano-tubes, coils), materials (e.g. metals, dielectrics) and states of aggregation (solid, liquid, gas) have been proposed and utilised by different groups. All these approaches try to optimise the ion acceleration process by influencing the absorption of laser energy, the pre-plasma formation, the electron transport and the ion emission characteristic. A comprehensive overview of experimental results, using different types of foil targets was prepared by Măgureanu *et al.* [284].

The ion acceleration experiments in this thesis employed different types of solid-state materials as target systems. Primarily, self-produced Formvar plastic foils ($C_5H_8O_2$, density: $\rho = 1.25\,\mathrm{g\,cm^{-3}}$, electron density: $n_e = 230\,n_c$ (800 nm) when fully ionised) were used. These plastic targets can be produced in a wide range of thicknesses, spanning from a few nanometre up to several hundreds of nanometres.
The production process involves dissolving synthetic resin/polymer (e.g. Formvar or polystyrene) in a suitable solvent (e.g. chloroform). A clean glass substrate is then dipped into the solution, resulting in the formation of a thin film of plastic on the surface of the substrate. After the thin film has dried, the edges of the slide are scored and the slide is slowly immersed in a water bath. This causes the film to detach from the glass surface and float in the water. Finally, the floating film is fished off and dried to yield the finished target. Alternative fabrication techniques for foil targets of a few nanometre thickness

involve ion sputtering [285], spin-coating or a method, where the dissolved plastic is directly dropped on a water surface and then collected by a substrate [286].

The foils were mounted between two ceramic (MACOR) or metal (stainless steel) holders in a sandwiched configuration. Figure 3.11 shows the target holder and an individual Formvar target. The target holder is made of PEEK (plastic) and holds nine target tiles

Figure 3.11: Left: Image of the target holder with nine target tiles, each containing 70 individual targets. The red dashed line marks a single tile and the red solid line an individual target. Right: Microscopy image of an individual Formvar target of 270 nm thickness. The reflection of background light causes the transparent target to appear orange.

with 70 holes (width: 3 mm, height: 1 mm) on each tile. Ideally, this gives a total number of 630 targets which can be utilised before the interaction chamber needs to be vented. This provides a sufficient number of targets to conduct systematic studies with different target thicknesses or materials.

3.4 Optical diagnostic

In laser-driven ion acceleration experiments, optical diagnostics are essential to measure the laser pulse parameters, such as the temporal or spatial intensity profile, but also to detect and analyse how the interaction with the plasma affects the optical properties of the laser. The results allow to study the interaction dynamics, such as the formation of plasma structures, the generation of electromagnetic radiation or a change of opacity as the laser propagates through the plasma.

3.4.1 Transmitted and reflected laser light

An experimental key diagnostic for investigating laser-driven ion acceleration from ultra-thin solid-state targets is the measurement of the transmitted and reflected laser light properties. This becomes particularly important when an initially opaque plasma undergoes relativistically induced transparency during the laser-target interaction, as discussed in subsection 2.1.3. These measurements allow to detect the onset and progression of target transparency, which is an important regime for enhancing ion acceleration (c.f. subsubsection 2.3.3). Furthermore, the spectral phase and the spectral intensity of the transmitted and reflected laser light, provide a deeper insight into the interaction dynamics between the laser and the plasma.

Beam profile and intensity

Typically a scatter screen is employed to diffuse light over a larger area, facilitating measurements of the light properties. The screen usually consists of a thin material, such as a ground glass substrate or a diffusing material like **Polytetrauoroethylene (PTFE)** which homogeneously scatters off light. It is important to position the screen perpendicular to the light beam to achieve accurate measurements. The distance between the interaction point and the screen must be carefully chosen to control the beam size on the screen and thus the intensity. If the intensity is too high, ionisation and ablation of the screen material will occur, affecting the measurements or, in the worst case, destroying the screen. The scatter screen is imaged onto a **Complementary Metal-Oxide-Semiconductor (CMOS)** or a similar imaging sensor. Equipping the imaging system with filters, such as bandpass filters or a coloured glass, enables to selectively isolate desired wavelengths or harmonic components of the transmitted and reflected light. Additionally, the use of suitable neutral density filters allows for the suppression of stray light and facilitates unsaturated measurements. After performing a calibration of the screen, the absolute intensity of the reflected and transmitted light can be determined.

At DRACO-PW the transmitted laser and reflected laser light was scattered off a PTFE screen placed $\approx 33\,\text{cm}$ and $\approx 85\,\text{cm}$ away from the target, respectively. The screens were imaged onto CMOS cameras (acA1300 from Basler), equipped with bandpass filters ($800\,\text{nm} \pm 25\,\text{nm}$).

Similarly, the experiments at J-KAREN-P used ground glass screens, placed $\approx 50\,\text{cm}$ away from the target, that were imaged onto bandpass filtered ($800\,\text{nm} \pm 25\,\text{nm}$) cameras.

Spectral intensity distribution

Two symmetrical Czerny-Turner [287] spectrometers (AVASPEC-ULS2048CL-EVO from Avantes) with a $300\,\text{l}\,\text{mm}^{-1}$ grating were used to measure the spectrum of the reflected and transmitted light. The measurements covered wavelengths from $200\,\text{nm}$ to $1100\,\text{nm}$. The intensity calibrated CMOS detector and the 16 bit analogue to digital converter enable a dynamic range of more than 10^3. Figure 3.12 shows the realised detector setup at the experimental area. The reflected light signal is collected by a spherical mirror ($f = 200\,\text{mm}$) and imaged onto a fibre. Similarly, the transmitted light is collected by a plano-convex lens ($f = 75\,\text{mm}$) and focussed onto another fibre. The fibres, both equipped with a cosine corrector to ensure accurate light collection angles, transport the collected reflected and transmitted light signal to the respective spectrometer for analysis.

3.4.2 Spectral phase measurements

The spectral phase of a laser pulse refers to the variation of its spectral components. Measurement and control of the spectral phase are crucial as this parameter directly affects the temporal intensity distribution of the laser pulse.

Spectral phase measurements rely on the principle that the spectral and temporal properties of a laser pulse are linked through the Fourier transform relationship. The spectral phase of the laser pulse can be retrieved by analysing the spectral interference pattern, which is typically obtained through nonlinear processes or interferometric setups. For the experiments presented in this thesis, two measurement techniques were used, which are explained below.
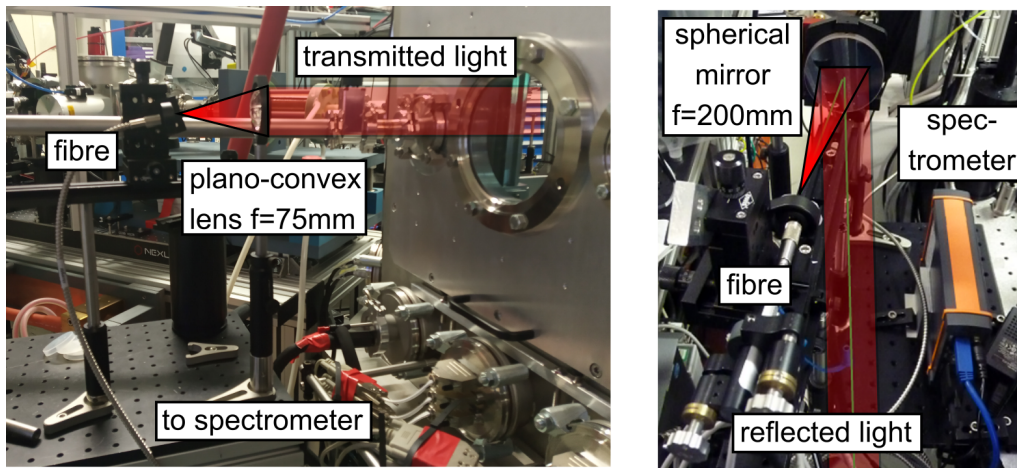
Figure 3.12: Photograph of the experimental setup for the spectral measurements of the transmitted (left) and reflected light (right).

Fourier-transform spectral interferometry

Fourier Transform Spectral Interferometry (FTSI) is a measurement technique used to characterise the electric field of an ultrashort laser pulse [288]. The method utilises the principles of interferometry and Fourier analysis to gain insights into the spectral and temporal properties of the laser pulse and to accurately reconstruct its temporal profile.

In a standard FTSI setup, the laser pulse of interest is combined with a reference pulse of known phase. The resulting interference pattern then contains information about the spectral phase of the pulse. A Fourier transformation of the interferogram converts the spectral phase difference between the pulses into a temporal phase. This enables the reconstruction of the temporal intensity profile of the laser pulse. In this thesis, two different implementations of the FTSI technique were used.

One method involves the widely recognised WIZZLER device from Fastlite, where the reference pulse is self-created by XPW generation from a pulse replica [289]. This technique is therefore also referred to as **Self-Referenced Spectral Interferometry (SRSI)**.

The other technique is a conceptual refinement of the SRSI method, labelled **Self-Referenced Spectral Interferometry with Extended Time Excursion (SRSI-ETE)**, enabling a higher dynamic range, a higher temporal resolution and a larger temporal window by introducing a small angle between the pulse of interest and the reference pulse [290]. In the framework of this thesis, two identical SRSI-ETE apparatus were developed and set up, consisting of an imaging interferometer, a two-dimensional optical spectrometer and readout electronics. One device is dedicated to experiments at DRACO-PW laser system, while the other one was shipped to Japan for the experiments at J-KAREN-P laser system.

SPIDER-technique

Spectral Phase Interferometry for Direct Electric-field Reconstruction (SPIDER) is a measurement technique that was introduced in 1998 [291] as a nonlinear variant of spectral interferometry. The SPIDER setup generates spectral interference by combining the pulse with its frequency-shifted replica, facilitated through upconversion within a nonlinear crystal. Analysing the modulation pattern enables to reconstruct the temporal pulse profile in the sub-ps range. This method has become a standard technique for measuring the spectral phase of ultrashort laser pulses. The experiments in this thesis employed the commercially available FC SPIDER from APE.

3.5 Particle diagnostic

This section introduces the different particle detectors used in the experiments of this thesis. These detectors capture and analyse the properties of the accelerated ion beam, offering valuable insights into the dynamics and characteristics of the laser-plasma interaction. Understanding the capabilities and limitations of the detectors is therefore essential for interpreting the experimental results.

The key characteristics of plasma-accelerated ions, including their short bunch length, high currents, angular divergence, and large energy spread were discussed in chapter 2. These characteristics outline the requirements for an ideal diagnostic system, which should enable fast acquisition, high dynamic range, high sensitivity, high energy resolution, and angular-resolved characterisation capabilities.

3.5.1 Thomson parabola spectrometer

The **Thomson Parabola Spectrometer (TPS)** is one of the most commonly used diagnostic tools for charged particle beams in laser-plasma acceleration experiments. It allows discrimination of different ion species and measurement of their energy spectra within a small solid angle. The first version of this detector was build in 1911 by J. J. Thomson [292], and the conceptual design has not changed since.

A TPS consists of parallel electric and magnetic fields, both oriented perpendicular to the propagation direction of the ion beam, and a detector. The particle beam enters the field zone through a small pinhole at the entrance of the TPS. Inside the field zone, the Lorentz force (c.f. Equation 2.34) acts on the particles of charge q. Depending on the charge to mass ratio (q/m) and the velocity of the particles, the Lorentz force results in a parabolic trace for each particle which can be captured by a detector. The electric field results in a q/m dependent component to the Lorentz force, differentiating different ion species. The magnetic field exerts a force on the particles that is proportional to their velocity. In combination with a calibrated detector system, this diagnostic enables precise measurements of the ion energy distribution (e.g. [293] and many others).

Multiple TPS with nearly identical setups were used during the experiments presented in this thesis. An aperture pinhole placed at the entrance of the TPS ensured that an almost collimated particle beam entered the TPS. The pinhole diameter determined the angular acceptance angle of the TPS, affecting the particle flux and energy resolution. Ion species separation was enabled by an electric field generated between two electrode plates with a high potential difference. A permanent dipole magnet, placed inside a yoke to minimise edge effects, generates a magnetic field with a strength of approximately 930 mT over a length of 200 mm.

The detector system at DRACO-PW consisted of a high resolution camera and a **Microchannel Plate (MCP)**, which is basically a photomultiplier tube. The MCP's central component is a 1 mm-thick Pb glass plate with numerous channels (inner diameter 20 μm) arranged in a honeycomb-like shape. The upper and lower sides of the glass plate are coated with a metal, typically an NiCr alloy. A voltage of tens of kV is commonly applied between the upper and lower sides of the glass plate. When ions collide with the channel wall, electrons are released. These electrons are then accelerated along the channel due to the applied voltage, leading to successive collisions with the channel's wall. This sequential cascade accelerates numerous electrons, which ultimately exit the MCP and hit a phosphor screen. This interaction generates a visible glow that is detected by a high resolution camera (scA1400-17fm from Basler), enabling an online read-out. The

MCP response up to 60 MeV was cross-calibrated to simultaneous measurements with a scintillator screen, which was absolutely calibrated with protons from a conventional accelerator.

Dose-sensitive **Imaging Plates (IP's)** were utilised as passive detectors for the TPS measurements at J-KAREN-P. IP's are widely used in the medical field, particularly in radiography but also for detecting electrons, ions and x-rays in laser-plasma interaction studies. The active layer within the IP contains chemical components that emit photoluminescent light when stimulated by energetic radiation or energy deposition resulting from particle impacts. Scanning and analysing IP's after irradiation enables to reconstruct the particle spectrum with remarkable spatial resolution and a wide dynamic range. To precisely determine the absolute number of particles interacting with the IP, calibration with the respective particle species is essential [294–297].

3.5.2 Time of flight measurements

Time-Of-Flight (TOF) measurements are an established and widely used technique for determining the energy of particles by measuring the time it takes them to travel a known distance. By accurately measuring this travel or flight time, the energy of the particle can be calculated when the particle mass is known. This technique was introduced as an advancement in mass spectrometry by Stephens in 1946 [298] and first realised as "*Ion Velocitron*" by Cameron and Eggers in 1947 [299] to retrieve the particle masses of the constituents of an ion beam when their energy values are known.

Using Equation 3.2 the energy of an ion E_{ion} with mass m_{ion} can be calculated for a known distance between ion source and detector d_{TOF} from the measured flight time t_{TOF} to the detector:

$$E_{ion} = (\gamma - 1)\, m_{ion}\, c^2 = \left(\left(1 - \frac{d_{TOF}^2}{c^2\, t_{TOF}^2} \right)^{-1/2} - 1 \right) m_{ion}\, c^2 \tag{3.2}$$

A TOF setup usually comprises three main components: the ion source, a field-free drift region, where ions get separated according to their mass and energy, and a detector capturing the ions for further analysis. A photograph of the realised setup at HZDR can be seen in Figure 3.13. The total distance between the target (ion source) and the de-
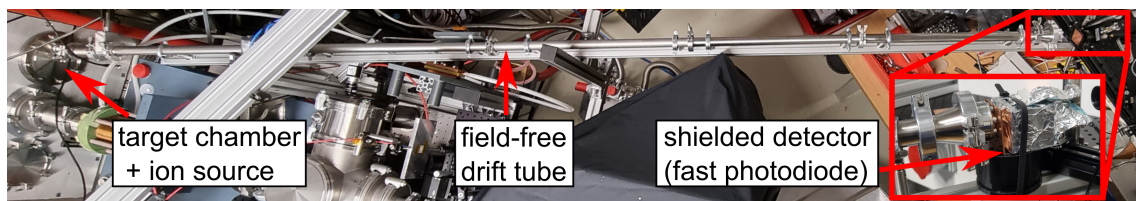
Figure 3.13: Photograph of the time-of-flight diagnostic setup at the experimental area at HZDR. Ions that are accelerated during laser-plasma interaction in the target chamber propagate along the field-free drift tube and are detected by a photodiode.

tector was $\approx 4\,\text{m}$. The angle between the laser propagation direction and the detector was measured to be 31.5°. A high sensitivity avalanche **PhotoDiode (PD)** (APD210 from MenloSystems) with a silicon detector of 0.5 mm^2 diameter and a rise time of 500 ps was employed, allowing for precise time-resolved measurements. When a particle deposits its energy in the active area of the PD, a photocurrent is generated by electron-hole pairs. A fast oscilloscope (MSO64 from Tektronix) enabled accurate measurements of this current on a long time scale due to its large bandwidth (6 GHz) and memory capacity (25 MSa). During the laser-plasma interaction strong **ElectroMagnetic Pulses (EMP)**

are generated, interfering with the TOF signal and degrading the measurement quality. To mitigate this EMP influence, a special aluminium foil shielded the PD and an EMP-protected high-frequency cable was used to transport the signal to the oscilloscope. TOF setups usually employ filter materials in front of the diode to prevent other ion species from contributing to the detected signal. For the experiments in this thesis, a 2 mm copper plate in front of the diode blocked protons with less than 34 MeV and other ion species (e.g. 64 MeV u^{-1} carbon and 75 MeV u^{-1} oxygen ions). An iterative deconvolution method is used to convert the measured raw signal into a proton energy spectrum [300]. An exemplary TOF measurement and the corresponding spectra is shown in Figure 3.14. The compact design of the TOF setup, coupled with an online readout capability, makes it
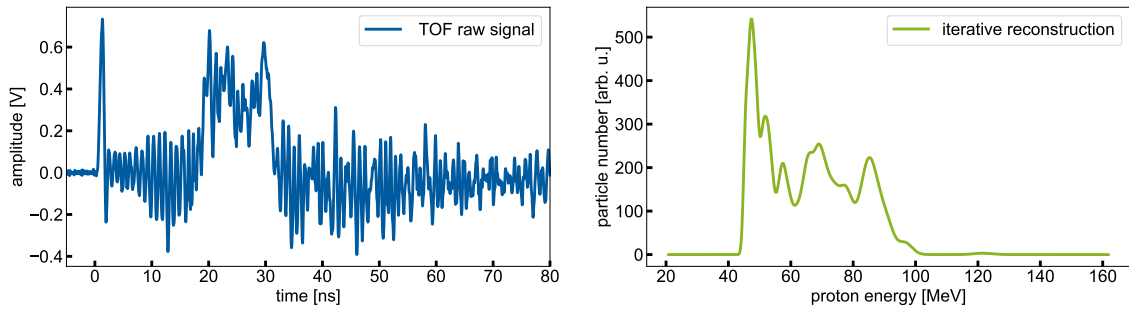
Figure 3.14: Exemplary time-of-flight measurement. Left: Raw signal of the photodiode. The first peak at $\approx$ 1 ns originates from fast electrons. The signal between 18 ns and 35 ns is caused by protons, arriving at different times due to different kinetic energies. Right: Reconstruction of the proton energy spectrum from the raw signal.

ideal for detecting ion beams of small diameter and low particle numbers. This approach has been extensively employed in characterising laser-accelerated ion beams [300–304].

3.5.3 Spatial proton beam profiler

TPS and TOF detectors offer the capability to characterise the particle beam within a restricted acceptance angle with high energy resolution. However, these methods do not allow to access the spatial distribution. Stacking materials that respond to the particle beam, such as CR39 or radiochromic films (details below), has demonstrated excellent spatial and energy resolution but is not suitable for high-repetition-rate experiments. To overcome this limitation, a novel detector for spatially-resolved proton beam measurements with online readout capabilities was developed and implemented for the experiments presented in this thesis.

The main concept of this proton beam profiler involves using a thin plastic scintillator and absorber material of different thickness, a widely adopted approach in the field of laser-plasma interaction [305–308]. A calibrated scintillator (DRZ High from MCI Optonix) screen (size: 100 mm × 150 mm, thickness: 500 µm) was positioned at a distance of 87 mm from the target. Upon interaction with protons, the scintillator converts the particle beam into an optical signal by emitting photons at the fluorescence wavelength of 546 nm [309]. The DRZ High scintillator offers good spatial resolution, high light yields and a decay time of less than 1 ms, enabling operations at high repetition rates and low particle fluxes. The emitted luminescence light was captured by a bandpass filtered (540 nm ± 2 nm) camera. Aluminium absorbers of distinct thickness (8 mm, 25 mm and 38 mm) ensured that only particles with sufficient energy to penetrate the specific absorber would deposit their energy in the scintillator. This modification enabled protons of specific energy levels to be spatially distinguished. A slit in the central horizontal plane

of the profiler allowed for the parallel operation of the TPS and TOF detectors. Figure 3.15 shows the proton beam profiler and the different absorber configurations used during the experiments.
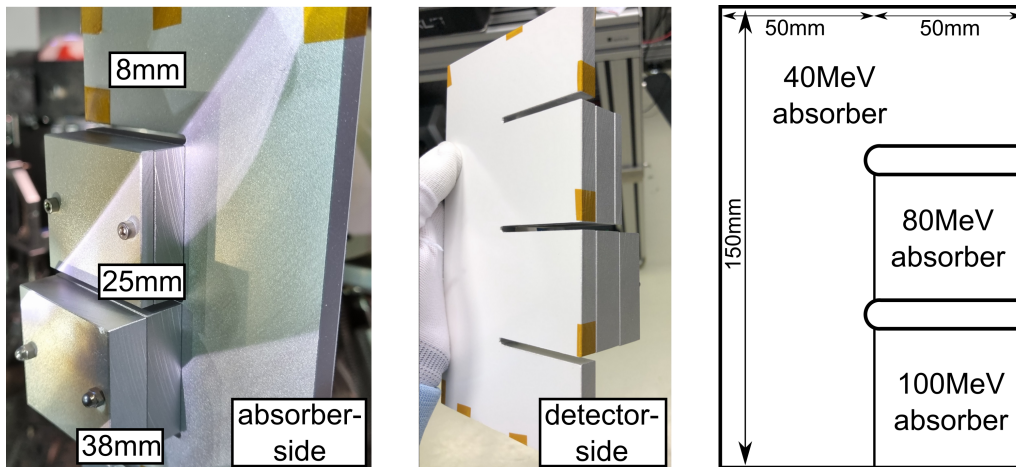

Figure 3.15: Photograph of the proton beam profiler (left: absorber-side, middle: detector-side). Absorbers of different thickness prevent ions below a certain threshold energy to reach the scintillator. Right: Sketch of the proton beam profiler, including the dimensions and the different threshold energies, as seen from the detector-side.

3.5.4 Radiochromic films

RadioChromic Films (RCFs) are polyester films, equipped with a self-developing active layer that reacts to ionising radiation. Upon impact of such radiation, the deposited energy causes polymerisation of the active layer (organic monomer), resulting in a persistent darkening of the film. The degree of darkening can be measured as **Optical Density (OD)** of the film and depends on the absorbed dose. The specific functional relationship[1] between OD and absorbed dose needs to be derived from reference irradiations, using the corresponding RCFs and calibrated scanning devices. Having this calibration function available, RCFs provide a two-dimensional spatial distribution (10's of µm resolution) of absorbed dose. Depending on the used film type, the dose ranges from 10^{-1} Gy (e.g. Gafchromic EBT3) up to 10^3 Gy (e.g. Gafchromic HD-V2) [310]. Height and width of the RCFs can be individually adjusted to fully cover the experiment-specific area of interest. Using a stacked configuration of RCFs and absorber material allows for an energy-resolved spatial dose distribution of the particle beam [311]. Each layer in such a stack can be associated with a specific energy value that a particle must have to penetrate up to this particular layer. Additionally, the absorber material (e.g. Cu, Al, Ni) itself can serve as a diagnostic (detailed in subsection 3.5.5). RCFs are insensitive to different ion species, meaning that e.g. carbon ions can only be distinguished by their specific energy deposition (Z^2 dependence of stopping power where Z denotes the atomic number of the ion) [312]. This dependence results in distinct stopping ranges for different ion species. Electrons and X-rays will also induce reactions in RCFs. However, their contribution can be differentiated from protons as they typically create a diffuse background signal with different energy deposition in successive layers.

A major drawback of RCFs is their offline nature, requiring replacement after each shot. For this reason, only a limited number of RCFs were used during the experiments presented in this thesis. A motorised wheel, equipped with multiple clamps, facilitated irra-

---

[1] $OD = \log_{10}(I_0 / I)$, I_0: incident light, I: transmitted light

diation of up to eight stacks. All deployed RCF stacks were wrapped in 30 μm aluminium foil to prevent transmitted laser light and target debris to interact with the films. Furthermore, this layer effectively blocked the majority of low energy ions (e.g. < 145 MeV C^{6+}). The lateral stack size was either 5 cm × 5 cm or 10 cm × 5 cm. The amount and thickness of the absorbers were adjusted for each experiment, ensuring that the stack provided good energy resolution in the range of expected maximum energies. Detecting proton energies > 100 MeV required copper plates with an accumulated thickness of 14.5 mm, resulting in a total weight of 650 g for the stack.

3.5.5 Nuclear activation measurements

A proton detection method that can be effectively used in conjunction with RCFs is based on nuclear activation measurements, a highly sensitive method that relies on the detection of gamma-rays emitted by a sample to identify and quantify the presence of specific elements. When a sample is irradiated with particles, such as neutrons, protons, electrons or photons, a nucleus in the sample might capture these particle, leading to the formation of an excited compound nucleus. This usually short-lived isotope undergoes radioactive decay, emitting gamma-rays with characteristic energies. By measuring the energy and the intensity of these gamma rays, it is possible to identify the different isotopes present in the sample. Other research groups have also explored the use of proton-induced reactions in copper as potential diagnostic tool [313–315].

In the context of this thesis, stacks of RCFs (c.f. subsection 3.5.4) are interleaved with absorber material to resolve the dose for different energy levels. The absorbers have a thickness of 1.3 mm and consists of copper in the natural abundance, comprising 69.17 % of ^{63}Cu and 30.83 % of ^{65}Cu. When the copper layers are exposed to the laser-accelerated proton beam, several radioactive isotopes are produced. After the irradiation, when the interaction chamber is returned to normal pressure and the RCF stacks are removed from the experimental setup, the different isotopes in the copper layer can be analysed by measuring the gamma-rays emitted. Gamma-ray detection was facilitated by a well-shielded high-purity germanium spectrometer (GR4020 from Canberra) with an energy resolution of 0.24 MeV. An example energy spectrum from such a measurement is shown in Figure 3.16.
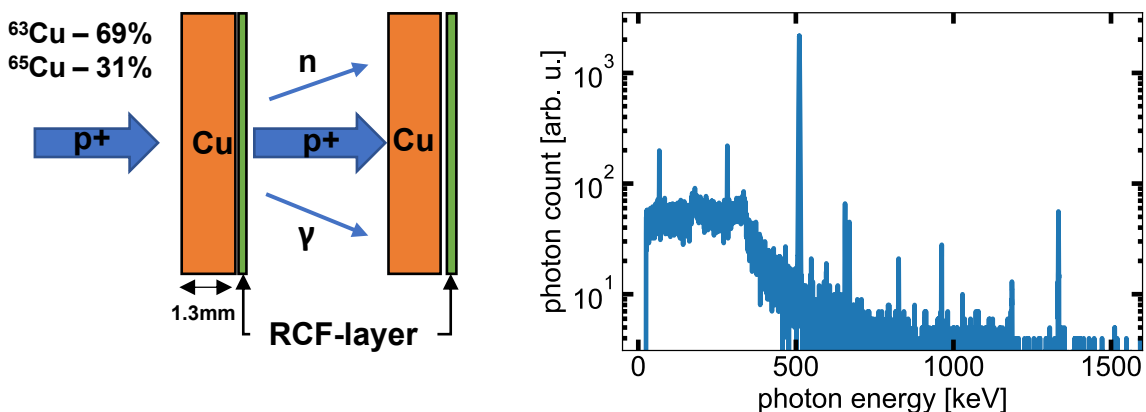
Figure 3.16: Nuclear activation measurement. Left: Illustration of detector technique. Protons hit the copper absorbers (composition: 69 % of ^{63}Cu, 31 % of ^{65}Cu) in the RCF stack, generating radioactive isotopes which decay by emitting neutrons or gamma rays. The subsequent copper layer absorbs protons and neutrons, forming compound isotopes that emit characteristic gamma rays. Right: Energy spectrum measured by a high-purity germanium detector. The different gamma ray peaks represent characteristic isotopes generated by proton-neutron reactions.

4 Optimisation of sheath acceleration for high-quality proton beams

This chapter presents results on the optimisation of laser-driven ion acceleration from solid plastic foil targets in the **Target Normal Sheath Acceleration (TNSA)** regime at DRACO-PW. The primary objective was to identify reasons for the initially low performance level at DRACO-PW, representing the starting point of this thesis, and to develop optimisation strategies to enhance the proton beam quality, including maximum energies, particle numbers and shot-to-shot stability.

As a first step, this involved implementing diagnostics for precise temporal pulse contrast characterisation and methods for contrast optimisation, as well as establishing standardised operation principles for final pulse compression of the laser. Building on these achievements, a systematic study on the laser pulse parameters and their effect on proton acceleration performance from thin plastic foil targets was conducted. An acousto-optic programmable dispersive filter was used to modify the spectral phase properties of the laser pulse and thus the intensity distribution during the last picoseconds around the main pulse. The experimental data revealed that highest proton energies and particle numbers were observed for asymmetric temporal pulse shapes significantly different from the standard conditions of a nearly ideally compressed pulse. Furthermore, the robustness of this enhancement effect across various laser-target parameters and over many months of operation is demonstrated. Simulations were performed to gain insights into the underlying microscopic details leading to the observed enhancement effect. The results of this chapter led to the publication of TZ3.

4.1 Introduction

TNSA stands out as the most robust, extensively studied and widely understood regime for laser-driven ion acceleration. It has therefore received particular attention for realising practical applications with plasma accelerators. The characteristics of TNSA accelerated particle beams is closely connected to the electrostatic sheath field, that establishes during the interaction with the laser (detailed in subsection 2.3.1). Particularly, the coupling of laser energy to the plasma electrons and their subsequent dynamics play a crucial role.

While highest proton energies have been primarily achieved using high-energy long-

pulse lasers, which deliver only a few shots per day, preventing application-relevant high average currents [139, 316], the advent of ultra-short pulse laser systems holds substantial promise. With pulse durations of a few tens of femtoseconds and repetition rates up to 10 Hz, these laser systems are ideally suited to bridge the gap towards applications. Today, numerous facilities worldwide [221, 233, 234, 239, 317, 318] approach or even surpass the PW-level (detailed in subsubsection 3.1.1) with on target intensities between 10^{21} W cm^{-2} and 10^{22} W cm^{-2}. Furthermore, these laser systems provide additional options for control, modifications and diagnostics, being of particular importance for the characterisation of laser pulse parameters in focus at these intensities.

Previous studies have already shown how different experimental control parameters impact on the beam properties of electrons and protons. Employing dedicated laser-target configurations, such as ultra-thin, low density or special shape targets, has allowed for control and establishment of an optimised TNSA-based acceleration regimes [29, 127, 319–322]. These efforts are complemented by a variety of laser pulse parameter scans (e.g. energy, duration, temporal contrast), aimed to determine the optimal acceleration performance [18–21, 30, 177, 323]. However, a major challenge for plasma accelerators has always been the limited knowledge of the exact plasma conditions at the arrival of the main pulse at the target, which may differ significantly from analytical models or idealised simulations due to pre-pulses as well as spatio-temporal couplings of the laser. To exploit the full potential of laser driven ion accelerators, on-shot diagnostics and real-time feedback routines guided by machine learning techniques, similar to those already applied for wakefield accelerators [324], will become essential.

The results presented in this chapter demonstrate that actively controlling the temporal laser pulse shape significantly enhances the proton acceleration performance using a state-of-the-art ultrashort-pulse laser system.

In a series of experiments under well-controlled contrast conditions and variations in target thickness, material, laser energy and temporal intensity contrast, a consistent increase in maximum proton energies and particle numbers was observed, when changing the temporal laser profile from a **Fourier Transform Limited (FTL)** pulse to an asymmetric shape. Applying positive third order dispersion values proved to optimise proton acceleration from solid foil targets, resulting in maximum energies of 70 MeV at 18 J laser energy on target. This represents a substantial enhancement in maximum energy compared to what has been achieved with the standard parameters ($\approx$ 30 MeV).

4.2 Temporal contrast at experimental environment

The temporal intensity distribution of a laser pulse can have an immense influence on the laser-plasma interaction processes as discussed in chapter 2. High-intensity laser systems, such as the one employed for this study, typically produce laser pulses with a substantial amount of energy distributed around the main pulse (detailed in subsection 3.1.2). Consequently, a detailed characterisation of this distribution is of central importance to understand the experimental results and to provide accurate and valid input for numerical simulations. Therefore, it is imperative to measure laser parameters under representative experimental conditions, capturing the energy levels relevant to the real experiment, rather than relying on measurements of an attenuated beam.

The temporal intensity distribution of the DRACO-PW laser is illustrated in Figure 3.5. The individual contributions to the measured intensity contrast and their origin were discussed in subsection 3.1.2 and subsubsection 3.1.3. The measurement has been done using the standard measurement procedure within the community, where typically a small fraction is picked off from the attenuated laser beam and sent towards the different diagnostics. However, the energy level and thus the fluence of the laser beam

during the experiments is significantly higher. Figure 4.1 shows the influence of different laser fluence levels on the temporal intensity contrast, measured just before the final focussing optic in the experimental chamber. The solid blue line represents the standard
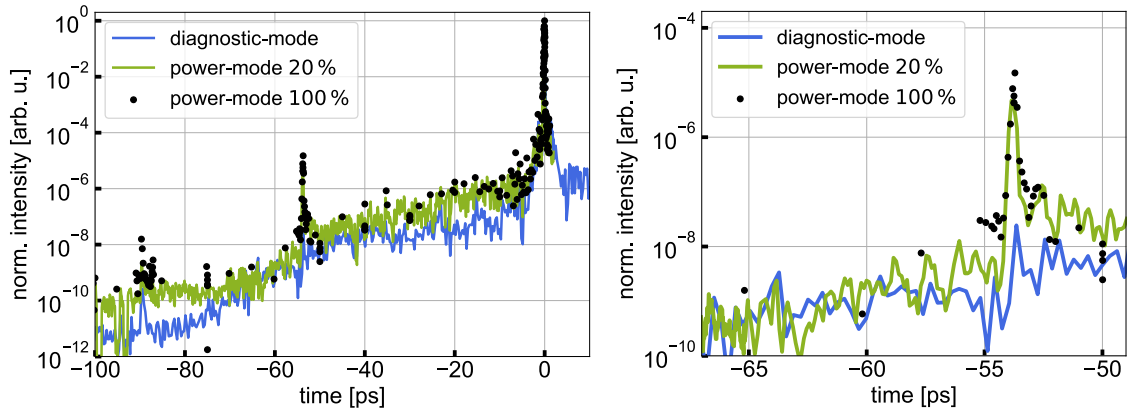
Figure 4.1: **Temporal contrast dependence on laser fluence.** The left plot shows the TOAC measured intensity contrast up to –100 ps before the main pulse for different laser output energies (diagnostic-mode: blue line, power-mode with 20 % amplification: green line, power-mode with 100 % amplification: black dots). Higher energies result in a higher ASE level and coherent contrast level. The right plot shows the influence of the different fluence levels on the pre-pulse intensity. With the laser in diagnostic mode, the pre-pulse was barely distinguishable from the background level at 10^{-8}, whereas increasing the laser fluence to the power-mode also increases the intensity level of the pre-pulse by ≥ 1000 to $\approx 10^{-5}$.

measurement using an attenuated laser beam in diagnostic-mode. In contrast, the green solid line and the black dots correspond to power-mode measurements with higher laser energy, i.e. 20 % and 100 % pumped main amplifier in the *Twin Multipass*. Higher laser fluences result in higher B-integral values and thus stronger nonlinear coupling [261, 263]. This effect is evident in the measured data, showing higher intensity levels for the **Amplified Spontaneous Emission (ASE)** component, the coherent contrast and individual pre-pulses. The left plot of Figure 4.1 shows the increase of the coherent contrast between –54 ps and –10 ps from $\geq 10^{13}$ W cm^{-2} to $\geq 10^{15}$ W cm^{-2}, assuming a focussed peak intensity of 5×10^{21} W cm^{-2}. The most important impact of the higher laser fluence is the substantial amplification (≈ 1000) of the pre-pulse intensity at –54 ps, which is shown in the right plot of Figure 4.1. Reaching an intensity level of 5×10^{16} W cm^{-2}, potentially even higher, this pre-pulse would promptly trigger ionisation and subsequent expansion of the target, thereby preventing optimal TNSA conditions.

Under these conditions, pre-pulse elimination or contrast enhancement methods such as a plasma mirror must be applied to achieve perfect starting conditions for TNSA.
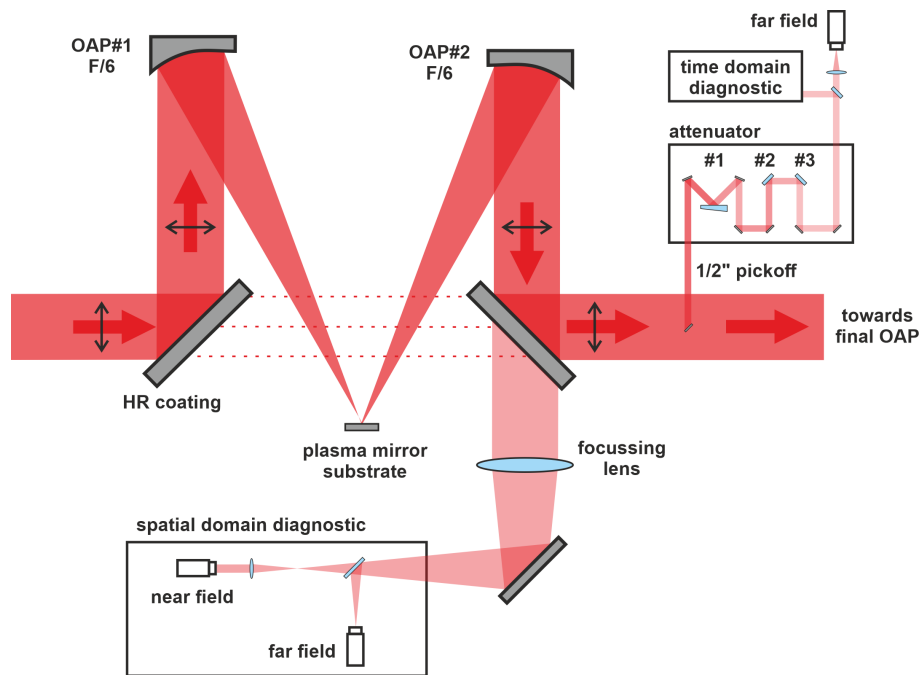
4.3 Plasma mirror

A **Plasma Mirror (PM)** is a self-induced ultrafast optical shutter enabling the suppression of unwanted pre-pulses and pedestals of high-intensity laser pulses. The shutter is activated by the laser light itself as soon as it reaches the ionisation intensity of the mirror substrate. The preceding laser light (ASE, coherent pedestal and pre-pulses) is usually not intense enough to trigger ionisation and instead transmitted through the substrate with a remaining Fresnel reflectivity. High-quality anti-reflection coatings can help to further suppress this component. Once the laser intensity is sufficient to cause ionisation of the substrate, the reflectivity of the PM changes significantly. The rapid ionisation leads

to the formation of a flat and dense plasma layer that reflects the incoming laser light efficiently. A fraction of the main pulse energy is absorbed by the material before ionisation and by the reflecting plasma after ionisation. The overall reflectivity and the contrast enhancement factor are important characterisation parameters of the PM.

The PM concept and the first realisation was already achieved in 1991 by Kapteyn *et al.* [325]. A detailed theoretical and experimental characterisation of a PM for high-intensity laser pulses was published by Doumy *et al.* [326] in 2004. A similar experimental characterisation study was published by Dromey *et al.* [327] in the same year. Under optimised conditions a reflectivity of 96 % [328] and an enhancement factor of 10^4 [329] was achieved using a single stage PM. Thaury *et al.* published the first realisation of a double PM setup in 2007. With such a double PM setup, Choi *et al.* [330] achieved a contrast enhancement factor of almost 10^6 with a reflectivity of 70 % using high-intensity laser pulses at a PW laser facility.

4.3.1 Plasma mirror implementation at DRACO-PW

An illustration of the realised PM setup for the DRACO-PW laser at the big target chamber is shown in Figure 4.2. The compressed laser pulses enter the chamber on the upper

Figure 4.2: Schematic layout of the plasma mirror setup at DRACO-PW. Compressed laser pulses enter the experimental chamber where they can either be sent to the final OAP directly (dotted beampath) or first towards the plasma mirror setup. The setup consists of a focussing (OAP#1) and a recollimating OAP (OAP#2), the rectangular plasma mirror substrate and diagnostics for the spatial and the temporal domain.

level with p-polarisation. Motorised high-reflectivity turning mirrors can be positioned in the beam path on demand to direct the laser towards the PM setup. The setup consists of a focussing and a recollimating **Off-Axis Parabola (OAP)** (f / 6, OAP angle = 25°) and the PM substrate. The rectangular substrate has an anti-reflection coating except for a small Al-coated stripe (width: 5 mm) on the side, enabling substrate alignment at low laser energies. The dimension of the substrate (100 mm × 75 mm) support 250 to 300 shots before it needs to be replaced. The setup further consists of imaging optics and diagnostics for on-shot near field and far field monitoring, requiring the specific transmis-

sion values of the turning mirrors after the recollimating OAP. Moreover, an all-reflective attenuation system was developed and implemented during this thesis, allowing for on-shot measurements with different time-domain diagnostics.

4.3.2 Plasma mirror characterisation at DRACO-PW

The implemented PM setup was characterised with respect to the achievable reflectivity and the influence on the temporal intensity contrast of the laser. The reflectivity measurements were done by imaging an energy-calibrated ceramic screen onto a camera. The temporal contrast measurements used a half inch beam that was picked off from the main, attenuated and directed towards different pulse diagnostic devices.

The substrate is positioned at the "working point", which is usually not the focal point of OAP#1 but somewhere in the mid-field where the intensity is lower. To determine the ideal working point, a fluence scan was conducted in a preparation study. The outcome of this scan identified the optimal substrate position, ensuring optimal contrast enhancement and a high reflectivity without any spatial distortion of the laser beam. Figure 4.3 shows on the left the result of the reflectivity measurement at the chosen working point as a function of different laser energy values. The reflectivity of the PM is $\geq 80\,\%$ for the
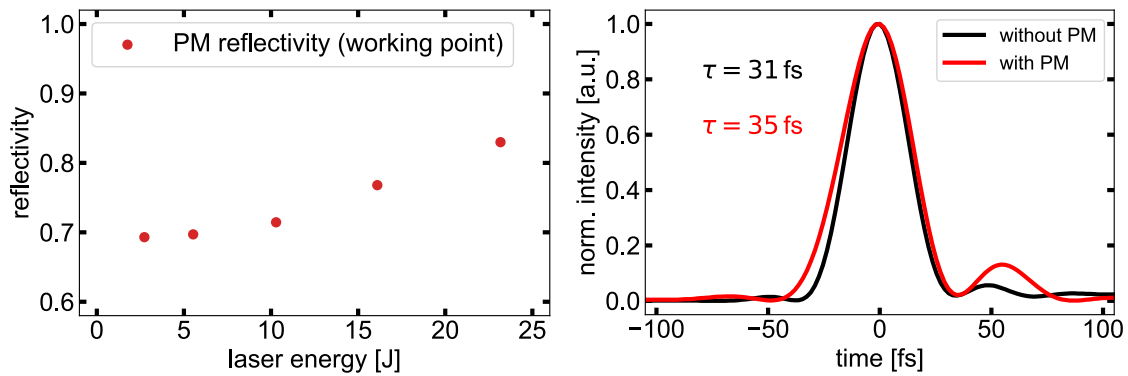

Figure 4.3: Characterisation of the plasma mirror setup. Left: Plasma mirror (PM) reflectivity as a function of laser energy. The used working point reaches a maximum reflectivity $\geq 80\,\%$ for 22.5 J. Lower laser energies result in a slightly lower reflectivity for the same working point. Right: Temporal pulse shape from SPIDER measurements with and without PM. For both cases, the characteristic Gaussian shape of the main pulse is preserved, indicating that the temporal intensity distribution of the main pulse is not affected by the PM.

maximum laser energy of this experiment (22.5 J). For lower laser energies the chosen working point maintains a slightly lower but still quite efficient reflectivity ranging from 70 % to 78 %.

The influence of the PM on the temporal intensity distribution of the main pulse is shown in the right plot of Figure 4.3. The primary pulse shape of the main pulse remains unaffected, preserving it's characteristic Gaussian shape. This specific measurement shows only a slight increase in the FWHM pulse duration from 31 fs to 35 fs, indicating that the PM does not significantly influence the spectral phase of the laser pulse at the chosen working point.

The most important parameter, characterising the performance of the PM, is the enhancement of the temporal intensity contrast. Figure 4.4 compares the contrast measurements with and without the PM. The left plot shows scanning **Third-Order AutoCorrelator (TOAC)** measurements on the tens of ps time scale, demonstrating the effectiveness of the PM in enhancing the temporal contrast. Evidently, the pre-pulse intensity at
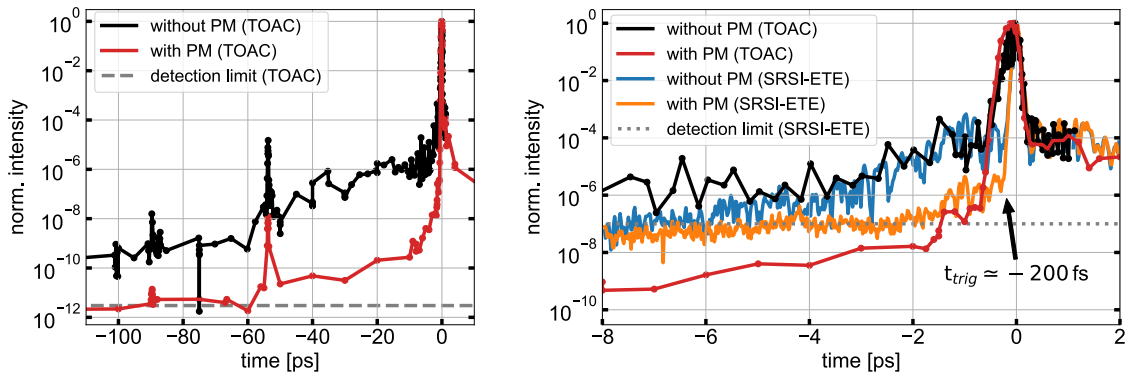
Figure 4.4: Temporal intensity contrast of DRACO-PW. The left plot compares the results of the TOAC measurements with (red) and without (black) plasma mirror (PM). In the tens of ps time scale, the enhancement is constant and the pre-pulse intensity at $\approx$ –54 ps insufficient to trigger ionisation. The right plot shows the sub-ten ps time scale, also including measurements using the single-shot SRSI-ETE technique (orange and blue). The PM trigger point was identified at $\approx$ –200 fs.

$\approx$ –54 ps is not sufficient to trigger ionisation of the PM, as the contrast enhancement remains constant after this pre-pulse. The right plot displays the results on the sub-ten ps time scale, also including averaged measurements obtained with the single-shot SRSI-ETE technique (detailed in subsubsection 3.4.2). Due to the different detection limits of the two detectors, a direct comparison of the different configurations is only viable between –2 ps and +4 ps. It is also essential to acknowledge the operational aspects of the two techniques: while the scanning TOAC method necessitates multiple shots, each requiring a new position on the PM substrate, the SRSI-ETE technique provides comprehensive data within a single shot, featuring superior temporal resolution. This accuracy allows to determine the trigger point of the PM to be at $\approx$ –200 fs, as can be seen in the right plot of Figure 4.4. Nevertheless, the SRSI-ETE's limited dynamic range currently restricts its analysis capabilities to a narrow time interval. Furthermore, the two techniques have different sensitivities regarding the accepted range of wavelengths. This might yield different results, particularly for ultra-short laser pulses that are characterised by a broad range of wavelengths.

The PM contrast enhancement was determined by two distinct methods. The results of these methods are illustrated in Figure 4.5. The left plot shows the absolute reflection of
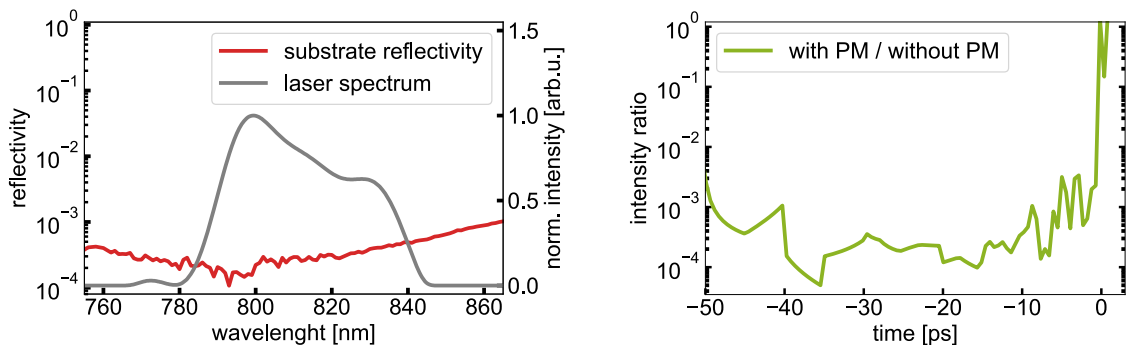
Figure 4.5: Contrast enhancement factor of plasma mirror. The left plot shows the spectrophotometer measurement of the plasma mirror (PM) substrate, yielding an average reflectivity of 2.3×10^{-4} (red) within the range of the laser spectrum (grey). The right panel shows the ratio between the TOAC measurements with and without PM, resulting in an intensity ratio of 2.1×10^{-4}.

the PM substrate as a function of wavelength, alongside an exemplary laser spectrum. The reflectivity data was obtained using the Cary7000 spectrophotometer from Agilent. Within the wavelength range of the laser, the reflectivity of the PM substrate falls within the range of $(1.5 - 5) \times 10^{-4}$, yielding an averaged reflectivity of 2.3×10^{-4}. This result is confirmed by the analysed TOAC measurements in the right panel of Figure 4.5. The figure shows the ratio between the measurement with PM and without PM, resulting in an intensity suppression of $\approx 2.1 \times 10^{-4}$. The contrast enhancement factor of the PM can be calculated from this value.

In conclusion, the characterisation results demonstrate that the PM setup at DRACO-PW is very effectively cleaning the temporal intensity contrast of a PW-class laser and that the performance of the setup is close to achieving the published optimum values attainable with a single stage PM.

4.4 Temporal pulse shaping by spectral phase modification

The spectral phase of a laser pulse affects its temporal profile and the interaction with the target. Manipulating the spectral phase allows for precise control over the temporal properties, enabling to tailor the laser pulses shape to achieve a specific intensity profile. Using this technique for picosecond pulse shaping was first published in 1985 by Heritage, Weiner and Thurston [331].

4.4.1 Theory on temporal pulse shaping

Following Maxwells equations and ignoring the spatial portion, the temporal evolution of the electric field of a linearly polarised laser pulse can be expressed as:

$$\mathcal{E}(t) = \frac{1}{2} \sqrt{\frac{1}{2} \varepsilon_0 \, c \, \mathcal{E}_0^2(t)} \, \exp\left(i\left(\omega\, t - \Phi(t)\right)\right) + c.c. \tag{4.1}$$

where $\mathcal{E}_0(t)$ and $\Phi(t)$ are the temporal amplitude and phase of the laser pulse, respectively. These two parameters contain all information to describe the laser pulse in the time domain. The expression in the root defines the period averaged temporal evolution of the intensity $I(t)$ of the electric field, i.e. the temporal contrast of the laser pulse:

$$I(t) = \frac{1}{2} \varepsilon_0 \, c \, \mathcal{E}_0^2(t) \tag{4.2}$$

By performing a Fourier transformation, the complex electric field of the laser pulse can also be described in the frequency domain.

$$\widetilde{\mathcal{E}}(\omega) = \frac{1}{2} \sqrt{\frac{1}{4\pi} \varepsilon_0 \, c \, \widetilde{\mathcal{E}}_0^2(\omega)} \, \exp\left(-i\,\varphi(\omega)\right) + c.c. \tag{4.3}$$

Analogue to the time domain, the laser pulse in the frequency domain is fully described by the spectral amplitude $\widetilde{\mathcal{E}}_0$ and the spectral phase $\varphi(\omega)$. Both expressions for the laser pulse, Equation 4.1 and Equation 4.3, are equivalent and yield the same pulse shape. The time integrated spectrum $\widetilde{I}(\omega)$, i.e. the spectral intensity distribution of the laser, is defined by:

$$\widetilde{I}(\omega) = \frac{1}{4\pi} \varepsilon_0 \, c \, \widetilde{\mathcal{E}}_0^2(\omega) \tag{4.4}$$

The spectral phase of a laser pulse describes how the different spectral components of the pulse (i.e. its frequencies) evolve in time. If all frequencies of the laser pulse have

the same phase, they interfere constructively, leading to the shortest and steepest pulse possible. Any deviation from this optimal condition shifts frequency components in time, resulting in a non-perfect pulse shape. Mathematically, the spectral phase is typically expanded into a Taylor series around a central frequency ω_0 for small deviations of ω:

$$\varphi(\omega) = \sum_{n=0}^{\infty} \varphi_n \frac{(\omega - \omega_0)^n}{n!} = \varphi_0 + \varphi_1 \frac{\omega - \omega_0}{1} + \varphi_2 \frac{(\omega - \omega_0)^2}{2} + \varphi_3 \frac{(\omega - \omega_0)^3}{6} + \dots \quad (4.5)$$

The expansion coefficients φ_n are defined as follows:

$$\varphi_n =: \frac{d^n \varphi(\omega_0)}{d\omega^n} \quad (4.6)$$

Each coefficient of Equation 4.6 can be related to a characteristic behaviour of the laser pulse. The first coefficient $\boldsymbol{\varphi_0}$ describes the **absolute phase** of the laser pulse and is identical in both the time and the frequency domain. The second term $\boldsymbol{\varphi_1}$, i.e. the first derivative or the first order phase term, represents a simple shift in time and is therefore also referenced as **group delay** or **Carrier Envelope Phase (CEP)** of the laser pulse. The second order phase term $\boldsymbol{\varphi_2}$, also known as **Group Velocity Dispersion (GVD)**, results in a linearly chirped pulse, where the frequency either linearly increases (positive chirp or up-chirp) or decreases (negative chirp or down-chirp) over time. The $\boldsymbol{\varphi_3}$ coefficient is termed **Third Order Dispersion (TOD)** and describes the frequency dependence of the GVD. For a qualitative description of a standard laser pulses, the first few terms of Equation 4.5 are usually sufficient.

The influence of different spectral phase parameters on the temporal pulse shape are qualitatively illustrated in Figure 4.6. For an ideal spectral phase distribution ($\varphi(\omega) = $const.)
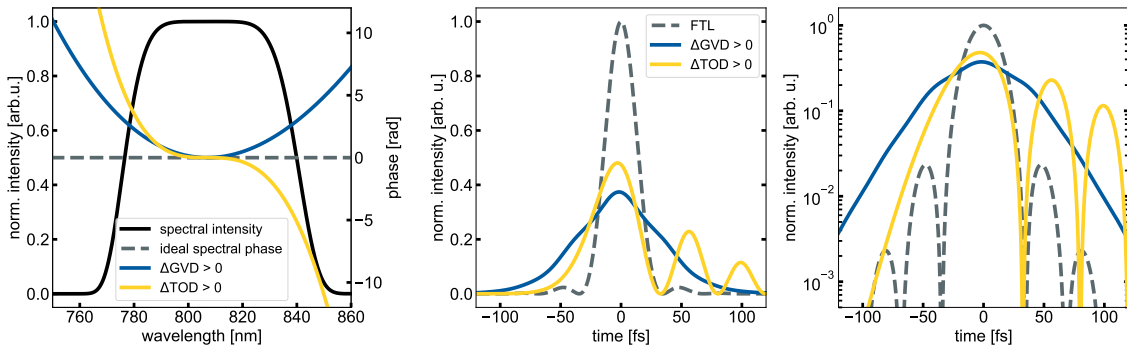
Figure 4.6: **Illustration of spectral phase influence on temporal pulse shape.** A flat spectral phase results in an ideally Fourier Transform Limited (FTL) pulse (grey dashed line) for a given laser spectrum (black solid line). A positive Group Velocity Dispersion (GVD) results in an homogeneous broadening of the pulse (blue solid line), while a modification of the Third Order Dispersion (TOD) yields an asymmetric pulse shape (yellow solid line) with significant post-pulses.

the temporal shape of the laser results in a **Fourier Transform Limited (FTL)** pulse (grey dashed line) for a given laser spectrum (black solid line). Positive GVD values (blue solid line) preserve the symmetric shape but temporally stretch the pulse, resulting in a reduction in peak intensity and an increased FWHM pulse duration. A pure modification of the TOD leads to an asymmetric pulse shape (yellow solid line), identified by a shallow rising and sharp falling edge (or vice versa if TOD value has opposite sign) and a reduction in peak intensity due to frequency components being shifted away from the main pulse, resulting in post- or pre-pulse generation and reduction. The intensity of these additional post- or pre-pulses increases with higher TOD values.

4.4.2 Experimental realisation and results

The experiments described below were performed using the DRACO-PW laser, which is described in detail in subsection 3.1.3. The DRACO-PW laser system features an **Acousto-Optic Programmable Dispersive Filter (AOPDF)** at each **Chirped Pulse Amplification (CPA)** stage, which enables to control the spectral phase of the stretched laser pulse (detailed in subsection 3.1.3). A simplified sketch of the laser system, the measurement setup and an illustration of the feedback control system can be found in Figure 4.7. In a systematic
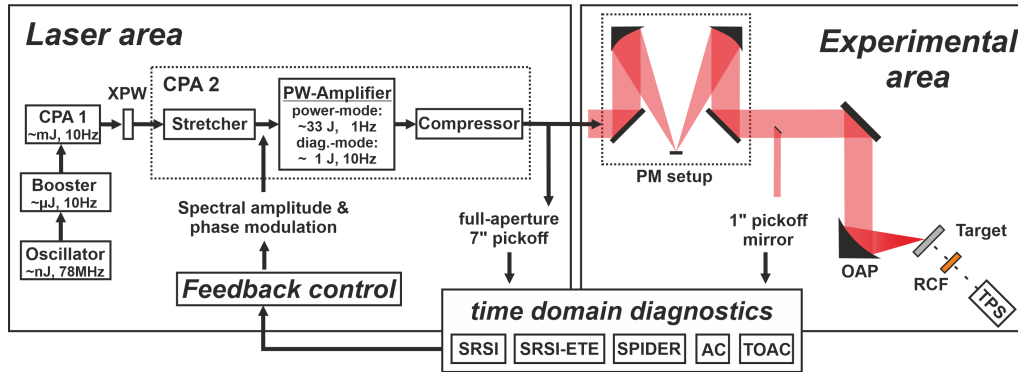

Figure 4.7: Illustration of the experimental spectral phase measurement and feedback control. The DRACO-PW laser pulses in two energy configurations (diagnostic-mode and power-mode) are analysed by multiple time-domain diagnostics at two different pickoff positions - one at the laser area and one at the experimental area. The results are used as feedback for the settings of the spectral phase control system of the AOPDF, located after the stretcher of the CPA2 stage.

study, the spectral phase parameters GVD and TOD were actively modified by presetting the according values in the control software of the AOPDF. The influence of these modifications on the temporal pulse shape of the laser was measured by multiple scanning and single-shot diagnostics, including second and third order autocorrelators (AC and TOAC), field autocorrelation methods like self-referenced spectral interferometry (SRSI & SRSI-ETE) and spectral phase interferometry for direct electric-field reconstruction (SPIDER). The measurements were conducted at different positions within the laser chain (vacuum compressor output & just before final focusing) and using different pick-off methods (full-aperture $\simeq$ 7" & 1" mirror) and laser energy settings (diagnostic-mode & power-mode, corresponding to 0 % or 100 % pumped main-amplifiers, respectively).

Initially, it was investigated whether the automatic feedback loop of the AOPDF provides a flat spectral phase profile over the entire laser spectrum. Additionally, it was verified if the different laser energy configurations or the implementation of the plasma mirror setup influence the spectral phase and thus the pulse profile. Figure 4.8 shows exemplary SPIDER measurements for the standard phase settings and different laser energy configurations. The measured pulse profile for all configurations is on the linear intensity scale very similar to an ideal FTL pulse (calculated from measured laser spectrum). Simultaneous measurements performed with the different redundant time domain diagnostics and pick-off ports delivered consistent results, thus all relative phase changes introduced in the following can be referenced to a 30 fs FWHM near-Gaussian pulse shape. However, some remaining pre- and post-pulse structures are clearly visible on the logarithmic scale, originating from a non-perfect pulse compression. A detailed stability study of the spectral phase distribution revealed periodic fluctuations in the spectral phase, especially at the edges of the laser spectrum, which are hard to compensate by the AOPDF.
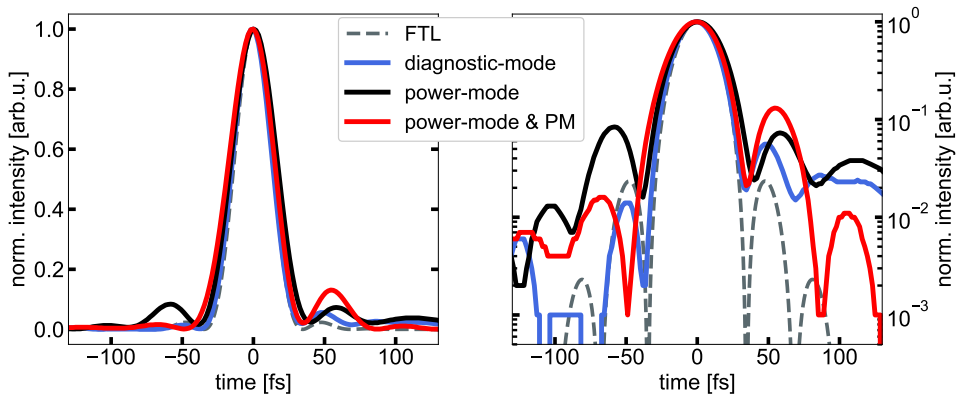
Figure 4.8: **Laser pulse shape for standard phase settings.** Temporal intensity distribution retrieved from SPIDER measurements for the automatic feedback-loop of the AOPDF and different laser energy configurations. Different laser energy configurations (diagnostic mode - blue, power mode - black, power mode & PM - red) show consistent pulse shapes on the linear (left) and the logarithmic (right) intensity scale.

As a next step, the AOPDF control software was used to modify the spectral phase parameters of the laser pulse. An exemplary result for additionally added GVD and TOD (ΔGVD: 1750 fs^2, ΔTOD: 40e3 fs^3) is shown in Figure 4.9. The SPIDER results reveal an
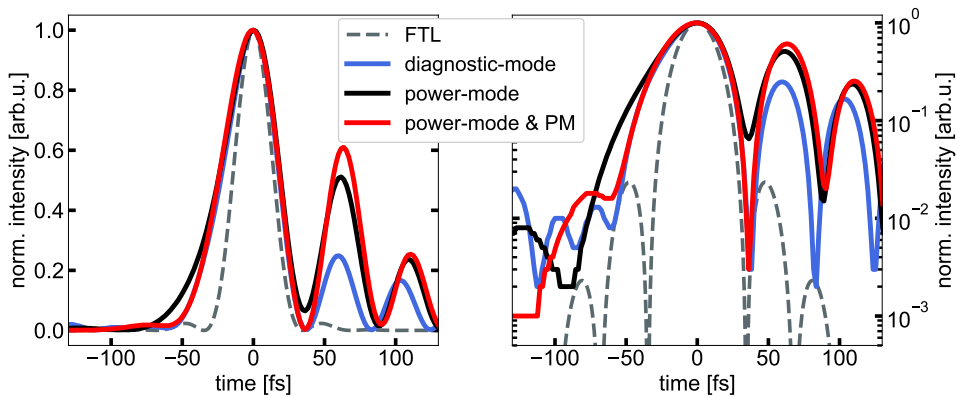
Figure 4.9: **Laser pulse shape for optimised phase settings.** Temporal intensity distribution retrieved from SPIDER measurements after manual phase modifications (ΔGVD 1750 fs^2, ΔTOD 40e3 fs^3) and different laser energy configurations. Different laser energy configurations (diagnostic mode - solid blue, power mode - dashed red, power mode & PM - dotted green) show consistent pulse shapes on the linear (left) and the logarithmic (right) intensity scale.

asymmetric pulse profile with a shallow rising edge and significant post-pulses, confirming the theoretical considerations in subsection 4.4.1. Measurement employing the SRSI and SRSI-ETE diagnostics reveal qualitatively similar laser pulse profiles.

A collection of multiple shots for identical spectral phase parameters is shown in each panel of Figure 4.10. The thick red line represents the mean value of the temporal intensity distribution, derived from all individual single-shot measurements (depicted as thin grey lines). Each plot corresponds to specific spectral phase parameters as indicated in the upper right corner of the respective plot. The data demonstrate, that the observed shot-to-shot fluctuations do not significantly impact the overall laser pulse shape of each setting and that the differences between the individual phase parameters remain more prominent.
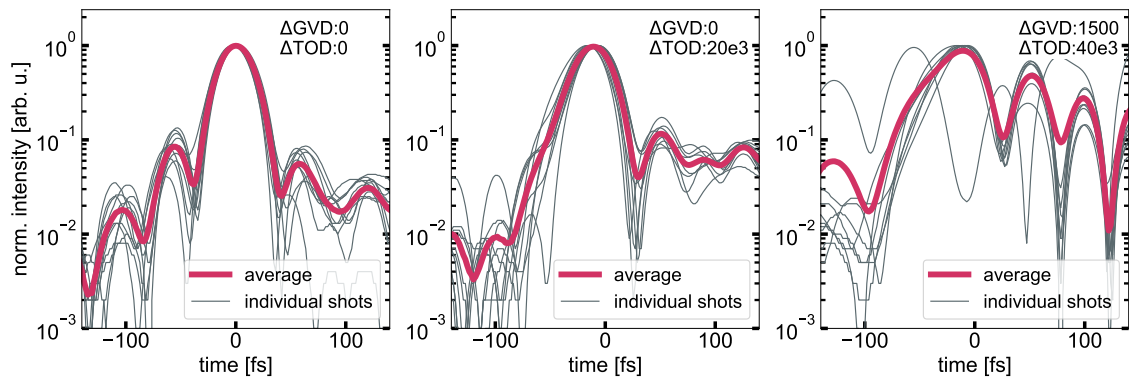
Figure 4.10: Temporal pulse shape stability for different spectral phase parameters. The different spectral phase parameters (indicated in the upper right corner of each plot) significantly influence the temporal pulse shape. Positive TOD values lead to an asymmetric pulse profile with a shallow rising edge and significant post-pulses. Single-shot measurements (grey) do not reveal significant differences from shot-to-shot, compared to the mean value of all shots (red).

4.5 Proton acceleration under optimised temporal contrast conditions

The influence of the actively modified spectral phase parameters GVD and TOD on the proton acceleration performance from solid-state targets is studied in this section. Figure 4.11 illustrated the experimental setup, including all used diagnostics. P-polarised
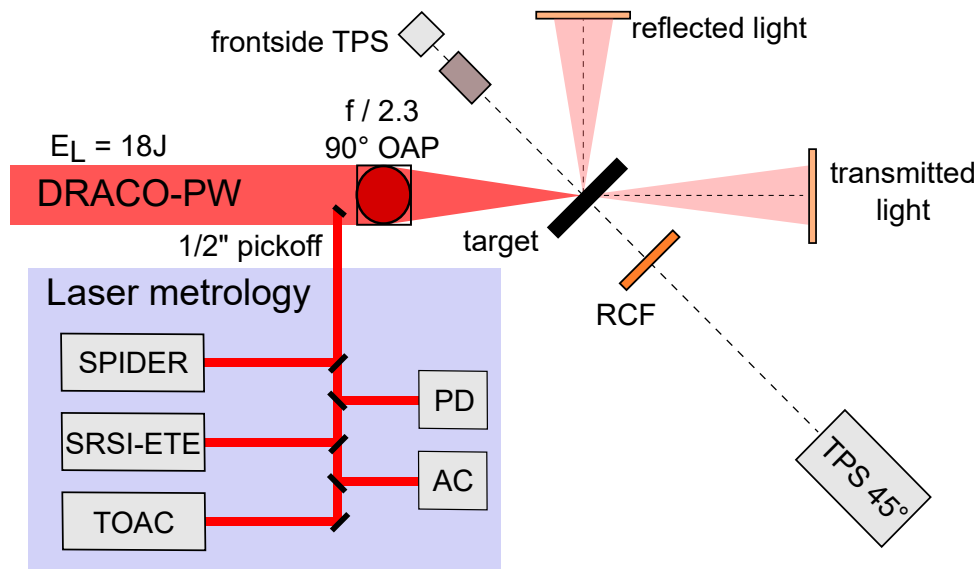

Figure 4.11: Illustration of the experimental setup. Laser pulses are focused by an f / 2.3 off-axis parabola (90°) onto thin plastic foil targets. The kinetic energy distribution of the accelerated protons is measured by two Thomson parabola spectrometers (frontside TPS and TPS45 positioned at –135° and 45° with respect to the laser propagation direction). The spatial proton beam profile is characterised by a radio-chromic film stack. Ceramic screens enable the collection of the reflected and transmitted laser light. The temporal intensity distribution of the laser pulse is measured by multiple scanning and single-shot detectors.

laser pulses with an FHWM pulse duration of $\approx$ 30 fs and a maximum energy of 22.4 J propagated from the laser area to the experimental area. A re-collimating single PM

could be incorporated to the setup on demand, facilitating temporal contrast enhancement by more than 10^3 (detailed in section 4.3). After the PM, the wave-front corrected laser pulse with a total remaining energy of 18 J was focused by an f / 2.3 off-axis parabola (90°) to an FWHM spotsize of 2.6 μm yielding a peak intensity of 5.4×10^{21} W cm^{-2}. Solid-state targets of different material and thickness were positioned at an angle of 45° with respect to the laser propagation direction.

A portion of the laser beam is picked off by a half inch mirror and directed to the laser metrology bench. There, the temporal intensity distribution of the laser pulse is measured before the shots using a scanning TOAC and on a single-shot basis during the experiment using a combination of multiple detectors (SPIDER, SRSI-ETE, AC). The energy contrast of the laser was measured before the shots by a fast photodiode. Ceramic screens enabled to collect the reflected and transmitted laser light.

The accelerated ion beam in target normal direction (45°) was analysed by a **Thomson Parabola Spectrometer (TPS)**, providing an energy dependent resolution of 5 % with a minimum detectable proton energy of 7 MeV. Another magnetic spectrometer was positioned in front side target normal direction, i.e. −135° with respect to the laser propagation direction. For selected shots, a stack of calibrated **RadioChromic Films (RCFs)** were inserted 55 mm behind the target, allowing for proton beam profile characterisation, absolute particle number calibration and complementary maximum energy detection.

4.6 Experimental results

Figure 4.12 shows the maximum proton energies at 45° from 400 nm Formvar targets for different spectral phase modifications of the second-order (ΔGVD) and third-order (ΔTOD) parameter. Initially, the GVD was kept constant (ΔGVD = 0 fs^2) and the TOD was
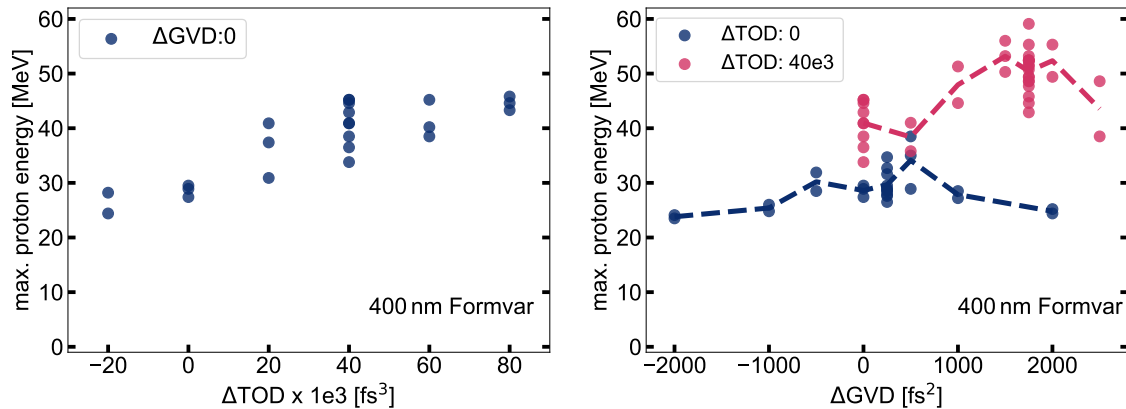
Figure 4.12: **Spectral phase influence on proton acceleration performance.** TPS results on maximum proton energies from 400 nm Formvar targets for different GVD and TOD parameters. Each marker represents one single shot, dashed lines connect mean values. While the maximum energy for the standard settings (ΔGVD = 0 fs^2, ΔTOD = 0 fs^3) is below 30 MeV, the optimised conditions (1750 fs^2, 40e3 fs^3) yield 60 MeV and thus an effective doubling of the maximum energy.

varied in 20e3 fs^3 steps from −20e3 fs^3 to +80e3 fs^3. Negative TOD values degrade the acceleration performance, whereas positive TOD values generally result in higher maximum proton energies, increasing from below 30 MeV to more than 40 MeV. However, a clear optimum is not apparent from this data set, especially since the TOD could not be further increased without producing deep and sharp modulations of the laser spectrum, which is critical for system safety.

To clarify whether the observed proton energy enhancement is attributed to the TOD-induced pulse shape modifications or a consequence of the simultaneously altered laser pulse duration, an additional GVD scan was performed for two distinct TOD values (ΔTOD : $0\,\mathrm{fs}^3$ and ΔTOD : $40e3\,\mathrm{fs}^3$). The results of these additional modifications are shown in the right plot of Figure 4.12. For TOD $0\,\mathrm{fs}^3$ the GVD was varied between $-2000\,\mathrm{fs}^2$ and $+2000\,\mathrm{fs}^2$, without substantially affecting the maximum proton energies. At GVD values of $\pm 2000\,\mathrm{fs}^2$, the maximum energies dropped below 25 MeV as a result of the significantly reduced laser intensity associated with the increased pulse duration ($\approx 10\times$ FTL pulse duration). Another GVD scan was performed between $0\,\mathrm{fs}^2$ and $2500\,\mathrm{fs}^2$ for a fixed TOD value of $40e3\,\mathrm{fs}^3$. Higher GVD values further increased the maximum proton energies, with a clear peak at $1750\,\mathrm{fs}^2$ reaching 60 MeV, followed by a decrease for even higher GVD values. RCF measurements not only validate the TPS results but also demonstrate a clear enhancement effect for the optimised spectral phase parameters, as shown in Figure 4.13. Consequently, the optimised phase settings result in a clear en-
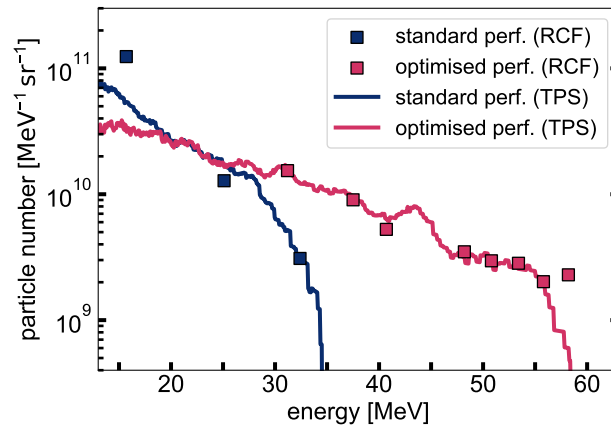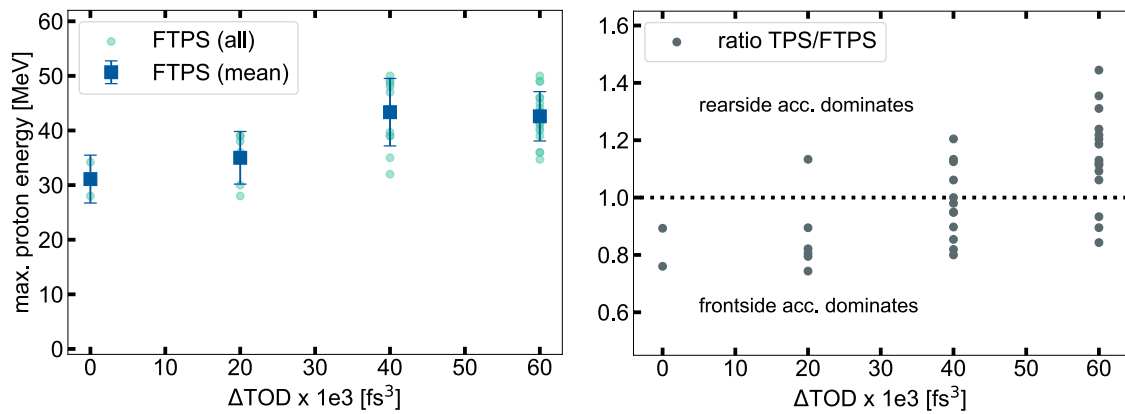

Figure 4.13: Proton energy spectra for different spectral phase configurations. The data is obtained from measurements with Thomson parabola spectrometers (solid lines) and radiochromic film stacks (individual markers) for standard (blue) and optimised (red) spectral phase parameters.

hancement of the laser-to-proton energy conversion efficiency from $\sim 2.1\,\%$ to $\sim 4.9\,\%$ for protons with kinetic energies of more than 15 MeV.

Comparing the SPIDER measurements to the proton energy results reveals that the best acceleration performance is achieved for non-ideal spectral phase parameters (ΔGVD $=1750\,\mathrm{fs}^2$, ΔTOD $=40e3\,\mathrm{fs}^3$), yielding a well compressed but asymmetric pulse shape represented by a shallow rising edge on the linear intensity scale followed tens of fs later by a non-negligible post-pulse structure. Symmetrically broadened pulse shapes (i.e. increased pulse durations), result in lower maximum proton energies as a result of the reduced peak intensity.

Another experiment studied how the proton acceleration from the target front side is affected for these changes of the spectral phase settings. Figure 4.14 shows the maximum proton energies from the target front side that were measured by the TPS at $-135°$ (FTPS) for an identical experimental setup with slightly higher on-target laser energy. With varying TOD a similar trend establishes for both front side and rear side accelerated protons. Adding TOD to the standard phase settings increased the mean energy of front side accelerated proton from ≈ 30 MeV to > 40 MeV. A comparison to the simultaneously measured proton energies in target normal direction reveals, that the acceleration from the target front side dominates for ΔTOD values $\leq 20e3\,\mathrm{fs}^3$. For higher values the ratio shifts towards a rear side dominated acceleration scenario. The compact setup

Figure 4.14: Spectral phase influence on proton acceleration from the target front side. The left plot shows FTPS results on maximum proton energies from 400 nm Formvar targets for different TOD parameters. Individual shots are indicated by round markers, the errorbars represent the standard deviation of the mean value (box) for a certain phase setting. The right plot illustrates the ratio between maximum proton energies accelerated from the rear side and the front side of the target.

of the FTPS only allowed for the detection of maximum proton energy but not for an analysis of absolute particle numbers. This task, along with a direct comparison of the effectiveness of front and rear side acceleration, needs to be addressed in a future study.

The results consistently indicate that the enhancement in proton energies and particle numbers is correlated to the applied TOD modifications. In the following, the stability of this enhancement effect is studied for different laser-target configurations, which were chosen to cover a wide parameter range and thus different initial interaction conditions. Figure 4.15 shows the effect of a pure TOD modification (ΔGVD = 0) on the maximum proton energy for 180 nm and 400 nm Formvar as well as 2 µm and 5 µm titanium targets. For shots on the 2 µm titanium targets, the PM was removed and the laser energy was reduced to 6.6 J.

The results confirm a consistent trend of proton energy enhancement for higher TOD values, across all studied cases. While the specific increase in maximum proton energies varies, a 20 % gain is always achieved. Positive TOD values consistently lead to higher maximum energies, while negative TOD values decrease the acceleration performance. An appropriate fine-adjustment of the GVD and higher-order terms of the spectral phase to maintain a short pulse duration is expected to further increase the gain.

The described optimisation of the spectral phase was established as a daily preparation routine during proton acceleration experiments at DRACO-PW. Based on a few shots each day, the optimal GVD-TOD combination was evaluated and applied throughout the experiment. Optimal TOD values generally ranged between (20 – 40)e3 fs^3 and GVD values were adapted accordingly to minimise the pulse duration. Figure 4.16 shows the maximum proton energy measured on 45 different shot-days (575 total shots) over a period of more than one year of operation. In the case of standard spectral phase settings, the maximum proton energy for individual shots varies between 25 MeV and 65 MeV, resulting in an average energy of (42.6 ± 9.1) MeV. After switching to optimised spectral phase settings, maximum energies fluctuate between 40 MeV and 71 MeV, with reduced shot-to-shot variation and an increased average energy of (58.2 ± 6.2) MeV. The presented spectral phase optimisation procedure leads to an averaged increase of ≈ 37 % in maximum proton energy over the entire dataset.
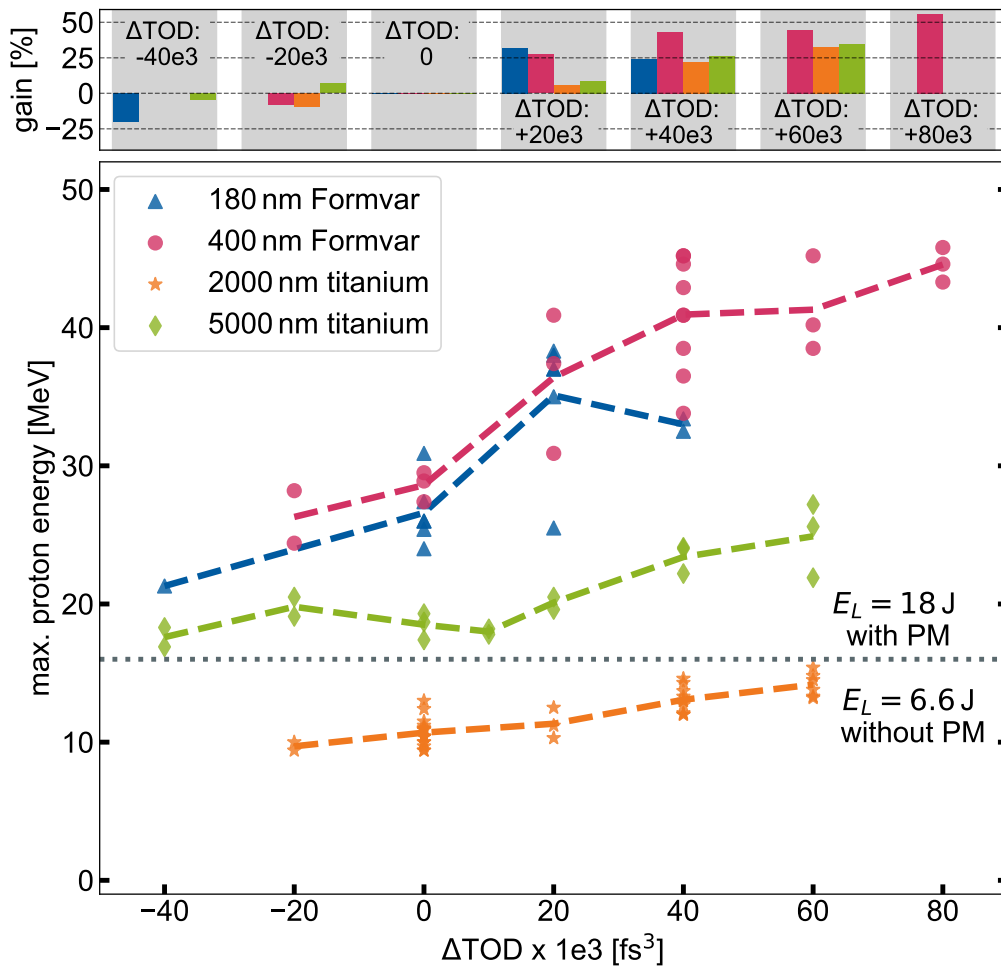
Figure 4.15: Spectral phase influence on different laser-target configurations. The figure shows the maximum proton energies as a function of additionally applied third-order dispersion ΔTOD for different target thicknesses and materials (represented by different markers and colors) as well as on target laser energy E_L and temporal contrast settings (with and without plasma mirror). Each shot is represented by an individual marker. Mean values of each configuration are connected by dashed lines of the same colour. The upper panel shows the relative energy gain with respect to the standard settings (ΔGVD = 0, ΔTOD = 0) for the different target types and TOD values.
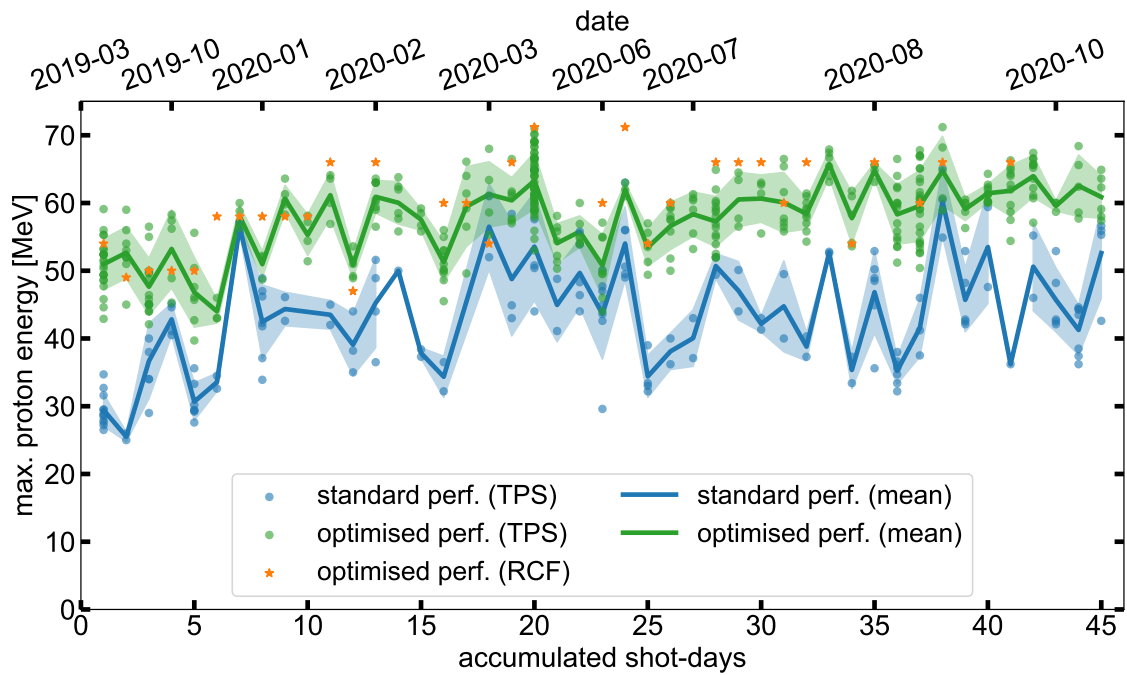
Figure 4.16: **Long-term stability of performance optimisation method.** Maximum proton energies for standard (blue) and optimised spectral phase settings (green) as a function of accumulated shot-days. Each circle represents the TPS result of one single shot, complemented by RCF stack data (orange stars). The shaded area depicts the standard deviation, the solid lines connect the mean of individual data sets serving as guide for the eye. Over more than one year of operation (from March 2019 until October 2020) and for a total of 575 shots on 45 accumulated shot-days the optimised phase settings yield higher maximum proton energies than the standard settings. The laser target configuration on all shot-days was very similar ($\approx 18\,J$ pulse energy, plasma mirror cleaned contrast, oblique laser incidence, $200 - 400\,nm$ Formvar targets).

4.7 Discussion on numerical simulations

Existing literature simulating asymmetric pulse shapes reports proton energy gain values from 50 % to 65 %, but is not conclusive about the required type of asymmetry. Souri *et al.* [332] performed 1D simulations ignoring the presence of any pre-plasma and found that a shallow rising edge enhances the proton acceleration performance in best case by 65 %. Kumar *et al.* [333] performed 2D simulations with a 10 μm pre-plasma ramp and found a gain of 50 % for a steeper rising edge. Both simulation studies thus yield a similar gain in proton energy for temporally asymmetric pulses, but the required asymmetry is just the opposite. Furthermore, the simulation do not meet the experimental conditions of this study (target: $\approx$ 230n_c, peak intensity: 5 × 10^{21} W cm^{-2}), as they assume target densities of only 12 – 20 n_c and peak intensities of $\approx$ 10^{20} W cm^{-2}. Double pulse structures may explain enhanced proton energies only when the second laser pulse contains either the same amount or the majority of the total laser energy [20, 334]. This scenario contradicts asymmetric pulse shapes induced by positive TOD values.

Consequently, new numerical investigations are necessary, that replicate the experimental conditions of this study. These simulations can provide further insights into the underlying laser-plasma interaction processes and the origin of the observed performance enhancement. The specific task of performing and analysing the simulations was beyond the scope of this thesis and has been assigned to two separate PhD projects [335, 336]. Additionally, this topic has served as a blueprint for simulation code developments and inspired several smaller research projects, including bachelor and master theses, aimed at studying the consequences of individual aspects of asymmetric laser pulses. The following section will provide a brief overview of the general approach and highlight the main results achieved so far. Details about the simulation setup can be found in the Appendix.

To investigate the influence of the modified temporal pulse shape, the asymmetric laser pulse was separated into three distinct scenarios, allowing to study the influence of each individually. The reference pulse is a Gaussian intensity distribution with 30 fs FWHM pulse duration. The integrated laser energy (18 J) is constant in all considered cases. First, the asymmetry of the main pulse on the linear intensity scale - hereafter called skewness - was studied. Therefore, the electric field envelope of the main pulse was modelled by two Gaussian halves with different σ. The ratio of these two values (σ_{rise} / σ_{fall}) is referenced as "rise-to-fall" (c.f. Figure A1). The imperfect intensity contrast on the sub-ps time scale was modelled by different exponential intensity ramps in front of the Gaussian main pulse. These ramps start –300 fs before the main pulse at a contrast level of 10^{-6} or 10^{-5} and increase exponentially to 10^{-5}, 10^{-4} and 10^{-3} at –100 fs, respectively (c.f. Figure A2). As third scenario, post-pulses of different intensities were simulated, following 80 fs and 120 fs after the main pulse. The intensity distribution of both pulses was modelled by a Gaussian intensity distribution, containing 10 %, 20 % or 40 % of the total laser energy (c.f. Figure A3).

All scenarios reveal similar maximum proton energies and particle numbers at the end of the simulation. The different pulse shapes only yield variations $\leq$ 10 %, significantly lower than the experimentally observed energy gain (up to 100 %). Overall, the simulation results significantly underestimate the experimentally observed gain in particle number and energy and variations in the rising edge of the main pulse or post pulses show only minimal influence on the final proton energies.

In a more recent simulation study (using the PIC code Smilei [337]), the temporal pulse

shape was initialised differently, resulting in promising overlap to the experimental data. In contrast to the previous approach, the laser pulse shape in this simulation was generated by a Fourier transformation of the spectral phase and amplitude (c.f. subsection 4.4.1). This results in more complex, i.e. realistic pulse shape that contains all the individual features from the previous simulation approach. The resulting maximum proton energies at the end of the simulation and the corresponding experimental data is shown in Figure 4.17. The simulation replicates the overall trend, where higher TOD val-
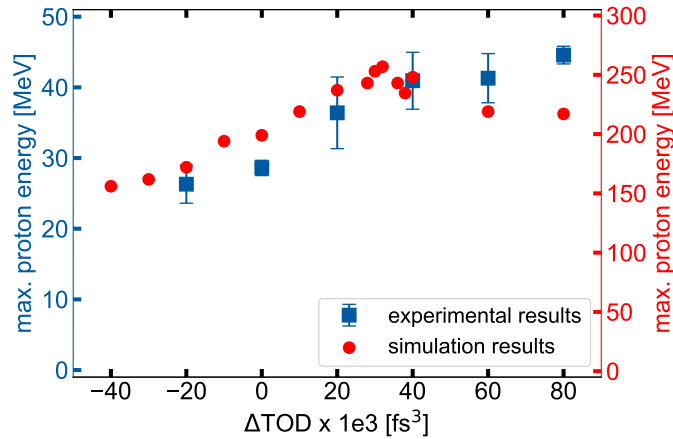
Figure 4.17: Simulation results. Maximum proton energies from 400 nm Formvar targets as a function of modified TOD value (ΔTOD).

ues lead to higher proton energies. Optimal acceleration performance is achieved for TOD values ranging between 30e3 – 40e3 fs^3, consistent to the experiment. Analysing the laser energy distribution and the proton phase space led to the following hypothesis to elucidate the observed effect. Positive TOD values result in lower laser energy deposition before the main pulse arrival, causing less pre-expansion of the target and steeper plasma density gradients at the target front and rear. Consequently, the absorption of laser energy by plasma electrons is increased. The most energetic protons get accelerated from the target bulk close to the origin of the rear side sheath. Subsequently, these protons propagate towards the front of the expanding particle population where they experience unshielded TNSA fields, leading to further acceleration. The experimental data supports the hypothesis of reduced target pre-expansion, as front side and rear side accelerated protons reach higher energies for positive TOD values. Furthermore, spectral measurements of the reflected laser light showed improved high-harmonic generation when TOD was added to the standard phase settings. A detailed analysis on these results will be part of another PhD project. The difference in absolute proton energy between the simulation and the experiment can be attributed to the simplified low-dimensionality of the simulation.

While the scenario of an asymmetric laser pulse may not appear overly complex at first glance, the results suggest that the influence of the detailed intensity distribution on the ion acceleration process is highly subtle. All performed simulations underline, that a more detailed understanding of the temporal plasma evolution coupled to the performed spectral phase changes of the laser is necessary to understand the experimentally observed energy enhancement. A major challenge on this way lies in determining the exact interaction conditions several picoseconds around the main pulse. This requires precise knowledge about the spatial and temporal laser intensity distribution and the corresponding plasma response for each shot. Currently, neither the experimental diagnostics nor the computational capabilities have reached a level of development to

fully address this task. Therefore, focussing on individual aspects of this multifaceted picture remains an important approach. The results of this study identified the relevant time and intensity scale that future experimental and numerical investigations should put into focus.

4.8 Conclusions

In summary, this chapter has shown that application-relevant proton beams with sufficient energy and particle yield and can be generated in a stable manner using a state-of-the-art high repetition rate PW-class laser system. This experimental breakthrough has been achieved through continuous efforts to understand and optimise the temporal intensity contrast of the DRACO-PW laser system.

Initially, this included the implementation of on-shot pulse diagnostic devices and metrology ports for target environment conditions. The implementation and characterisation of an intensity dependent filter systems, i.e. a single stage re-collimating plasma mirror, has proven to significantly improve the temporal contrast by reducing pre-pulse intensity and steepening the rising edge of the main laser pulse. Optimal operation conditions for the plasma mirror result in a total energy reflectance above 80 % and a contrast improvement by more than three orders of magnitude. Having established such efficient on-demand laser contrast cleaning, the plasma dynamics has been restricted to the last ps before the main pulse arrives at the target. This enabled to modify even the sub-ps range by individually adjusting the instantaneous frequencies of the electric field and thus the temporal shape of the laser pulse by means of an acousto-optic programmable dispersive filter. Studying the influence of different pulse shape modifications on the quality of the accelerated particle beam revealed, that highest proton cut-off energies and particle numbers were measured for temporal pulse parameters well different from those of ideally compressed Fourier transform limited pulses. The demonstrated stability of this effect during a long period of operation and over a wide range of interaction parameters like target thickness and material as well as laser energy and temporal intensity contrast implies that this method could be easily transferred to other laser systems operating in the PW range. Note, in perspective of future applications, automated dispersion control for performance optimisation is a readily applicable method to be combined with real-time feedback routines based on advanced computing schemes.

All these efforts have cumulated in performing dose-controlled "*in vivo*" studies with a laser-driven protons at the DRACO-PW laser system. This accomplishment represents a milestone in the translation process of plasma accelerators towards practical applications. After applying the performance optimisation procedure, the generated particle beam reached the desired energy and particle numbers to perform such a demanding experiment. The combination of the optimised particle source with an energy selective pulsed two-solenoid beam transport system [338] allowed to shape the particle beam spectrally and spatially to generate a homogeneous 3D dose distribution. The achieved dose distribution was monitored by a plethora of online and retrospective dosimetry diagnostics allowing to achieve a very high precision in mean dose delivery ($\pm$10 %) and dose homogeneity ($\pm$5 %). The generated particle beams were applied in two different volumetric irradiation scenarios. At high precision with respect to predefined dose value and homogeneity dedicated tumors prepared in the ear of mice were irradiated with a single dose value of 4 ($\pm$0.4) Gy. In contrast, highest single-shot values of beyond 20 Gy could be applied at only slightly reduced beam quality to tackle the ultra-high dose rate regime. The data and results of the two series of experiments were published by Kroll *et al.* [16].

5 Enhanced ion acceleration in the relativistic transparency regime

In the pursuit of enhancing achievable particle energies beyond the limitations posed by the modest energy scaling of standard sheath acceleration, this chapter reports on an advanced ion acceleration scheme occurring in the **Relativistically Induced Transparency (RIT)** regime. Previous experiments in the RIT regime have shown promising results [13, 130–138, 140, 141] and that proton energies up to 100 MeV are achievable [139]. However, additional advancements are required, particularly in terms of reproducibility and adaptability to ultrashort pulse lasers. These laser systems are of great importance in facilitating systematic studies on the influences of laser and target parameters due to their high repetition rate.

This chapter demonstrates the enormous potential of ion acceleration in the RIT regime using high-power laser systems with ultashort pulse durations (tens of fs). The combination of thin plastic foil targets with precisely matched temporal contrast conditions of the laser enabled a transition of the initially opaque targets to transparency upon main pulse arrival and full exploitation of the acceleration capabilities in this regime. Protons with energies exceeding 60 MeV and fully ionised carbon ions with energies surpassing 30 MeV u^{-1} could be generated using the J-KAREN-P laser system and only 10 J of laser energy on target. A complementary investigation using the DRACO-PW laser replicated the experimental results, highlighting the robustness and controllability of the identified acceleration scheme. Additionally, the temporal laser contrast of DRACO-PW was actively modified by incorporating a plasma mirror to the setup, efficiently reducing the preceding laser light which resulted in a decreased optimal target thickness. A combination of hydrodynamic and 3D particle-in-cell simulations revealed that the most energetic particles are accelerated by a strong space charge induced electric field, followed by further acceleration in a diffuse sheath. The extremely localised space charge field, exceeding 30 TV m^{-1}, arises from the rapid expulsion of electrons from the target bulk due to RIT.

The presented results mark the culmination of several years of progress in operation and instrumentation for laser-driven ion sources. During a series of experiments on both laser systems, standardised operation principles, experimental procedures, high-quality beam characterisation capabilities and analysis methods were established. Conducting systematic scans of laser and target parameters using two different laser systems, complementary insights into microscopic plasma dynamics were gained and the optimal interaction conditions for ion acceleration in the RIT regime identified. Ultimately, these

collective efforts facilitated the successful replication of experimental results across two distinct laser facilities. The results of this chapter led to the publication of TZ2.

5.1 Introduction

Target Normal Sheath Acceleration (TNSA) has proven to be a robust technique for generating energetic ions by laser irradiation of foil targets [4, 5]. However, the mechanism's modest energy scaling [27, 52, 53, 339] poses significant challenges when attempting to increase the beam energy. In contrast, advanced acceleration schemes promise higher ion energies when using ultraintense pulses at the same laser energy level. For example, in the light sail scenario of radiation pressure acceleration, an opaque ultrathin target is collectively propelled by the laser [79, 129]. However, such ultrathin foils are extremely fragile and require an almost perfect temporal laser intensity contrast, the ratio between the main pulse and preceding light (c.f. subsection 3.1.2). Experiments and simulations with realistic, i.e. non-perfect, laser parameters revealed difficulties in achieving coherent acceleration throughout the entire interaction with the laser pulse. Instead, target instabilities and heating of target electrons can cause rapid expansion, reducing the plasma core density and suppressing light sail acceleration [123, 126]. Eventually, the electron density n_e drops below the relativistically corrected critical density $n_{cr} = \gamma n_c$, where γ is the electron Lorentz factor and n_c is the classical critical density. This results in laser propagation through the target, referenced as the RIT regime (c.f. subsection 2.3.3).

It has been shown that for targets undergoing this transition to transparency, various acceleration mechanisms can produce energetic ions, including volumetrically-enhanced sheath acceleration [103, 130, 138], break-out afterburner [133, 146], magnetic vortex acceleration [143], acceleration synchronised to the relativistic transparency front [99, 100], and hybrid mechanisms [127, 135, 139, 154]. Experiments in the RIT regime have demonstrated carbon ions exceeding 1 GeV [134] and protons approaching 100 MeV [139], both using high energy ($\simeq 100$ J) glass laser systems with ≈ 1 ps pulse duration. Experiments with ultrashort laser pulses (pulse duration tens of fs) and relatively low laser energy (≤ 5 J) also demonstrated an impact of RIT on ion acceleration performance [127, 158]. Recent simulation studies infer the importance of RIT over a wide range of laser intensities [157, 340].

Many applications of laser driven ion sources require an advancement from single-shot proof-of-principle studies to sustainable repetitive operation. The requirement of high repetition rate (> 1 Hz) currently necessitates the use of ultrashort pulse lasers, providing high intensities at modest laser energies compared to glass laser systems with high energies and $\approx$ ps pulse durations. Despite recent advances in improving the inherent contrast of ultrashort pulse laser systems [267, 268], they are not yet suitable for light sail acceleration without applying additional contrast enhancement techniques (e.g. plasma mirrors). These additional techniques usually complicate the overall setup and limit the ultimate repetition rate. Consequently, there is a great interest in optimising ion acceleration using ultrashort pulse lasers, and in particular further investigating advanced acceleration schemes like RIT with these laser systems. The effective utilisation of advanced acceleration schemes for applications necessitates a comprehensive understanding of the underlying acceleration mechanism and sufficient control over relevant experimental parameters. Historically, many experiments, reporting results from advanced acceleration schemes obtained at a particular laser system could not be reproduced at other laser facilities. However, replication of experimental results at different facilities is a fundamental prerequisite for enabling a widespread adoption and application of plasma accelerators.

5.2 Experimental setup using the J-KAREN-P laser

The effect of changing target thickness on ion acceleration was investigated using the J-KAREN-P laser at the **Kansai Photon Science Institute (KPSI)** [233]. Details about the laser system and the experimental area at KPSI can be found in subsection 3.1.4 and subsection 3.2.2. The detailed experimental setup of this study is illustrated in Figure 5.1. P-polarised laser pulses with 10 J on-target energy and 45 fs FWHM duration were fo-
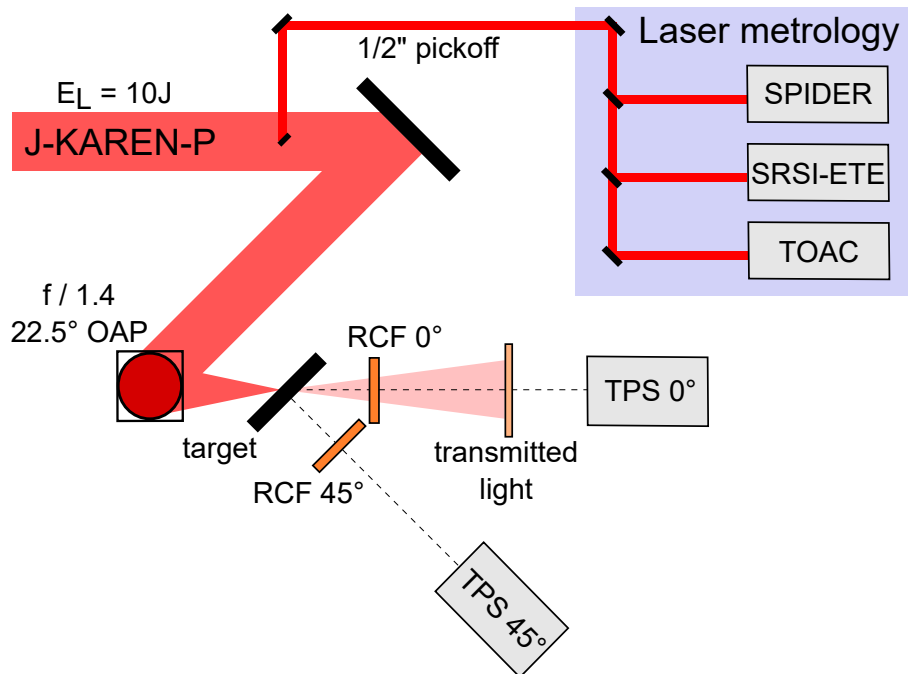
Figure 5.1: Illustration of the experimental setup at KPSI. The J-KAREN-P laser was focused by an f/1.4 off-axis parabola (OAP) onto Formvar films at 45°. Accelerated particles were detected spatially by two radiochromic film (RCF) stacks and spectrally by two Thomson Parabola Spectrometers (TPS) oriented at 0° and 45° with respect to the laser axis. When RCFs are not used, a ground glass screen diffusely scattered transmitted laser light for detection by a filtered CCD camera. The temporal intensity distribution of the laser pulse was measured by a suite of scanning and single-shot detectors.

cused by an f/1.4 off-axis parabola onto Formvar targets placed at 45° to the incident laser. The thickness of the Formvar plastic foils (c.f. section 3.3) ranged from $d = 20$ nm to 1000 nm. The FWHM focal spot diameter was $\approx 1.5\,\mu$m, resulting in a laser peak intensity of $(3.5 \pm 0.5) \times 10^{21}$ W cm^{-2} [283]. The laser was used with inherent contrast, i.e. without a contrast enhancing plasma mirror system. The temporal intensity contrast of the J-KAREN-P laser is shown in Figure 3.7. Laser light transmitted through the target was scattered off ground glass screens placed ≈ 50 cm behind the target and then imaged onto a bandpass filtered (800 nm $\pm$ 25 nm) and calibrated camera.

Two **Thomson Parabola Spectrometers (TPS)** positioned at 0° and 45° with respect to the laser axis measured the proton and ion energy spectra. BAS-SR Fujifilm imaging plates were used as particle detectors inside the TPS. Over the whole thickness range investigated, the prominent light ion species had $Z/A = 0.5$. Considering the target composition, this is dominated by C^{6+} with a contribution from O^{8+} and therefore labelled as carbons for simplicity. Two **RadioChromic Film (RCF)** stacks were used to measure the spatial distribution of the proton beam. They were placed behind the target, one along the laser axis and the other along the target normal at a distance of 100 mm and

60 mm, respectively. The RCF enabled discretised energy detection in the full opening angle between laser forward and target normal direction. The XR-RV3 films [310] were 70 mm × 70 mm in size, with a horizontal slit through the centre to enable simultaneous measurement with the TPS.

5.3 Experimental results

The maximum energies per nucleon $\mathcal{E}_m$ of the two dominant ion species (protons and C^{6+}) together with the transmitted 1ω laser light energy ε_{trans} as a function of initial target thickness d are plotted in the left panel of Figure 5.2. An optimal thickness $d_{opt} \approx 250$ nm
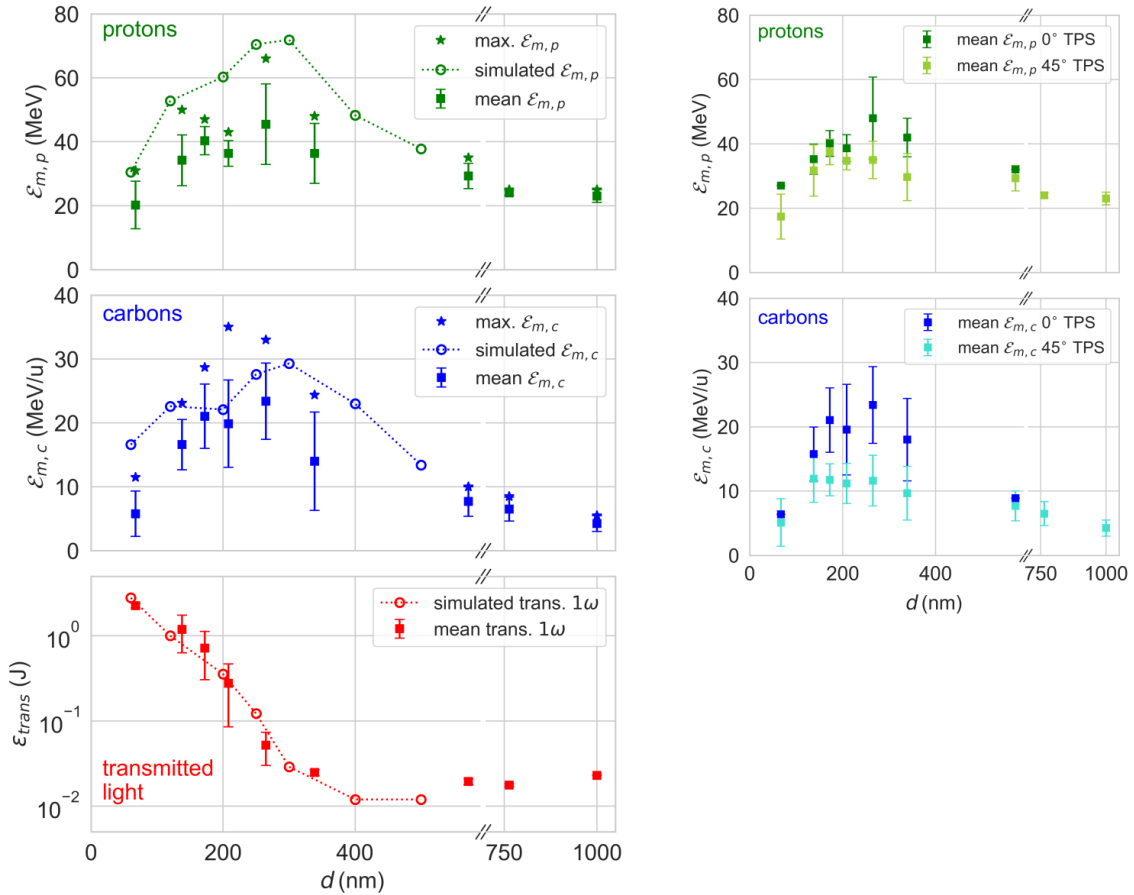

Figure 5.2: Experimental results using the J-KAREN-P laser. The left panel shows the maximum proton and carbon energies per nucleon $\mathcal{E}_m$ recorded on the TPS detectors for different target thicknesses, together with the corresponding transmitted 1ω laser light energy ε_{trans}. Over 50 shots are included over the entire thickness range. Error bars represent the standard deviation and stars show the maximum $\mathcal{E}_m$ in each thickness bin. Circles show the corresponding $\mathcal{E}_m$ and ε_{trans} values from 3D PIC simulations. The right panel shows a comparison of maximum ion energy $\mathcal{E}_m$ measured on the TPS at 0° and 45° for protons and carbon ions.

can be detected, where energies of both ion species reach a maximum ($\mathcal{E}_{m,p} > 60$ MeV for protons and $\mathcal{E}_{m,c} > 30$ MeV u^{-1} for carbons). Thinner or thicker targets result in lower energies for both species. For $d < 700$ nm the most energetic particles were measured by the 0° TPS, whereas for $d > 700$ nm particles were only observed in the 45° TPS as can be seen in the right panel of Figure 5.2. The amount of transmitted light also indicates a clear thickness dependency. Targets with $d > 300$ nm show a constant and nearly neg-

ligible amount of transmitted light (ε_{trans} < 30 mJ $\simeq$ 0.3% input energy), while transmission increases exponentially for thinner targets, reaching ε_{trans} $\gg$ 500 mJ (> 5 % of input energy) for d < 200 nm. This sudden increase in transmission for target thicknesses between 200 nm and 300 nm indicates a pronounced decrease in the peak density of the targets at the arrival of the main pulse. There is a clear correlation between the onset of transparency and a dramatic increase in the generated beam energies. However, for very thin targets with high transmission, the ion energy reduces again. The measurable but relatively low transmission for optimum ion energies indicates an efficient conversion of laser energy in the transparent but still dense target.

Full-beam energy spectra deconvolved from RCF stacks for three representative shots at different target thicknesses are shown in Figure 5.3. Targets which are either highly
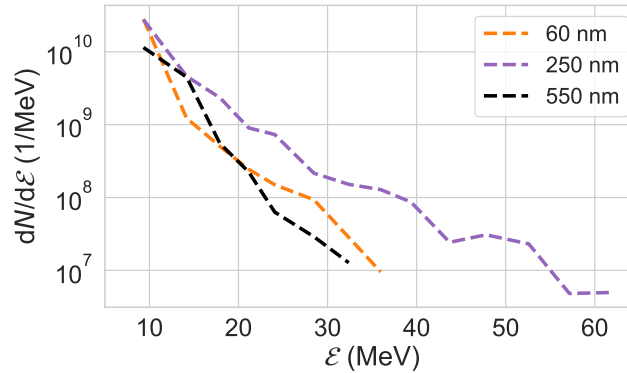
Figure 5.3: **Proton spectrum from RCF.** Reconstructed particle spectra from RCF measurements, combining both RCF stacks, for an exemplary shot with initial target thickness of 60 nm, 250 nm and 550 nm, respectively.

transmissive (d = 60 nm) or opaque (d = 550 nm) show a similar spectral shape and $\varepsilon_{m,p}$ $\approx$ 35 MeV. In contrast, for d = d_{opt}, there is an increase in both cutoff energy, to $\varepsilon_{m,p}$ $\approx$ 60 MeV, as well as particle flux at high energies, while maintaining a thermal spectral shape.

An example of the energy dependent spatial-dose distribution of protons generated at the optimum target thickness (d = 250 nm) is shown in Figure 5.4, together with a synthetic spatial beam profile derived from simulations (discussed in section 5.5). Lower energy protons (9 MeV) show a confined round beam profile along the target normal direction with a low flux divergent emission evident along the laser axis. With increasing particle energy, the beam profile centre shifts towards the laser axis, with significant spatial structure apparent. At the highest energies (e.g. 52 MeV), the beam is directed primarily along the laser axis. This observation of the most energetic protons propagating closer to the laser axis is consistent with TPS data, showing significantly higher energies along laser axis than target normal for targets d $\approx$ d_{opt} (c.f. Figure 5.2). Conversely, for the thickest targets where laser transmission is negligible, no protons are observed along the laser axis. The TPS also confirm that the beam direction dependence on target thickness is identical for accelerated carbon ions. This change in beam directionality and shape, correlated with the increase in transmitted light, suggests a strong influence on the acceleration mechanism due to relativistically induced transparency.

5.4 Laser-induced breakdown and target pre-expansion

Understanding the pre-expansion of the target is essential for elucidating the high intensity laser-plasma interaction at the peak of the pulse. Laser light preceding the main
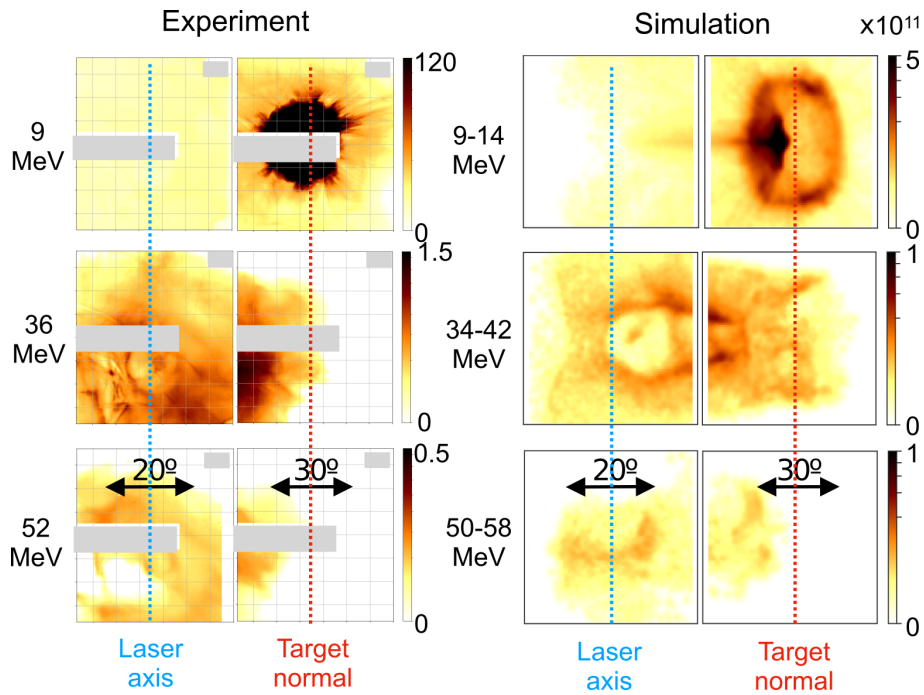
Figure 5.4: Spatial proton beam profile. **Left:** Experimental data (same shot as purple line in Figure 5.3) giving dose (Gy) from RCF at different Bragg peak energies. The grey shaded area indicates regions not measured by the RCF. **Right:** Synthesised profiles from 3D PIC simulations, giving the number of particles per steradian over the indicated energy range. The ring feature from 9 – 14 MeV is due to the small simulation box size, which artificially limits the transverse extent of the sheath at the rear surface.

pulse ionises and heats the target, resulting in significant target decompression before the arrival of the peak of the pulse. This effect on the target density is illustrated on the left in Figure 5.5. Changing the initial target thickness therefore varies not only the areal
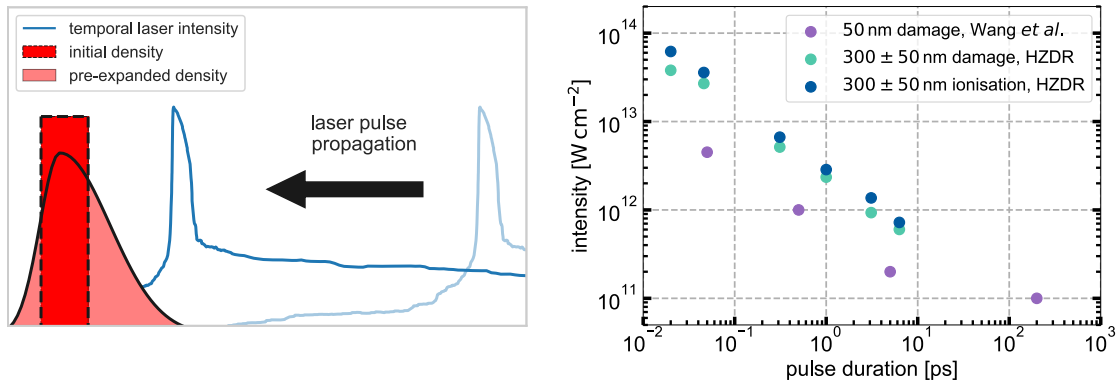

Figure 5.5: **Left:** Illustration of target expansion and density modification before main pulse arrival. **Right:** Pulse length dependent ionisation intensity and damage intensity for Formvar foils of 50 nm and 300 nm thickness, respectively.

density, but also the peak density of the target interacting with the main pulse.

The experiments in this chapter used Formvar, a transparent dielectric material with a high band-gap. For such a material, the absorption of laser light is negligible until it is ionised by **Laser-Induced Breakdown (LIB)** [341, 342]. After LIB, free electrons absorb laser energy at the target front surface, leading to ablation and the generation of a shockwave propagating into the target. For sufficiently thin targets, the shock can

break through the back of the target, causing a reduction of the core density before the main pulse arrival. Identifying the precise timing, when the preceding laser light, either pre-pulses, the coherent pedestal or **Amplified Spontaneous Emission (ASE)** (c.f. sub-section 3.1.2) trigger LIB is therefore crucial. This moment marks the onset of target expansion and pre-plasma generation.

A separate PhD project [343] determined the threshold values for LIB for different pulse lengths and target materials. This also included 300 nm ± 50 nm Formvar foils, which were irradiated using the DRACO-PW laser and an optical probing setup for visual target inspection. Similar experimental measurements have been conducted by Haffa *et al.* [341] and Wang *et al.* [344]. The results of the measurements at DRACO-PW and the results from Wang *et al.* are shown on the right of Figure 5.5. A comparison of those values with the measured temporal contrast of the J-KAREN-P and the DRACO-PW laser under similar conditions (attenuated beam) is shown in Figure 5.6. For both
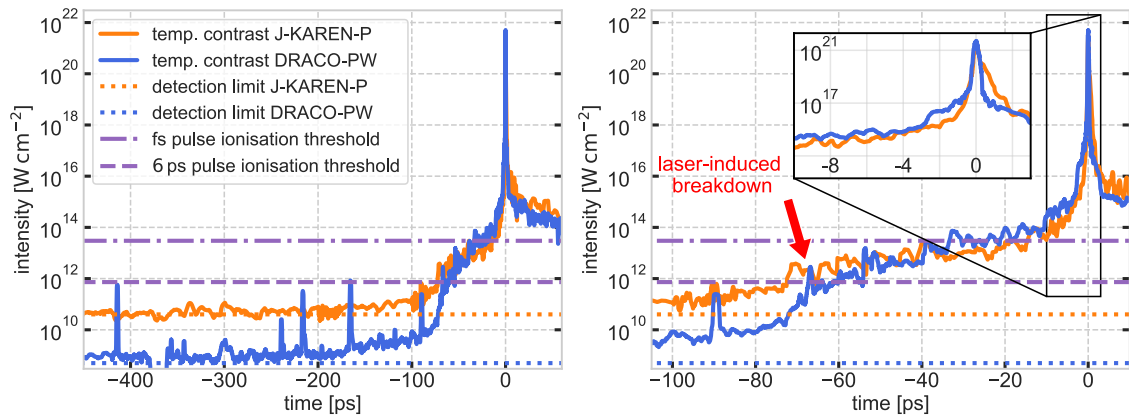
Figure 5.6: Comparison of temporal intensity contrast measurements. Experimental results from scanning third-order auto-correlator (Sequoia and SequoiaHD from Amplitude) measurements of J-KAREN-P (solid orange line) and DRACO-PW (solid blue line) laser pulse contrast up to −500 ps (left panel) and up to −105 ps (right panel) before the main peak. The intensity during the rising edge of the coherent pedestal at −67 ps reaches the threshold for laser induced breakdown of ps pulses (dashed purple line). The similarity of the contrast levels between both laser systems implies a similar pre-pulse driven plasma expansion.

laser systems, the ASE level < −100 ps is significantly lower than the relevant LIB threshold [344] as seen in the left plot. Moreover, there are no pre-pulses with intensities sufficient for LIB prior to −70 ps. The right plot of Figure 5.6 indicates, that the intensity level of the coherent pedestal reaches the LIB threshold between −70 ps and −65 ps.

It should be noted, that different dielectrics or metal targets would be affected by the preceding light differently due to different breakdown times and material properties [344]. The importance of understanding this process in elucidating the high intensity laser-plasma interaction motivates detailed material dependent studies of the LIB process in comparison with high dynamic range, full-power measurements of the temporal contrast.

5.5 Elucidating ion acceleration in the relativistically induced transparency regime

To consider the effect of the preceding laser light and target expansion, a two-stage simulation method was implemented, involving hydrodynamic simulations of the low-

intensity rising edge after LIB followed by 3D **Particle-In-Cell (PIC)** simulations of the final high-intensity ramp and main pulse using the FLASH and EPOCH codes respectively.

5.5.1 Details on simulation methodology

The FLASH code (v4.6.2) [345] is used in 2D cylindrical geometry with adaptive mesh refinement and models the absorption of the preceding laser light using ray tracing coupled to an inverse bremsstrahlung heating model. Wave effects, such as resonance heating, are not included, which may slightly underestimate the heating absorption rate. However, a small uncertainty in absorption does not make a significant difference in simulations which vary laser intensity over many orders of magnitude. A tabulated Formvar EOS was generated using the FEOS code [346]. The resultant density profile at 1 ps before the main pulse arrival was used to initialise the 3D PIC simulations of the high-intensity interaction.

The main pulse interaction were modelled using EPOCH 3D (v4.17) [347]. A simulation box of $30\,\mu m \times 25\,\mu m \times 14\,\mu m$ was simulated with a spatial resolution of $20\,nm \times 40\,nm \times 40\,nm$, where the highest spatial resolution was along the laser propagation direction. The cylindrically symmetric density profile from the FLASH simulation was mapped into 3D and used as the initial density profile, assuming full ionisation and no species separation. 14 electrons, 8 carbon/oxygen ions and 8 protons were initialised per cell. Density regions with a fully ionised density below $1\,n_c$ were removed during initialisation. The laser was focused to a Gaussian spot (1.5 μm FWHM) on the front surface of the target in p-polarisation, with a peak intensity $I_L = 4\times10^{21}\,W\,cm^{-2}$. The temporal intensity profile was matched to an average single-shot measurement from the SRSI-ETE diagnostic.

It should be mentioned, that the wide range of laser intensities and target conditions present during the interaction with the preceding laser light poses challenges for current modelling techniques. Hydrodynamic codes often use oversimplified models for laser heating and the behaviour of the low temperature solid bulk before target decompression. Especially the rising edge of the laser pulse traverses an intensity range between $10^{15}\,W\,cm^{-2}$ to $10^{17}\,W\,cm^{-2}$ where the target is still relatively cold, but non local heating can become important.

5.5.2 Simulation results

The variation in $\mathcal{E}_m$ and ε_{trans} with changing d from the two-stage simulations is shown overlaid (circles) on the experimental data in Figure 5.2. There is good agreement with the experiment over the entire thickness range. The simulations accurately recreate the optimum target thickness and maximum ion energies. The plotted simulation data gives the maximum energy in any angular direction, whereas the TPS measurements are restricted to 0° and 45°. For simulations of targets with $d > d_{opt}$ the highest energies were often found between laser axis and target normal and the simulations show that the plasma remains opaque throughout the interaction. There is high laser absorption into electron kinetic energy, and this drives large diffuse thermally driven sheath fields on the rear side of the target. No significant transmitted laser light is observed, and there is no contribution of relativistic transparency to the ion acceleration. On the other hand, when targets are too thin, for example $d = 60\,nm$, the target is already well below the classical critical density by the peak of the pulse. There is still significant absorption in the target, as electrons are injected from the periphery of the relativistic plasma aperture into the strong laser fields [168]. The accelerated electrons again contribute strongly to widespread thermally driven diffuse sheath fields, but the ion density in the target remnants is too small to generate the larger amplitude localised space charge field.

In the following, the ion acceleration process for the optimal initial thickness $d_{opt} = 250\,nm$ and the main pulse interaction with the pre-expanded plasma is discussed in detail. During the final rising edge of the pulse, laser energy is strongly absorbed by a still opaque plasma. The high intensity of this rising edge results in a strong $v \times B$ radiation pressure, accelerating electrons in bunches along the laser axis. Thereby, energetic electrons generate sheath fields, accelerate ions and cause a rapid expansion of the target. A 2D slice from the simulation at the peak of the pulse is shown in Figure 5.7a. As shown by
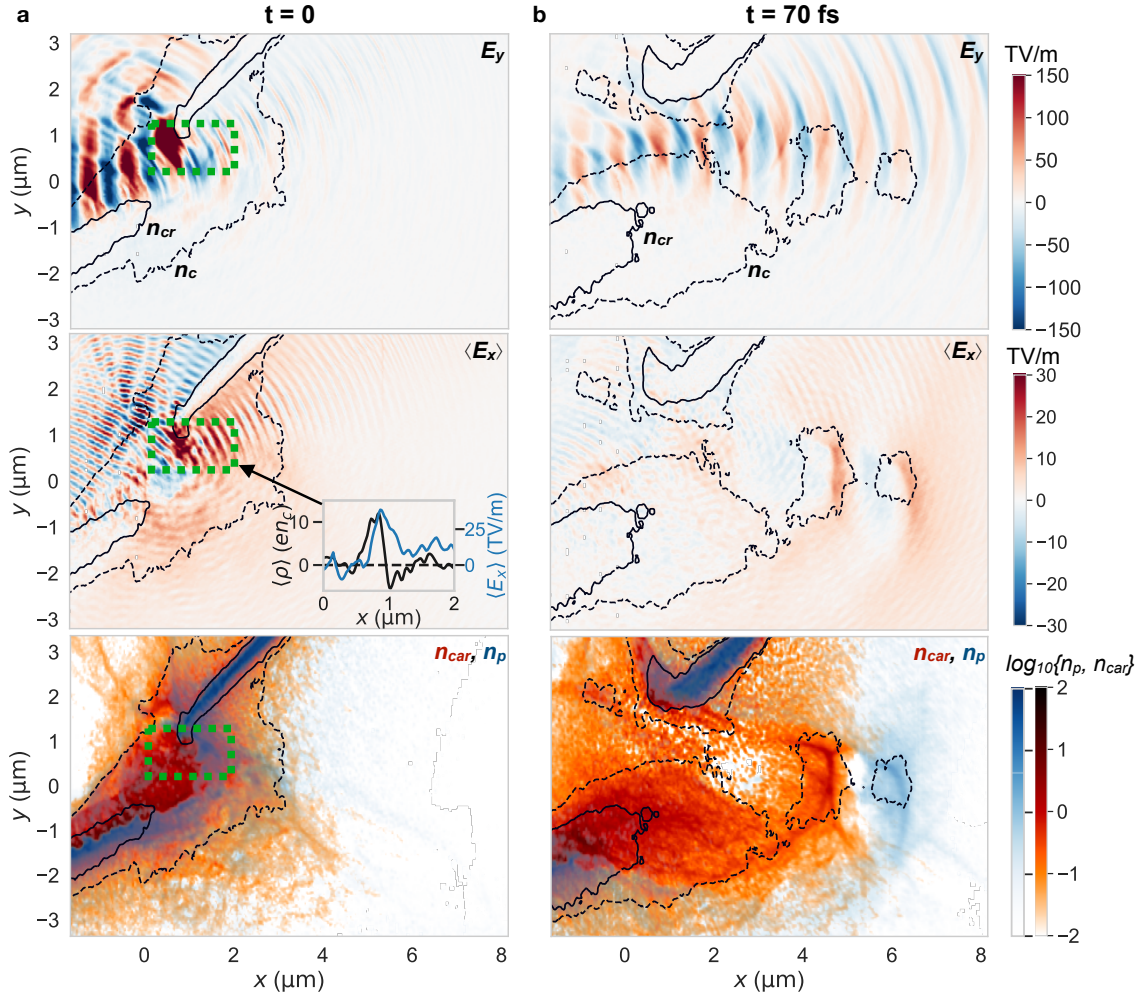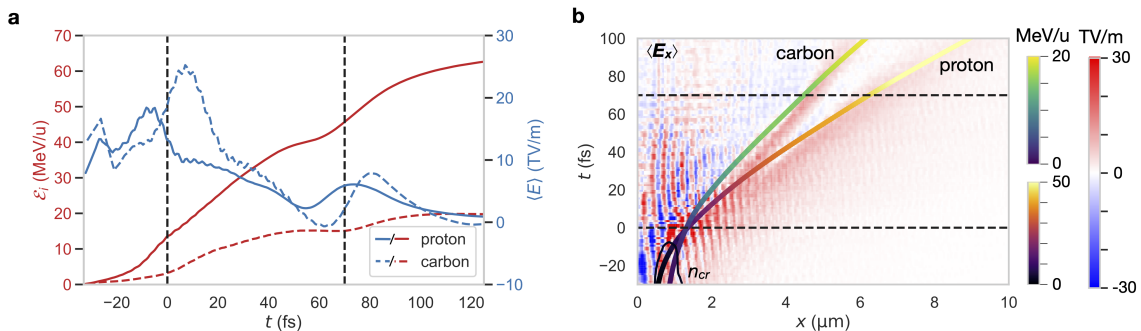

Figure 5.7: Plasma density from 3D PIC simulations for expanded target. **a** 2D slice ($z = 0$) of E_y, $\langle E_x \rangle$ and carbon/proton density (n_{car}, n_p normalised to n_c) for a 250 nm target at $t = 0$, when the peak of the pulse arrives. The solid (dashed) contours give the relativistic (classical) critical electron density. The region of strong electron expulsion is highlighted by the green box. The inset shows the cycle-averaged space charge density $\langle \rho \rangle$ and $\langle E_x \rangle$ for a lineout through the centre of the green box, averaging over $\Delta y = 400\,nm$. **b** The same 2D slices at $t = 70\,fs$, at the end of the main pulse interaction, showing the acceleration of the separated ion species in the thermal sheath fields.

the electron density contours, the electrons in the centre of the target have been heated and expanded such that $n_c < n_e < n_{cr}$, and the laser has started to penetrate the target. The laser volumetrically interacts with target electrons, leading to strong absorption. This results in electrons being rapidly expelled from the focal region by the $v \times B$ force. As ions are not significantly accelerated by the laser fields due to their lower charge-to-mass ratio, a region of large space charge develops in the transparent region highlighted by the green box. This space charge is maintained by the continuous expulsion of electrons

due to the radiation pressure of the laser. Although the electron expulsion is not complete, unlike total expulsion in the Coulomb explosion regime (c.f. subsubsection 2.3.3), the magnitude of the time-averaged space charge can reach $\langle \rho \rangle > 10\,e\,n_c$, which results in a region of large cycle-averaged quasi-static electric field $\langle E_x \rangle \sim 30\,\mathrm{TV\,m^{-1}}$, with a spatial extent of $\sim 500 \times 500 \times 500\,\mathrm{nm^3}$ (see inset in Figure 5.7a). Unlike the break-out afterburner regime [133, 154], there are no apparent low-frequency electrostatic wave structures resonant with the accelerated ions. However, the ions experience an oscillating longitudinal field E_x as the forward moving relativistic electron bunches pass through them, without gaining net energy. Due to their higher charge-to-mass ratio, the protons have started to separate from the more abundant carbon ions, but they are still both present in the region of strong $\langle E_x \rangle$. Additionally, there is a weaker $\langle E_x \rangle$ apparent over a large extent at the target rear. These are characteristic pre-thermal sheath fields [30] along the long density scale lengths at the rear surface sustained by electron pressure, differentiating it from the stronger localised field due to radiation pressure sustained electron expulsion. After the end of the most intense part of the laser pulse, acceleration continues in a thermal sheath field of significantly lower intensity. Complete ion species separation becomes prominent due to the faster velocity of the protons, as shown in Figure 5.7b. At this point, the bunching of the forward accelerated protons and ions results in two distinct sheath fields around each species, with $\langle E_x \rangle < 10\,\mathrm{TV\,m^{-1}}$.

Particle tracking reveals that the most energetic carbons and protons originate from the region of strong electric field generated by electron expulsion in the ion core during RIT. The time history of the kinetic energy of exemplary proton and carbon ions is given in Figure 5.8a, along with the cycle-averaged electric field driving the acceleration. The ions

Figure 5.8: Plasma density from 3D PIC simulations. **a** Time history of kinetic energy $\mathcal{E}_i$ (red) and local electric field $\langle E \rangle$ (blue) experienced by exemplary proton (solid lines) and carbon ion (dashed). **b** Time history of $\langle E_x \rangle$ along x lineout through the region of largest accelerating gradient, with overlaid trajectory of the same proton and carbon ion. The solid black line shows the n_{cr} contour. Black dashed lines indicate the time of the two snapshots in Figure 5.7.

are accelerated by strong fields up to $\langle E \rangle \geq 20\,\mathrm{TV\,m^{-1}}$ around the peak of the pulse. These are the fields sustained by the electron expulsion, and they provide a significant kick to the ions. The relative time offset between the peak of the field experienced by the proton and carbon is due to an offset in starting position of the selected particles, as the laser sustained space charge moves along with the expanding ions. Figure 5.8b shows a waterfall plot of $\langle E_x \rangle$ along a line through the centre of acceleration ($z = 0$, $y = 0.7\,\mu\mathrm{m}$) as a function of time, overlaid with the n_{cr} contour. The strongest field is generated near the peak of the pulse ($t = 0$), just after the onset of transparency. As the target ions are accelerated forwards, the laser sustained space charge also moves forwards, decreasing as the ion density decreases. The ions in this region are therefore in a moving potential, increasing their energy gain. Eventually, at $t \approx 20\,\mathrm{fs}$, both the ion

density and the laser pressure have decreased to such an extent that a strong localised field is no longer apparent above the thermally driven sheath. After this point, the ions continue to be accelerated by the ambient sheath fields. The ions which received the largest velocity kick from the laser-sustained space charge record a further energy gain as they are accelerated through weaker sheath fields $E < 10\,\mathrm{TV\,m^{-1}}$, as seen in Figure 5.8b. Therefore, at $d \approx d_{opt}$, the majority of the most energetic ions are accelerated by a hybrid mechanism - a swift acceleration due to laser-driven electron expulsion in the dense transparent plasma core followed by further acceleration in the diffuse sheath.

Spatial proton beam profiles are shown in Figure 5.4. These synthetic RCF layers were generated from the simulated particle distribution, assuming ballistic motion after the end of the simulation. Similar to the experiment, the lower particle energies show a dominant emission towards the target normal direction, which is caused by protons accelerated by the diffuse sheath at the periphery of the target at radii larger than the laser focal spot size. This beam is limited to energies < 20 MeV. For higher particle energies, the target normal beam is not seen. Instead a divergent and diffuse particle beam is observed directed predominantly along the laser axis.

5.6 Acceleration in the RIT regime for modified temporal contrast.

The previous section demonstrated that the key to maximising the ion energy is target expansion in such a way, that $n_e = n_{cr}$ is reached upon main pulse arrival. Consequently, the optimal initial target thickness d_{opt} is expected to dependent on both the temporal laser contrast, which determines the maximum target density, and the laser intensity, which affects the electron heating and therefore the density required for transparency. To investigate this dependency of the RIT regime further, the previously described experiment was repeated using the DRACO-PW laser.

The DRACO-PW laser system at **Helmholtz-Zentrum Dresden-Rossendorf (HZDR)** has comparable laser parameters to the J-KAREN-P laser and is therefore ideally suited for such a complementary study. In particular, the temporal contrast on the multi-ps time scale is very similar on both systems as can be seen in Figure 5.6. A detailed comparison between the two laser systems reveals, that the temporal intensity distribution after LIB at $\approx$ –67 ps is almost identical. Therefore, the subsequent plasma expansion is expected to be similar in both experiments. The focussed laser peak intensity is also comparable, although slightly higher at DRACO-PW ($I_L \approx 5 \times 10^{21}\,\mathrm{W\,cm^{-2}}$). Additionally, there is an option for on-demand contrast improvement using a single-shot **Plasma Mirror (PM)**, enhancing the contrast level by almost four orders of magnitude (c.f. section 4.3). The PM essentially limits the plasma dynamics to the last picosecond before the main pulse arrival and significantly suppresses target pre-expansion. This enables two different pre-plasma conditions to be realised.

5.6.1 Experimental setup using the DRACO-PW laser

The setup at DRACO-PW used an identical target irradiation geometry as the J-KAREN-P experiment and similar diagnostics, allowing for comparable measurements. A detailed illustration of the experimental setup at DRACO-PW is shown in Figure 5.9. Laser pulses with an on-target energy of 17.6 J (without PM) or 18 J (with PM) were focused by an f / 2.3 90° OAP to an FWHM spot size of ($\approx$ 2.6 μm), yielding a peak intensity $\geq 5 \times 10^{21}\,\mathrm{W\,cm^{-2}}$. The intense laser pulses irradiated Formvar foils in a thickness range from $d = 20\,\mathrm{nm}$ to 400 nm at an incidence angle of 45° with p-polarisation. The temporal contrast was
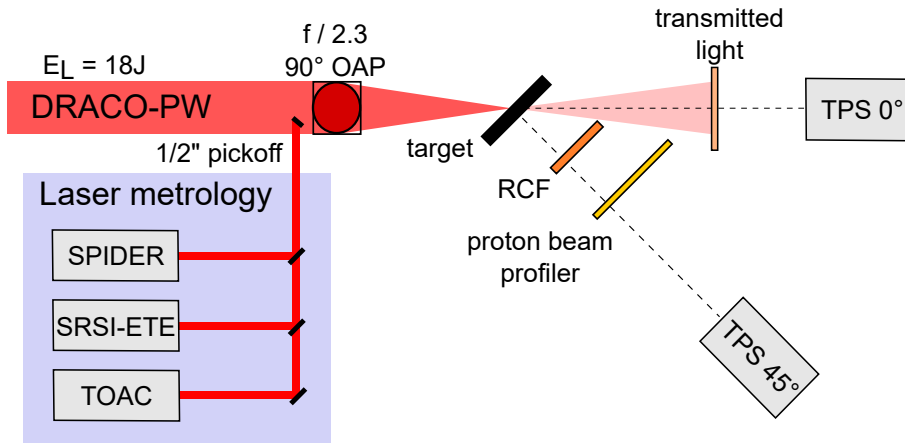
Figure 5.9: Illustration of the experimental setup at HZDR. Laser pulses from the DRACO-PW are focused by an f/2.3 off-axis parabola (OAP) onto thin plastic foil targets. The kinetic energy distribution of the accelerated protons was measured by two Thomson parabola spectrometers (TPS0 and TPS45 positioned at 0° and 45° with respect to the laser propagation direction). An imaged scintillator screen or RCF stacks were used to characterise the spatial proton beam distribution. Laser light transmitted through the target was collected by a ceramic screen. A suite of scanning and single-shot detectors measured the temporal intensity distribution of the laser.

characterised by picking off a fraction of the incoming laser beam and sending it to the laser metrology bench. There, identical measurement methods and instruments (TOAC, SPIDER, SRSI-ETE) as at J-KAREN-P ensured comparability of the results. A ceramic screen placed in the laser propagation direction collected the transmitted laser light. Two TPS, positioned at 0° and 45° measured the proton and ion spectra of the accelerated particle beam. For selected shots, a stack of calibrated RCFs was inserted 55 mm behind the target allowing for proton beam profile characterisation, absolute particle number calibration and complementary maximum energy detection. A scintillator-based beam profiler provided spatially resolved measurements for proton energies > 40 MeV.

5.6.2 Experimental results using the DRACO-PW laser

The maximum proton energies $\mathcal{E}_{m,p}$ and the amount of transmitted 1ω light ε_{trans} as a function of initial target thickness d are shown in Figure 5.10. When the PM is not applied, an optimum thickness is observed for $d_{opt} \approx 230$ nm. The target thickness dependency closely matches the J-KAREN-P experiment and also the maximum proton energies are comparable, albeit with a slightly higher maximum energy $\mathcal{E}_{m,p} \approx 70$ MeV which can be attributed to the slightly higher peak intensity of DRACO-PW. The thickness dependency of ε_{trans} is also similar to the previous observations at J-KAREN-P. While thicker targets have a low and almost unvarying amount of transmitted light, there is a rapid increase in transmission at $d \approx d_{opt}$. For decreasing target thicknesses, ε_{trans} continues to increase while $\mathcal{E}_{m,p}$ decreases. The agreement of these experimental key parameters indicates that the target was in a similar pre-expanded state as described for the J-KAREN-P experiments. The striking similarity of the results from two different laser facilities with similar temporal contrast implies robustness of the acceleration scheme.

In a next step, the PM was integrated to the setup, and the target thickness scan was repeated. Between 115 nm and 360 nm, a plateau-like region can be identified where almost no transmission occurs and $\mathcal{E}_{m,p} \approx 55$ MeV. As before, there is a region of optimal acceleration performance, where the proton energies reach their highest values $\mathcal{E}_{m,p} =$
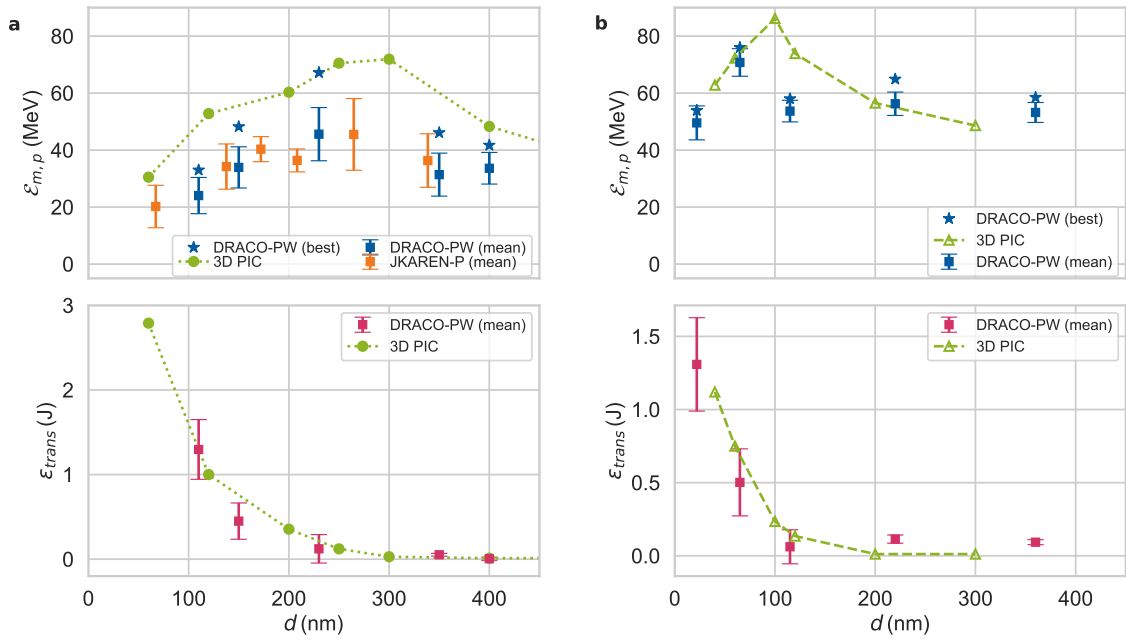
Figure 5.10: Experimental results studying pre-expansion influence. Maximum proton energy $\mathcal{E}_{m,p}$ (blue squares) and transmitted 1ω light ε_{trans} (red squares) for different target thicknesses d from experiments at DRACO-PW. The proton energy data from the J-KAREN-P experiment (orange squares) is included for comparison. The error bars represent the standard deviation of the plotted mean values, stars represent maximum values of $\mathcal{E}_{m,p}$. Green circles and triangles show reference $\mathcal{E}_{m,p}$ and ε_{trans} from 3D PIC simulations. Results for inherent and plasma mirror cleaned temporal contrast are shown in **a** and **b** respectively.

76 MeV and the amount of transmitted light slightly increases to $\approx 0.5\,$J. Compared to experiments without PM, the optimum thickness is reduced to $d_{opt} \approx 65\,$nm. Targets with $d < d_{opt}$ show significant amounts of transmitted light (up to $1.6\,$J $\simeq 9\,$% of input energy) and a reduction in $\mathcal{E}_{m,p}$.

5.6.3 Simulation results for modified temporal contrast

The influence of the preceding laser light on the simulation results of the key parameters (maximum energy of protons $\mathcal{E}_{m,p}$ and carbons $\mathcal{E}_{m,c}$ as well as the transmitted 1ω laser light energy ε_{trans}) is shown as a function of target thickness d in Figure 5.11a. Open circles represent data obtained from simulation including the preceding laser light, while triangles show the simulation results when the preceding light is ignored.

Simulations without preceding laser light started 50 fs before the peak of the pulse and used an unexpanded target density, i.e. omitting a hydrodynamic simulation. The remaining simulation procedures were consistent with those outlined in subsection 5.5.1. The simulations without preceding laser light show a significant reduction in optimum thickness to $\approx 100\,$nm, as well as a slight increase in $\mathcal{E}_m$ compared to the simulation where the preceding light is considered. Overlaying the simulation results with the experimental data reveals a clear agreement, as can be seen in Figure 5.10. This agreement demonstrates that the implementation of the PM confined the plasma dynamics to the last picosecond before the main pulse arrival. This result also aligns with the experimental observations in chapter 4.

The impact of the preceding laser light on the plasma density distribution is illustrated
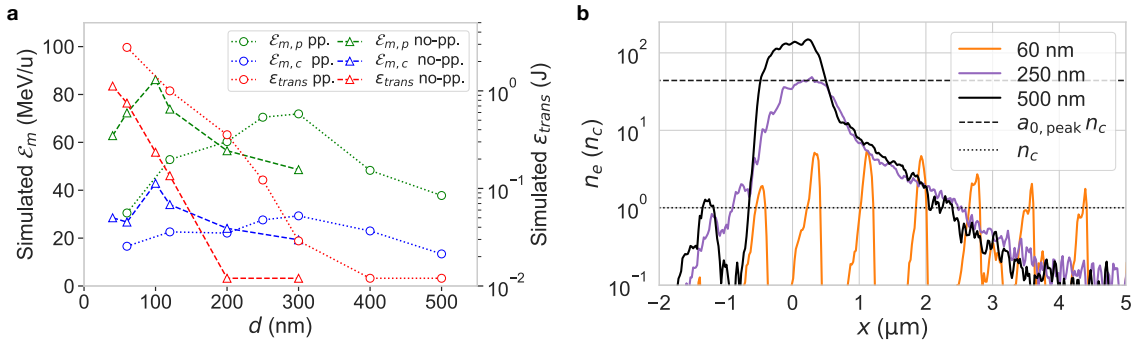
Figure 5.11: Modelling target pre-expansion. **a** Maximum carbon and proton energies $\mathcal{E}_m$ and transmitted laser energy ε_{trans} as a function of target thickness d from simulations including (dotted/circles) and excluding (dashed/triangles) the preceding laser light. Simulations without preceding laser light started 50 fs before the peak of the pulse. **b** Electron density n_e lineouts 35 fs before main pulse arrival for different target thicknesses and considering the preceding laser light. While for $d = 250$ nm and $d = 500$ nm n_e is still overcritical, the target gets transparent for $d = 60$ nm, resulting in electron bunching.

in Figure 5.11b, showing the simulated electron density from a lineout through the central axis of the target 35 fs before laser peak arrival for three initial target thicknesses. For the thickest target, $d = 500$ nm, although displaying a reduction in peak density and formation of significant scale lengths on the front and rear surface, the core density still greatly exceeds the roughly estimated relativistic critical density of the peak of the pulse $n_{cr} \approx a_{0,peak} n_c$, where $a_{0,peak}$ is the normalised vector potential at the peak of the pulse and assuming an electron $\gamma \approx a_0$ for $a_0 \gg 1$. The ensuing intense laser-plasma interaction is therefore with a fully opaque plasma. For $d = 250$ nm, although still opaque at this stage, the peak density is very well matched with the estimated n_{cr} at the peak of the pulse, implying a relativistically transparent interaction. However, for the thinnest target $d = 60$ nm, bunching at the laser frequency is observed even before the peak of the pulse. The target centre is already transparent, with time-averaged densities lower than the classical critical density. This demonstrates that a combination of adjusting the target thickness and utilising the preceding laser light provides a method to prime plasma for RIT.

Evidently, including the preceding laser light is essential to accurately model the target expansion of the experiment and to predict the target density distribution at the arrival of the main pulse. A detailed analysis of the simulations neglecting the preceding laser light shows similar plasma and field dynamics to the optimised pre-expanded target, which was described in subsection 5.5.2. This similarity can be seen in Figure 5.12, which shows the particle tracking results, and Figure 5.13, which shows the analysed 2D slices of the simulation for the optimal target thickness, assuming no target pre-expansion. Particle tracking of the most energetic carbons and protons reveals several similarities to the ion acceleration in the pre-expanded scenario (c.f. Figure 5.8). Figure 5.12a shows the time history of the kinetic energy of an exemplary proton and carbon ion, along with the cycle-averaged electric field driving the acceleration. The dominant acceleration contribution for both ion species are the strong space charge fields up to $\langle E \rangle \sim 60$ TV m^{-1} around the peak of the pulse. These space charge induced fields are significantly stronger than in the pre-expanded scenario. On the other hand, the influence of the sheath field later in the interaction is slightly lower, and the overall energy gain of the ions is dominated by the fields around the peak of the pulse. The waterfall plot in Figure 5.12b also underlines that the strongest $\langle E_x \rangle$ fields are generated shortly after the main pulse has hit the target
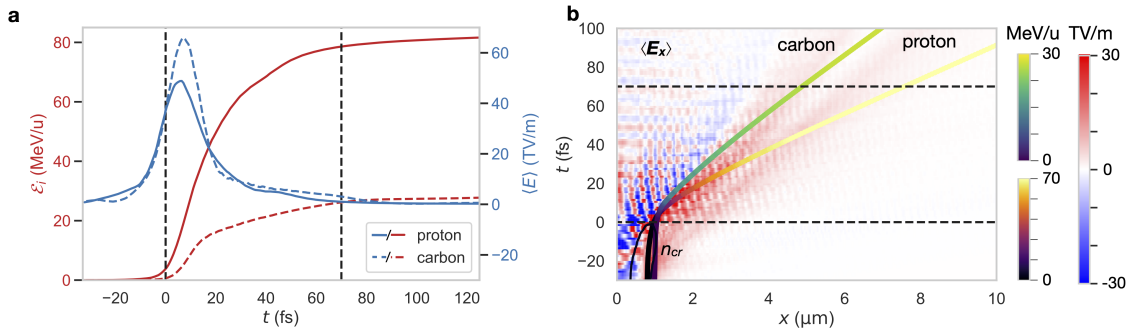
Figure 5.12: Particle tracking for simulations without preceding light. **a** Example of energy history (red) and local electric field (blue) $\langle E \rangle$ at the particle location for a typical energetic proton (solid lines) and carbon ion (dashed). **b** Time history of $\langle E_x \rangle$ in a lineout along x through the centre of the region of largest accelerating gradient, with the trajectory of the same proton and carbon ion overlaid. The black line shows the relativistically critical contour.

and RIT occurred. Notably, the position of the sheath field is shifted for such ultrathin targets, making it difficult to distinguish between the different acceleration components. The electron density contours show again, that electrons in the centre of the target have been heated and expanded such that $n_c < n_e < n_{cr}$, and that the laser has started to penetrate the target. Similarly, the volumetric interaction between laser and electrons leads to a strong space charge in the transparent region highlighted by the green box. The magnitude of the time-averaged space charge can reach $\langle \rho \rangle > 10\,e\,n_c$, resulting in a region of large cycle-averaged quasi-static electric field $\langle E_x \rangle \sim 50\,\text{TV m}^{-1}$ (c.f. inset in Figure 5.13a). Eventually, this space charge field is even higher than in the expanded target scenario. Protons have started to separate from the more abundant carbon ions due to their higher charge-to-mass ratio. However, both species are still present in the region of strong $\langle E_x \rangle$.

Figure 5.13b shows the same 2D slice 70 fs after the most intense part of the laser pulse has passed. Ion acceleration still continues at this point in a thermal sheath field, with significantly lower electric fields. The absolute field strength and the energy gain contribution of the thermal sheath field contribution is in the unexpanded case clearly lower than previously discussed (c.f. subsection 5.5.2). Complete ion species separation becomes prominent due to the faster velocity of the protons and the bunching of the two particle species results in two distinct sheath fields around each species, with $\langle E_x \rangle < 10\,\text{TV m}^{-1}$.

5.7 Conclusions

The results of this chapter demonstrate that relativistic transparency occurring at the peak of an ultrashort laser pulse is strikingly beneficial for plasma-based ion acceleration. This is similar to what has been observed at experiments using glass lasers with lower intensity and longer pulse durations, where volumetric laser heating [130] or hybrid RPA-TNSA [139] results in higher ion energies. All these scenarios share similar experimental phenomenology, including measurable laser transmission through the target and highest ion energies when target transparency is timed to the peak of the pulse. The novel aspect of this study lies in the ultrashort laser pulse duration and that the highest accelerating gradients arise from significantly higher space charge fields resulting from electron expulsion from the relativistically transparent target core.

The RIT-enhanced acceleration mechanism described in this chapter represents a
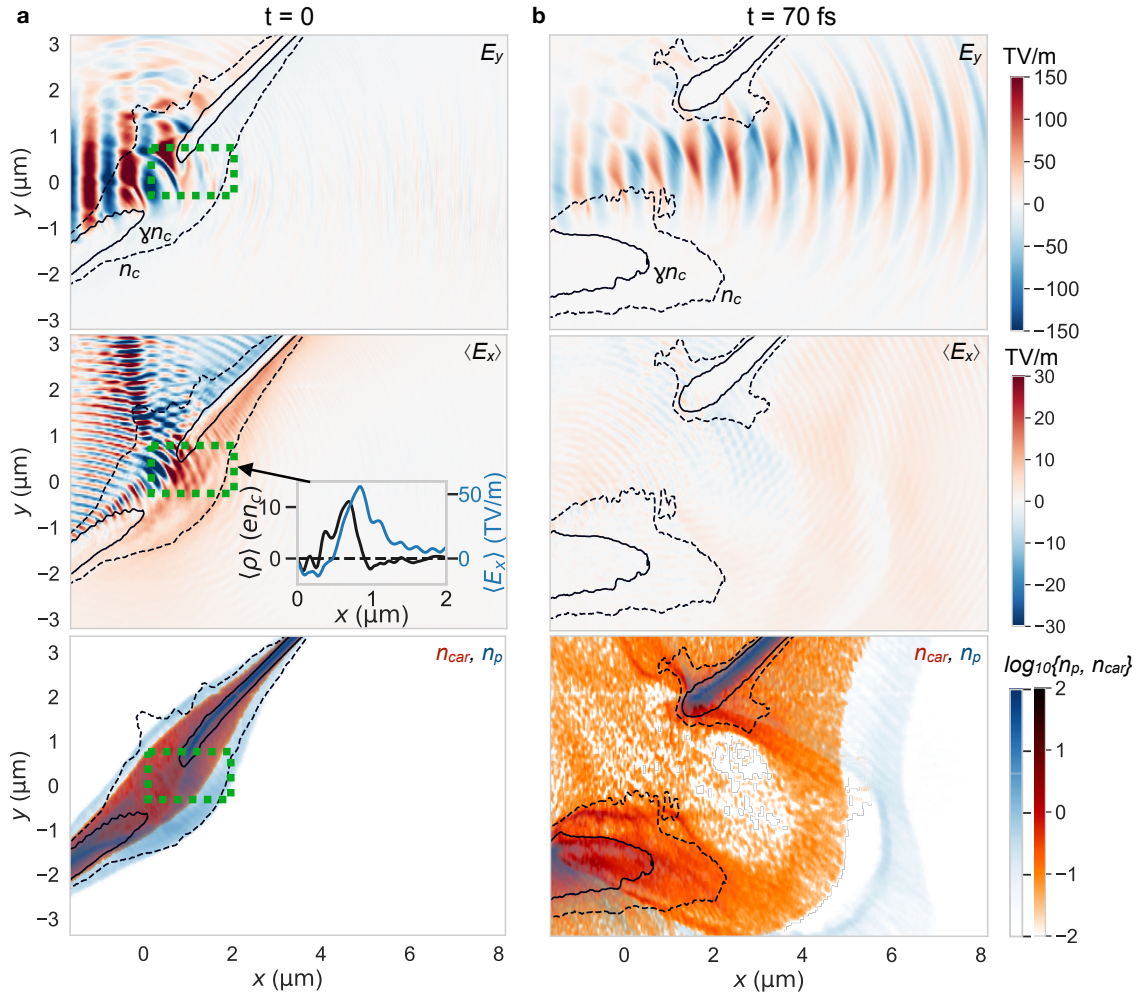
Figure 5.13: Plasma density from 3D PIC simulations for unexpanded target. a E_y, $\langle E_x \rangle$ and carbon/proton density (n_{car}, n_p normalised to n_c) for a 2D slice at $z = 0$ for a 65 nm target at $t = 0$, when the peak of the pulse arrives. The solid (dashed) contours give the relativistic (classical) critical electron density. The region of strong electron expulsion is highlighted by the green box. The inset shows the cycle-averaged space charge density $\langle \rho \rangle$ and $\langle E_x \rangle$ for a lineout through the centre of the green box, averaging over $\Delta y = 400$ nm. b The same 2D slices shown at $t = 70$ fs, at the end of the main pulse interaction.

promising avenue for application-oriented ion acceleration to high energies. In contrast to recent efforts utilising single- or double-stage plasma mirrors to enhance the temporal contrast, the results of this chapter demonstrate how the preceding laser light can be used to prime the target for transparency upon main pulse arrival. This not only significantly reduced the complexity, size and cost of the ion source but also removed one of the limits to continuous high repetition rate operation. The required target thickness, a few hundred nanometres, improves robustness compared to ultrathin ($d \sim 10\,\mathrm{nm}$) or specially designed near-critical density targets required for light sail acceleration at the same intensity range, which are easily damaged during handling, pump down or by preceding shots on the target system.

The investigations on different preceding laser light conditions revealed that the temporal intensity contrast of the laser is the most important factor for determining the optimal target thickness for this regime. The laser contrast determines the target density at the peak of the pulse for a given target thickness, whereas the laser peak intensity determines the density required for RIT.

In summary, this chapter investigated ion acceleration from the interaction of ultrashort laser pulses with thin plastic foils and identified an optimal target thickness for acceleration of protons and carbon ions in the RIT regime to energies $> 60\,\mathrm{MeV}$ and $> 30\,\mathrm{MeV}\,\mathrm{u}^{-1}$, respectively. The preceding laser light was found to play an essential role in priming the plasma density for the onset of relativistic transparency upon arrival of the main pulse. Using a laser with enhanced temporal contrast reduced the optimal target thickness and slightly improved the maximum proton energies. The highest energetic ions were accelerated by strong space charge fields generated by expulsion of electrons during RIT, followed by a further energy gain in an ambient sheath field.

The reproduction of the experimental results at two different laser facilities underlines the robustness of the acceleration regime, and a comprehensive understanding and control of the laser and target parameters. The fact that plasma mirrors and ultrathin nanometre scale targets are not required for high-energy ion acceleration implies that this acceleration scheme is suitable for already existing high-power lasers delivering ultrashort pulses. This conceptual breakthrough establishes a path towards the development of $\sim 100\,\mathrm{MeV}$ class repetitive ion sources using currently available laser technology.

6 Ion acceleration beyond the 100 MeV frontier from cascading acceleration schemes

This chapter reports on experimental and simulation results of proton acceleration from thin plastic targets, reaching kinetic energies beyond 100 MeV. This study was conducted as a follow-up to the experimental results described in chapter 5. Based on these findings, the initial target thickness was chosen to ensure the interaction of the laser main pulse with a near critical target, due to the pre-expansion of the target early in the interaction. The experimental setup was further optimised to allow angularly resolved high-energy protons to be measured simultaneously with multiple detectors based on different detection methods.

The results demonstrate the capability of laser-driven plasma accelerators to generate proton beams with a spectrally separated high-energy component, reaching maximum energies up to 150 MeV. Target transparency was identified as a simple control parameter for determining the high-performance domain, showing sensitivity to subtle changes in the initial laser-target conditions. Simulations considering the complete interaction, from the picosecond-long pre-expansion of the target to the proton acceleration during the high-intensity laser pulse, reveal that multiple known acceleration regimes cascade efficiently at the onset of **Relativistically Induced Transparency (RIT)**. The ultrashort pulse duration facilitates a rapid succession of these regimes at highest intensity, leading to the observed beam parameters and enabling proton acceleration to unprecedented energy levels. The results of this chapter led to the publication of TZ1.

6.1 Introduction

A central emphasis within the research field of laser-driven ion acceleration is to increase the achievable proton energies, in particular to exceed the 100 MeV frontier. Historically, record-breaking proton energies have been achieved primarily with large-scale, high-energy laser systems, irradiating micrometer-thick foil targets [4, 139, 316, 348]. Ion acceleration was thereby achieved through the **Target Normal Sheath Acceleration (TNSA)** mechanism, wherein laser energy is converted into hot electrons that initiate a plasma expansion process (detailed in subsection 2.3.1). The effectiveness of this mechanism is primarily enhanced by increasing the laser energy coupled into the plasma [18]. High-energy laser systems are capable to produce laser pulses with hun-

dreds of joules energy, but are limited by their repetition rate of a few shots per day. Furthermore, the constrained access and availability of these facilities and laser systems, make it almost impossible to translate laser-driven ion beams towards applications.

Advanced acceleration mechanisms are conceptually different to TNSA and drive ions in a more coherent manner with a more favourable scaling with laser energy (detailed in subsection 2.3.2 and subsection 2.3.3). Such advanced concepts enabled compact high-intensity laser systems with ultrashort pulses and significantly reduced laser pulse energies of a few joules, to achieve comparable acceleration performance levels [28, 29, 127, 349]. These laser systems also posses the capability to operate at relatively high repetition rates (> 1 Hz), an important prerequisite for practical applications and for conducting studies that rely on statistical methods.

In the past, numerous advanced acceleration mechanisms have been explored and refined through numerical simulations under idealised conditions. However, transferring these theoretical concepts to practical experimental conditions has posed considerable challenges to the field. The scarcity of experimental data for isolated advanced mechanisms reflects this fact. Furthermore, the coexistence of multiple acceleration mechanisms under typical experimental conditions can lead to ambiguous signatures. Identifying the optimal combination of mechanisms to efficiently exploit the laser-induced acceleration fields is therefore an important, albeit complex, endeavour.

Previous research has shown that plasma acceleration is enhanced when the laser main pulse arrival coincides with the onset of target transparency, allowing multiple acceleration regimes to take place [103, 130, 133, 146, 153, 157]. This approach further promises to optimise the parameters of the accelerated particle, including energy and directionality. The recent accomplishment of near-100 MeV proton energies by a transparency-enhanced hybrid RPA-TNSA scheme illustrates this high potential [139]. The point at which the initially opaque target becomes transparent to the laser is termed onset of relativistic transparency [169], occurring when the plasma frequency drops below the laser frequency due to the relativistic mass increase of the electrons (detailed in subsection 2.1.3).

Experiments typically use laser pulses with non-perfect temporal contrast, causing the solid-density foil targets to expand due to laser light that precedes the main laser pulse. Consequently, the core density of the target may approach the onset of RIT upon main pulse arrival. Experimental studies investigating plasma acceleration at the onset of RIT require the determination of the optimal initial target thickness according to the specific interaction parameters of the laser system used. To achieve this, the initial target thickness was varied over a wide range and the acceleration performance was compared to numerical simulations. An optimum target thickness between 200 nm and 300 nm was found, where the expulsion of electrons from the bulk of the target resulted in extremely localised space charge fields. These findings, discussed in detail in the previous chapter 5, provide the basis for both the experimental setup and the subsequent analysis described in this chapter.

6.2 Experimental setup

This experiment was performed employing the DRACO-PW laser at HZDR. A detailed description and core parameters of the DRACO-PW laser system can be found in subsection 3.1.3. Laser pulses with p-polarisation, ≈ 30 fs FWHM pulse duration and a maximum laser energy of 22.4 J were sent to the experimental area. Figure 6.1 illustrates the experimental setup. Laser pulses from the DRACO-PW system were focused by an f / 2.3 off-axis parabola (90°) to an FWHM spotsize of $\approx 2.1\,\mu$m, containing 32 % of the total laser energy after compression. The achievable peak intensity on target for this experi-
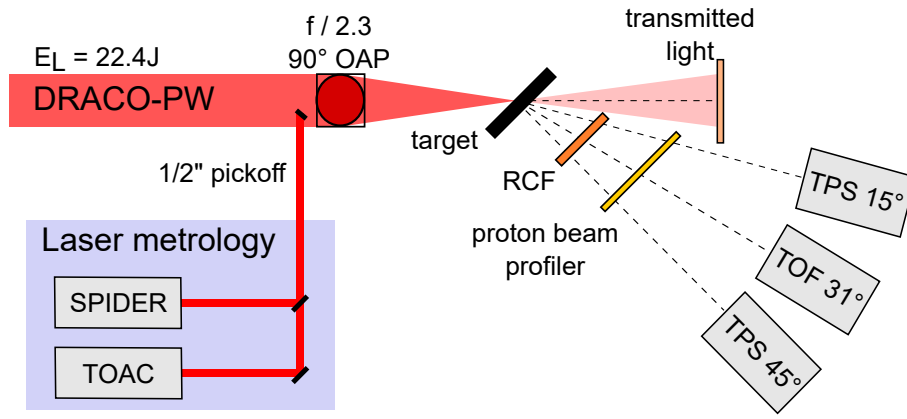
Figure 6.1: Illustration of the experimental setup. Laser pulses are focused by an f/2.3 off-axis parabola (OAP) onto thin plastic foil targets, thereby generating a plasma. The kinetic energy distribution of the ions was measured by two Thomson parabola spectrometers (TPS15 and TPS45 positioned at 15° and 45° with respect to the laser propagation direction) and a time-of-flight detector (TOF31 positioned at 31°). The spatial distribution of protons was characterised either by an imaged scintillator screen (proton beam profiler) or by a radio-chromic film (RCF) stack. A ceramic screen in laser propagation direction collected the transmitted laser light. The temporal intensity distribution of the laser pulse was measured before the shots by a scanning TOAC and on a single-shot basis during the experiment using a SPIDER detector.

ment was $\approx 6.5 \times 10^{21}$ W cm^2. The temporal intensity distribution of the laser pulse was measured before the shots by a scanning TOAC and on a single-shot basis during the experiment using a SPIDER detector (details in subsubsection 3.4.2).

The laser pulses were directed onto plastic foils of 250 nm $\pm$ 25 nm thickness at an incidence angle of 50°. The oblique incident ensured a clear distinction between acceleration components directed along the target-normal axis (i.e. TNSA) and along the laser propagation direction (advanced schemes, e.g. RPA and others).

A combination of multiple detectors based on different detection principles was used to characterise the generated particle beam and to provide robust and reliable measurements of the maximum particle energy. Details about the different detection methods can be found in section 3.5.

Two **Thomson Parabola Spectrometers (TPS)**, positioned at 15° (TPS15) and 45° (TPS45) with respect to the laser propagation direction (0°), enabled the analysis of particle spectra with high energy resolution. The minimal detectable proton energy of the TPS was 7 MeV and the energy resolution was dominated by the corresponding pinhole size (TPS15: 1 mm, TPS45: 0.3 mm), resulting in an uncertainty better than $\pm 4\,\%|\pm 10\,\%$ for a maximum proton energy of 60 MeV | 150 MeV, respectively.

Another particle detection method was realised by **Time-Of-Flight (TOF)** measurements. Therefore a high sensitivity avalanche photodetector was placed at a distance of 4 m from the target at an angle of 31° with respect to the laser propagation direction. Carbons and heavier ions were blocked by a 2 mm thick copper plate just in front of the diode (threshold: 34 MeV for protons, 64 MeV u^{-1} for carbons). Signal read-out was provided by a fast oscilloscope (6 GHz, 25 GSamples s^{-1}). The ability of the implemented TOF setup to provide detailed information about particle numbers is limited by its restricted acceptance angle. Nevertheless, the TOF remains a suitable detector for validating the maximum energy level of the accelerated protons.

A scintillator-based beam profiler, equipped with absorbers of varying thicknesses, enabled a spatially resolved measurements of the accelerated proton beam at specific threshold energies. Similar to the TOF, the proton beam profiler is suited to detect par-

ticles of a certain energy level in a specific direction. For selected shots a **RadioChromic Film (RCF)** stack was placed 55 mm behind the target, blocking all other particle diagnostics. Gafchromic EBT3 (size: 100 mm × 50 mm, dose range: 0.1 Gy to 20 Gy) films interleaved with copper plates as absorber material were used. These copper layers were analysed by a high-purity germanium spectrometer (GR4020 from Canberra) after the experiment, to detect isotopes originating from proton-neutron reactions.

The transmitted laser light was collected by a ceramic screen, that was imaged onto a previously calibrated camera to enable absolute measurements.

6.3 Experimental results

The following section presents results obtained from the experimental campaign carried out at the DRACO-PW laser system, using the setup outlined in the previous section. The analysis concentrates on shots executed on comparable targets without intentional variations in the laser parameters. The resulting changes in the ion acceleration performance, the acceleration direction and the correlation to the transmitted light are discussed.

6.3.1 Analysis of acceleration performance

Figure 6.2 shows the measured maximum proton energy as a function of initial target thickness (left) and transmitted laser light (right) for the different particle detectors (TPS15, TOF31 and TPS45). Each data point represents the maximum proton energy of an individual shot. The error bars denote the systematic uncertainties in target thickness, transmitted light and maximum energy determination, respectively.

The highest maximum proton energy measured in this study is $150\,\mathrm{MeV}^{+15}_{-11}\,\mathrm{MeV}$ at 15°, $101\,\mathrm{MeV} \pm 5\,\mathrm{MeV}$ at 31° and $63\,\mathrm{MeV} \pm 3\,\mathrm{MeV}$ at 45°. While there appears to be no influence on the initial target thickness, the data clearly demonstrates a correlation between the maximum energy and the transmitted light. The best acceleration performance across all spatial directions is achieved for transmission values in the range of 0.5 % to 3 %. These values are consistent to the results of chapter 5, where best acceleration performance and the onset of RIT was identified at similar values of transmitted laser light and target thickness. Higher or lower amounts of transmitted light result in weaker acceleration performance. Shots with transmission values exceeding 5 % show strongly reduced acceleration performance, leading to maximum proton energies of less than 20 MeV in both TPS axes. The threshold energy of the TOF detector was 34 MeV, rendering this detector unsuitable for a quantitative analysis of the minimal proton energies. The observed fluctuations in the maximum proton energy and the amount of transmitted light can be attributed to shot-to-shot fluctuations of the detailed laser-plasma parameters during the entire interaction process. Particularly in tight focusing experiments with ultrathin foils (like this study), even small differences in the spatial and temporal intensity distribution can lead to significant differences in the target pre-expansion dynamics, laser absorption and plasma-heating processes.

Figure 6.3 shows TPS15 readout images (background subtraction applied) for the five most energetic shots on the left, and the analysed particle spectra for the corresponding shots on the right. The most notable observation is the spectral constriction of the separated high-energy component in the proton traces of the TPS15 spectra, featuring a low-energy (< 40 MeV) exponential and a separated high-energy (≥ 100 MeV) component. The TPS45 spectra consistently exhibit an exponentially decaying component
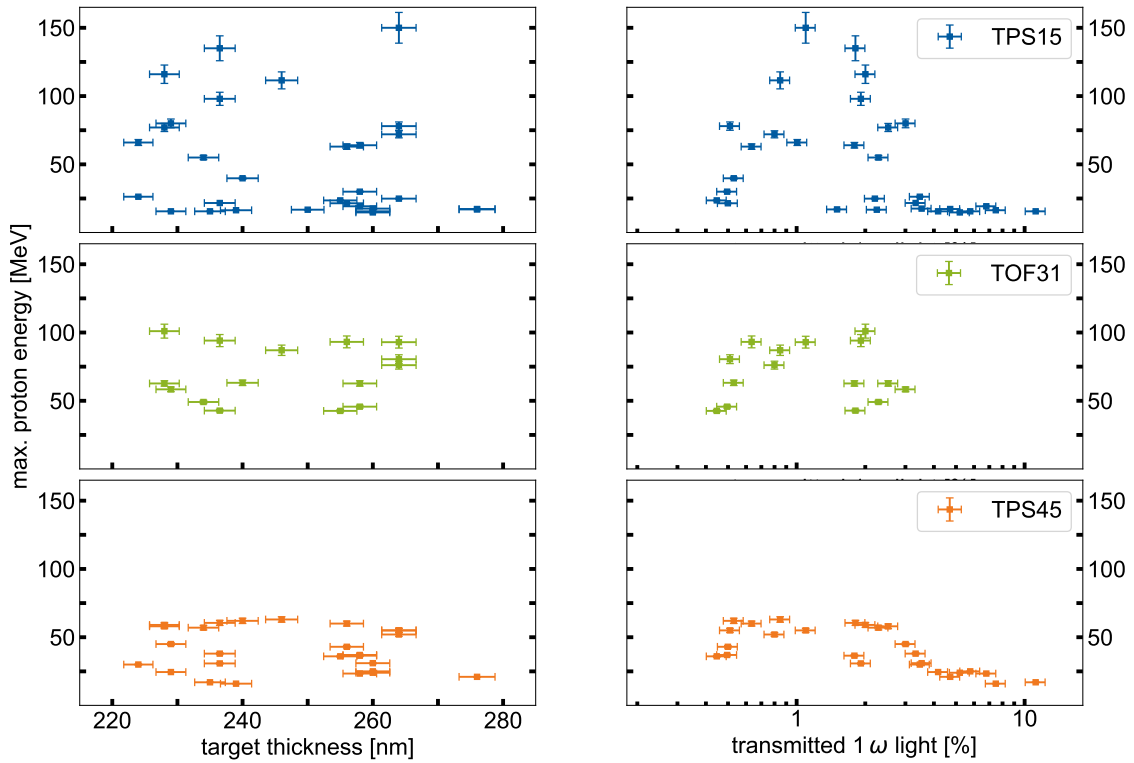
Figure 6.2: **Proton acceleration performance.** Maximum proton energy as a function of initial target thickness (left) and transmitted 1ω light (right). Each data point represents an individual shot. Error bars indicate the precision of the target thickness, and energy determination, respectively. The initial target thickness and the maximum proton energies show no correlation, while sorting the data by transmitted light reveals a clear optimum in acceleration performance.
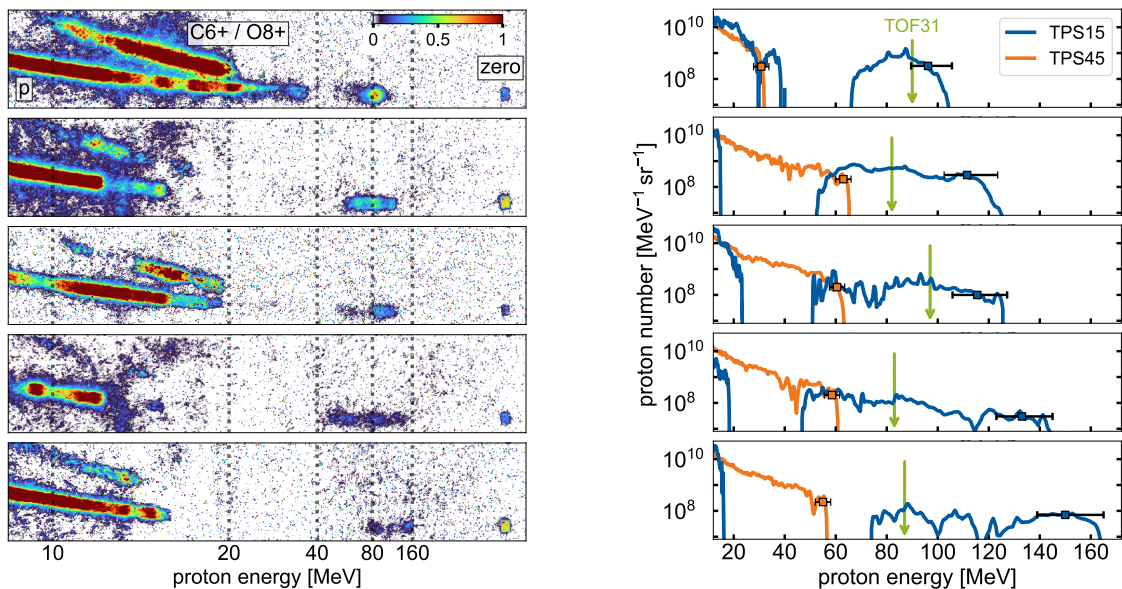
Figure 6.3: **Proton energy spectra. Left:** Background substracted and normalised TPS15 raw images, showing the zero deflection axis (zero) and parabolic traces from protons (p) and ions (C6+ / O8+) for the five most energetic shots (#1 – #5). **Right:** TPS15 and TPS45 particle spectra (solid lines) and maximum energies (squares). Errorbars indicate the energy uncertainty, defined by the projected pinhole size. The green arrow displays the maximum energy measured by the TOF in the 31° direction.

only. TOF measurements with reduced sensitivity at 31° show proton energies exceeding those measured by the TPS45, yet remaining below those observed by the TPS15.

6.3.2 Spatial proton beam profile

The analysis of the proton beam profiler and the RCF stacks provides valuable insights into the distribution and concentration of proton energies across different spatial directions.

Figure 6.4 shows images of the segmented proton beam profiler for multiple shots, including the high-energy shots of Figure 6.3 (labelled #1 – #5). The upper and the lower
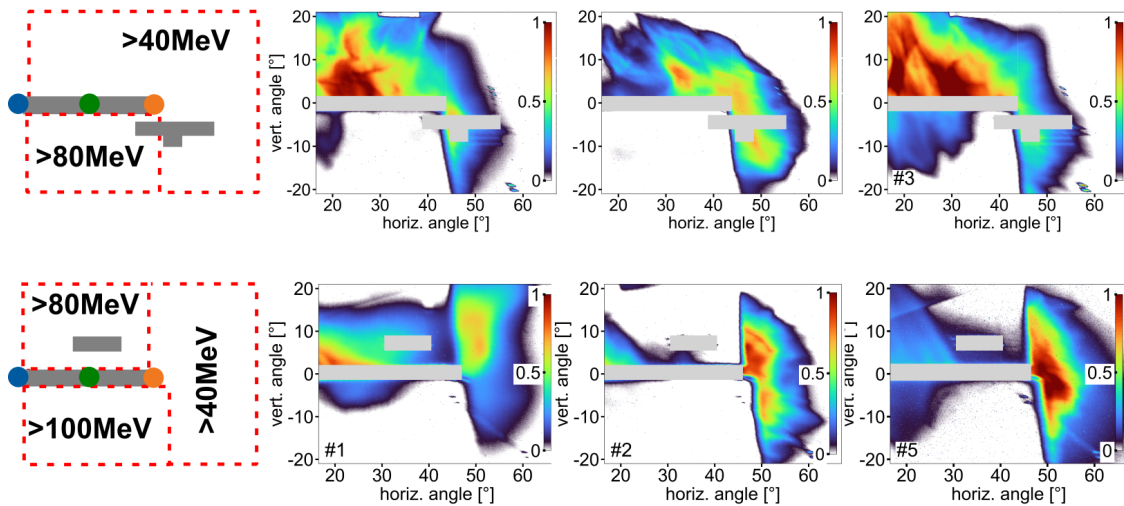

Figure 6.4: **Spatial proton beam profile:** Results from proton beam profiler measurements for two different absorber configurations (sketched on the left) with spatially varying threshold energies (40 MeV, 80 MeV and 100 MeV respectively). The acceleration direction of high energetic protons is shifted towards the laser propagation direction, while lower energetic protons are detected predominantly in target normal direction. The spectrometer axes are indicated by coloured circles (TPS15-blue, TOF31-green, TPS45-orange), grey areas indicate parts without data.

row represent different absorber configurations, as illustrated by the sketch on the left side of the figure. All presented shots show signal behind the 40 MeV threshold energy absorber. The beam profile has a ring-like intensity distribution, gradually decreasing from the inner to the outer regions, with a divergence of about ±15 degrees in the vertical plane. The absorber configuration in the top row allows to study the upper half of the particle beam with the same threshold energy, indicating that the most intense part of the particle beam is not aligned with the target normal direction, but instead shifted towards the laser propagation direction. The entire beam profile could not be captured by the profiler screen as the divergence of the particle beam in the horizontal plane is significantly higher than in the vertical plane. However, the geometry and design of the proton beam profiler allowed for a parallel operation with the TPS and TOF detectors. These particle detectors revealed the highest energies at 15° (c.f. subsection 6.3.1), which is just at the edge of the proton beam profiler. Signal behind the 80 MeV and 100 MeV threshold energy absorbers of the profiler, as shown in the lower row for three of most energetic shots (#1, #2 and #5), is only measured between the edge of the profiler at 14.5° and 30°. This observation is consistent with the results from the TPS measurements.

Figure 6.5 presents the results of two analysed RCF stacks (labelled 21CD and 21CE),

serving as representative examples for the observed high-performance shots. The an-
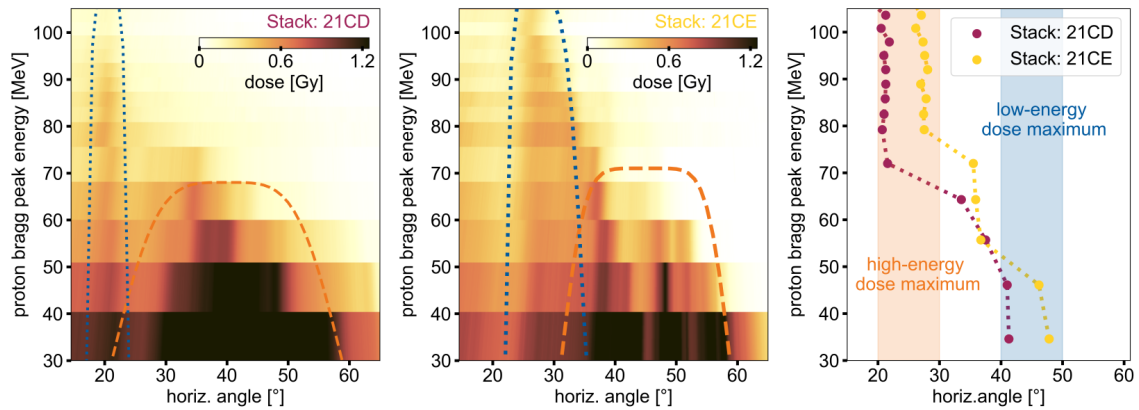
Figure 6.5: RCF results: Angular dose distribution for two representative high energy shots (labelled 21CD and 21CE). The right plot shows the horizontal angle under which the maximum dose on each energy layer of the two stacks was measured. For lower proton energies the dose maximum is in target normal direction, while for higher energies the dose maximum shift towards the laser propagation direction.

gular dose distribution was derived from lineouts along the horizontal axis covering a vertical angle of $6.5°$ for each energy layer of the corresponding stack. Notably, the dose maximum of the 35 MeV - 60 MeV layers of the two stacks are centred along $45°$ with a divergence of approximately $\pm 15°$. Layers for proton energies above 60 MeV show almost no dose in this direction. In contrast, the detected dose between $20°$ and $30°$ is characterised by a significantly reduced divergence ($\pm 3°$) and persists in both stacks until the last available layer at 104 MeV. This shift of the maximum dose of the proton beam from the target normal (low-energy component) towards the laser propagation direction (high-energy component), is shown in the right part of Figure 6.5. The results also show, that the emission direction of the high-energy dose component (blue dotted line) varied by $10°$ just between these two shots.

The results of the proton beam profiler and the RCF stacks confirm the energy level of the TPS measurements and that the accelerated particle beam comprises a medium-energy (< 70 MeV) broadband component in target normal direction and a spectrally and angularly separated high-energy component with reduced divergence.

6.3.3 Nuclear activation measurement

To increase the reliability of the measured high proton energies and to validate the particle species detected by the RCF, nuclear activation measurements (as introduced in subsection 3.5.5) were performed. Following the completion of the shots, the RCF stacks were extracted from the experimental setup. Due to time limitations of this detection method, only a subset of copper layers within each RCF stack was scanned using a high-purity germanium spectrometer. The layers were selected in such a way that there was still a clearly visible signal on the subsequent RCF of the stack.

As an example, the analysed copper absorber corresponding to 72 MeV Bragg peak energy of RCF stack 21CE is shown in Figure 6.6. The energy spectrum of the gamma ray measurement revealed the characteristic emission lines at 548.4 keV + 596.6 keV and 669.6 keV + 962.2 keV associated with the ^{62}Zn and ^{63}Zn isotopes, respectively. These isotopes originate from proton neutron reactions inside the copper absorber, requiring a minimal proton energy of 13.5 MeV and 4.2 MeV, respectively. The decay time of these
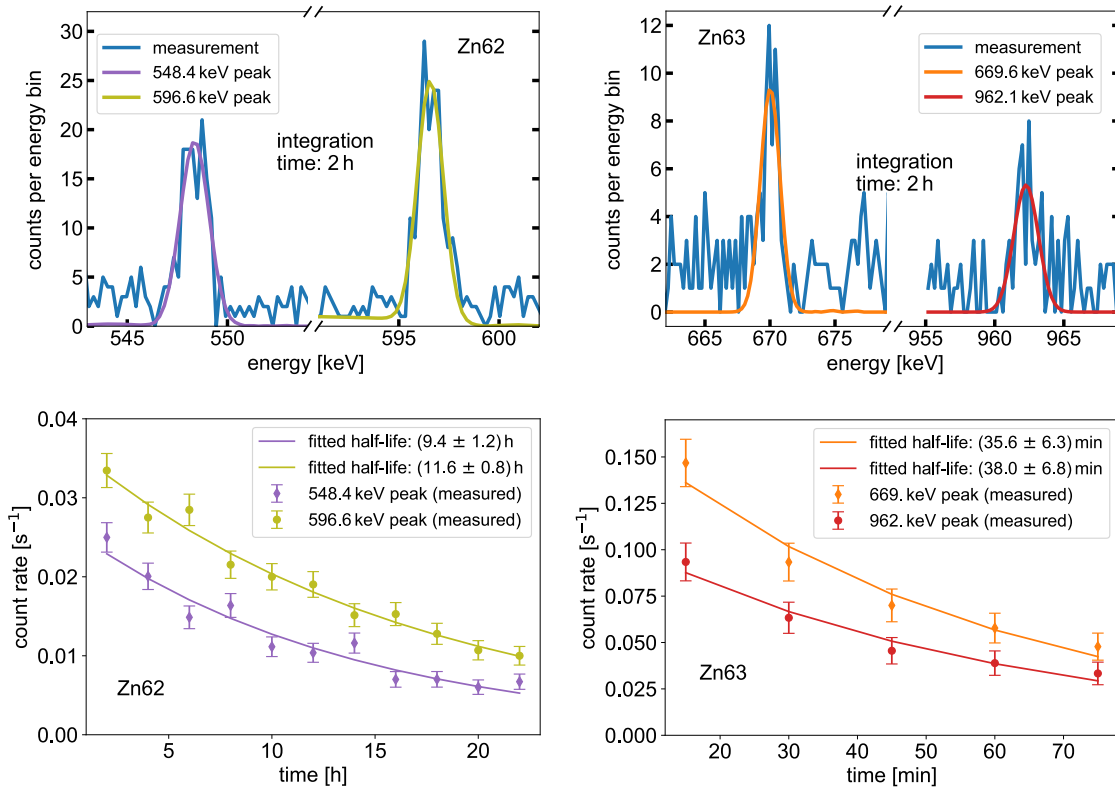
Figure 6.6: **Results of activation analysis:** Gamma-ray decay spectrum of a copper absorber of Stack 21 CE measured by the germanium spectrometer after an integration time of 2 h and 0.25 h respectively (upper row). The lower row shows the gamma-ray decay of the same absorber over time. The markers represent the measured data and the solid line the result of an exponential fit. The analysis was done for the two prominent ^{62}Zn and ^{63}Zn isotopes (left and right).

peaks provides further evidence, that the measured gamma emissions stem from ^{62}Zn and ^{63}Zn isotopes. These results indicate, that the reactions in the copper absorber are induced by protons with kinetic energies > 72 MeV and that the observed signal on the corresponding RCF layer originates from protons.

6.3.4 Scaling of maximum proton energy

Figure 6.7 shows on the left the scaling of the maximum proton energy of the best performance shot for different laser pulse energies. A striking difference emerges for the
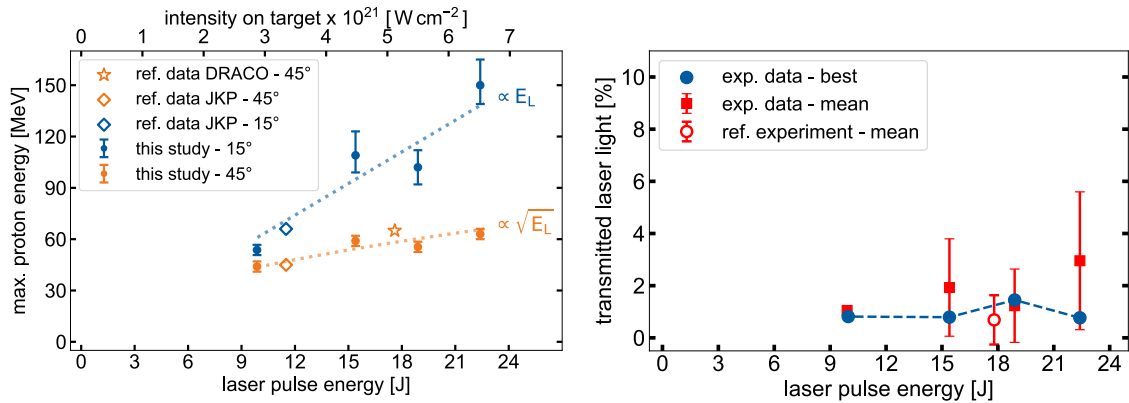
Figure 6.7: Scaling of best performance shots: **Left:** Maximum proton energies measured by TPS15 and TPS45 for different laser pulse energies E_L. The dotted lines represent different proton energy scalings (linear and square-root) for better trend visualisation. **Right:** Transmitted laser light for the best shots, i.e. highest proton energies for different laser pulse energies E_L.

two surveyed directions within the investigated range of laser energy. The maximum proton energies at 15° scale much faster with laser pulse energy than at 45°, indicating a fundamental change in the underlying acceleration scheme for the different directions. The energies at 15° reveal an almost linear relation to the laser pulse energy, while the maximum proton energies at 45° follow a square-root fit. The results from the previous experiments (c.f. chapter 5) at the DRACO PW laser (ref. data DRACO [26], orange star) and the J KAREN P laser (ref. data JKP [26], orange and blue diamond) with reduced laser energy are overlaid with the results of this study in the left plot of Figure 6.7.

For all realised laser energy settings, best acceleration performance in 15° and 45° is consistently achieved between 0.5 % and 2.7 % of transmitted laser light, as can be seen on the right of Figure 6.7. The blue dots represent the transmitted laser light for the best performing shot at a given laser energy, the error bars represent the standard deviation of the plotted mean values (red boxes). The dataset clearly shows that the initial laser pulse energy does not effect the relative amount of transmitted light, affirming that this parameter is suited for identifying the optimal performance regime across varying laser conditions.

6.4 Numerical simulations

To investigate the microscopic physics for the present laser and target parameters of the experiment, a combination of 2D hydrodynamic and 3D **Particle-In-Cell (PIC)** simulations were performed. The following section presents the results of these simulations and discusses their agreement to the experimental data. A comprehensive presentation of

all simulation details as well as further analysis and investigations are part of a separate doctoral thesis [336].

6.4.1 Simulation setup

The influence of the preceding laser light on plastic foil target of 270 nm thickness and the resulting expansion was simulated using the FLASH code (v4.6.2) [345] in a 2D radially symmetric geometry with adaptive mesh refinement. The FLASH simulation started 100 ps before the laser main pulse, when **Laser-Induced Breakdown (LIB)** is known to occur, up to 1 ps before the laser main pulse arrival. The onset of LIB was derived using the measured temporal laser contrast and optical probing studies as described in the previous chapter and in reference [342]. The FLASH simulation used an experimentally measured temporal intensity profile of the laser (c.f. Figure 3.5), sampled with 256 individual points for the simulation.

The final high-intensity interaction was modelled using the fully relativistic PIC code PIConGPU [350, 351]. The PIC simulation covered the time range from 1 ps before the main laser pulse reached the target until 220 fs after main pulse arrival. The simulation box had a total size of 40 μm × 54 μm × 20 μm and each simulation cell a dimension of 20 nm × 20 nm × 20 nm. The density profile resulting from the 2D hydrodynamic simulation was rotated around its axis of symmetry and used as initial input for the 3D PIC simulation. Densities below $0.04\,n_c$ were discarded to minimise the computational time of the simulation. Each cell was initialised with one carbon and eight hydrogen macroparticles (thus, 13 electrons in total), weighted according to the obtained density profile. The p-polarised laser was focused to a Gaussian spot ($w_0 = 2.14\,\mu m$) on the front surface of the target. The target was positioned at oblique incidence (45°) so that the laser hit the centre of the initially unexpanded foil. The temporal intensity profile was matched to the measured data (c.f. subsubsection 3.1.3) by fitting two exponential ramps and a Gaussian pulse (30 fs FWHM duration) with a peak intensity of $a_0 \simeq 50$. The simulation was performed on the JUWELS Booster cluster at Forschungszentrum Jülich [352] using 900 A100-GPU's for 35000 timesteps.

6.4.2 Simulation results & discussion

The angular proton emission distribution in the horizontal plane at the end of the simulation is shown in Figure 6.8b. Highest proton energies and spectral modulations are observed in laser propagation direction, while protons in target normal direction show lower energies and an exponentially decaying spectrum. This behaviour is illustrated in Figure 6.8a, showing the extracted particle spectra along the different directions that exhibit a remarkable similarity to the experimental spectra in Figure 6.3. To gain deeper insights into the acceleration dynamics during the laser-plasma interaction, a subset of tracer protons was randomly selected upon initialisation. The trajectories of these protons were recorded and analysed to understand their individual acceleration based on the respective plasma density and electric field at their position at each simulation time step.

When the relativistic laser pulse penetrates into the expanded plasma, it gets reflected near the front of the relativistic critical density $n_{cr} = \gamma\,n_c$. γ is the electron Lorentz factor and n_c the classical critical density, which is defined as $n_c = \varepsilon_0\,m_e\,\omega_L^2\,/\,e^2$, with vacuum permittivity ε_0, electron mass m_e, angular laser frequency ω_L and electron charge e. Electrons at n_{cr} are pushed into the target, thereby creating a charge separation field. This field triggers different **Radiation Pressure Acceleration (RPA)** mechanisms such as hole-
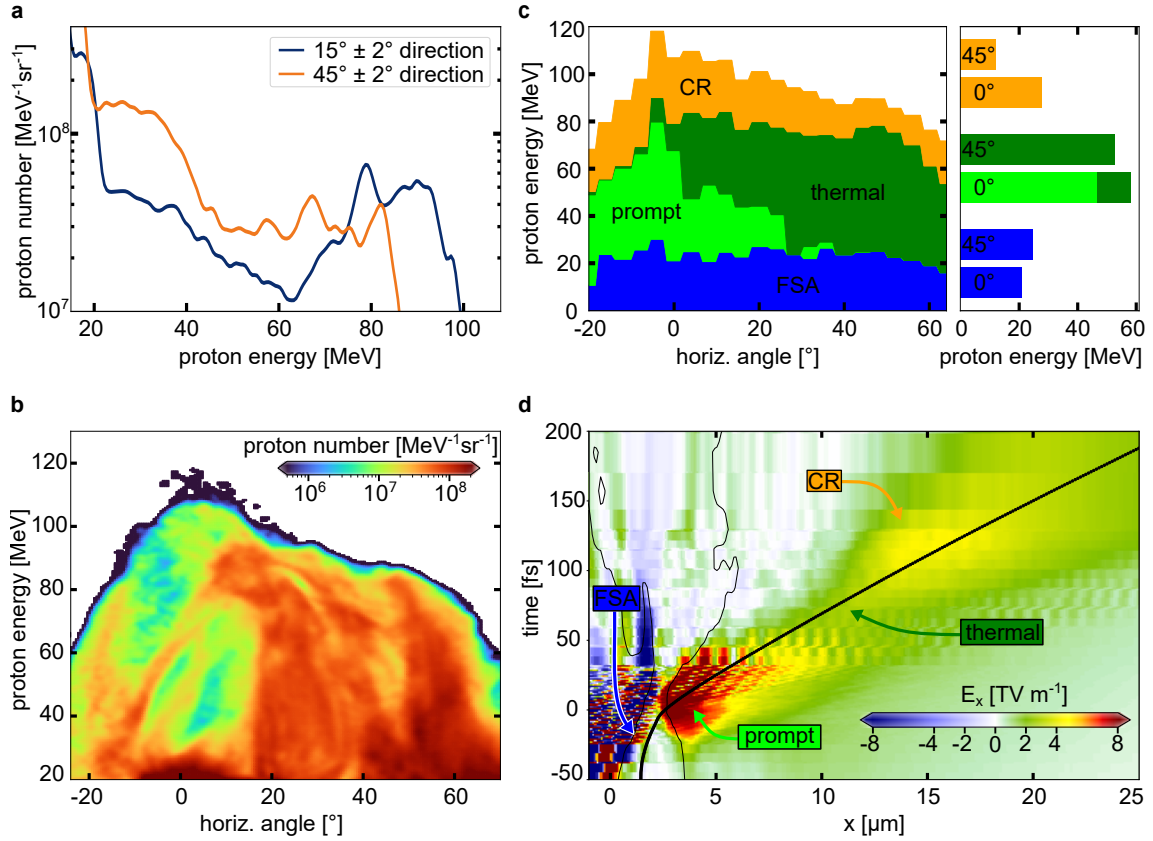
Figure 6.8: Simulation results revealing multiple acceleration contributions in different directions. **a** Proton energy spectra extracted from 3D PIC simulation for different spatial directions. **b** Simulation results of proton emission distribution. Only protons in the central slice of ±1 μm around the symmetry plane within a vertical emission range of ±3° are shown. **c** Angularly resolved contribution of different mechanisms to the acceleration cascade of the fastest protons (CR: Coulomb repulsion, thermal: diffuse sheath field set up by thermal and recirculating electrons, prompt: $j \times B$ accelerated electron bunches, FSA: target front and bulk acceleration). **d** Time history of the electric field E_x along the propagation direction x of the most energetic tracer proton. The trajectory of this proton is depicted by the thick black line. The contour of the relativistically corrected critical density $\gamma\, n_c$ of the target is shown by the thin black line.

boring RPA [28, 97, 139], relativistic transparency front RPA [100] or collisionless shock acceleration [102]. For the sake of simplicity, we refer to these acceleration contributions as **Front Surface Acceleration (FSA)**, which is mainly induced by the radiation pressure of the laser and is maintained until the expanding target undergoes RIT. The distinction between acceleration happening at the target front side (FSA component) and at the target rear side is made according to the position of the particle within the plasma density profile. FSA ends at the target rear side boundary which is defined at the position where the plasma density falls below the relativistic critical density γn_c.

Throughout the interaction with the plasma, the relativistic laser pulse directly generates electron bunches through the oscillating $j \times B$ term of the Lorentz force [135, 353, 354], and thermal laser absorption mechanisms [355, 356]. The former, prompt electrons [30, 357] are directed primarily in laser propagation direction and closely follow the oscillating field structure of the laser. In contrast, thermal and recirculating electrons generate a diffuse sheath field at the target rear, which dominates in target normal direction. The characteristic oscillation of the accelerating field, induced by the prompt electrons, allows distinction between proton acceleration during the interaction with the ultrashort laser pulse at highest intensity and acceleration within the diffuse non-oscillating sheath field, which can occur on larger spatial and temporal scales. The field oscillations in the prompt phase are detected by relative comparison with the temporally smoothed (over half a laser period) field evolution. The prompt phase ends when this relative difference becomes smaller than a threshold value. Since the transition from oscillating fields to a constant field is smooth, the choice of this threshold is somewhat arbitrary. Here, the threshold value has been set to 1, i.e. the field energy in the oscillating field component is half that of the constant field.

Protons reaching the highest energies were initially located close to the target front and subjected to a cascade of multiple acceleration mechanisms. Figure 6.8c shows the individual contributions of these distinct mechanisms to the total energy of the fastest protons at the end of the simulation. The time history of the entire acceleration cascade for the most energetic tracer proton is shown in Figure 6.8d. In all directions, the fastest protons gain > 50 % of their energy from either the prompt or the thermal acceleration phase, in which they were injected with $\approx$ 20 MeV from the FSA phase. The fastest protons in the 45° direction gain most of their energy within the thermal sheath field, while the most energetic protons in laser propagation direction experience a significant acceleration contribution due to the field induced by the prompt electron bunches. This field is highest at the rear surface of the target bulk and extends throughout the rear side plasma sheath. Within the first 70 fs after the laser main pulse arrival, protons in the rear side sheath get accelerated by this field in laser forward direction. Simultaneously, this field prevents electrons from neutralising the charge of the escaping protons beyond the effective Debye length. The resulting charge separation within the sheath induces an additional ambipolar electric field. This field affects the fast protons originating from the front surface, resulting in a momentum spread that further enhances the energy of the fastest particles. This acceleration contribution is referred to as additional **Coulomb repulsion (CR)**. As the prompt electrons generate the highest electron density in the laser propagation direction, CR is particularly relevant for fast protons moving in that direction. These protons gain > 25 % of their total energy by CR, while for protons in target normal direction CR is responsible for only 13 % of their total energy. The CR phase is numerically identified to start when the proton charge in the expanding sheath starts to exceed that of the electrons and the electric accelerating field increases with time. The CR field then partially overlaps with the sheath acceleration field. A distinction between the two components is conducted by comparing the field evolution at late times with an extrapolated decreasing sheath field, estimating it with a power law $E(t) \propto t^{-n}$ as

expected for TNSA. The energy gain by CR is then calculated using the temporally integrated difference of the actual field and the extrapolated TNSA field up to the end of the simulation.

The angular dependent spectral modulations of the proton emission distribution result from the complex interplay of the various mechanisms. Typically, spectral modulations manifest when a part of the proton ensemble traverses field gradients localised in space and time. A detailed analysis of the phase space development in the simulation revealed spectral signatures of each mechanism, which all superimpose to form the spectrally resolved angular distribution in Figure 6.8b. This includes mono-energetic features in the RPA phase, an exponential energy distribution due to the expansion phase [183, 358], ambipolar field structures at the target rear side where carbon ions and protons undergo demixing [359], as well as strong field gradients during the CR phase [192, 358].

Despite performing state-of-the-art simulations based on detailed experimental measurements, assigning the present simulation to a specific shot of the experiment requires more precise knowledge of the corresponding interaction parameters and less numerical simplifications. This necessitates progress in experimental metrology and an increase in accessible computational resources. Nonetheless, the simulation results replicate the experimental observations for an average good shot, including the angular proton emission distribution, the spectral modulation in laser propagation direction and the amount of transmitted laser light.

While the observation of multiple acceleration phases is similar to previous research in the RIT regime [130, 139, 358], the fundamental difference of this work is the role of the prompt electrons for ultra-short laser pulses and target densities at the onset of RIT. These prompt electrons facilitate efficient energy transfer from the ultra-intense laser pulse to the protons, both during and after the interaction with the laser pulse. The difference in proton energy scaling between the laser propagation direction and target normal direction can be attributed to the differently weighted contributions of hole boring RPA, prompt and thermal TNSA, as well as CR. Particularly, the strong influence of prompt electrons in laser propagation direction, characterised by a linear scaling [30], can be associated with the experimentally observed linear scaling of maximum proton energies at 15°. Moreover, there is an anticipated variation in the individual contribution of each acceleration mechanism for different laser-target geometries as the absorption of the laser, electron heating, and the sheath field's geometry are known to vary with the angle of incidence and laser polarisation. It is also plausible that several distinct combinations of acceleration mechanisms may result in similarly high beam energies. In any scenario, cascades involving all observed mechanisms will persist, although their individual contribution are expected to fluctuate (e.g. greater influence of RPA component at normal incidence). Experimentally, a deeper understanding of the composition of the cascades is most likely to be achieved by investigating the plasma density distribution and the transmitted light properties both requiring complex diagnostics [160, 161, 360].

6.5 Conclusions

In summary, the results presented in this chapter demonstrate the capability of laser-driven plasma accelerators to generate proton beams with a spectrally separated high-energy component at maximum energies well exceeding 100 MeV. Multiple detectors based on different detection principles simultaneously confirmed the experimental results. This proof-of-principle achievement marks an important milestone in the field of plasma accelerators, paving the way towards the use of laser-driven ion sources for various demanding applications. Based on the experimental energy scaling, maximum

proton energies beyond 250 MeV can be extrapolated at twice the laser pulse energy, provided suitable interaction parameters for an efficient cascade of mechanisms are achieved.

Target transparency was identified as a simple control parameter for determining the high-performance domain, owing to its sensitivity to subtle changes in the initial laser-target conditions. Using the transmitted laser light as an independent feedback parameter related to acceleration performance is ideal for future automated laser and target optimisation. Advanced experimental diagnostics, involving self-generated and transmitted laser light [160, 161, 360], in conjunction with advanced simulation approaches [157, 340], can be employed for this purpose. In combination with the relatively high repetition rate ($\geq$ 1 Hz) of ultrashort pulse lasers, these approaches have the potential to enhance the acceleration stability for practical applications.

Simulations considering the complete interaction, from picosecond-long target expansion to proton acceleration during the high-intensity laser pulse, reveal a cascade of acceleration regimes that lead to proton energies exceeding 100 MeV. The ultrashort pulse duration of the laser promotes a rapid succession of multiple acceleration regimes at highest intensities. Orchestrating this acceleration cascade requires careful consideration of pre-expansion, species separation, and timing to achieve the maximum energy. Therefore, future simulation work should address these factors as well as the experimentally observed energy scaling in the various directions. This requires extensive multi-parameter scans and investigations into different combinations as well as relative timings between the involved acceleration mechanisms.

7 Summary and outlook

This thesis investigated effective optimisation strategies for enhancing ion acceleration from thin foil targets in ultra-intense laser-plasma interactions. The presented work results from a series of experiments that were conducted at two state-of-the-art high-power laser systems: the J-KAREN-P laser at the **Kansai Photon Science Institute (KPSI)** and the DRACO-PW laser at the **Helmholtz-Zentrum Dresden-Rossendorf (HZDR)**.

The performed research enabled realisation of several experimental milestones in the field of plasma-based proton acceleration. Performing worlds first "*in vivo*" pilot study on human tumours in mice using a laser-driven proton beam marks one of these accomplishments and a long-awaited landmark within the scientific community. This achievement was possible by aggregating input from multiple research projects at HZDR, covering aspects of radiobiology, dosimetry, beam transport and source development. The latter represents the contribution of this thesis, as the proton beam parameter at the beginning of this work were insufficient for the study's requirements. Through meticulous efforts in monitoring and enhancing the temporal intensity contrast of the laser, precise control over the **Target Normal Sheath Acceleration (TNSA)** process has been achieved. The implementation of a plasma mirror significantly improved the temporal contrast, restricting the plasma dynamics to the last picoseconds before the arrival of the main pulse. Fine-tuning of the laser pulse shape was achieved by actively tailoring the instantaneous frequencies of the electric field of the laser. A systematic study revealed an optimal setting for asymmetric pulses, resulting in significantly enhanced proton energies and particle numbers. The experimental results and a detailed description of the the the optimisation technique have led to the publication of TZ3. 2D **Particle-In-Cell (PIC)** simulations with temporally asymmetric laser pulses were performed to investigate the microscopic details leading to the observed energy gain. The results indicate that proton acceleration is enhanced when the laser energy deposition before the main pulse arrival is minimised, resulting in steeper plasma density gradients and increased absorption of laser energy by plasma electrons. Consequently, the temporal pulse shape optimisation leads to stronger rear side fields, accelerating protons from the target. The experimental data supports this hypothesis and the fact that the relevant time and intensity scales for the observed enhancement have been identified. However, questions remain regarding whether the detailed microscopic processes involved are the same in three dimensions, necessitating future simulations to focus on this aspect. The experimentally developed optimisation procedure and it's robustness established the foundation for stable and efficient generation of application-relevant proton beams. It became a daily preparation routine for ion acceleration experiments at DRACO-PW and has also been adopted by

other groups. The integration of automated dispersion control for performance optimisation is a readily applicable method, especially when combined with real-time feedback routines. The synergy of high repetition rate lasers and machine learning techniques presents a valuable opportunity for advancing the capabilities and performance of plasma accelerators in the future.

To overcome the scaling limitations of TNSA, the second part of the thesis focussed on investigating ion acceleration in the **Relativistically Induced Transparency (RIT)** regime for ultrashort laser pulses and solid-density targets. Multiple experiments were conducted, using the high-power laser systems at KPSI and HZDR, to perform systematic scans of laser and target parameters. Despite differences in laser system architecture, these experiments provided complementary results and insights into the detailed plasma dynamics. Optimal interaction conditions for ion acceleration in the RIT regime were identified by matching the initial target thickness to the temporal contrast of the laser. 3D PIC simulations replicated the experimental results, indicating that best acceleration performance is achieved when the initially opaque target becomes transparent upon arrival of the main pulse. The intense laser field causes a rapid expulsion of electrons from the target bulk, resulting in an extremely localised and intense space charge field that accelerates ions to several tens of MeV within a few femtoseconds. Investigations on the influence of the temporal laser contrast revealed that the preceding laser light primes the plasma density for the onset of RIT upon main pulse arrival. Fostering this technique has the potential to simplify ion acceleration in this regime, making it suitable for a wide range of laser parameters and operation at high repetition rates. These advantages align with the preference for robust and easy-to-implement solutions in various applications, avoiding sophisticated approaches for plasma density shaping or individually designed targets that are usually expensive and susceptible to damage. The detailed insights into the role of the ultrashort pulse duration and the temporal contrast of the laser represent a significant step forward in understanding and controlling ion acceleration in the RIT regime. Focussing on the laser as the initial driver of the plasma interaction was central to achieving these results and a pivotal element of this thesis. This involved establishing and linking laser diagnostic and operational techniques to enhance control of on-target laser performance. These efforts enabled the successful replication of experimental results across two distinct laser facilities by incorporating standardised operation principles, experimental procedures, high-quality beam characterisation capabilities, and analysis methods. The results of this study lead to the publication of TZ2.

All the expertise acquired in setting up and performing experiments under optimised interaction conditions culminated in the full exploitation of ion acceleration in the RIT regime. Using DRACO-PW and only 22 J laser energy on target, laser-driven proton acceleration to a record energy of 150 MeV was achieved. This experimental demonstration of highly efficient ion acceleration to unprecedented energy levels using laser systems suitable for repetitive operation at moderate laser energies, represent another experimental milestone that was achieved within this thesis. Strategically selecting the initial target thickness ensured that the main laser pulse interacted with a target undergoing RIT as a result of pre-expansion early in the interaction. The experimental setup was adapted to facilitate angle-resolved measurement using several detectors based on different detection methods. The accelerated proton beam featured a high-energy component with low divergence, which is spectrally and spatially separated from the lower energetic TNSA component. Notably, this high-energy component showed a linear scaling of maximum proton energy with increased laser energy, which is fundamentally different to the square-root scaling of the TNSA component. Target transparency, measured by the

amount of transmitted laser light, was found to define the interaction conditions for best acceleration performance. The observed sensitivity to subtle changes in the initial laser-target conditions makes this parameter ideal for future studies aiming for guided or fully automated optimisation of interaction parameters. Combining hydrodynamic and PIC simulations enabled to study the microscopic details of the complete interaction from picosecond-long target pre-expansion to proton acceleration during the high-intensity laser pulse. The results not only replicated the experimental observations but also revealed that multiple known acceleration schemes cascade efficiently at the onset of RIT. The ultrashort pulse duration of the laser promotes a rapid succession of these regimes at highest intensities, leading to the observed beam parameters and enabling ion acceleration to unprecedented energy levels. Central to achieving these results and distinguishing them from previously published studies in the RIT regime is the importance of directly accelerated electrons in the presence of ultrashort laser pulses and solid-density foil targets. These prompt electrons facilitate efficient energy transfer from the ultra-intense laser to the ions, both during and after the interaction with the laser pulse. In particular, the scaling of the maximum proton energy in this regime is very promising, allowing to access an energy range of considerable interest for applications. Based on the experimental results, maximum proton energies beyond 250 MeV can be extrapolated at twice the laser pulse energy, provided suitable interaction parameters for an efficient cascade of mechanisms are achieved. As these findings coincide with the advent of novel application-dedicated ultrashort pulse laser systems in the multi-petawatt regime, the results of this study TZ1 , published in Nature Physics, will be of highest importance for those facilities and the associated research. Achieving precise control over the experimental interaction conditions to stabilise this promising acceleration regime represents the next important step that future work should focus on. This requires careful attention to target pre-expansion, ion species separation, as well as optimal timing of the individual mechanisms and should be addressed using both numerical and experimental methods. Analytical approaches along with PIC simulations and machine learning techniques, will be essential in studying and connecting the multi-dimensional parameter space for an optimal interplay of acceleration mechanisms. Future experimental efforts should prioritise the development of single-shot methods for real-time intensity characterisation in the focal plane, reducing assumptions and providing more realistic input parameters for simulation studies. Moreover, the exploration of the transmitted light properties with advanced diagnostic techniques should be pursued in future experiments, as this might be key to accessing the detailed plasma conditions upon main pulse arrival.

In conclusion, this thesis presented viable optimisation strategies for laser-driven ion sources from solid targets at intensities beyond 10^{21} W cm^{-2}. A central aspect of this work was the establishment and integration of laser diagnostics and operational techniques to advance control of the interactions conditions in this intensity regime for best ion beam quality. The impact of laser parameters on plasma-based ion acceleration has been thoroughly investigated in a series of experiments conducted on two high-power laser systems. The obtained findings allowed for precise adjustment of the interaction conditions for sheath acceleration and exploration of an advanced acceleration scheme for relativistically transparent targets. The results from the latter significantly exceeded the maximum proton energies that were previously achieved via laser-driven ion acceleration. Combining experimental and numerical research allowed to elucidate new insights about the detailed plasma dynamics for the interaction of ultrashort laser pulses with expanding foil targets. The findings of this thesis and the outlined optimisation strategies may become the guiding step for advancing laser-driven ion acceleration, paving the way towards the use of plasma accelerators as a reliable high-energy proton source.

Appendix

Simulation results for asymmetric laser pulse shapes

Numerical simulations of the experiments presented in chapter 4 were performed with the fully relativistic particle-in-cell code PIConGPU in a 2D3V geometry. The simulation box size was 16 µm in transversal direction and 10 µm + 37 µm before and after the foil in longitudinal direction respectively. The target was modelled as an unexpanded (no pre-plasma) flat foil of 400 nm thickness, consisting of H^+ and C^{2+} ions with a density of $200\,n_c$ and 10 particles per cell and ion species upon initialisation. The laser pulse had a Gaussian-shaped spatial profile (2.6 µm FWHM) and peak intensity of $a_0 = 50$. The influence of the modified temporal pulse shape was studied by separating the asymmetric laser pulse profile into three distinct cases. The temporal laser pulse profile and the resulting proton energy spectra at the end of the simulation are shown in Figure A1, Figure A2 and Figure A3.
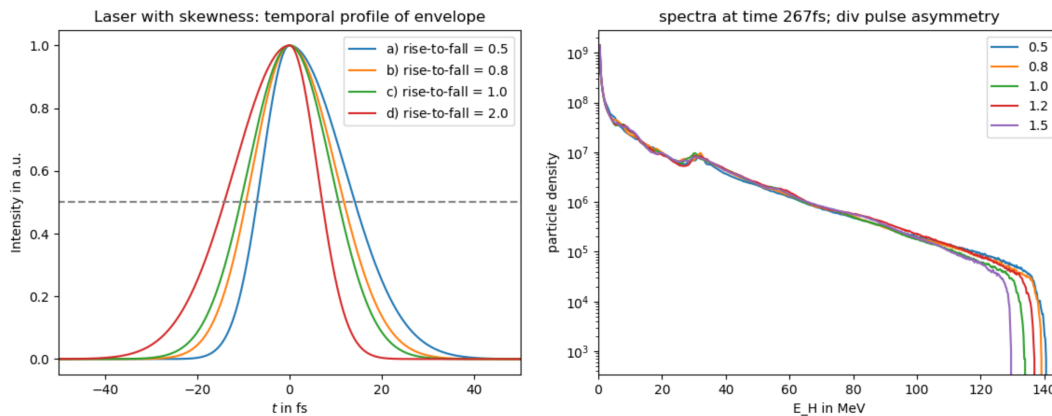

Figure A1: First scenario: Asymmetric laser pulse. Temporal laser pulse profile (left) and proton energy spectra (right) for a Gaussian laser pulses with different rise-to-fall ratios.
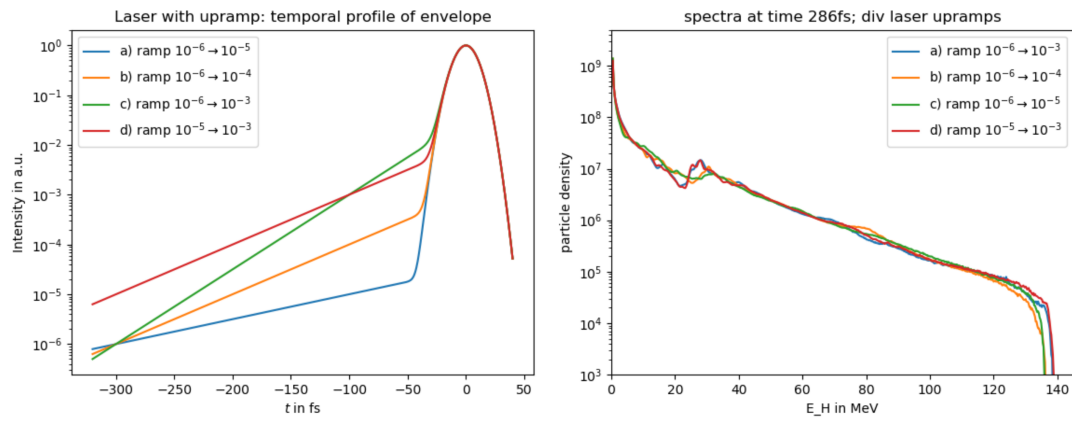
Figure A2: Second scenario: Gaussian pulse with exponential ramp. Temporal laser pulse profile (left) and proton energy spectra (right) for different exponential ramps.
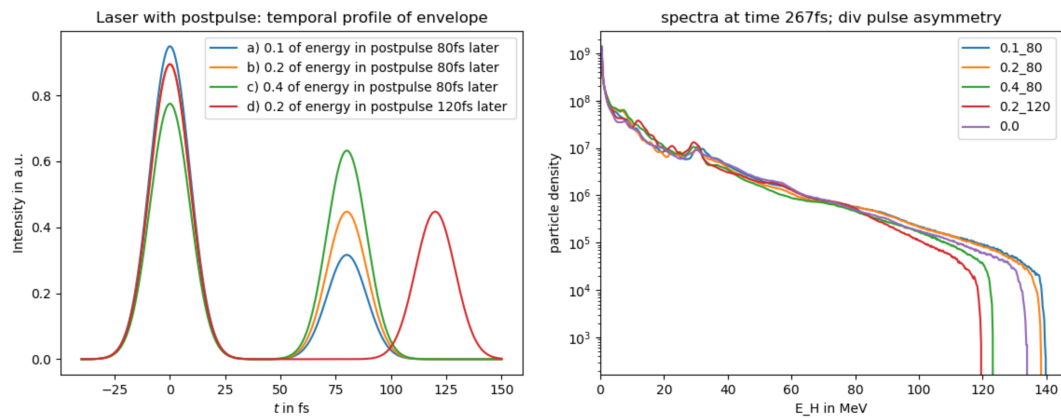

Figure A3: Third scenario: Gaussian pulse with post-pulse. Temporal laser pulse profile (left) and proton energy spectrum (right) for different post-pulse configurations.

References

[1] S Doebert. "Gradient Limitations for High-Frequency Accelerators". In: *Tech. rep. Stanford Linear Accelerator Center, Menlo Park, CA (United States)* (2004). DOI: `10.2172/833031` (cit. on p. 1).

[2] H Daido, M Nishiuchi, and AS Pirozhkov. "Review of laser-driven ion sources and their applications". In: *Reports on Progress in Physics* 75 (5 2012), p. 056401. DOI: `10.1088/0034-4885/75/5/056401` (cit. on pp. 1, 19).

[3] A Macchi, M Borghesi, and M Passoni. "Ion acceleration by superintense laser-plasma interaction". In: *Reviews of Modern Physics* 85 (2 2013), pp. 751–793. DOI: `10.1103/RevModPhys.85.751` (cit. on pp. 1, 19, 23).

[4] RA Snavely et al. "Intense High-Energy Proton Beams from Petawatt-Laser Irradiation of Solids". In: *Physical Review Letters* 85 (14 2000), pp. 2945–2948. DOI: `10.1103/PhysRevLett.85.2945` (cit. on pp. 1, 19, 36, 78, 95).

[5] EL Clark et al. "Measurements of Energetic Proton Transport through Magnetized Plasma from Intense Laser Interactions with Solids". In: *Physical Review Letters* 84 (4 2000), pp. 670–673. DOI: `10.1103/PhysRevLett.84.670` (cit. on pp. 1, 19, 78).

[6] M Roth et al. "Fast Ignition by Intense Laser-Accelerated Proton Beams". In: *Physical Review Letters* 86 (3 2001), pp. 436–439. DOI: `10.1103/PhysRevLett.86.436` (cit. on p. 1).

[7] JC Fernández et al. "Progress and prospects of ion-driven fast ignition". In: *Nuclear Fusion* 49 (6 2009), p. 065004. DOI: `10.1088/0029-5515/49/6/065004` (cit. on p. 1).

[8] S Bulanov et al. "Oncological hadrontherapy with laser ion accelerators". In: *Physics Letters A* 299 (2-3 2002), pp. 240–247. DOI: `10.1016/S0375-9601(02)00521-2` (cit. on p. 1).

[9] V Malka et al. "Practicability of protontherapy using compact laser systems". In: *Medical Physics* 31 (6 2004), pp. 1587–1592. DOI: `10.1118/1.1747751` (cit. on p. 1).

[10] P Patel et al. "Isochoric Heating of Solid-Density Matter with an Ultrafast Proton Beam". In: *Physical Review Letters* 91 (12 2003), p. 125004. DOI: `10.1103/PhysRevLett.91.125004` (cit. on p. 1).

[11] M Barberio et al. "Laser-accelerated particle beams for stress testing of materials". In: *Nature Communications* 9 (1 2018), p. 372. DOI: `10.1038/s41467-017-02675-x` (cit. on p. 1).

[12] A Prasselsperger et al. "Real-Time Electron Solvation Induced by Bursts of Laser-Accelerated Protons in Liquid Water". In: *Physical Review Letters* 127 (18 2021), p. 186001. DOI: 10.1103/PhysRevLett.127.186001 (cit. on p. 1).

[13] M Roth et al. "Bright Laser-Driven Neutron Source Based on the Relativistic Transparency of Solids". In: *Physical Review Letters* 110 (4 2013), p. 044802. DOI: 10.1103/PhysRevLett.110.044802 (cit. on pp. 1, 28, 77).

[14] S Kar et al. "Beamed neutron emission driven by laser accelerated light ions". In: *New Journal of Physics* 18 (5 2016), p. 053002. DOI: 10.1088/1367-2630/18/5/053002 (cit. on p. 1).

[15] P Chaudhary et al. "Radiobiology Experiments With Ultra-high Dose Rate Laser-Driven Protons: Methodology and State-of-the-Art". In: *Frontiers in Physics* 9 (2021). DOI: 10.3389/fphy.2021.624963 (cit. on p. 1).

[16] F Kroll et al. "Tumour irradiation in mice with a laser-accelerated proton beam". In: *Nature Physics* 18 (3 2022), pp. 316–322. DOI: 10.1038/s41567-022-01520-3 (cit. on pp. 1, 75).

[17] SC Wilks et al. "Energetic proton generation in ultra-intense laser–solid interactions". In: *Physics of Plasmas* 8 (2 2001), pp. 542–549. DOI: 10.1063/1.1333697 (cit. on pp. 1, 19).

[18] J Fuchs et al. "Laser-driven proton scaling laws and new paths towards energy increase". In: *Nature Physics* 2 (1 2006), pp. 48–54. DOI: 10.1038/nphys199 (cit. on pp. 2, 22, 58, 95).

[19] M Kaluza et al. "Influence of the Laser Prepulse on Proton Acceleration in Thin-Foil Experiments". In: *Physical Review Letters* 93 (4 2004), p. 045003. DOI: 10.1103/PhysRevLett.93.045003 (cit. on pp. 2, 58).

[20] CM Brenner et al. "High energy conversion efficiency in laser-proton acceleration by controlling laser-energy deposition onto thin foil targets". In: *Applied Physics Letters* 104 (8 2014), p. 081123. DOI: 10.1063/1.4865812 (cit. on pp. 2, 58, 73).

[21] M Tayyab et al. "Effect of temporally modified ultra-short laser pulses on ion acceleration from thin foil targets". In: *Physics of Plasmas* 25 (8 2018), p. 083113. DOI: 10.1063/1.5037260 (cit. on pp. 2, 58).

[22] H Schwoerer et al. "Laser-plasma acceleration of quasi-monoenergetic protons from microstructured targets". In: *Nature* 439 (7075 2006), pp. 445–448. DOI: 10.1038/nature04492 (cit. on pp. 2, 36).

[23] BM Hegelich et al. "Laser acceleration of quasi-monoenergetic MeV ion beams". In: *Nature* 439 (7075 2006), pp. 441–444. DOI: 10.1038/nature04400 (cit. on p. 2).

[24] CN Danson et al. "Petawatt and exawatt class lasers worldwide". In: *High Power Laser Science and Engineering* 7 (2019), e54. DOI: 10.1017/hpl.2019.36 (cit. on pp. 2, 35).

[25] A Henig et al. "Radiation-Pressure Acceleration of Ion Beams Driven by Circularly Polarized Laser Pulses". In: *Physical Review Letters* 103 (24 2009), p. 245003. DOI: 10.1103/PhysRevLett.103.245003 (cit. on pp. 2, 28).

[26] S Buffechoux et al. "Hot Electrons Transverse Refluxing in Ultraintense Laser-Solid Interactions". In: *Physical Review Letters* 105 (1 2010), p. 015005. DOI: 10.1103/PhysRevLett.105.015005 (cit. on p. 2).

[27] K Zeil et al. "The scaling of proton energies in ultrashort pulse laser plasma acceleration". In: *New Journal of Physics* 12 (4 2010), p. 045015. DOI: 10.1088/1367-2630/12/4/045015 (cit. on pp. 2, 78).

[28] IJ Kim et al. "Radiation pressure acceleration of protons to 93MeV with circularly polarized petawatt laser pulses". In: *Physics of Plasmas* 23 (7 2016), p. 070701. DOI: 10.1063/1.4958654 (cit. on pp. 2, 96, 106).

[29] WJ Ma et al. "Laser Acceleration of Highly Energetic Carbon Ions Using a Double-Layer Target Composed of Slightly Underdense Plasma and Ultrathin Foil". In: *Physical Review Letters* 122 (1 2019), p. 014803. DOI: 10.1103/PhysRevLett.122.014803 (cit. on pp. 2, 58, 96).

[30] K Zeil et al. "Direct observation of prompt pre-thermal laser ion sheath acceleration". In: *Nature Communications* 3 (1 2012), p. 874. DOI: 10.1038/ncomms1883 (cit. on pp. 3, 58, 86, 106, 107).

[31] W Crookes. "On radiant matter". In: *Journal of the Franklin Institute* 108 (5 1879), pp. 305–316. DOI: 10.1016/0016-0032(79)90319-3 (cit. on p. 5).

[32] I Langmuir. "Oscillations in Ionized Gases". In: *Proceedings of the National Academy of Sciences* 14 (8 1928), pp. 627–637. DOI: 10.1073/pnas.14.8.627 (cit. on pp. 5, 7).

[33] FF Chen. *Introduction to Plasma Physics and Controlled Fusion*. Springer, 1984 (cit. on pp. 5, 15, 21).

[34] P Drude. "Zur Elektronentheorie der Metalle". In: *Annalen der Physik* 306 (3 1900), pp. 566–613. DOI: 10.1002/andp.19003060312 (cit. on p. 6).

[35] M Dressel and M Scheffler. "Verifying the Drude response". In: *Annalen der Physik* 15 (7-8 2006), pp. 535–544. DOI: 10.1002/andp.200510198 (cit. on p. 6).

[36] GA Mourou, T Tajima, and SV Bulanov. "Optics in the relativistic regime". In: *Reviews of Modern Physics* 78 (2 2006), pp. 309–371. DOI: 10.1103/RevModPhys.78.309 (cit. on p. 10).

[37] LV Keldysh. "Ionization in the field of a strong electromagnetic wave". In: *J. Exptl. Theoret. Phys. (U.S.S.R.)* 20 (5 1965), pp. 1945–1957 (cit. on p. 12).

[38] VS Popov. "Tunnel and multiphoton ionization of atoms and ions in a strong laser field (Keldysh theory)". In: *Physics-Uspekhi* 47 (9 2004), pp. 855–885. DOI: 10.1070/PU2004v047n09ABEH001812 (cit. on p. 12).

[39] P Gibbon. *Short pulse laser interactions with matter : an introduction*. Imperial College Pr., 2005 (cit. on pp. 12, 15).

[40] P Woodward and J Lawson. "The theoretical precision with which an arbitrary radiation-pattern may be obtained from a source of finite size". In: *Journal of the Institution of Electrical Engineers - Part III: Radio and Communication Engineering* 95 (37 1948), pp. 363–370. DOI: 10.1049/ji-3-2.1948.0094 (cit. on p. 14).

[41] JD Lawson. "Lasers and Accelerators". In: *IEEE Transactions on Nuclear Science* 26 (3 1979), pp. 4217–4219. DOI: 10.1109/TNS.1979.4330749 (cit. on p. 14).

[42] D Bauer, P Mulser, and W Steeb. "Relativistic Ponderomotive Force, Uphill Acceleration, and Transition to Chaos". In: *Physical Review Letters* 75 (25 1995), pp. 4622–4625. DOI: 10.1103/PhysRevLett.75.4622 (cit. on p. 15).

[43] B Quesnel and P Mora. "Theory and simulation of the interaction of ultraintense laser pulses with electrons in vacuum". In: *Physical Review E* 58 (3 1998), pp. 3719–3732. DOI: 10.1103/PhysRevE.58.3719 (cit. on p. 15).

[44] W Kruer. *The Physics Of Laser Plasma Interactions*. CRC Press, 2019 (cit. on pp. 15, 21).

[45] SC Wilks and WL Kruer. "Absorption of ultrashort, ultra-intense laser light by solids and overdense plasmas". In: *IEEE Journal of Quantum Electronics* 33 (1997), pp. 1954–1968. DOI: 10.1109/3.641310 (cit. on pp. 15, 17).

[46] F Brunel. "Not-so-resonant, resonant absorption". In: *Physical Review Letters* 59 (1 1987), pp. 52–55. DOI: 10.1103/PhysRevLett.59.52 (cit. on p. 17).

[47] SC Wilks et al. "Absorption of ultra-intense laser pulses". In: *Physical Review Letters* 69 (9 1992), pp. 1383–1386. DOI: 10.1103/PhysRevLett.69.1383 (cit. on pp. 18, 25).

[48] FN Beg et al. "A study of picosecond laser–solid interactions up to 10^{19} W/cm^2". In: *Physics of Plasmas* 4 (2 1997), pp. 447–457. DOI: 10.1063/1.872103 (cit. on p. 18).

[49] H Chen et al. "Hot electron energy distributions from ultraintense laser solid interactions". In: *Physics of Plasmas* 16 (2 2009), p. 020705. DOI: 10.1063/1.3080197 (cit. on p. 18).

[50] T Tanimoto et al. "Measurements of fast electron scaling generated by petawatt laser systems". In: *Physics of Plasmas* 16 (6 2009), p. 062703. DOI: 10.1063/1.3155086 (cit. on p. 18).

[51] MG Haines et al. "Hot-Electron Temperature and Laser-Light Absorption in Fast Ignition". In: *Physical Review Letters* 102 (4 2009), p. 045008. DOI: 10.1103/PhysRevLett.102.045008 (cit. on p. 18).

[52] T Kluge et al. "Electron temperature scaling in laser interaction with solids". In: *Physical Review Letters* 107 (20 2011), p. 205003. DOI: 10.1103/PhysRevLett.107.205003 (cit. on pp. 18, 78).

[53] NP Dover et al. "Effect of Small Focus on Electron Heating and Proton Acceleration in Ultrarelativistic Laser-Solid Interactions". In: *Physical Review Letters* 124 (8 2020), p. 084802. DOI: 10.1103/PhysRevLett.124.084802 (cit. on pp. 18, 78).

[54] T Yabuuchi et al. "Transport study of intense-laser-produced fast electrons in solid targets with a preplasma created by a long pulse laser". In: *Physics of Plasmas* 17 (6 2010), p. 060704. DOI: 10.1063/1.3447878 (cit. on p. 18).

[55] J Peebles et al. "Investigation of laser pulse length and pre-plasma scale length impact on hot electron generation on OMEGA-EP". In: *New Journal of Physics* 19 (2 2017), p. 023008. DOI: 10.1088/1367-2630/aa5a21 (cit. on p. 18).

[56] H Padamsee, J Knobloch, and T Hays. *RF Superconductivity for Accelerators*. Wiley Series in Beam Physics and Accelerator Technology. Wiley, 1998 (cit. on p. 19).

[57] A Maksimchuk et al. "Forward Ion Acceleration in Thin Films Driven by a High-Intensity Laser". In: *Physical Review Letters* 84 (18 2000), pp. 4108–4111. DOI: 10.1103/PhysRevLett.84.4108 (cit. on p. 19).

[58] AJ Mackinnon et al. "Enhancement of Proton Acceleration by Hot-Electron Recirculation in Thin Foils Irradiated by Ultraintense Laser Pulses". In: *Physical Review Letters* 88 (21 2002), p. 215006. DOI: 10.1103/PhysRevLett.88.215006 (cit. on p. 19).

[59] Y Sentoku et al. "High energy proton acceleration in interaction of short laser pulse with dense plasma target". In: *Physics of Plasmas* 10 (5 2003), pp. 2009–2015. DOI: 10.1063/1.1556298 (cit. on p. 19).

[60] TE Cowan et al. "Ultralow Emittance, Multi-MeV Proton Beams from a Laser Virtual-Cathode Plasma Accelerator". In: *Physical Review Letters* 92 (20 2004), p. 204801. DOI: 10.1103/PhysRevLett.92.204801 (cit. on p. 20).

[61] P McKenna et al. "Lateral Electron Transport in High-Intensity Laser-Irradiated Foils Diagnosed by Ion Emission". In: *Physical Review Letters* 98 (14 2007), p. 145001. DOI: 10.1103/PhysRevLett.98.145001 (cit. on p. 20).

[62] J Schreiber et al. "Analytical Model for Ion Acceleration by High-Intensity Laser Pulses". In: *Physical Review Letters* 97 (4 2006), p. 045005. DOI: 10.1103/PhysRevLett.97.045005 (cit. on pp. 20, 22).

[63] JS Green et al. "Effect of Laser Intensity on Fast-Electron-Beam Divergence in Solid-Density Plasmas". In: *Physical Review Letters* 100 (1 2008), p. 015003. DOI: 10.1103/PhysRevLett.100.015003 (cit. on p. 20).

[64] A Debayle et al. "Divergence of laser-driven relativistic electron beams". In: *Physical Review E* 82 (3 2010), p. 036405. DOI: 10.1103/PhysRevE.82.036405 (cit. on p. 20).

[65] VY Bychenkov et al. "Ion acceleration in expanding multispecies plasmas". In: *Physics of Plasmas* 11 (6 2004), pp. 3242–3250. DOI: 10.1063/1.1738649 (cit. on p. 20).

[66] J Psikal et al. "Ion acceleration by femtosecond laser pulses in small multispecies targets". In: *Physics of Plasmas* 15 (5 2008), p. 053102. DOI: 10.1063/1.2913264 (cit. on p. 20).

[67] M Hegelich et al. "MeV Ion Jets from Short-Pulse-Laser Interaction with Thin Foils". In: *Physical Review Letters* 89 (8 2002), p. 085002. DOI: 10.1103/PhysRevLett.89.085002 (cit. on p. 20).

[68] C Perego et al. "Extensive comparison among Target Normal Sheath Acceleration theoretical models". In: *Nuclear Instruments and Methods in Physics Research Section A: Accelerators, Spectrometers, Detectors and Associated Equipment* 653 (1 2011), pp. 89–93. DOI: 10.1016/j.nima.2011.01.100 (cit. on p. 21).

[69] P Mora. "Plasma Expansion into a Vacuum". In: *Physical Review Letters* 90 (18 2003), p. 185002. DOI: 10.1103/PhysRevLett.90.185002 (cit. on p. 21).

[70] J Fuchs et al. "Comparative spectra and efficiencies of ions laser-accelerated forward from the front and rear surfaces of thin solid foils". In: *Physics of Plasmas* 14 (5 2007), p. 053105. DOI: 10.1063/1.2720373 (cit. on p. 22).

[71] P Mora. "Thin-foil expansion into a vacuum". In: *Physical Review E* 72 (5 2005), p. 056401. DOI: 10.1103/PhysRevE.72.056401 (cit. on p. 22).

[72] J Schreiber, F Bell, and Z Najmudin. "Optimization of relativistic laser–ion acceleration". In: *High Power Laser Science and Engineering* 2 (2014), e41. DOI: 10.1017/hpl.2014.46 (cit. on p. 23).

[73] M Passoni and M Lontano. "Theory of Light-Ion Acceleration Driven by a Strong Charge Separation". In: *Physical Review Letters* 101 (11 2008), p. 115001. DOI: 10.1103/PhysRevLett.101.115001 (cit. on p. 23).

[74] BJ Albright et al. "Theory of Laser Acceleration of Light-Ion Beams from Interaction of Ultrahigh-Intensity Lasers with Layered Targets". In: *Physical Review Letters* 97 (11 2006), p. 115002. DOI: 10.1103/PhysRevLett.97.115002 (cit. on pp. 23, 28).

[75] APL Robinson, AR Bell, and RJ Kingham. "Effect of Target Composition on Proton Energy Spectra in Ultraintense Laser-Solid Interactions". In: *Physical Review Letters* 96 (3 2006), p. 035005. DOI: 10.1103/PhysRevLett.96.035005 (cit. on p. 23).

[76] A Andreev et al. "Fast-Ion Energy-Flux Enhancement from Ultrathin Foils Irradiated by Intense and High-Contrast Short Laser Pulses". In: *Physical Review Letters* 101 (15 2008), p. 155002. DOI: 10.1103/PhysRevLett.101.155002 (cit. on p. 23).

[77] VI Veksler. "The principle of coherent acceleration of charged particles". In: *The Soviet Journal of Atomic Energy* 2 (5 1957), pp. 525–528. DOI: `10.1007/BF01491001` (cit. on p. 23).

[78] G Marx. "Interstellar vehicle propelled by terrestrial laser beam". In: *Nature* 211 (1966), pp. 22–23. DOI: `https://doi.org/10.1038/211022a0` (cit. on p. 23).

[79] T Esirkepov et al. "Highly Efficient Relativistic-Ion Generation in the Laser-Piston Regime". In: *Physical Review Letters* 92 (17 2004), p. 175003. DOI: `10.1103/PhysRevLett.92.175003` (cit. on pp. 24, 78).

[80] T Esirkepov, M Yamagiwa, and T Tajima. "Laser Ion-Acceleration Scaling Laws Seen in Multiparametric Particle-in-Cell Simulations". In: *Physical Review Letters* 96 (10 2006), p. 105001. DOI: `10.1103/PhysRevLett.96.105001` (cit. on p. 24).

[81] X Zhang et al. "Multistaged acceleration of ions by circularly polarized laser pulse: Monoenergetic ion beam generation". In: *Physics of Plasmas* 14 (7 2007), p. 073101. DOI: `10.1063/1.2746810` (cit. on pp. 24, 25).

[82] XQ Yan et al. "Generating High-Current Monoenergetic Proton Beams by a CircularlyPolarized Laser Pulse in the Phase-StableAcceleration Regime". In: *Physical Review Letters* 100 (13 2008), p. 135003. DOI: `10.1103/PhysRevLett.100.135003` (cit. on p. 24).

[83] O Klimo et al. "Monoenergetic ion beams from ultrathin foils irradiated by ultrahigh-contrast circularly polarized laser pulses". In: *Physical Review Special Topics - Accelerators and Beams* 11 (3 2008), p. 031301. DOI: `10.1103/PhysRevSTAB.11.031301` (cit. on pp. 24, 28).

[84] APL Robinson et al. "Radiation pressure acceleration of thin foils with circularly polarized laser pulses". In: *New Journal of Physics* 10 (1 2008), p. 013021. DOI: `10.1088/1367-2630/10/1/013021` (cit. on p. 24).

[85] APL Robinson et al. "Relativistically correct hole-boring and ion acceleration by circularly polarized laser pulses". In: *Plasma Physics and Controlled Fusion* 51 (2 2009), p. 024004. DOI: `10.1088/0741-3335/51/2/024004` (cit. on pp. 24, 25).

[86] A Macchi, S Veghini, and F Pegoraro. ""Light Sail" Acceleration Reexamined". In: *Physical Review Letters* 103 (8 2009), p. 085003. DOI: `10.1103/PhysRevLett.103.085003` (cit. on p. 24).

[87] B Qiao et al. "Stable GeV Ion-Beam Acceleration from Thin Foils by Circularly Polarized Laser Pulses". In: *Physical Review Letters* 102 (14 2009), p. 145002. DOI: `10.1103/PhysRevLett.102.145002` (cit. on p. 24).

[88] T Schlegel et al. "Relativistic laser piston model: Ponderomotive ion acceleration in dense plasmas using ultraintense laser pulses". In: *Physics of Plasmas* 16 (8 2009), p. 083103. DOI: `10.1063/1.3196845` (cit. on p. 24).

[89] B Qiao et al. "Radiation-Pressure Acceleration of Ion Beams from Nanofoil Targets: The Leaky Light-Sail Regime". In: *Physical Review Letters* 105 (15 2010), p. 155002. DOI: `10.1103/PhysRevLett.105.155002` (cit. on p. 24).

[90] SS Bulanov et al. "Radiation pressure acceleration: The factors limiting maximum attainable ion energy". In: *Physics of Plasmas* 23 (5 2016), p. 056703. DOI: `10.1063/1.4946025` (cit. on pp. 24, 28).

[91] A Macchi et al. "Laser Acceleration of Ion Bunches at the Front Surface of Overdense Plasmas". In: *Physical Review Letters* 94 (16 2005), p. 165003. DOI: `10.1103/PhysRevLett.94.165003` (cit. on p. 25).

[92] MP Kalashnikov et al. "Dynamics of Laser-Plasma Interaction at 10^{18} W/cm²". In: *Physical Review Letter* 73 (2 1994), pp. 260–263. DOI: `10.1103/PhysRevLett.73.26` (cit. on p. 25).

[93] M Zepf et al. "Measurements of the hole boring velocity from Doppler shifted harmonic emission from solid targets". In: *Physics of Plasmas* 3 (9 1996), pp. 3242–3244. DOI: `10.1063/1.871606` (cit. on p. 25).

[94] R Sauerbrey. "Acceleration in femtosecond laser-produced plasmas". In: *Physics of Plasmas* 3 (12 1996), pp. 4712–4716. DOI: `10.1063/1.872038` (cit. on p. 25).

[95] N Iwata et al. "Plasma density limits for hole boring by intense laser pulses". In: *Nature Communications* 9 (1 2018), p. 623. DOI: `10.1038/s41467-018-02829-5` (cit. on p. 25).

[96] J Hornung et al. "Time-resolved study of holeboring in realistic experimental conditions". In: *Nature Communications* 12 (1 2021), p. 6999. DOI: `10.1038/s41467-021-27363-9` (cit. on p. 25).

[97] CAJ Palmer et al. "Monoenergetic Proton Beams Accelerated by a Radiation Pressure Driven Shock". In: *Physical Review Letters* 106 (1 2011), p. 014801. DOI: `10.1103/PhysRevLett.106.014801` (cit. on pp. 26, 106).

[98] D Haberberger et al. "Collisionless shocks in laser-produced plasma generate monoenergetic high-energy proton beams". In: *Nature Physics* 8 (1 2012), pp. 95–99. DOI: `10.1038/nphys2130` (cit. on p. 26).

[99] A Brantov et al. "Synchronized Ion Acceleration by Ultraintense Slow Light". In: *Physical Review Letters* 116 (8 2016), p. 085004. DOI: `10.1103/PhysRevLett.116.085004` (cit. on pp. 26, 78).

[100] I Göthel et al. "Optimized laser ion acceleration at the relativistic critical density surface". In: *Plasma Physics and Controlled Fusion* 64 (4 2022), p. 044010. DOI: `10.1088/1361-6587/ac4e9f` (cit. on pp. 26, 78, 106).

[101] J Denavit. "Absorption of high-intensity subpicosecond lasers on solid density targets". In: *Physical Review Letters* 69 (21 1992), pp. 3052–3055. DOI: `10.1103/PhysRevLett.69.3052` (cit. on p. 26).

[102] LO Silva et al. "Proton Shock Acceleration in Laser-Plasma Interactions". In: *Physical Review Letters* 92 (1 2004), p. 015002. DOI: `10.1103/PhysRevLett.92.015002` (cit. on pp. 26, 106).

[103] E d'Humières et al. "Proton acceleration mechanisms in high-intensity laser interaction with thin foils". In: *Physics of Plasmas* 12 (6 2005), p. 062704. DOI: `10.1063/1.1927097` (cit. on pp. 26, 78, 96).

[104] M Chen et al. "Collisionless electrostatic shock generation and ion acceleration by ultraintense laser pulses in overdense plasmas". In: *Physics of Plasmas* 14 (5 2007), p. 053102. DOI: `10.1063/1.2722723` (cit. on p. 26).

[105] X Zhang et al. "Effect of plasma temperature on electrostatic shock generation and ion acceleration by laser". In: *Physics of Plasmas* 14 (11 2007), p. 113108. DOI: `10.1063/1.2811930` (cit. on p. 26).

[106] A Macchi, AS Nindrayog, and F Pegoraro. "Solitary versus shock wave acceleration in laser-plasma interactions". In: *Physical Review E* 85 (4 2012), p. 046402. DOI: `10.1103/PhysRevE.85.046402` (cit. on p. 26).

[107] MS Wei et al. "Ion Acceleration by Collisionless Shocks in High-Intensity-Laser–Underdense-Plasma Interaction". In: *Physical Review Letters* 93 (15 2004), p. 155003. DOI: `10.1103/PhysRevLett.93.155003` (cit. on p. 26).

[108]   O Tresca et al. "Spectral Modification of Shock Accelerated Ions Using a Hydrody-namically Shaped Gas Target". In: *Physical Review Letters* 115 (9 2015), p. 094802. DOI: 10.1103/PhysRevLett.115.094802 (cit. on p. 26).

[109]   L Romagnani et al. "Observation of Collisionless Shocks in Laser-Plasma Experi-ments". In: *Physical Review Letters* 101 (2 2008), p. 025004. DOI: 10.1103/PhysRevLett.101.025004 (cit. on p. 26).

[110]   E d'Humières et al. "Investigation of laser ion acceleration in low-density targets using exploded foils". In: *Plasma Physics and Controlled Fusion* 55 (12 2013), p. 124025. DOI: 10.1088/0741-3335/55/12/124025 (cit. on p. 26).

[111]   M Gauthier et al. "Investigation of longitudinal proton acceleration in exploded targets irradiated by intense short-pulse laser". In: *Physics of Plasmas* 21 (1 2014), p. 013102. DOI: 10.1063/1.4853475 (cit. on p. 26).

[112]   H Zhang et al. "Collisionless shocks driven by 800nm laser pulses generate high-energy carbon ions". In: *Physics of Plasmas* 22 (1 2015), p. 013113. DOI: 10.1063/1.4907194 (cit. on p. 26).

[113]   H Zhang et al. "Collisionless Shock Acceleration of High-Flux Quasimonoenergetic Proton Beams Driven by Circularly Polarized Laser Pulses". In: *Physical Review Let-ters* 119 (16 2017), p. 164801. DOI: 10.1103/PhysRevLett.119.164801 (cit. on p. 26).

[114]   A Henig et al. "Laser-Driven Shock Acceleration of Ion Beams from Spherical Mass-Limited Targets". In: *Physical Review Letters* 102 (9 2009), p. 095002. DOI: 10.1103/PhysRevLett.102.095002 (cit. on p. 26).

[115]   F Fiuza et al. "Laser-Driven Shock Acceleration of Monoenergetic Ion Beams". In: *Physical Review Letters* 109 (21 2012), p. 215001. DOI: 10.1103/PhysRevLett.109.215001 (cit. on p. 26).

[116]   YK Kim et al. "Shock ion acceleration by an ultrashort circularly polarized laser pulse via relativistic transparency in an exploded target". In: *Physical Review E* 92 (4 2015), p. 043102. DOI: 10.1103/PhysRevE.92.043102 (cit. on p. 26).

[117]   AS Novo et al. "Optimizing laser-driven proton acceleration from overdense tar-gets". In: *Scientific Reports* 6 (1 2016), p. 29402. DOI: 10.1038/srep29402 (cit. on p. 26).

[118]   A Macchi et al. "Radiation pressure acceleration of ultrathin foils". In: *New Journal of Physics* 12 (4 2010), p. 045013. DOI: 10.1088/1367-2630/12/4/045013 (cit. on p. 27).

[119]   S Kar et al. "Experimental investigation of hole boring and light sail regimes of RPA by varying laser and target parameters". In: *Plasma Physics and Controlled Fusion* 55 (12 2013), p. 124030. DOI: 10.1088/0741-3335/55/12/124030 (cit. on p. 27).

[120]   B Gonzalez-Izquierdo et al. "Radiation Pressure-Driven Plasma Surface Dynamics in Ultra-Intense Laser Pulse Interactions with Ultra-Thin Foils". In: *Applied Sciences* 8 (3 2018), p. 336. DOI: 10.3390/app8030336 (cit. on p. 27).

[121]   F Pegoraro and SV Bulanov. "Photon Bubbles and Ion Acceleration in a Plasma Dominated by the Radiation Pressure of an Electromagnetic Pulse". In: *Physical Review Letters* 99 (6 2007), p. 065002. DOI: 10.1103/PhysRevLett.99.065002 (cit. on p. 28).

[122]   A Sgattoni, S Sinigardi, and A Macchi. "High energy gain in three-dimensional sim-ulations of light sail acceleration". In: *Applied Physics Letters* 105 (8 2014), p. 084105. DOI: 10.1063/1.4894092 (cit. on p. 28).

[123]   F Dollar et al. "Finite Spot Effects on Radiation Pressure Acceleration from Intense High-Contrast Laser Interactions with Thin Targets". In: *Physical Review Letters* 108 (17 2012), p. 175005. DOI: 10.1103/PhysRevLett.108.175005 (cit. on pp. 28, 78).

[124]   S Kar et al. "Ion Acceleration in Multispecies Targets Driven by Intense Laser Radiation Pressure". In: *Physical Review Letters* 109 (18 2012), p. 185006. DOI: 10.1103/PhysRevLett.109.185006 (cit. on p. 28).

[125]   S Steinke et al. "Stable laser-ion acceleration in the light sail regime". In: *Physical Review Special Topics - Accelerators and Beams* 16 (1 2013), p. 011303. DOI: 10.1103/PhysRevSTAB.16.011303 (cit. on p. 28).

[126]   CAJ Palmer et al. "Rayleigh-Taylor Instability of an Ultrathin Foil Accelerated by the Radiation Pressure of an Intense Laser". In: *Physical Review Letters* 108 (22 2012), p. 225002. DOI: 10.1103/PhysRevLett.108.225002 (cit. on pp. 28, 78).

[127]   J Bin et al. "Ion Acceleration Using Relativistic Pulse Shaping in Near-Critical-Density Plasmas". In: *Physical Review Letters* 115 (6 2015), p. 064801. DOI: 10.1103/PhysRevLett.115.064801 (cit. on pp. 28, 58, 78, 96).

[128]   C Scullion et al. "Polarization Dependence of Bulk Ion Acceleration from Ultrathin Foils Irradiated by High-Intensity Ultrashort Laser Pulses". In: *Physical Review Letters* 119 (5 2017), p. 054801. DOI: 10.1103/PhysRevLett.119.054801 (cit. on p. 28).

[129]   A McIlvenny et al. "Selective Ion Acceleration by Intense Radiation Pressure". In: *Physical Review Letters* 127 (19 2021), p. 194801. DOI: 10.1103/PhysRevLett.127.194801 (cit. on pp. 28, 78).

[130]   A Henig et al. "Enhanced Laser-Driven Ion Acceleration in the Relativistic Transparency Regime". In: *Physical Review Letters* 103 (4 2009), p. 045002. DOI: 10.1103/PhysRevLett.103.045002 (cit. on pp. 28, 30, 77, 78, 91, 96, 107).

[131]   B Hegelich et al. "Experimental demonstration of particle energy, conversion efficiency and spectral shape required for ion-based fast ignition". In: *Nuclear Fusion* 51 (8 2011), p. 083011. DOI: 10.1088/0029-5515/51/8/083011 (cit. on pp. 28, 30, 77).

[132]   D Jung et al. "Monoenergetic Ion Beam Generation by Driving Ion Solitary Waves with Circularly Polarized Laser Light". In: *Physical Review Letters* 107 (11 2011), p. 115002. DOI: 10.1103/PhysRevLett.107.115002 (cit. on pp. 28, 30, 77).

[133]   BM Hegelich et al. "Laser-driven ion acceleration from relativistically transparent nanotargets". In: *New Journal of Physics* 15 (8 2013), p. 085015. DOI: 10.1088/1367-2630/15/8/085015 (cit. on pp. 28, 30, 77, 78, 86, 96).

[134]   D Jung et al. "Laser-driven 1GeV carbon ions from preheated diamond targets in the break-out afterburner regime". In: *Physics of Plasmas* 20 (8 2013), p. 083103. DOI: 10.1063/1.4817287 (cit. on pp. 28, 30, 77, 78).

[135]   HW Powell et al. "Proton acceleration enhanced by a plasma jet in expanding foils undergoing relativistic transparency". In: *New Journal of Physics* 17 (10 2015), p. 103033. DOI: 10.1088/1367-2630/17/10/103033 (cit. on pp. 28, 30, 31, 77, 78, 106).

[136]   S Palaniyappan et al. "Efficient quasi-monoenergetic ion beams from laser-driven relativistic plasmas". In: *Nature Communications* 6 (1 2015), p. 10170. DOI: 10.1038/ncomms10170 (cit. on pp. 28, 30, 77).

[137] M King et al. "Ion acceleration and plasma jet formation in ultra-thin foils undergoing expansion and relativistic transparency". In: *Nuclear Instruments and Methods in Physics Research, Section A: Accelerators, Spectrometers, Detectors and Associated Equipment* 829 (2016), pp. 163–166. DOI: 10.1016/j.nima.2016.02.032 (cit. on pp. 28, 31, 77).

[138] NP Dover et al. "Buffered high charge spectrally-peaked proton beams in the relativistic-transparency regime". In: *New Journal of Physics* 18 (1 2016), p. 013038. DOI: 10.1088/1367-2630/18/1/013038 (cit. on pp. 28, 77, 78).

[139] A Higginson et al. "Near-100 MeV protons via a laser-driven transparency-enhanced hybrid acceleration scheme". In: *Nature Communications* 9 (1 2018), p. 724. DOI: 10.1038/s41467-018-03063-9 (cit. on pp. 28, 30, 31, 58, 77, 78, 91, 95, 96, 106, 107).

[140] J Li et al. "Laser-driven acceleration of quasi-monoenergetic, near-collimated titanium ions via a transparency-enhanced acceleration scheme". In: *New Journal of Physics* 21 (10 2019), p. 103005. DOI: 10.1088/1367-2630/ab4454 (cit. on pp. 28, 30, 77).

[141] O McCusker et al. "Multi-species ion acceleration from sub-ps, PW interactions with ultra-thin foils". In: *Plasma Physics and Controlled Fusion* 65 (1 2023), p. 015005. DOI: 10.1088/1361-6587/aca1dc (cit. on pp. 28, 31, 77).

[142] AV Kuznetsov et al. "Efficiency of ion acceleration by a relativistically strong laser pulse in an underdense plasma". In: *Plasma Physics Reports* 27 (3 2001), pp. 211–220. DOI: 10.1134/1.1354219 (cit. on pp. 28, 32).

[143] SV Bulanov et al. "Ion Acceleration in a Dipole Vortex in a Laser Plasma Corona". In: *Plasma Physics Reports* 31 (5 2005), p. 369. DOI: 10.1134/1.1925787 (cit. on pp. 28, 32, 78).

[144] L Yin et al. "GeV laser ion acceleration from ultrathin targets: The laser break-out afterburner". In: *Laser and Particle Beams* 24 (2 2006), pp. 291–298. DOI: 10.1017/S0263034606060459 (cit. on pp. 28, 29).

[145] BJ Albright et al. "Relativistic Buneman instability in the laser breakout afterburner". In: *Physics of Plasmas* 14 (9 2007), p. 094502. DOI: 10.1063/1.2768933 (cit. on pp. 28, 30).

[146] L Yin et al. "Monoenergetic and GeV ion acceleration from the laser breakout afterburner using ultrathin targets". In: *Physics of Plasmas* 14 (5 2007), p. 056706. DOI: 10.1063/1.2436857 (cit. on pp. 28, 29, 78, 96).

[147] SS Bulanov et al. "Generation of GeV protons from 1 PW laser interaction with near critical density targets". In: *Physics of Plasmas* 17 (4 2010), p. 043105. DOI: 10.1063/1.3372840 (cit. on pp. 28, 32).

[148] XQ Yan et al. "Theory of laser ion acceleration from a foil target of nanometer thickness". In: *Applied Physics B* 98 (4 2010), pp. 711–721. DOI: 10.1007/s00340-009-3707-5 (cit. on pp. 28, 29).

[149] HB Zhuo et al. "Quasimonoenergetic Proton Bunch Generation by Dual-Peaked Electrostatic-Field Acceleration in Foils Irradiated by an Intense Linearly Polarized Laser". In: *Physical Review Letters* 105 (6 2010), p. 065003. DOI: 10.1103/PhysRevLett.105.065003 (cit. on pp. 28, 30).

[150] L Yin et al. "Three-Dimensional Dynamics of Breakout Afterburner Ion Acceleration Using High-Contrast Short-Pulse Laser and Nanoscale Targets". In: *Physical Review Letters* 107 (4 2011), p. 045003. DOI: 10.1103/PhysRevLett.107.045003 (cit. on pp. 28, 29).

[151] AA Sahai et al. "Relativistically induced transparency acceleration of light ions by an ultrashort laser pulse interacting with a heavy-ion-plasma density gradient". In: *Physical Review E* 88 (4 2013), p. 043105. DOI: `10.1103/PhysRevE.88.043105` (cit. on p. 28).

[152] H Padda et al. "Intra-pulse transition between ion acceleration mechanisms in intense laser-foil interactions". In: *Physics of Plasmas* 23 (6 2016), p. 063116. DOI: `10.1063/1.4954654` (cit. on pp. 28, 31).

[153] R Mishra, F Fiuza, and S Glenzer. "Enhanced ion acceleration in transition from opaque to transparent plasmas". In: *New Journal of Physics* 20 (4 2018), p. 043047. DOI: `10.1088/1367-2630/aab8db` (cit. on pp. 28, 31, 96).

[154] DJ Stark et al. "A detailed examination of laser-ion acceleration mechanisms in the relativistic transparency regime using tracers". In: *Physics of Plasmas* 25 (4 2018), p. 043114. DOI: `10.1063/1.5028129` (cit. on pp. 28, 30, 78, 86).

[155] B Qiao et al. "Revisit on ion acceleration mechanisms in solid targets driven by intense laser pulses". In: *Plasma Physics and Controlled Fusion* 61 (1 2019), p. 014039. DOI: `10.1088/1361-6587/aaf18e` (cit. on pp. 28, 30).

[156] XF Shen et al. "Scaling laws for laser-driven ion acceleration from nanometer-scale ultrathin foils". In: *Physical Review E* 104 (2 2021), p. 025210. DOI: `10.1103/PhysRevE.104.025210` (cit. on p. 28).

[157] J Goodman et al. "Optimisation of multi-petawatt laser-driven proton acceleration in the relativistic transparency regime". In: *New Journal of Physics* 24 (5 2022), p. 053016. DOI: `10.1088/1367-2630/ac681f` (cit. on pp. 28, 31, 78, 96, 108).

[158] B Gonzalez-Izquierdo et al. "Towards optical polarization control of laser-driven proton acceleration in foils undergoing relativistic transparency". In: *Nature Communications* 7 (1 2016), p. 12891. DOI: `10.1038/ncomms12891` (cit. on pp. 28, 78).

[159] B Gonzalez-Izquierdo et al. "Optically controlled dense current structures driven by relativistic plasma aperture-induced diffraction". In: *Nature Physics* 12 (5 2016), pp. 505–512. DOI: `10.1038/nphys3613` (cit. on p. 28).

[160] V Bagnoud et al. "Studying the Dynamics of Relativistic Laser-Plasma Interaction on Thin Foils by Means of Fourier-Transform Spectral Interferometry". In: *Physical Review Letters* 118 (25 2017), p. 255003. DOI: `10.1103/PhysRevLett.118.255003` (cit. on pp. 28, 107, 108).

[161] S Williamson et al. "Self-Referencing Spectral Interferometric Probing of the Onset Time of Relativistic Transparency in Intense Laser-Foil Interactions". In: *Physical Review Applied* 14 (3 2020), p. 034018. DOI: `10.1103/PhysRevApplied.14.034018` (cit. on pp. 28, 107, 108).

[162] TP Frazer et al. "Enhanced laser intensity and ion acceleration due to self-focusing in relativistically transparent ultrathin targets". In: *Physical Review Research* 2 (4 2020), p. 042015. DOI: `10.1103/PhysRevResearch.2.042015` (cit. on p. 28).

[163] MJ Duff et al. "High order mode structure of intense light fields generated via a laser-driven relativistic plasma aperture". In: *Scientific Reports* 10 (1 2020), p. 105. DOI: `10.1038/s41598-019-57119-x` (cit. on p. 28).

[164] EFJ Bacon et al. "High order modes of intense second harmonic light produced from a plasma aperture". In: *Matter and Radiation at Extremes* 7 (5 2022), p. 054401. DOI: `10.1063/5.0097585` (cit. on p. 28).

[165] A Pukhov, ZM Sheng, and J Meyer-ter-Vehn. "Particle acceleration in relativistic laser channels". In: *Physics of Plasmas* 6 (7 1999), pp. 2847–2854. DOI: 10.1063/1.873242 (cit. on p. 29).

[166] AV Arefiev et al. "Beyond the ponderomotive limit: Direct laser acceleration of relativistic electrons in sub-critical plasmas". In: *Physics of Plasmas* 23 (5 2016), p. 056704. DOI: 10.1063/1.4946024 (cit. on p. 29).

[167] ON Rosmej et al. "High-current laser-driven beams of relativistic electrons for high energy density research". In: *Plasma Physics and Controlled Fusion* 62 (11 2020), p. 115024. DOI: 10.1088/1361-6587/abb24e (cit. on p. 29).

[168] PK Singh et al. "Vacuum laser acceleration of super-ponderomotive electrons using relativistic transparency injection". In: *Nature Communications* 13 (1 2022), p. 54. DOI: 10.1038/s41467-021-27691-w (cit. on pp. 29, 84).

[169] VA Vshivkov et al. "Nonlinear electrodynamics of the interaction of ultra-intense laser pulses with a thin foil". In: *Physics of Plasmas* 5 (7 1998), pp. 2727–2741. DOI: 10.1063/1.872961 (cit. on pp. 29, 96).

[170] F Cattani et al. "Threshold of induced transparency in the relativistic interaction of an electromagnetic wave with overdense plasmas". In: *Physical Review E* 62 (1 2000), pp. 1234–1237. DOI: 10.1103/PhysRevE.62.1234 (cit. on p. 29).

[171] VV Goloviznin and TJ Schep. "Self-induced transparency and self-induced opacity in laser-plasma interactions". In: *Physics of Plasmas* 7 (5 I 2000), pp. 1564–1571. DOI: 10.1063/1.873976 (cit. on p. 29).

[172] VI Eremin, AV Korzhimanov, and AV Kim. "Relativistic self-induced transparency effect during ultraintense laser interaction with overdense plasmas: Why it occurs and its use for ultrashort electron bunch generation". In: *Physics of Plasmas* 17 (4 2010), p. 043102. DOI: 10.1063/1.3368791 (cit. on p. 29).

[173] M Tushentsov et al. "Electromagnetic Energy Penetration in the Self-Induced Transparency Regime of Relativistic Laser-Plasma Interactions". In: *Physical Review Letters* 87 (27 2001), p. 275002. DOI: 10.1103/PhysRevLett.87.275002 (cit. on p. 29).

[174] SM Weng et al. "Ultra-intense laser pulse propagation in plasmas: from classic hole-boring to incomplete hole-boring with relativistic transparency". In: *New Journal of Physics* 14 (6 2012), p. 063026. DOI: 10.1088/1367-2630/14/6/063026 (cit. on p. 29).

[175] E Siminos et al. "Effect of electron heating on self-induced transparency in relativistic-intensity laser-plasma interactions". In: *Physical Review E* 86 (5 2012), p. 056404. DOI: 10.1103/PhysRevE.86.056404 (cit. on p. 29).

[176] J Fuchs et al. "Ion acceleration using high-contrast ultra-intense lasers". In: *Journal de Physique IV (Proceedings)* 133 (2006), pp. 1151–1153. DOI: 10.1051/jp4:2006133235 (cit. on p. 29).

[177] D Neely et al. "Enhanced proton beams from ultrathin targets driven by high contrast laser pulses". In: *Applied Physics Letters* 89 (2 2006), p. 021502. DOI: 10.1063/1.2220011 (cit. on pp. 29, 58).

[178] P McKenna et al. "High-intensity laser-driven proton acceleration: influence of pulse contrast". In: *Philosophical Transactions of the Royal Society A: Mathematical, Physical and Engineering Sciences* 364 (1840 2006), pp. 711–723. DOI: 10.1098/rsta.2005.1733 (cit. on p. 29).

[179]   O Buneman. "Instability, Turbulence, and Conductivity in Current-Carrying Plasma". In: *Physical Review Letters* 1 (1 1958), pp. 8–9. DOI: `10.1103/PhysRevLett.1.8` (cit. on p. 30).

[180]   D Jung et al. "Efficient carbon ion beam generation from laser-driven volume acceleration". In: *New Journal of Physics* 15 (2 2013), p. 023007. DOI: `10.1088/1367-2630/15/2/023007` (cit. on p. 30).

[181]   D Jung et al. "Beam profiles of proton and carbon ions in the relativistic transparency regime". In: *New Journal of Physics* 15 (12 2013), p. 123035. DOI: `10.1088/1367-2630/15/12/123035` (cit. on p. 30).

[182]   D Jung et al. "Scaling of ion energies in the relativistic-induced transparency regime". In: *Laser and Particle Beams* 33 (4 2015), pp. 695–703. DOI: `10.1017/S0263034615000828` (cit. on p. 30).

[183]   B Qiao et al. "Dominance of Radiation Pressure in Ion Acceleration with Linearly Polarized Pulses at Intensities of 10^{21} W cm^{-2}". In: *Physical Review Letters* 108 (11 2012), p. 115002. DOI: `10.1103/PhysRevLett.108.115002` (cit. on pp. 30, 107).

[184]   F Wagner et al. "Simultaneous observation of angularly separated laser-driven proton beams accelerated via two different mechanisms". In: *Physics of Plasmas* 22 (6 2015), p. 063110. DOI: `10.1063/1.4922661` (cit. on p. 31).

[185]   TZ Esirkepov et al. "Ion acceleration by superintense laser pulses in plasmas". In: *Journal of Experimental and Theoretical Physics Letters* 70 (2 1999), pp. 82–89. DOI: `10.1134/1.568134` (cit. on p. 32).

[186]   F Peano, RA Fonseca, and LO Silva. "Dynamics and Control of Shock Shells in the Coulomb Explosion of Very Large Deuterium Clusters". In: *Physical Review Letters* 94 (3 2005), p. 033401. DOI: `10.1103/PhysRevLett.94.033401` (cit. on p. 32).

[187]   K Nishihara et al. "High energy ions generated by laser driven Coulomb explosion of cluster". In: *Nuclear Instruments and Methods in Physics Research Section A: Accelerators, Spectrometers, Detectors and Associated Equipment* 464 (1-3 2001), pp. 98–102. DOI: `10.1016/S0168-9002(01)00014-6` (cit. on p. 32).

[188]   AE Kaplan, BY Dubetsky, and PL Shkolnikov. "Shock Shells in Coulomb Explosions of Nanoclusters". In: *Physical Review Letters* 91 (14 2003), p. 143401. DOI: `10.1103/PhysRevLett.91.143401` (cit. on p. 32).

[189]   T Ditmire et al. "High-energy ions produced in explosions of superheated atomic clusters". In: *Nature* 386 (6620 1997), pp. 54–56. DOI: `10.1038/386054a0` (cit. on p. 32).

[190]   E Springate et al. "Explosion of atomic clusters irradiated by high-intensity laser pulses: Scaling of ion energies with cluster and laser parameters". In: *Physical Review A* 61 (6 2000), p. 063201. DOI: `10.1103/PhysRevA.61.063201` (cit. on p. 32).

[191]   J Braenzel et al. "Coulomb-Driven Energy Boost of Heavy Ions for Laser-Plasma Acceleration". In: *Physical Review Letters* 114 (12 2015), p. 124801. DOI: `10.1103/PhysRevLett.114.124801` (cit. on p. 32).

[192]   P Hilz et al. "Isolated proton bunch acceleration by a petawatt laser pulse". In: *Nature Communications* 9 (1 2018), p. 423. DOI: `10.1038/s41467-017-02663-1` (cit. on pp. 32, 107).

[193]   E Fourkal, I Velchev, and CM Ma. "Coulomb explosion effect and the maximum energy of protons accelerated by high-power lasers". In: *Physical Review E* 71 (3 2005), p. 036412. DOI: `10.1103/PhysRevE.71.036412` (cit. on p. 32).

[194]   SS Bulanov et al. "Accelerating monoenergetic protons from ultrathin foils by flat-top laser pulses in the directed-Coulomb-explosion regime". In: *Physical Review E* 78 (2 2008), p. 026412. DOI: 10.1103/PhysRevE.78.026412 (cit. on p. 32).

[195]   SS Bulanov et al. "Accelerating protons to therapeutic energies with ultraintense, ultraclean, and ultrashort laser pulses". In: *Medical Physics* 35 (5 2008), pp. 1770–1776. DOI: 10.1118/1.2900112 (cit. on p. 32).

[196]   EA Govras, VY Bychenkov, and VF Kovalev. "Acceleration of light ions from an expanding ultrathin foil of complex ion composition". In: *Plasma Physics Reports* 36 (8 2010), pp. 709–718. DOI: 10.1134/S1063780X10080076 (cit. on p. 32).

[197]   EA Govras, VY Bychenkov, and AV Brantov. "Coulomb acceleration of light ions from homogeneous and layered targets". In: *Journal of Experimental and Theoretical Physics* 114 (5 2012), pp. 748–767. DOI: 10.1134/S1063776112040073 (cit. on p. 32).

[198]   IM Gabdrakhmanov and EA Govras. "Analytical Model of the Coulomb Explosion of a Flat Uniform Target with Two Sorts of Ions". In: *Plasma Physics Reports* 48 (2 2022), pp. 155–169. DOI: 10.1134/S1063780X22020064 (cit. on p. 32).

[199]   T Nakamura et al. "High-Energy Ions from Near-Critical Density Plasmas via Magnetic Vortex Acceleration". In: *Physical Review Letters* 105 (13 2010), p. 135002. DOI: 10.1103/PhysRevLett.105.135002 (cit. on p. 32).

[200]   J Park et al. "Ion acceleration in laser generated megatesla magnetic vortex". In: *Physics of Plasmas* 26 (10 2019), p. 103108. DOI: 10.1063/1.5094045 (cit. on p. 32).

[201]   S Hakimi et al. "Laser–solid interaction studies enabled by the new capabilities of the iP2 BELLA PW beamline". In: *Physics of Plasmas* 29 (8 2022), p. 083102. DOI: 10.1063/5.0089331 (cit. on p. 32).

[202]   K Matsukado et al. "Energetic Protons from a Few-Micron Metallic Foil Evaporated by an Intense Laser Pulse". In: *Physical Review Letters* 91 (21 2003), p. 215001. DOI: 10.1103/PhysRevLett.91.215001 (cit. on p. 32).

[203]   A Yogo et al. "Laser ion acceleration via control of the near-critical density target". In: *Physical Review E* 77 (1 2008), p. 016401. DOI: 10.1103/PhysRevE.77.016401 (cit. on p. 32).

[204]   L Willingale et al. "Characterization of High-Intensity Laser Propagation in the Relativistic Transparent Regime through Measurements of Energetic Proton Beams". In: *Physical Review Letters* 102 (12 2009), p. 125002. DOI: 10.1103/PhysRevLett.102.125002 (cit. on p. 32).

[205]   L Willingale et al. "High-power, kilojoule laser interactions with near-critical density plasma". In: *Physics of Plasmas* 18 (5 2011), p. 056706. DOI: 10.1063/1.3563438 (cit. on p. 32).

[206]   L Willingale et al. "Collimated Multi-MeV Ion Beams from High-Intensity Laser Interactions with Underdense Plasma". In: *Physical Review Letters* 96 (24 2006), p. 245002. DOI: 10.1103/PhysRevLett.96.245002 (cit. on p. 32).

[207]   Y Fukuda et al. "Energy Increase in Multi-MeV Ion Acceleration in the Interaction of a Short Pulse Laser with a Cluster-Gas Target". In: *Physical Review Letters* 103 (16 2009), p. 165002. DOI: 10.1103/PhysRevLett.103.165002 (cit. on p. 32).

[208]   M Helle et al. "Laser-Accelerated Ions from a Shock-Compressed Gas Foil". In: *Physical Review Letters* 117 (16 2016), p. 165001. DOI: 10.1103/PhysRevLett.117.165001 (cit. on p. 32).

[209]   SV Bulanov and TZ Esirkepov. "Comment on "Collimated Multi-MeV Ion Beams from High-Intensity Laser Interactions with Underdense Plasma"". In: *Physical Review Letters* 98 (4 2007), p. 049503. DOI: `10.1103/PhysRevLett.98.049503` (cit. on p. 32).

[210]   L Willingale et al. "Willingale et al. Reply:" in: *Physical Review Letters* 98 (4 2007), p. 049504. DOI: `10.1103/PhysRevLett.98.049504` (cit. on p. 32).

[211]   TH Maiman. "Stimulated Optical Radiation in Ruby". In: *Nature* 187 (4736 1960), pp. 493–494 (cit. on p. 33).

[212]   FJ McClung and RW Hellwarth. "Giant Optical Pulsations from Ruby". In: *Journal of Applied Physics* 33 (3 1962), pp. 828–829. DOI: `10.1063/1.1777174` (cit. on p. 34).

[213]   WE Lamb. "Theory of an Optical Maser". In: *Physical Review* 134 (6A 1964), A1429–A1450. DOI: `10.1103/PhysRev.134.A1429` (cit. on p. 34).

[214]   LE Hargrove, RL Fork, and MA Pollack. "Locking of He–Ne Laser Modes Induced by Synchronous Intracavity Modulation". In: *Applied Physics Letters* 5 (1 1964), pp. 4–5. DOI: `10.1063/1.1754025` (cit. on p. 34).

[215]   J Brons et al. "Energy scaling of Kerr-lens mode-locked thin-disk oscillators". In: *Optics Letters* 39 (22 2014), p. 6442. DOI: `10.1364/OL.39.006442` (cit. on p. 34).

[216]   PF Moulton. "Spectroscopic and laser characteristics of $Ti : Al_2O_3$". In: *Journal of the Optical Society of America B* 3 (1 1986), p. 125. DOI: `10.1364/JOSAB.3.000125` (cit. on pp. 35, 38).

[217]   D Strickland and G Mourou. "Compression of amplified chirped optical pulses". In: *Optics Communications* 56 (3 1985), pp. 219–221. DOI: `10.1016/0030-4018(85)90120-8` (cit. on p. 35).

[218]   A Dubietis, G Jonušauskas, and A Piskarskas. "Powerful femtosecond pulse generation by chirped and stretched pulse parametric amplification in BBO crystal". In: *Optics Communications* 88 (4-6 1992), pp. 437–440. DOI: `10.1016/0030-4018(92)90070-8` (cit. on pp. 35, 45).

[219]   I Ross et al. "The prospects for ultrashort pulse duration and ultrahigh intensity using optical parametric chirped pulse amplifiers". In: *Optics Communications* 144 (1-3 1997), pp. 125–133. DOI: `10.1016/S0030-4018(97)00399-4` (cit. on pp. 35, 45).

[220]   X Zeng et al. "Multi-petawatt laser facility fully based on optical parametric chirped-pulse amplification". In: *Optics Letters* 42 (10 2017), p. 2014. DOI: `10.1364/OL.42.002014` (cit. on pp. 35, 36, 45).

[221]   K Nakamura et al. "Diagnostics, Control and Performance Parameters for the BELLA High Repetition Rate Petawatt Class Laser". In: *IEEE Journal of Quantum Electronics* 53 (4 2017), pp. 1–21. DOI: `10.1109/JQE.2017.2708601` (cit. on pp. 36, 58).

[222]   V Yanovsky et al. "Ultra-high intensity- 300-TW laser at 0.1 Hz repetition rate". In: *Optics Express* 16 (3 2008), p. 2109. DOI: `10.1364/OE.16.002109` (cit. on p. 36).

[223]   EW Gaul et al. "Demonstration of a 1.1 petawatt laser based on a hybrid optical parametric chirped pulse amplification/mixed Nd:glass amplifier". In: *Appl. Opt.* 49.9 (2010), pp. 1676–1681. DOI: `10.1364/AO.49.001676` (cit. on p. 36).

[224]   JH Kelly et al. "OMEGA EP: High-energy petawatt capability for the OMEGA laser facility". In: *Journal de Physique IV (Proceedings)* 133 (2006), pp. 75–80. DOI: `10.1051/jp4:2006133015` (cit. on p. 36).

[225]   C Barty et al. "An overview of LLNL high-energy short-pulse technology for advanced radiography of laser fusion experiments". In: *Nuclear Fusion* 44 (12 2004), S266–S275. DOI: 10.1088/0029-5515/44/12/S18 (cit. on p. 36).

[226]   S Vallières et al. "The laser-driven ion acceleration beamline on the ALLS 200 TW for testing nanowire targets". In: *Laser Acceleration of Electrons, Protons, and Ions V* (2019). Ed. by E Esarey, CB Schroeder, and J Schreiber, p. 2. DOI: 10.1117/12.2520178 (cit. on p. 36).

[227]   J Zhu et al. "Analysis and construction status of SG-II 5PW laser facility". In: *High Power Laser Science and Engineering* 6 (2018), e29. DOI: 10.1017/hpl.2018.23 (cit. on p. 36).

[228]   Z Zhang et al. "The 1 PW / 0.1 Hz laser beamline in SULF facility". In: *High Power Laser Science and Engineering* 8 (2020), e4. DOI: 10.1017/hpl.2020.3 (cit. on p. 36).

[229]   AX Li et al. "Acceleration of 60 MeV proton beams in the commissioning experiment of SULF-10 PW laser". In: *High Power Laser Science and Engineering* 10 (2022), pp. 1–20. DOI: 10.1017/hpl.2022.17 (cit. on p. 36).

[230]   Z Wang et al. "High-contrast 1.16PW Ti:sapphire laser system combined with a doubled chirped-pulse amplification scheme and a femtosecond optical-parametric amplifier". In: *Optics Letters* 36 (16 2011), p. 3194. DOI: 10.1364/OL.36.003194 (cit. on p. 36).

[231]   YX Geng et al. "Generating Proton Beams Exceeding 10MeV Using High Contrast 60TW Laser". In: *Chinese Physics Letters* 35 (9 2018), p. 092901. DOI: 10.1088/0256-307X/35/9/092901 (cit. on p. 36).

[232]   W Hong et al. "Commissioning experiment of the high-contrast SILEX-II multi-petawatt laser facility". In: *Matter and Radiation at Extremes* 6 (6 2021), p. 064401. DOI: 10.1063/5.0016019 (cit. on p. 36).

[233]   H Kiriyama et al. "High-contrast high-intensity repetitive petawatt laser". In: *Optics Letters* 43 (11 2018), p. 2595. DOI: 10.1364/OL.43.002595 (cit. on pp. 36, 44, 58, 79).

[234]   JH Sung et al. "4.2PW, 20fs Ti:sapphire laser at 0.1Hz". In: *Optics Letters* 42 (11 2017), p. 2058. DOI: 10.1364/OL.42.002058 (cit. on pp. 36, 58).

[235]   VV Lozhkarev et al. "Compact 0.56 Petawatt laser system based on optical parametric chirped pulse amplification in KD*P crystals". In: *Laser Physics Letters* 4 (6 2007), pp. 421–427. DOI: 10.1002/lapl.200710008 (cit. on p. 36).

[236]   E Kroupp et al. "Commissioning and first results from the new 2×100TW laser at the WIS". In: *Matter and Radiation at Extremes* 7 (4 2022), p. 044401. DOI: 10.1063/5.0090514 (cit. on p. 36).

[237]   V Bagnoud et al. "Commissioning and early experiments of the PHELIX facility". In: *Applied Physics B* 100 (1 2010), pp. 137–150. DOI: 10.1007/s00340-009-3855-7 (cit. on p. 36).

[238]   M Cerchez et al. "ARCTURUS laser: a versatile high-contrast, high-power multi-beam laser system". In: *High Power Laser Science and Engineering* 7 (2019), e37. DOI: 10.1017/hpl.2019.21 (cit. on p. 36).

[239]   U Schramm et al. "First results with the novel petawatt laser acceleration facility in Dresden". In: *Journal of Physics: Conference Series* 874 (1 2017), p. 012028. DOI: 10.1088/1742-6596/874/1/012028 (cit. on pp. 36, 58).

[240] D Albach et al. "Performance demonstration of the PEnELOPE main amplifier HE-PA1 using broadband nanosecond pulses". In: *High Power Laser Science and Engineering* 7 (2019), e1. DOI: `10.1017/hpl.2018.59` (cit. on p. 36).

[241] M Hornung et al. "54J pulses with 18nm bandwidth from a diode-pumped chirped-pulse amplification laser system". In: *Optics Letters* 41 (22 2016), p. 5413. DOI: `10.1364/OL.41.005413` (cit. on p. 36).

[242] J Hartmann et al. "Commissioning of the laser-driven ion acceleration beamline at the Centre for Advanced Laser Applications". In: *Laser Acceleration of Electrons, Protons, and Ions VI* (2021). Ed. by SS Bulanov, CB Schroeder, and J Schreiber, p. 21. DOI: `10.1117/12.2592407` (cit. on p. 36).

[243] C Danson et al. "Vulcan Petawatt—an ultra-high-intensity interaction facility". In: *Nuclear Fusion* 44 (12 2004), S239–S246. DOI: `10.1088/0029-5515/44/12/S15` (cit. on p. 36).

[244] CJ Hooker et al. "The Astra Gemini Petawatt Ti:Sapphire Laser". In: *The Review of Laser Engineering* 37 (6 2009), pp. 443–448. DOI: `10.2184/lsj.37.443` (cit. on p. 36).

[245] SM Wiggins et al. "Application programmes at the Scottish Centre for the Application of Plasma-based Accelerators (SCAPA)". In: *Relativistic Plasma Waves and Particle Beams as Coherent and Incoherent Radiation Sources III* (2019), p. 28. DOI: `10.1117/12.2520717` (cit. on p. 36).

[246] JL Miquel and E Prene. "LMJ & PETAL status and program overview". In: *Nuclear Fusion* 59 (3 2019), p. 032005. DOI: `10.1088/1741-4326/aac343` (cit. on p. 36).

[247] D Raffestin et al. "Enhanced ion acceleration using the high-energy petawatt PETAL laser". In: *Matter and Radiation at Extremes* 6 (5 2021), p. 056901. DOI: `10.1063/5.0046679` (cit. on p. 36).

[248] T Ceccotti et al. "Proton Acceleration with High-Intensity Ultrahigh-Contrast Laser Pulses". In: *Physical Review Letters* 99 (18 2007), p. 185002. DOI: `10.1103/PhysRevLett.99.185002` (cit. on p. 36).

[249] A Flacco et al. "Dependence on pulse duration and foil thickness in high-contrast-laser proton acceleration". In: *Physical Review E* 81 (3 2010), p. 036405. DOI: `10.1103/PhysRevE.81.036405` (cit. on p. 36).

[250] J Fuchs et al. "Laser-Foil Acceleration of High-Energy Protons in Small-Scale Plasma Gradients". In: *Physical Review Letters* 99 (1 2007), p. 015002. DOI: `10.1103/PhysRevLett.99.015002` (cit. on p. 36).

[251] K Burdonov et al. "Characterization and performance of the Apollon short-focal-area facility following its commissioning at 1 PW level". In: *Matter and Radiation at Extremes* 6 (6 2021), p. 064402. DOI: `10.1063/5.0065138` (cit. on p. 36).

[252] L Roso. "High repetition rate Petawatt lasers". In: *EPJ Web of Conferences* 167 (2018). Ed. by L Torrisi and M Cutroneo, p. 01001. DOI: `10.1051/epjconf/201816701001` (cit. on p. 36).

[253] F Schillaci et al. "The ELIMAIA Laser–Plasma Ion Accelerator: Technological Commissioning and Perspectives". In: *Quantum Beam Science* 6 (4 2022), p. 30. DOI: `10.3390/qubs6040030` (cit. on p. 36).

[254] S Kühn et al. "The ELI-ALPS facility: the next generation of attosecond sources". In: *Journal of Physics B: Atomic, Molecular and Optical Physics* 50 (13 2017), p. 132002. DOI: `10.1088/1361-6455/aa6ee8` (cit. on p. 36).

[255] D Doria et al. "Overview of ELI-NP status and laser commissioning experiments with 1 PW and 10 PW class-lasers". In: *Journal of Instrumentation* 15 (09 2020), pp. C09053–C09053. DOI: 10.1088/1748-0221/15/09/C09053 (cit. on p. 36).

[256] MP Kalashnikov et al. "Double chirped-pulse-amplification laser: a way to clean pulses temporally". In: *Optics Letters* 30 (8 2005), p. 923. DOI: 10.1364/OL.30.000923 (cit. on p. 38).

[257] J Itatani et al. "Suppression of the amplified spontaneous emission in chirped-pulse-amplification lasers by clean high-energy seed-pulse injection". In: *Optics Communications* 148 (1-3 1998), pp. 70–74. DOI: 10.1016/S0030-4018(97)00638-X (cit. on pp. 38, 44).

[258] H Kiriyama et al. "Generation of high-contrast and high-intensity laser pulses using an OPCPA preamplifier in a double CPA, Ti:sapphire laser system". In: *Optics Communications* 282 (4 2009), pp. 625–628. DOI: 10.1016/j.optcom.2008.10.067 (cit. on pp. 38, 44).

[259] MP Kalashnikov et al. "Characterization of a nonlinear filter for the front-end of a high contrast double-CPA Ti:sapphire laser". In: *Optics Express* 12 (21 2004), p. 5088. DOI: 10.1364/OPEX.12.005088 (cit. on p. 38).

[260] MP Kalashnikov et al. "Temporal contrast of high intensity laser systems above 10^{11} with double CPA technique". In: 1462 (2012), pp. 108–111. DOI: 10.1063/1.4736771 (cit. on p. 38).

[261] NV Didenko et al. "Contrast degradation in a chirped-pulse amplifier due to generation of prepulses by postpulses". In: *Optics Express* 16 (5 2008), p. 3178. DOI: 10.1364/oe.16.003178 (cit. on pp. 38, 44, 59).

[262] DN Schimpf et al. "The impact of spectral modulations on the contrast of pulses of nonlinear chirped-pulse amplification systems". In: *Optics Express* 16 (14 2008), p. 10664. DOI: 10.1364/OE.16.010664 (cit. on pp. 38, 44).

[263] H Kiriyama et al. "Experimental investigation on the temporal contrast of pre-pulses by post-pulses in a petawatt laser facility". In: *Optics Letters* 45 (5 2020), p. 1100. DOI: 10.1364/OL.384759 (cit. on pp. 38, 44, 59).

[264] C Hooker et al. "Improving coherent contrast of petawatt laser pulses". In: *Optics Express* 19 (3 2011), p. 2193. DOI: 10.1364/OE.19.002193 (cit. on p. 39).

[265] V Bagnoud and F Salin. "Influence of optical quality on chirped-pulse amplification: characterization of a 150-nm-bandwidth stretcher". In: *Journal of the Optical Society of America B* 16 (1 1999), p. 188. DOI: 10.1364/JOSAB.16.000188 (cit. on p. 39).

[266] L Ranc et al. "Improvement in the temporal contrast in the tens of ps range of the multi-PW Apollon laser front-end". In: *Optics Letters* 45 (16 2020), p. 4599. DOI: 10.1364/ol.401272 (cit. on p. 39).

[267] H Kiriyama et al. "Enhancement of pre-pulse and picosecond pedestal contrast of the petawatt J-KAREN-P laser". In: *High Power Laser Science and Engineering* 9 (2021), e62. DOI: 10.1017/hpl.2021.51 (cit. on pp. 39, 46, 78).

[268] X Lu et al. "Reducing temporal pedestal in a Ti:sapphire chirped-pulse amplification system by using a stretcher based on two concave mirrors". In: *Optics Letters* 46 (21 2021), p. 5320. DOI: 10.1364/OL.435145 (cit. on pp. 39, 44, 78).

[269] N Khodakovskiy et al. "Degradation of picosecond temporal contrast of Ti:sapphire lasers with coherent pedestals". In: *Optics Letters* 41 (19 2016). DOI: 10.1364/OL.41.004441 (cit. on p. 39).

[270] G Cheriaux et al. "Aberration-free stretcher design for ultrashort-pulse amplification". In: *Optics Letters* 21 (6 1996), p. 414. DOI: 10.1364/OL.21.000414 (cit. on pp. 39, 45).

[271] P Tournois. "Acousto-optic programmable dispersive filter for adaptive compensation of group delay time dispersion in laser systems". In: *Optics Communications* 140 (4-6 1997), pp. 245–249. DOI: 10.1016/S0030-4018(97)00153-3 (cit. on p. 39).

[272] F Verluise et al. "Amplitude and phase control of ultrashort pulses by use of an acousto-optic programmable dispersive filter: pulse compression and shaping". In: *Optics Letters* 25 (8 2000), p. 575. DOI: 10.1364/OL.25.000575 (cit. on p. 39).

[273] T Oksenhendler et al. "Intracavity acousto-optic programmable gain control for ultra-wide-band regenerative amplifiers". In: *Applied Physics B* 83 (4 2006), pp. 491–494. DOI: 10.1007/s00340-006-2231-0 (cit. on p. 41).

[274] A Jullien et al. "10^{-10} temporal contrast for femtosecond ultraintense lasers by cross-polarized wave generation". In: *Optics Letters* 30 (8 2005), p. 920. DOI: 10.1364/OL.30.000920 (cit. on p. 41).

[275] F Druon et al. "Wave-front correction of femtosecond terawatt lasers by deformable mirrors". In: *Optics Letters* 23 (13 1998), p. 1043. DOI: 10.1364/OL.23.001043 (cit. on p. 42).

[276] P Bon et al. "Quadriwave lateral shearing interferometry for quantitative phase microscopy of living cells". In: *Optics Express* 17 (15 2009), p. 13080. DOI: 10.1364/OE.17.013080 (cit. on p. 42).

[277] F Zernike and FJM Stratton. "Diffraction Theory of the Knife-Edge Test and its Improved Form, The Phase-Contrast Method". In: *Monthly Notices of the Royal Astronomical Society* 94 (5 1934), pp. 377–384. DOI: 10.1093/mnras/94.5.377 (cit. on p. 42).

[278] H Kiriyama et al. "Laser Output Performance and Temporal Quality Enhancement at the J-KAREN-P Petawatt Laser Facility". In: *Photonics* 10 (9 2023), p. 997. DOI: 10.3390/photonics10090997 (cit. on p. 44).

[279] M Aoyama et al. "0.85-PW, 33-fs Ti:sapphire laser". In: *Optics Letters* 28 (17 2003), p. 1594. DOI: 10.1364/OL.28.001594 (cit. on p. 44).

[280] H Kiriyama et al. "High temporal and spatial quality petawatt-class Ti:sapphire chirped-pulse amplification laser system". In: *Optics Letters* 35 (10 2010), p. 1497. DOI: 10.1364/OL.35.001497 (cit. on p. 44).

[281] H Kiriyama et al. "Temporal contrast enhancement of petawatt-class laser pulses". In: *Optics Letters* 37 (16 2012), p. 3363. DOI: 10.1364/OL.37.003363 (cit. on p. 44).

[282] H Kiriyama et al. "High-Contrast, High-Intensity Petawatt-Class Laser and Applications". In: *IEEE Journal of Selected Topics in Quantum Electronics* 21 (1 2015), pp. 232–249. DOI: 10.1109/JSTQE.2014.2336774 (cit. on p. 44).

[283] AS Pirozhkov et al. "Approaching the diffraction-limited, bandwidth-limited Petawatt". In: *Optics Express* 25 (17 2017), p. 20486. DOI: 10.1364/OE.25.020486 (cit. on pp. 46, 79).

[284] A Măgureanu et al. "Target Characteristics Used in Laser-Plasma Acceleration of Protons Based on the TNSA Mechanism". In: *Frontiers in Physics* 10 (2022). DOI: 10.3389/fphy.2022.727718 (cit. on p. 48).

[285] V Liechtenstein et al. "Preparation and evaluation of thin diamond-like carbon foils for heavy-ion tandem accelerators and time-of-flight spectrometers". In: *Nuclear Instruments and Methods in Physics Research Section A: Accelerators, Spectrometers, Detectors and Associated Equipment* 397 (1 1997), pp. 140–145. DOI: `10.1016/S0168-9002(97)00732-8` (cit. on p. 49).

[286] S Seuferling et al. "Efficient offline production of freestanding thin plastic foils for laser-driven ion sources". In: *High Power Laser Science and Engineering* 5 (2017), e8. DOI: `10.1017/hpl.2017.7` (cit. on p. 49).

[287] M Czerny and AF Turner. "Über den Astigmatismus bei Spiegelspektrometern". In: *Zeitschrift für Physik* 61 (11-12 1930), pp. 792–797. DOI: `10.1007/BF01340206` (cit. on p. 50).

[288] C Froehly, A Lacourt, and JC Viénot. "Time impulse response and time frequency response of optical pupils.:Experimental confirmations and applications". In: *Nouvelle Revue d'Optique* 4 (4 1973), pp. 183–196. DOI: `10.1088/0335-7368/4/4/301` (cit. on p. 51).

[289] T Oksenhendler et al. "Self-referenced spectral interferometry". In: *Applied Physics B* 99 (1-2 2010), pp. 7–12. DOI: `10.1007/s00340-010-3916-y` (cit. on p. 51).

[290] T Oksenhendler et al. "High dynamic, high resolution and wide range single shot temporal pulse contrast measurement". In: *Optics Express* 25 (11 2017), p. 12588. DOI: `10.1364/OE.25.012588` (cit. on p. 51).

[291] C Iaconis and I Walmsley. "Self-referencing spectral interferometry for measuring ultrashort optical pulses". In: *IEEE Journal of Quantum Electronics* 35 (4 1999), pp. 501–509. DOI: `10.1109/3.753654` (cit. on p. 51).

[292] J Thomson. "Rays of positive electricity". In: *The London, Edinburgh, and Dublin Philosophical Magazine and Journal of Science* 21 (122 1911), pp. 225–249. DOI: `10.1080/14786440208637024` (cit. on p. 52).

[293] A Alejo et al. "High resolution Thomson Parabola Spectrometer for full spectral capture of multi-species ion beams". In: *Review of Scientific Instruments* 87 (8 2016), p. 83304. DOI: `10.1063/1.4961028` (cit. on p. 52).

[294] K Zeil et al. "Absolute response of Fuji imaging plate detectors to picosecond-electron bunches". In: *Review of Scientific Instruments* 81 (1 2010). DOI: `10.1063/1.3284524` (cit. on p. 53).

[295] CG Freeman et al. "Calibration of a Thomson parabola ion spectrometer and Fujifilm imaging plate detectors for protons, deuterons, and alpha particles". In: *Review of Scientific Instruments* 82 (7 2011), p. 73301. DOI: `10.1063/1.3606446` (cit. on p. 53).

[296] D Doria et al. "Calibration of BAS-TR image plate response to high energy (3-300 MeV) carbon ions". In: *Review of Scientific Instruments* 86 (12 2015), p. 123302. DOI: `10.1063/1.4935582` (cit. on p. 53).

[297] D Golovin et al. "Calibration of imaging plates sensitivity to high energy photons and ions for laser-plasma interaction sources". In: *Journal of Instrumentation* 16 (02 2021), T02005–T02005. DOI: `10.1088/1748-0221/16/02/T02005` (cit. on p. 53).

[298] WE Stephens. "A Pulsed Mass Spectrometer with Time Dispersion". In: *Proceedings of the American Physical Society* 69 (1946) (cit. on p. 53).

[299] A Cameron and D Eggers. *THE ION VELOCITRON*. Divison of Technical Information Extension, 1947. DOI: `10.2172/4369457` (cit. on p. 53).

[300] M Reimold et al. "Time-of-flight spectroscopy for laser-driven proton beam monitoring". In: *Scientific Reports* 12 (1 2022), p. 21488. DOI: `10.1038/s41598-022-25120-6` (cit. on p. 54).

[301] V Scuderi et al. "Time of Flight based diagnostics for high energy laser driven ion beams". In: *Journal of Instrumentation* 12 (03 2017), pp. C03086–C03086. DOI: `10.1088/1748-0221/12/03/C03086` (cit. on p. 54).

[302] G Milluzzo et al. "A new energy spectrum reconstruction method for time-of-flight diagnostics of high-energy laser-driven protons". In: *Review of Scientific Instruments* 90 (8 2019), p. 083303. DOI: `10.1063/1.5082746` (cit. on p. 54).

[303] V Scuderi et al. "TOF diagnosis of laser accelerated, high-energy protons". In: *Nuclear Instruments and Methods in Physics Research Section A: Accelerators, Spectrometers, Detectors and Associated Equipment* 978 (2020), p. 164364. DOI: `10.1016/j.nima.2020.164364` (cit. on p. 54).

[304] M Salvadori et al. "Accurate spectra for high energy ions by advanced time-of-flight diamond-detector schemes in experiments with high energy and intensity lasers". In: *Scientific Reports* 11 (1 2021), p. 3071. DOI: `10.1038/s41598-021-82655-w` (cit. on p. 54).

[305] JS Green et al. "Scintillator-based ion beam profiler for diagnosing laser-accelerated ion beams". In: 44 (2011). Ed. by KWD Ledingham et al., p. 807919. DOI: `10.1117/12.888967` (cit. on p. 54).

[306] J Metzkes et al. "An online, energy-resolving beam profile detector for laser-driven proton beams". In: *Review of Scientific Instruments* 87 (8 2016), p. 083310. DOI: `10.1063/1.4961576` (cit. on p. 54).

[307] NP Dover et al. "Scintillator-based transverse proton beam profiler for laser-plasma ion sources". In: *Review of Scientific Instruments* 88 (7 2017), p. 073304. DOI: `10.1063/1.4994732` (cit. on p. 54).

[308] H Tang et al. "Scintillator detector characterization for laser-driven proton beam imaging". In: *Review of Scientific Instruments* 91 (12 2020), p. 123304. DOI: `10.1063/5.0022166` (cit. on p. 54).

[309] A Buck et al. "Absolute charge calibration of scintillating screens for relativistic electron detection". In: *Review of Scientific Instruments* 81 (3 2010). DOI: `10.1063/1.3310275` (cit. on p. 54).

[310] Gafchromic. `http://www.gafchromic.com/gafchromic-film/radiotherapy-films/index.asp`. [Online; accessed 19-October-2022] (cit. on pp. 55, 80).

[311] F Nürnberg et al. "Radiochromic film imaging spectroscopy of laser-accelerated proton beams". In: *Review of Scientific Instruments* 80 (3 2009), p. 033301. DOI: `10.1063/1.3086424` (cit. on p. 55).

[312] JF Ziegler and JP Biersack. *The Stopping and Range of Ions in Matter*. Springer US, 1985. DOI: `10.1007/978-1-4615-8103-1_3` (cit. on p. 55).

[313] JM Yang et al. "Nuclear reactions in copper induced by protons from a petawatt laser-foil interaction". In: *Applied Physics Letters* 84 (5 2004), pp. 675–677. DOI: `10.1063/1.1645314` (cit. on p. 56).

[314] M Tarisien et al. In: *Review of Scientific Instruments* 82.2 (2011), p. 023302. DOI: `10.1063/1.3527061` (cit. on p. 56).

[315] MM Günther et al. "NAIS: Nuclear activation-based imaging spectroscopy". In: *Review of Scientific Instruments* 84 (7 2013), p. 073305. DOI: `10.1063/1.4815826` (cit. on p. 56).

[316] F Wagner et al. "Maximum Proton Energy above 85 MeV from the Relativistic In-teraction of Laser Pulses with Micrometer Thick CH2 Targets". In: *Physical Review Letters* 116 (20 2016), p. 205002. DOI: `10.1103/PhysRevLett.116.205002` (cit. on pp. 58, 95).

[317] D Papadopoulos et al. "The Apollon 10PW laser: experimental and theoretical investigation of the temporal characteristics". In: *High Power Laser Science and En-gineering* 4 (2016), e34. DOI: `10.1017/hpl.2016.34` (cit. on p. 58).

[318] Z Gan et al. "200 J high efficiency Ti:sapphire chirped pulse amplifier pumped by temporal dual-pulse". In: *Optics Express* 25 (5 2017), p. 5169. DOI: `10.1364/0E.25.005169` (cit. on p. 58).

[319] JS Green et al. "High efficiency proton beam generation through target thickness control in femtosecond laser-plasma interactions". In: *Applied Physics Letters* 104 (21 2014), p. 214101. DOI: `10.1063/1.4879641` (cit. on p. 58).

[320] D Margarone et al. "Laser-driven high-energy proton beam with homogeneous spatial profile from a nanosphere target". In: *Physical Review Special Topics - Acceler-ators and Beams* 18 (7 2015), p. 071304. DOI: `10.1103/PhysRevSTAB.18.071304` (cit. on p. 58).

[321] J Bin et al. "Enhanced Laser-Driven Ion Acceleration by Superponderomotive Elec-trons Generated from Near-Critical-Density Plasma". In: *Physical Review Letters* 120 (7 2018), p. 074801. DOI: `10.1103/PhysRevLett.120.074801` (cit. on p. 58).

[322] LA Gizzi et al. "Intense proton acceleration in ultrarelativistic interaction with nanochan-nels". In: *Physical Review Research* 2 (3 2020), p. 033451. DOI: `10.1103/PhysRevResearch.2.033451` (cit. on p. 58).

[323] L Obst et al. "On-shot characterization of single plasma mirror temporal contrast improvement". In: *Plasma Physics and Controlled Fusion* 60 (5 2018), p. 054007. DOI: `10.1088/1361-6587/aab3bb` (cit. on p. 58).

[324] RJ Shalloo et al. "Automation and control of laser wakefield accelerators using Bayesian optimization". In: *Nature Communications* 11 (1 2020), p. 6355. DOI: `10.1038/s41467-020-20245-6` (cit. on p. 58).

[325] HC Kapteyn et al. "Prepulse energy suppression for high-energy ultrashort pulses using self-induced plasma shuttering". In: *Optics Letters* 16 (7 1991), p. 490. DOI: `10.1364/0L.16.000490` (cit. on p. 60).

[326] G Doumy et al. "Complete characterization of a plasma mirror for the produc-tion of high-contrast ultraintense laser pulses". In: *Physical Review E* 69 (2 2004), p. 026402. DOI: `10.1103/PhysRevE.69.026402` (cit. on p. 60).

[327] B Dromey et al. "The plasma mirror - a subpicosecond optical switch for ultrahigh power lasers". In: *Review of Scientific Instruments* 75 (3 2004), pp. 645–649. DOI: `10.1063/1.1646737` (cit. on p. 60).

[328] GG Scott et al. "Optimization of plasma mirror reflectivity and optical quality using double laser pulses". In: *New Journal of Physics* 17 (3 2015), p. 033027. DOI: `10.1088/1367-2630/17/3/033027` (cit. on p. 60).

[329] S Inoue et al. "Single plasma mirror providing 10^4 contrast enhancement and 70% reflectivity for intense femtosecond lasers". In: *Applied Optics* 55 (21 2016), p. 5647. DOI: `10.1364/A0.55.005647` (cit. on p. 60).

[330] IW Choi et al. "Highly efficient double plasma mirror producing ultrahigh-contrast multi-petawatt laser pulses". In: *Optics Letters* 45 (23 2020), p. 6342. DOI: `10.1364/0L.409749` (cit. on p. 60).

[331] JP Heritage, AM Weiner, and RN Thurston. "Picosecond pulse shaping by spectral phase and amplitude manipulation". In: *Optics Letters* 10 (12 1985), p. 609. DOI: `10.1364/OL.10.000609` (cit. on p. 63).

[332] S Souri, R Amrollahi, and R Sadighi-Bonabi. "Laser-driven proton acceleration enhancement by the optimized intense short laser pulse shape". In: *Physics of Plasmas* 24 (5 2017), p. 053108. DOI: `10.1063/1.4982611` (cit. on p. 73).

[333] S Kumar, K Gopal, and DN Gupta. "Proton acceleration from overdense plasma target interacting with shaped laser pulses in the presence of preplasmas". In: *Plasma Physics and Controlled Fusion* 61 (8 2019), p. 085001. DOI: `10.1088/1361-6587/ab216e` (cit. on p. 73).

[334] J Ferri et al. "Proton acceleration by a pair of successive ultraintense femtosecond laser pulses". In: *Physics of Plasmas* 25 (4 2018), p. 43115. DOI: `10.1063/1.5026391` (cit. on p. 73).

[335] M Garten. "Temporal contrast-dependent modeling of laser-driven solids". PhD thesis. Technische Universität Dresden, 2022 (cit. on p. 73).

[336] I Göthel. "Numerical simulations on proton acceleration from near-critical density targets". in preparation. PhD thesis. Technische Universität Dresden, 2024 (cit. on pp. 73, 104).

[337] J Derouillat et al. "Smilei : A collaborative, open-source, multi-purpose particle-in-cell code for plasma simulation". In: *Computer Physics Communications* 222 (2018), pp. 351–373. DOI: `10.1016/j.cpc.2017.09.024` (cit. on p. 73).

[338] FE Brack et al. "Spectral and spatial shaping of laser-driven proton beams using a pulsed high-field magnet beamline". In: *Scientific Reports* 10 (1 2020), p. 9118. DOI: `10.1038/s41598-020-65775-7` (cit. on p. 75).

[339] J Fuchs et al. "Comparison of Laser Ion Acceleration from the Front and Rear Surfaces of Thin Foils". In: *Physical Review Letters* 94 (4 2005), p. 045004. DOI: `10.1103/PhysRevLett.94.045004` (cit. on p. 78).

[340] EJ Dolier et al. "Multi-parameter Bayesian optimisation of laser-driven ion acceleration in particle-in-cell simulations". In: *New Journal of Physics* 24 (7 2022), p. 073025. DOI: `10.1088/1367-2630/ac7db4` (cit. on pp. 78, 108).

[341] D Haffa et al. "Temporally Resolved Intensity Contouring (TRIC) for characterization of the absolute spatio-temporal intensity distribution of a relativistic, femtosecond laser pulse". In: *Scientific Reports* 9 (1 2019), p. 7697. DOI: `10.1038/s41598-019-42683-z` (cit. on pp. 82, 83).

[342] C Bernert et al. "Transient Laser-Induced Breakdown of Dielectrics in Ultrarelativistic Laser-Solid Interactions". In: *Physical Review Applied* 19 (1 2023), p. 014070. DOI: `10.1103/PhysRevApplied.19.014070` (cit. on pp. 82, 104).

[343] C Bernert. "Plasma dynamics between laser-induced breakdown and relativistically induced transparency". submitted. PhD thesis. Technische Universität Dresden, 2023 (cit. on p. 83).

[344] D Wang et al. "Laser-induced damage thresholds of ultrathin targets and their constraint on laser contrast in laser-driven ion acceleration experiments". In: *High Power Laser Science and Engineering* 8 (2020), e41. DOI: `10.1017/hpl.2020.40` (cit. on p. 83).

[345] B Fryxell et al. "FLASH: An Adaptive Mesh Hydrodynamics Code for Modeling Astrophysical Thermonuclear Flashes". In: *The Astrophysical Journal Supplement Series* 131 (1 2000), pp. 273–334. DOI: `10.1086/317361` (cit. on pp. 84, 104).

[346] S Faik, A Tauschwitz, and I Iosilevskiy. "The equation of state package FEOS for high energy density matter". In: *Computer Physics Communications* 227 (2018), p. 117. DOI: `10.1016/j.cpc.2018.01.008` (cit. on p. 84).

[347] TD Arber et al. "Contemporary particle-in-cell approach to laser-plasma modelling". In: *Plasma Physics and Controlled Fusion* 57 (2015), p. 113001. DOI: `10.1088/0741-3335/57/11/113001` (cit. on p. 84).

[348] SA Gaillard et al. "Increased laser-accelerated proton energies via direct laser-light-pressure acceleration of electrons in microcone targets". In: *Physics of Plasmas* 18 (5 2011), p. 056710. DOI: `10.1063/1.3575624` (cit. on p. 95).

[349] T Ziegler et al. "Proton beam quality enhancement by spectral phase control of a PW-class laser system". In: *Scientific Reports* 11 (1 2021), p. 7338. DOI: `10.1038/s41598-021-86547-x` (cit. on p. 96).

[350] H Burau et al. "PIConGPU: A Fully Relativistic Particle-in-Cell Code for a GPU Cluster". In: *IEEE Transactions on Plasma Science* 38 (10 2010), pp. 2831–2839. DOI: `10.1109/TPS.2010.2064310` (cit. on p. 104).

[351] M Bussmann et al. "Radiative signatures of the relativistic Kelvin-Helmholtz instability". In: *Proceedings of the International Conference on High Performance Computing, Networking, Storage and Analysis* (2013), pp. 1–12. DOI: `10.1145/2503210.2504564` (cit. on p. 104).

[352] S Kesselheim et al. "JUWELS Booster – A Supercomputer for Large-Scale AI Research". In: vol. 12761 LNCS. Springer Science and Business Media Deutschland GmbH, 2021, pp. 453–468. DOI: `10.1007/978-3-030-90539-2_31` (cit. on p. 104).

[353] S Baton et al. "Evidence of ultrashort electron bunches in laser-plasma interactions at relativistic intensities". In: *Physical Review Letters* 91.10 (2003), p. 105001. DOI: `10.1103/PhysRevLett.91.105001` (cit. on p. 106).

[354] T Kluge et al. "High proton energies from cone targets: electron acceleration mechanisms". In: *New Journal of Physics* 14.2 (2012), p. 023038. DOI: `10.1088/1367-2630/14/2/023038` (cit. on p. 106).

[355] RB White and FF Chen. "Amplification and absorption of electromagnetic waves in overdense plasmas". In: *Plasma Physics* 16 (7 1974), pp. 565–587. DOI: `10.1088/0032-1028/16/7/002` (cit. on p. 106).

[356] P Mulser, D Bauer, and H Ruhl. "Collisionless laser-energy conversion by anharmonic resonance". In: *Physical Review Letters* 101.22 (2008), p. 225002. DOI: `10.1103/PhysRevLett.101.225002` (cit. on p. 106).

[357] NP Dover et al. "Enhanced ion acceleration from transparency-driven foils demonstrated at two ultraintense laser facilities". In: *Light: Science & Applications* 12 (1 2023), p. 71. DOI: `10.1038/s41377-023-01083-9` (cit. on p. 106).

[358] IJ Kim et al. "Transition of Proton Energy Scaling Using an Ultrathin Target Irradiated by Linearly Polarized Femtosecond Laser Pulses". In: *Physical Review Letters* 111 (16 2013), p. 165003. DOI: `10.1103/PhysRevLett.111.165003` (cit. on p. 107).

[359] A Huebl et al. "Spectral control via multi-species effects in PW-class laser-ion acceleration". In: *Plasma Physics and Controlled Fusion* 62 (12 2020), p. 124003. DOI: `10.1088/1361-6587/abbe33` (cit. on p. 107).

[360] S Palaniyappan et al. "Dynamics of relativistic transparency and optical shuttering in expanding overdense plasmas". In: *Nature Physics* 8 (10 2012), pp. 763–769. DOI: `10.1038/nphys2390` (cit. on pp. 107, 108).

Danksagung

Mit der Fertigstellung dieser Arbeit ist ein anstrengender aber auch ungemein interessanter Abschnitt meines bisherigen Wegs abgeschlossen. Dieser war geprägt von vielen spannenden Themen, Diskussionen, Erfahrungen, Reisen und natürlich Menschen. Für all diese Dinge bin ich sehr dankbar und möchte mich daher bei den Personen bedanken, die diesen Weg mit mir gegangen sind.

Zuerst sei dabei den beiden Direktoren unseres Instituts Professor Ulrich Schramm und Professor Thomas Cowan dafür gedankt, dass ich die Möglichkeit hatte in einem perfekt ausgestattetem Umfeld an spannenden und zukunftsrelevanten Themen zu arbeiten. Danke für die Betreuung dieser Dissertation, die schnelle Anfertigung der Gutachten sowie die Chance meine Arbeit auf internationalen Konferenzen präsentieren und dabei mit interessanten Personen ins Gespräch kommen zu können. Mit Tom über Physik zu diskutieren ist ebenso unterhaltsam wie fordernd. Sein Enthusiasmus ansteckend, die neuen Blickwinkel konstruktiv und seine knappe Zeit hilfreich um inhaltliche Argumente präzise zu formulieren. Bei Uli möchte ich mich sehr für die große Unterstützung und Förderung bedanken, die ich während meiner Zeit am HZDR erfahren habe. Das einem deine Tür (fast) immer offen steht, macht es leichter administrative oder wissenschaftliche Dinge anzusprechen und bestenfalls zu klären. Danke zudem für den Feinschliff an so einigen Texten, die Inspiration für Vorträge sowie die spannenden Einblicke in die politische Seite der Wissenschaft.

An zweiter Stelle möchte ich mich bei der kompletten Arbeitsgruppe Ionenbeschleunigung und dessen Leitfigur Karl Zeil bedanken. Studien von derartiger Komplexität und mit so großem Umfang wären ohne ein gut funktionierendes und entsprechend koordiniertes Team nicht möglich gewesen. Ich bin wirklich sehr dankbar mit so motivierten Doktoranden wie Constantin, Elias, Florian B., Lennart, Lotti, Martin, Marvin, Milenko, Stefan A. sowie den erfahrenen Postdoc's Josefine, Florian K., Hans-Peter und Stephan zusammengearbeitet zu haben. Durch unsere gemeinsamen Anstrengungen, konnten wir in den Jahren wirklich viele anspruchsvolle Experimente planen, aufbauen, durchführen, gemeinsam besprechen und auswerten. Besonders hervorzuheben ist zudem die schier unerschöpfliche Motivation und Zeit, die Karl aufbringt, um bei bestehenden Probleme zu helfen. Sei es durch Ratschläge, Textüberarbeitung, als Diskussionspartner oder als Mensch gewordenes Laborlexikon. Dein Ehrgeiz bestehende Probleme mit absoluter Hingabe zu bewältigen und die ehrliche Selbstreflexion deiner eigenen Ansichten dienen sicherlich vielen in unserer Gruppe als Vorbild.

Die Reisen nach Japan und die Durchführung der Experimente dort stellen einen besonderen Teil meiner Promotionszeit dar. Hier konnte ich eine Menge sowohl über die Kul-

Selbstständigkeitserklärung

Hiermit versichere ich, dass ich die vorliegende Arbeit ohne unzulässige Hilfe Dritter und ohne Benutzung anderer als der angegebenen Hilfsmittel angefertigt habe; die aus fremden Quellen direkt oder indirekt übernommenen Gedanken sind als solche kenntlich gemacht. Die Arbeit wurde bisher weder im Inland noch im Ausland in gleicher oder ähnlicher Form einer anderen Prüfungsbehörde vorgelegt.
Die Promotionsordnung der Fakultät Mathematik und Naturwissenschaften an der Technischen Universität Dresden vom 23.02.2011 mit letzten Änderungen vom 23.05.2018 erkenne ich an.

Dresden, 15.01.2024

Tim Ziegler